Recent Progress on Spherical Torus Research*

Masayuki Ono and Robert Kaita

Plasma Physics Laboratory, Princeton University, Princeton, New Jersey 08543, USA

Abstract: The spherical torus or spherical tokamak (ST) is a member of the tokamak family with its aspect ratio ($A = R_0/a$) reduced to A ~ 1.5, well below the normal tokamak operating range of A ≥ 2.5. As the aspect ratio is reduced, the ideal tokamak beta β (radio of plasma to magnetic pressure) stability limit increases rapidly, approximately as $\beta \sim 1/A$. The plasma current it can sustain for a given edge safety factor q-95 also increases rapidly. Because of the above, as well as the natural elongation κ, which makes its plasma shape appear spherical, the ST configuration can yield exceptionally high tokamak performance in a compact geometry. Due to its compactness and high performance, the ST configuration has various near term applications, including a compact fusion neutron source with low tritium consumption, in addition to its longer term goal of attractive fusion energy power source. Since the start of the two mega-ampere class ST facilities in 2000, National Spherical Torus Experiment (NSTX) in the US and Mega Ampere Spherical Tokamak (MAST) in UK, active ST research has been conducted worldwide. More than sixteen ST research facilities operating during this period have achieved remarkable advances in all of fusion science areas, involving fundamental fusion energy science as well as innovation. These results suggest exciting future prospects for ST research both near term and longer term. The present paper reviews the scientific progress made by the worldwide ST research community during this new mega-ampere-ST era.

Contents:

I. Introduction

A spherical torus or tokamak (ST) is a tokamak with an aspect-ratio (A = R/a) of less than 2, where R is the plasma major radius and a is the minor radius. After over a decade of ST research at the megaampere (MA) level with over 16 ST facilities (shown in Figs. 1 and 2), there are a large number of significant ST results which are unique to STs, while at the same time reaffirming many common physics features with conventional tokamaks [1-19]. As a member of the tokamak family [20], ST research contributes to advancing conventional tokamaks such as ITER [21, 22] by providing data that extends into a unique plasma and device parameter space. Since ITER represents a significant extrapolation from the present day tokamaks, ST research provides a different set of tokamak-related data for the improvement of predictive capabilities by providing leverage over a wide range of parameter space. The plan of the review starts with a short overview of the ST research (Sec. IA), the present facilities (Sec. I-B), and the new 2 MA-class ST facilities NSTX-U [23] and MAST-U [24] presently under construction (Sec. I-C). The ST fusion energy development path is described in Sec. II. The science topical areas are covered in sections on macrostability (Sec. III), solenoid-free start-up (Sec. IV), turbulence and transport (Sec. V), H-mode physics (Sec. VI), boundary physics (VII), energetic particle physics (VIII), and wave physics (IX). In Sec. X, integration results and issues are discussed. The conclusions and discussion are in Sec. XI. As

supplemental information, in Appendix A, the basic properties of the ST/tokamak configuration is given along with the definitions of key ST/tokamak parameters. In Appendix B, a brief history of ST concept development in the context of the tokamak research is given. In Appendix C, the ST's relationship with other confinement concepts is described. It should be noted that the present paper mainly utilizes material from peer-reviewed journals, but where appropriate, major conference-related publications are included. This particularly holds for descriptions of the most recent results, since ST research is very much a rapidly evolving area in the magnetic fusion. Since the present paper is an ST review article, the references are mainly given for ST research publications. We should note, however, that there is a strong synergy between on-going ST research and other configurations, particularly the very active tokamak research conducted worldwide. The relevant research on tokamaks and other configurations can generally be found in the references in the ST publications cited in this review paper. Also, since there are a larger number of published ST related papers, only the most recent publications on a given topic are referenced. The main purpose of this review paper is to give a comprehensive description of recent progress in ST research, rather than give a historical perspective on the research. For those readers interested in the historical development of the ST, relevant references are usually given within the publications cited in this paper.

A. Overview – In this overview of ST research, we emphasize those aspects that are unique to the ST. We revisit the original mission elements of NSTX and MAST as stated in References 1-4. Many of the objectives have been achieved and expectations have been exceeded, while many surprises were encountered as well. There are also many unresolved issues and the parameters not yet reached. One of the high-level goals for NSTX was to achieve the high β regime of ~ 40% toroidal beta (β_T). As shown in Fig. 3, the present ST data base spans a large plasma beta space, extending well beyond that obtained in tokamak research reaching β_T of ~ 40%. This milestone was successfully achieved, and reaffirmed the basic soundness of theoretical MHD predictions. Another important goal was to attain a high normalized β (β_N) of ~ 8, which is needed to obtain a high bootstrap current fraction (f_{BS}) in the ~ 90% range at high β_T ~ 40% required for a

compact ST power plant. The highest β_N in NSTX was about 6.5 as shown in Fig. 4, and the highest f_{BS} was $\leq 50 - 60$ %. While these values are sufficient for a fusion nuclear science facility (FNSF) where the required $f_{BS} \sim 50 - 60$ %, higher β_N will require the further optimization of plasma pressure and current profiles. For profile control, off-axis NBI and EBW heating and current drive techniques will be explored in NSTX-U and MAST-U. Improved RWM stabilization using sophisticated control coils is also planned on NSTX-U. An alternative for an ST power plant is an ST with superconducting TF magnets (SCST), which is larger in size ($R \geq 4.5$ m compared to $R \sim 3$m for a compact copper based power plant). This is due to the need for increased inboard shielding, but because of reduced recirculating power and increased volume, the required β_N and β_T would be much lower, i. e., close to presently achieved values or that required for FNSF. The SCST power plant is also technically less challenging due to lower neutron wall loading and divertor heat flux. The plasma disruptivity is also an important topic for accessing reliable steady-state operation of future devices, and disruptivity trends have been investigated over various parameter ranges. While this work has just begun, disruptivity trends appear to be favorable for future expected operating parameters.

A tokamak typically requires an inboard ohmic solenoid, i. e., along the central axis of the torus, to generate its plasma current. However, since compact ST-FSNF and ST power plant designs provide little to no space for the inboard ohmic solenoid, "solenoid-free" techniques for plasma current startup and ramp-up are needed. Even for a tokamak reactor design, it is highly desirable to eliminate the solenoid. Naturally, this has been an area of significant research emphasis within the world ST research community, and there are a number of solenoid-free ST start-up concepts already demonstrated as shown in Fig. 5 [27 – 29]. Concepts based on radio-frequency wave heating and current drive are the most widely pursued, utilizing electron cyclotron heating (ECH), electron Bernstein waves (EBW), and lower hybrid (LH) waves. The most successful approach is ECH-based start-up, which has generated solenoid-free plasma current of ~ 70 kA in MAST and QUEST with high efficiency. MW-level ECH start-up experiments are planned on NSTX-U, QUEST, and MAST-U. The coaxial helicity injection (CHI) method uses electrical discharges to generate plasma current. On NSTX, ~ 200 kA of start-up current

was generated. While this was less than ~ 500 kA initially projected in Ref. 1, the improved means of injecting poloidal flux in NSTX-U should help achieve the desired plasma start-up current. High harmonic fast wave heating was shown to heat ~ 300 eV ohmically-heated plasmas to a few keV, as anticipated in Ref. 1. However, the electron temperature in CHI-generated plasmas was only ≤ 50 eV, and not sufficiently high to be heated by HHFW. A MW-class ECH heating is being prepared for NSTX-U to bridge this electron temperature gap. The merging-compression concept creates smaller current rings at the top and bottom, and then merges them at the mid-plane to form a larger current tokamak plasma. Using this method, a relatively high plasma current of ~ 400 kA has been generated in MAST. However, non-inductive current ramp-up from the start-up plasma to the high current operating range is one research area requiring considerable development in the future, as preparations for longer pulse operation in NSTX-U, MAST-U, and QUEST are being made with higher heating and current drive power.

In the area of plasma transport and confinement, the microscopic nature of the physical processes involved makes accurate predictions very challenging. Good energy confinement is essential for compact high performance ST reactor regimes, and is generally desirable from the perspective of fusion reactor economics. The observed ST H-mode plasma ion transport is quite close to neo-classical levels at most plasma radii in NSTX and MAST as shown in Fig. 6 [30]. This good ion confinement was predicted for STs due to the high level of ExB shear flow rate that can stabilize ion-scale turbulence in the ST geometry as noted in Ref. 1. Some unexpected positive results were also obtained. The plasma energy confinement was found to improve with reduced collisionality $\tau_{E,Thermal} \propto \nu_e^{*-1.0}$ in NSTX and MAST as shown in Fig. 7 [23, 31]. This trend correlated well with the behavior of micro-tearing modes that tend to be stabilized as the collisionality is reduced. Extending this favorable trend to lower collisionality is a high priority research topic for both NSTX-U and MAST-U. At present, overall H-mode confinement however appears to be similar to that of tokamaks. But an enhanced pedestal H-mode was found to give about a 50% improvement over the H-mode. The utilization of lithium was found to improve confinement by about 30%. Another significant advance is the understanding of electron transport by electron temperature

gradient modes (ETGs), where the high-k microwave scattering system enabled the measurement of ETGs and modeling has shown good agreement with the observed electron transport enhancement by ETGs in NSTX.

Power and particle handling at the plasma boundary is recognized as a highly challenging magnetic fusion research area, due to the very high expected steady-state divertor power flux. In Ref. 1, because of the compact nature of the ST geometry, the importance of developing practical methods for heat and particle handling was stressed. There are a number of important advances in this area. Multi-machine experiments (including both tokamaks and STs) showed the $1/B_p$ scaling of the divertor heat flux width. This unanticipated scaling appears to be favorable for relatively lower field STs, while posing a serious challenge for large current, high field tokamak reactors such as ITER. To mitigate the high heat flux problem, a large flux expansion of ~ 10 for NSTX was suggested in Ref. 1. In NSTX, an even larger flux expansion of ~ 50 was achieved with the snow-flake (SF) configuration, which resulted in a ~ 3 heat flux reduction (shown in Fig. 8) [32]. Another innovative divertor configuration that can lead to high flux expansion, the super-X configuration, is planned on MAST-U. Utilization of lithium as an alternative plasma facing material has been also actively pursued. A surprising reduction in divertor peak heat flux of ~ 2 was observed in NSTX with an application of relatively thin layer of lithium coating on the divertor PFCs. This observation has led to a radiative liquid lithium divertor concept proposed for future devices.

For the energetic particle (e.g., fusion alpha particle) physics research, ST plasmas are well suited to investigate the super-Alfvén regime, where the alpha or energetic particle velocity exceeds the Alfvén velocity and strong Alfvén wave excitation is expected. This condition is satisfied in reacting fusion plasmas including those anticipated for ITER. Since the Alfvén velocity V_A scales as $\beta^{-0.5}$ Cs, where Cs is the acoustic velocity, it is possible to access the super-Alfvén regime in NBI heated, high-β ST plasmas. As shown in Fig. 9 [33], STs can explore a very wide energetic particle parameter space. The most commonly excited toroidal Alfvén eigenmodes (TAEs) showed modification and stabilization in high β ST regimes. However, Alfvén avalanches involving overlapping

multiple TAE modes can be also triggered in the strongly-driven regime, causing significant energetic particle transport. The NSTX-U and MAST-U parameters with higher magnetic field (i. e., faster V_A) will also enable exploration of both sub- and super-Alfvénic regimes

Integrated scenario development synthesizes all the knowledge learned from the science topical areas and applies it to formulate and test the best possible operating scenarios for future applications. Naturally, the main aim is to come up with scenarios for sustained high performance non-inductive operations relevant for FNSF and power plant operations. For steady-state operation , it is highly important to increase f_{BS} as much as practical, since that would reduce the need for direct current drive and its associated recirculating power requirements and cost. In Fig. 10, an example of the rapid progress made in this area is shown, where the n=1 resistive wall mode instability which normally causes plasmas to terminate (particularly at low plasma rotation) was stabilized using passive and active feedback [34]. This resulted in the sustainment of a high $\beta_N \sim 6.0$ plasma, which is about 50% above the so-called no wall beta limit even at low plasma rotation in NSTX.

B. Description of Present ST Facilities - At the dawn of the 21st century, world ST research is being led in two magnetic fusion research laboratories on both sides of Atlantic. Plasma operation started nearly simultaneously on newly completed mega-ampere-class spherical tokamak (ST) facilities after a multi-year design and construction effort. Since the National Spherical Torus Experiment (NSTX) [1, 2] at PPPL in the US and the Mega Ampere Spherical Tokamak (MAST) [3, 4] at the Culham Laboratory in the UK began operating in 2000, very active ST research has been conducted worldwide. In Fig. 1, schematics of the MA-class ST facilities NSTX and MAST are shown. Both devices are similar in size and operating parameters, standing about three stories high, but with complementary engineering designs. More than sixteen ST research facilities operated during this period as shown in Fig. 1 and 2 [1 - 19]. Those ST facilities operated before 2000 including the START device are covered in the previous

review/overview papers [35, 36]. It also should be noted that the most of the ST facilities are located at universities with a strong student education mission.

NSTX and MAST - Mega Ampere-Class STs: There are two mega-ampere class ST facilities, both of which started research operation in 2000, the National Spherical Torus Experiment (NSTX) in the U.S. [1, 2] and the Mega-Ampere Spherical Tokamak (MAST) in the U.K [3, 4]. Both NSTX and MAST are equipped with strong auxiliary heating and advanced diagnostics for comprehensive ST physics and integrated operational scenario development capabilities. In Fig. 1, schematics of the NSTX and MAST devices and their key features are shown. The NSTX and MAST device and plasma parameters are similar: the major radius, R_0 = 80 - 85 cm, the minor radius, a = 55 - 65 cm, the plasma elongation, κ = 1.7 - 3.0, the plasma triangularity, δ = 0.3 - 0.8, the toroidal magnetic field, $B_{T0} \leq 5.5$ kG, the plasma current, $I_p \leq 1.5$ MA, the plasma volume, $V_p \leq 14$ m^3, and the plasma energy, $E_p \leq 0.5$ MJ. While NSTX and MAST have similar device and plasma parameters, they have important complementary features. As can be seen in Fig. 11, NSTX has a near-spherical vacuum vessel with a set of passive stabilizing plates near the plasma to offer effective wall stabilization at high β. NSTX also has electrical insulation between the center-stack and the outer vacuum vessel to allow up to 2 kV of DC electrical bias voltage for co-axial helicity injection (CHI) plasma start-up.

In a somewhat contrasting design, as can be seen in Fig. 12, MAST has a large cylindrical vacuum vessel with internal poloidal field (PF) coil sets which provide flexibility for plasma shaping and divertor configuration. The internal PF coils, being closer to the plasma, generally require less power for plasma control, and can also be used for PF coil-based plasma start up. MAST also has a large number of internal control (ELM) coils. Both devices have demountable TF coils, but MAST uses sliding joints and NSTX uses bolted flex joints. Both devices are heated by neutral beam injection (NBI), with $P_{NBI} \leq 7.4$ MW for NSTX and $P_{NBI} \leq 5.0$ MW for MAST. For radio frequency (RF) heating, NSTX has ~ 4 MW of high harmonic fast wave (HHFW) heating for electron heating and current drive, and MAST has ~ 0.2 MW of 28 GHz electron cyclotron heating for start-up and electron Bernstein wave (EBW) heating studies. Both MAST

and NSTX are in the midst of facility upgrades as described in Sec. C. Experimental research progress on NSTX and MAST is summarized in the overview Nuclear Fusion papers associated with the IAEA Fusion Energy Conferences [29, 37 - 49].

***GLOBUS-M*:** GLOBUS-M in the Russian Federation is a medium-sized ST shown in Fig. 13, with an emphasis in its research program on RF and NBI auxiliary heating at relatively high magnetic field [5]. The Globus-M device and plasma parameters are R_0 = 36 cm, a = 24 cm, κ = 1.5-2.0, $\delta \leq 0.5$, $B_{T0} \leq 4$ kG, and $I_p \sim 0.2$ MA. Globus-M plasmas are heated by $P_{NBI} \leq 0.8$ MW and $P_{ICRF} \leq 0.3$ MW. Globus-M can operate at relatively low edge safety factor $q_a = 2.7 – 5$, compared to typical STs which operate at relatively large $q_a \geq 6$ - 10. Globus-M is undergoing an upgrade (Globus-M2) on its magnets to operate at $B_{T0} \leq 1$ T with $I_p \sim 0.4$ MA [50]. Globus-M2 is scheduled to start plasma operation in 2015.

PEGASUS: PEGASUS at the University of Wisconsin is an ultra-low aspect-ratio medium size ST, and is presently focusing on plasma start-up and the MHD research [6, 51, 52]. The device has a highly-engineered ohmic heating solenoid, with very high magnetic field ($B_{sol} \leq 15$) capability within the constraints of very tight space. As shown in Fig. 14, with a very slender center-post, the device can access an ultra-low $A \geq 1.13$ regime with ohmic current drive. The Pegasus device and plasma parameters are $R_0 \leq 40$ cm, $RB_T \leq 0.028$ Tm, and $I_p \leq 0.2$ MA. Because of the high ohmic resistivity, Pegaus has achieved up to $\beta_T \sim 20\%$ and also the H-mode by ohmic heating alone.

CDX-U/LTX: The Current Drive Experiment-Upgrade (CDX-U) device and plasma parameters were R_0 = 34 cm, a = 22 cm, $B_{T0} \leq 2.1$ kG, and $I_p \sim 0.1$ MA. The CDX-U was the first fusion device to test the effectiveness of large free surface liquid lithium as a plasma facing component [7]. The CDX-U facility was upgraded significantly in 2009 to become the Lithium Tokamak Experiment (LTX) [8]. The projected LTX device and plasma parameters are R_0 = 40 cm, a = 26 cm, $B_{T0} \leq 3.4$ kG, and $I_p \sim 0.4$ MA with > 100 msec current flat top. The device has an internal plasma wall conformed to the plasma,

as shown Fig. 15. The main objective of the LTX experiment is to investigate the tokamak plasma performance enhancement under extremely low wall recycling.

HIT-II : The Helicity Injected Torus II (HIT-II) was a follow-on device to the Helicity Injected Torus (HIT) device [9] at the University of Washington. As shown in Fig. 16, HIT-II is a low-aspect-ratio tokamak with R_0 = 0.3 m, a = 0.2 m, and an on-axis toroidal field of up to 0.5 T. It had demonstrated 0.2 MA of toroidal plasma current, using either CHI or induction separately. The HIT group completed HIT-II operation in 2005, and is presently investigating a new current drive concept based on continuous helicity injection using a spheromak (HIT-SI).

QUEST / CPD – The Q-shu University Experiment with Steady State Spherical Tokamak (QUEST) is the newest and largest spherical tokamak at Kyushu University in Japan. It came into operation in 2008, with the goal of achieving long-pulse non-inductive ST operations. The QUEST device parameters are R_0 = 0.7 m, a = 0.48 m, A = 1.47, and B_T ~ 0.25 T [10]. The facility has 2.45GHz (50 kW), 8.2 GHz (400 kW), and 28GHz (500 kW) ECH sources and an all metal wall with tungsten limiters. The device schematic is shown in Fig. 17. QUEST eventually aims to achieve about 100 kA of steady-state (~1000 sec) non-inductive operation with 1 MW of ECH/EBW power. In order to address physics and technology issues for steady-state ST operation, three research areas are being pursued: non-inductive current drive, heat and particle handling, and integrated control research including the core plasma, plasma wall interactions, and the wall itself. The QUEST device has installed a hot wall, which can be heated to 300 – 500°C to study issues related to particle retention in walls. Prior to QUEST operation, the Kyushu group built a smaller ST called CPD, which operated for 2006 – 2008, investigating non-inductive plasma start-up.

TST-2: TST-2 device is located at the University of Tokyo, Japan. The device and plasma parameters are R_0 = 38 cm, a = 25 cm, $B_{T0} \leq$ 3.0 kG, and I_p ~ 0.2 MA [11]. The facility has radio frequency heating with high-harmonic fast wave (HHFW) power of up to 400 kW. The TST-2 device interior view is shown in Fig. 18. A variety of start-up research has been conducted by the group [12].

LATE: The Low Aspect Ratio Torus Experiment (LATE) device at Kyoto University, Japan was built utilizing the former WT-3 tokamak facility [13]. The main objective of the LATE device is to demonstrate formation of spherical torus (ST) plasmas by electron cyclotron heating (ECH) alone. The device cross section is shown in Fig. 19. With a relatively large vacuum vessel (about 1 m wide and 1 m height), and a center post only 11.4 cm wide, it is an ultra low aspect ratio device with $B_T \sim 1.15$ kG and $R_0 = 25$cm. The facility has 2.45GHz (20 kW) and 5 GHz (200 kW) ECH sources.

TS3//4: The TS-3 ST/CT merging device is a highly flexible basic physics facility with $R_0 = 0.18$-0.22 m, $R_0/a=1.5$, and $B_T \sim 0.5$ kG at the University of Tokyo, Japan [14]. It produces two ST plasmas as shown in Fig. 20. This is followed by so-called co-helicity merging, and an ultra-high beta (up to 80%) ST plasma is formed. The plasma is transiently heated by the conversion of magnetic energy through reconnection during the merging process. The TS-3 has recently started the NBI heating at the ~ 1 MW level to heat and sustain the formed plasma. TS-4 is a similar device to TS-3, but has larger dimensions.

UTST – The University of Tokyo Spherical Tokamak (UTST) is a new addition to the impressive collection of STs at the University of Tokyo, Japan. The device parameters are $R_0 = 0.4$ m (with a tall chamber height of 2.0 m), $R_0/a > 1.2$, $B_T = 1.8$ kG, and $I_p \sim 150$ kA [15]. The device is constructed to demonstrate the merging start-up scheme for a high-beta ST with ex-vessel PFC coils as shown in Fig. 21. To allow relatively rapid field penetration, the top and bottom sections of the UTST vacuum vessel are made of a thin stainless steel (1.5 mm) wall, supported by a 20 mm thick non-conducting material and 16 ribs. A 45 kV, 1 MW NBI system will be used for plasma heating and sustainment.

HIST – The Helicity Injected Spherical Torus (HIST) at Hyogo University, Japan is an ST facility which evolved from spheromak research. The device parameters are $R_0 = 0.3$ m, $a = 0.24$m, $R_0/a = 1.25$, $B_T = 1.0$ (3) kG, and $I_{TF} < 150$ kA [16]. The HIST device is similar in size and design to the HIT device. The main objectives of HIST is to use multi-pulse or repetitive transient CHI to achieve simultaneously quasi-steady plasma

sustainment and good confinement.

VEST – The Versatile Experiment Spherical Torus (VEST) is the newest ST located in Seoul National University, Korea, and it came on line in 2012 [17]. The device parameters are R_0 = 0.4 m (with a tall chamber height of 2.4 m), $R_0/a > 1.3$, B_T = 1.0 (3) kG, and $I_p \sim 30$ (100) kA as shown in Fig. 22. The main objectives of VEST is to conduct basic research on a compact, high-β ST with an elongated chamber with a partial ohmic solenoid to study innovative partial solenoid start-up, divertor physics, etc.

SUNIST – The Sino United Spherical Tokamak (SUNIST) is an ST device located in Tsinghua University, China. The device parameters are R_0 = 0.3 m with $R_0/a > 1.3$, B_T = 1.5 kG, and $I_p \sim 50$ kA [18]. The main objectives of SUNIST research is to investigate the properties of low aspect ratio toroidal plasmas and non-inductive plasma startup and current drive using both electron cyclotron and Alfven waves.

Other international STs - There are also other spherical tokamaks. The C-TOKASTAR device at Nagoya University, Japan is a low-aspect-ratio tokamak-helical hybrid device [53]. In Brazil, ETE is presently exploring wall eddy current effects [19]. In Italy, a new type of ST, PROTO-SPHERA, is being pursued [54]. This concept is composed of an ST with closed flux surfaces and a force-free screw pinch with open flux surfaces, and driven by electrodes to eliminate the in-board toroidal magnet entirely.

C. Description of NSTX-U and MAST-U – After over a decade of operations, both NSTX and MAST facilities are presently undergoing significant upgrades. Both devices are planning to nearly double the toroidal magnetic field, plasma current, and heating power, and extend the plasma pulse length from ~ 1 sec to ~ 3-5 sec. The anticipated plasma performance enhancement is a quadrupling of the plasma stored energy and near doubling of the plasma confinement time, which would result in 5 – 10 fold increase in the well-known fusion performance parameter of $n\tau T$. Even though the device sizes remain relatively compact, with ~ 1T toroidal magnetic fields and ~ 25% toroidal beta values, the absolute plasma pressure expected in the upgrade STs could be comparable to

that of the present day tokamaks. This should insure that the contributions of the ST community will continue to be at the forefront of magnetic confinement fusion research. Both NSTX-U and MAST-U retain the basic configuration of NSTX and MAST (see Figures 11 and 12), as much of each facility is utilized including the vacuum vessel, PF coils, and outer TF coils. Both upgraded facilities therefore continue to provide complementary physics and technology capabilities. For example, the 2nd NSTX-U neutral beam injection (NBI) achieves off-axis CD by strong tangential injection on the mid-plane. The MAST-U beams, on the other hand, utilize vertically off-set NBI to achieve off-axis CD. The divertor plasma material interaction (PMI) heat load solutions to be pursued for NSTX-U are the snow-flake / "x" configuration and liquid lithium, while on MAST-U, the "super-x" configuration will be pursued. The mission elements of the upgrades are in three areas: 1. Provide the necessary data base for ST-FNSF or ST-CTF, 2. Develop demo-relevant divertor PMI solutions, and 3. Advance toroidal plasma physics to develop better predictive capabilities to support ITER. A brief description of each of the upgrades is given below.

NSTX-Upgrade - An upgrade to the NSTX facility (NSTX-U) was proposed to provide timely input for the FNSF construction decision, develop new solutions for the plasma-material interface, and better support ITER [23]. The main elements of the NSTX Upgrade Project are a new and more powerful center-stack [55] and a tangentially-aimed 2nd Neutral Beam Injection (NBI) system. NSTX-U will double the toroidal field from ~ 0.5 T to 1 T, the plasma current from ~ 1 MA to 2 MA, the NBI heating and current drive power from ~ 7 MW to 14 MW at 90 kV, and it will greatly increase the peak field plasma pulse length from 1 sec to 7 sec. The larger cross section inner TF coil enables the doubling of the field and seven-fold increase in the pulse length as shown in Fig. 23. The NSTX-U and NSTX device parameters are given in Table 1. The tangential injection angles of the 2nd NBI, as shown in Fig. 24, enables much higher (~ 2 x) plasma current drive efficiency and current profile control needed for fully non-inductive plasma operation. The vacuum vessel and associated magnetic field coil support structures are being enhanced in order to handle the anticipated 4 x greater electromagnetic forces. The

NSTX upgrade project is now in the final construction phase, to be completed in March 2015, and NSTX-U research operations is planned to start in May 2015.

MAST-Upgrade – An upgrade to MAST (MAST-U) has been planned for a similar time frame as NSTX-U [56]. The MAST and MAST-U device parameters are shown in Table. 2. There are two programmatic emphases for the MAST-U design. The first goal is to test a novel "Super-X" divertor configuration (SXD) to reduce divertor peak heat loads, and to access predominantly non-inductively driven discharges with stationary plasma currents ~ 1 MA for longer than 2-3 current diffusion time. The MAST-U construction period is planned for 2013 – 2016, and its research operation is planned to start in 2017.
A cross-section of MAST-U is shown in Fig. 25. Both the MAST top and bottom divertors will be upgraded from the existing open configuration without density control to a closed, pumped divertor (cryogenic pumps based on supercritical helium) in both divertors to provide density control and access to low densities.
The demonstration of predominantly non-inductively driven scenarios in MAST-U will be achieved using an upgraded neutral beam configuration. The first stage will have three neutral beam sources, each injecting up to 2.5 MW, with two of the sources installed in elevated positions (Z=0.65m) for off-axis current drive as shown in Fig. 26. Two of the beam sources will be installed in a new Double Beam Box.

II. ST Fusion Development Path

A. Unique ST Features - In the limit of high aspect–ratio, the tokamak plasma cross section is circular without active shaping. As the aspect-ratio $A \equiv R / a$ is reduced, the plasma current ring starts to experience the influence of the poloidal fields generated by the current element on the opposite side of the torus. This self-generated field interaction causes the vertical elongation $\kappa \equiv b/a$ of the current ring to increase toward ~ 2, and the overall plasma shape becomes spherical as shown in Fig. 27 This formation of a sphericallyshaped tokamak plasma, even without active shaping, is the origin of the term "spherical" torus/tokamak [57, 58]. This property makes an ST MHD stable even at relatively high $\kappa > 2$. As noted in Fig. 27, the presence of the toroidal field coils provides robust MHD stability. This distinguishes an ST from other high β compact toroids such as the spheromak and field reversed configuration as noted in Appendix C. Earlier advanced ST configurations reactor studies with high bootstrap current fractions have motivated the ST fusion development path [59 - 62]. As the aspect ratio is reduced, there are a number of important changes in the device characteristics. Perhaps the most significant is the toroidal coil current I_{TF} compared to the plasma current I_p. Their relationship can be approximated by,

$$I_{TF} / I_p \sim (2 A^2 q^*) / (1 + \kappa^2) \qquad (1)$$

where $\kappa \equiv b/a$ is the plasma elongation and $q^* \equiv L_p B_{T0} / 2 \pi R_0 B_p$ is the cylindrical safety factor, where q^* should be ≥ 2 for stable tokamak/ST operations [21, 63]. Because of its low aspect ratio, STs can sustain almost as much plasma current as the toroidal coil current, while a conventional tokamak can support only about 10%.

The ST property of $I_{TF} \sim I_p$ makes the TF coil current in the ST relatively modest, and utilization of copper-based TF coils [64] becomes practical as shown in Fig. 28. Vertical replacement concepts of the center post have been developed for STs as described below. While the copper TF coil system increases recirculating power because of the copper coil ohmic loss, a copper coil-based power plant design study shows that the recirculating power fraction can be significant but manageable. The 1 GW-e ARIES-ST power plant design [65], for example, has the TF-coil ohmic loss (329 MW) to require about ~ 1 GW more total thermal power output as described in Sec. II. C.

Another important parameter is β_T, since the thermal fusion power output scales as β_T^2. The inherently high β_T operation for STs can be seen in the following relation derived from Eq. 1,

$$\beta_T \equiv \beta_N \; I_p / (aB_{T0}) = \beta_N \, (5 \, I_p / I_{TF}) \, A \sim \beta_N \; 5 \, (1 + \kappa^2) \; / (2 \, A \, q^*) \qquad (2)$$

where the normalized β (or β_N) is considered to be relatively constant, though there is a tendency for β_N to increase by about 50% for an ST compared to a conventional tokamak. As can be seen in Eq. (2), for a given β_N and β_T, $I_p / (aB_{T0})$ increases strongly with higher κ and reduced A and q^*. An ST tends to be able to access relatively high κ because of the natural elongation, which makes STs more vertically stable for a given κ. In Fig. 29, calculated ideal MHD stability limits for β_T, κ, and β_N for fully self-sustained wall-stabilized equilibria as a function of aspect ratio are plotted [66, 67]. The calculations show that β_T increases rapidly as A decreases. The rapid β_T increase is due to the combined effect of increasing κ and β_N as A is decreased by Eq. (2). The fusion power plant operating regime which requires near fully self-sustained plasma is usually intended to be designed below this ideal stability limit with a safety margin ~ 10%.

Another important quantity for an ST and tokamak power plant is the bootstrap current fraction f_{BS}. The bootstrap current is the neoclassical pressure driven current driven by the toroidal momentum transfer between trapped and passing particles, and has been confirmed in tokamak experiments [68, 69]. Ideally, one would like to have a large bootstrap current fraction, maintained by the pressure gradient from the fusion alpha heating power, for economical tokamak / ST based power plant operation. The f_{BS} can be expressed as

$$f_{BS} \equiv I_{BS} / I_p = C_{BS} \, \beta_p / A^{0.5} = (C_{BS}/20) \, A^{0.5} \, q^* \, \beta_N \; \propto A^{-0.5} \, (1+\kappa^2) \, \beta_N^2 / \beta_T \qquad (3)$$

where C_{BS} is a profile-dependent constant, typically ~ 0.6, and β_p is the poloidal beta. Since β_N rises by 50% as A is reduced from 3 to 1.5, $\beta_N \, A^{0.5}$ tends to be relatively constant. As there is a tendency for an ST power plant to run with higher values of q^*, the ST may be somewhat more favorable for achieving the high f_{BS} required for economical power plant operation. The plasma profiles are shown in Fig. 30 for A = 1.6 and 3.3 [66]. The profiles are quite similar for both

cases except for the q-profiles. The A = 1.6 case maintains nearly monotonic q-profile throughout all radii whereas the A = 3.3 case q-profile is relatively flat with reversed shear profile as envisioned for the Advanced Tokamak (AT). While the reversed shear may have the advantage of improved confinement, it maybe be more prone to global MHD instabilities. This q-profile difference between the ST and AT may become an important consideration for choosing a future DEMO/Power Plant design option. To provide information on the aspect-ratio choice for a tokamak DEMO/power plant is another important mission for on-going ST research. It should be pointed out that since the bootstrap current profile is determined by the plasma pressure profile, and fusion DEMO/Power Plant is mainly heated by the fusion α-particles, the plasma pressure profile is determined mainly by the plasma energy transport. It is therefore highly desirable to develop a tool to control the plasma energy transport for a high bootstrap current fraction DEMO/Power Plant [70].

A copper-based ST appears to be particularly attractive in the near term for a compact fusion neutron science facility (FNSF), where net electrical power generation is not its primary mission [71, 72]. A simplified schematic is shown in Fig. 28, where a single turn (solid copper) TF post generates the required toroidal field. As shown in the figure, some space (Δ) between the in-board TF magnet and the plasma is inevitably needed. At minimum, one would need an appropriate tile material to protect the copper TF coil from the plasma in that vicinity, where Δ maybe only a few cm. For simplicity, we assume a uniform current density j_{TF} within the TF center post with radius R_{TF}. Then the total TF center rod current I_{TF} goes up as R_{TF}^2 or $I_{TF} = \pi R_{TF}^2 j_{TF}$. But since $R_{TF} \propto R$ for a fixed A, I_{TF} scales as R^2. Since the device toroidal field $B_{TF} \propto I_{TF}/R$, $B_{TF} \propto R$ or B_{TF} goes up linearly with device major radius R for a fixed A. There are two ways to generate fusion neutrons, thermal fusion and beam-target fusion reactions. The thermal fusion power P_{fusion} generated for a given device is proportional to $V\,x\,(nT)^2$, or $P_{fusion} \propto V\,x\,B_T^4\,\beta_T^2$ where V is the plasma volume, nT is the plasma pressure, and $\beta_T \propto nT / B_T^2$. Since $V \propto R^3$, we obtain

$$P_{fusion} \sim V\,x\,(nT)^2 \propto V\,x\,B_T^4\,\beta_T^2 \propto R^3\,R^4\,\beta_T^2 \propto R^7\,\beta_T^2 \qquad (4).$$

As can be seen from Eq. 4, P_{fusion} has a particularly strong size scaling. The neutron flux $F_{neutron}$ on the first wall, which is relevant for blanket development (one of the main purposes of the FNSF), also has a strong dependence on the device size as $F_{neutron} \propto P_{fusion} / R^2 \propto R^5 \beta_T^2$. For this reason, the thermal fusion power output rises dramatically as the size of a copper-based ST increases. Accordingly, there is a minimum size for the FNSF facility required for significant thermal neutron production where the ITER-like plasma pressure is required. A smaller FNSF, however, can produce fusion neutrons via NBI (neutral beam injection) driven beam-target reactions in a similar manner to the TFTR/JET DT experiments [73, 74].

To achieve the plasma parameters necessary for an FNSF, one may need plasma pressure (*n T)* or $B_T^2 \beta_T$ values comparable to those achieved for TFTR/JET. The $B_{T0}^2 \beta_T$ product (in units of T^2 *%*) is ~ 30 for TFTR/JET-level plasma pressures, ~ 70 for ITER, and ~ 120 – 200 for DEMO. It is instructive to examine what level of plasma pressure certain-sized STs can attain. In Fig. 31, $B_{T0}^2 \beta_T$ is plotted as a function of R_0 (as a measure of the achievable plasma pressure) for possible FNSF parameters: $A = 1.6$, $q^* = 3$, $\kappa = 3$, and a relatively modest beta of $\beta_N = 3$ at the two gap distances of $\Delta = 0$ and 10 cm. In this FNSF regime, neutral beams are assumed to provide both plasma heating and the required current drive, where the bootstrap current fraction is ~ 50 %. In the in-board TF center rod, we assume $j_{TF} = 2$ *kA/cm*^{2}, which is a typical value if steady-state water cooling is assumed. For $\Delta = 0$, TFTR-JET-like $B_{T0}^2 \beta_T \sim 30$ may be achieved with an ultra-compact ST device with $R_0 \sim 50$ cm, provided that the plasma energy confinement is sufficiently high to attain $\beta_N = 3$. This would correspond to an H-factor 1.5 (i.e., 50% better than typical H-mode confinement).

For a low-aspect-ratio geometry, Δ is a particularly a high-leverage quantity. In Fig. 31, one can see that the impact of such a gap is quite significant. A relatively modest gap distance of $\Delta = 10$ *cm* would increase the device size R_0 by 50 cm (which is five times Δ) to produce plasmas with equivalent $B_{T0}^2 \beta_T$. So for a very compact FNSF, it is essential to keep the gap distance to a minimum, perhaps to ~ 2-3 cm, or one must develop an engineering design to accommodate higher $j_{TF} > 2$ *kA/m*^{2}. In Fig. 32, a similar plot is shown for ST DEMOs, one for the ARIES-like copper design and another for a superconducting coil ST design. The copper ST DEMO

operating design point is $B_{T0}^2\ \beta_T \sim 200$, to produce the ~ 3 GW of fusion power needed to provide the 1 GW-electric to accommodate the TF ohmic recirculating power loss. For a copper design, we assumed an ARIES-like $A = 1.6$, $q^* = 3$, and a relatively conservative $j_{TF} = 1\ kA$. For plasma parameters, a relatively advanced $\kappa = 3.3$ and $\beta_N = 6.5$ are assumed to ensure high bootstrap current fraction f_{BS} at high current. The $\Delta = 20\ cm$ is assumed to provide sufficient shielding for the center-post, and a $B_{max} = 7$ T which is again quite modest. For Fig. 32, the operating point of $R_0 \sim 3.2\ m$ is used. For a superconducting magnet ST (SC-ST) design, a conservative $j_{TF} = 3\ kA$ was assumed. The SC-ST DEMO operating design point is $R_0 \sim 4.4\ m$ with $B_{T0}^2\ \beta_T \sim 120$, since only 2.2 GW of fusion power is needed for 1 GW-electric due to the lower recirculating power. The target device and plasma dimensionless design parameters for various future devices are shown in Table III.

In Sec. B, the fusion neutron science facilities (FNSF) are discussed. While there are many versions of FNSF, we consider here three representative ST-FNSF designs as shown in Table III. FNSF-I represents the ORNL-led design [75], FNSF-II the PPPL-led design [76], and FNSF-III the Culham-led design [77]. The neutron wall loading $W_L = 1\ MW/m^2$ is assumed for the FNSF design point.

As shown in Table III, the ST-FNSF facilities are designed with relatively modest values of β_N and β_T which have been already achieved in present-day STs, at least transiently. The required confinement H factor of 1.2 – 1.3 is also close to the range observed in present-day STs as discussed in Sec. V. The size variation and therefore the potential facility cost variation among three design points are quite large, even though they are producing same W_L. A larger facility such as FNSF-I tends to have more conservative physics assumptions. On the other hand, q^* tends to be proportionally lower (more MHD unstable and more prone to disruptions) for a smaller FNSF, which results in similar values of I_p for comparable plasma/fusion performance. A pilot plant study has been led by PPPL [76], and it has similar plasma parameters as the FNSF-II since the NSTX database motivated the choice of its operating parameters. Compared to FNSF, the pilot plant is a much larger device (~ x 2) with a larger fusion power output (~ x 10), and attempts to achieve an engineering Q =1 with the possibility of net electricity generation [78]. As shown in Table III, the pilot plant operates with plasma parameters closer to the ST power

plant study (ARIES-ST) in terms of κ, q^*, β_N, β_T, and f_{BS} [65]. The ARIES-ST operates with a very high β_N and f_{BS} to minimize the recirculating power needed for non-inductive current drive for power generation.

B. Fusion Neutron Science Facilities - Fusion tritium breeding blanket module development represents a major technological challenge for magnetic fusion research, regardless of magnetic configuration. An international study on a high-volume plasma-based neutron source (VNS) for fusion blanket development was conducted to determine the requirements for a neutron source for fusion nuclear technology development [71]. This international team considered the technical issues and the required testing facilities for fusion blanket and first wall systems, to meet the goal of demonstrating blanket availability in DEMO >50%. Due to its potentially low cost, the ST-based compact VNS has attracted numerous studies since the VNS assessment study. We should note here that the volumetric fusion neutron source test facility has been called by many names including VNS (Volume Neutron Source) in earlier times, CTF (Component Test Facility) mainly used in the UK and RF to refer to a device with a similar mission to VNS, and more recently, FNSF (Fusion Neutron Science Facility) as a general term for a fusion neutron science facility encompassing the mission of the VNS / CTF. In this paper, for simplicity, we shall call all of these volumetric neutron facilities as the FNSF. While ST-FNSF studies have been carried out since 1990's [72, 79, 80], we shall mention three newer ST-FNSF conceptual design studies performed since 2000, as the experimental data from NSTX and MAST became available (see Table III). They are the newest design studies led by the Culham [77], ORNL [75], and PPPL [76, 78] groups. In Fig. 33, schematics of the three facility designs are shown.

The Culham-led effort is shown in Fig. 33(a), and represents the most compact design with $R_0 \sim 85$ *cm,* $A = 1.55$, $\kappa = 2.4$ at a I_{TF} of 10.5 MA and $I_p = 6.5$ *MA* at a $q^*=2.3$ [77]. Relatively modest values of β_N of 3.5 and β_T of 17% are assumed. About 50% of the plasma current is driven by NBI, and another 50% by the bootstrap current. An H-mode confinement factor (ITER 98-pby2) of 1.3 is assumed to produce 35 MW of total fusion power with 44 MW of auxiliary heating, yielding 1 MW/m^2 neutron wall loading. The Culham FNSF center-rod cross section is

shown in Fig. 34. In addition to the water-cooled TF center rod, it includes the 2.5 cm thick inboard shield, and a small start-up solenoid. The average rod current density is ~ 7 kA/cm^2 for this design. An operating point of $B_{T0}^2\,\beta_T \sim 100$ is expected to result in significant thermal fusion neutron production along with those produced by beam-target reactions. A vertical core replacement concept has also been developed. As a variation of the Culham design, there are even more compact FNSF device designs with $R_0 \leq 50$ cm, where neutron generation is based mainly on beam-target reactions at $B_{T0}^2\,\beta_T \leq 20$ [81].

The ORNL-led FNSF design is shown in Fig. 33 (b), based on a medium-sized ST design with $R_0 = 130$ cm, and A = 1.7 with $B_{T0} = 2.9 – 3.6$ T. As with other FNSF designs, about 50% of the current is driven by NBI and another 50% by the bootstrap current [75]. The operating beta is a relatively conservative $\beta_N \leq 3.5$, operating at ~ 20% below the no-wall beta stability limit. The vertical remote handing concept is shown in Fig. 35 [80]. An H-mode confinement factor of ≥ 1.25 is assumed. There are two operating points for blanket R&D. At $B_{T0} = 2.9$ T, $I_p = 6.7$ MA, $\beta_N = 3.3$, and β_T of 10%, 76 MW of total fusion power is produced with 44 MW of auxiliary heating, yielding 1 MW /m^2 of neutron wall loading. For a higher neutron wall loading of 2 MW /m^2, operating at $B_{T0} = 3.6$ T, $I_p = 8.4$ MA, $\beta_N = 3.5$, and β_T of 11% produces 152 MW of total fusion power with 60 MW of auxiliary heating. The average rod current density for this design is more manageable at ≤ 4 kA/cm^2 from the engineering view-point, or about the half of the Culham design. A study for optimizing the cooling channels was also conducted to minimize the temperature in the centerpost [82].

The PPPL led FNSF/pilot plant design is shown in Fig. 33 (c) and it addresses the ST pilot plant mission with a relatively large device having $R_0 \sim 220$ cm and $A = 1.7$ at $B_{T0} = 2.4$ T [78]. This device is smaller than a DEMO but runs essentially at the DEMO-level plasma performance. Its aim is to test all of the essential DEMO physics and technology functions, including net power generation and tritium self-sufficiency. Accordingly, the physics parameters are DEMO-like with $\kappa \sim 3.3$, $q^* \sim 3$, $\beta_N \sim 6$, $\beta_T \sim 30 – 40\%$, and $f_{BS} \sim 90\%$. An H-mode confinement factor of 1.35 is assumed, which is a similar value to other FNSF designs. The total fusion power of 600 – 1000 MW (which could be used to run the plant) can be generated with a heating power of 50 – 60 MW, producing a DEMO-like neutron wall loading of 2 - 3 MW /m^2. For this design, $B_{T0}^2\,\beta_T \sim$

200, which is a similar plasma pressure to that in a typical DEMO design. A vertical disassembly procedure has been developed, as shown in Fig. 36.

C. Other Possible Near Term ST Facilities – In addition to the ST-FNSF facilities described in Sec. B, there are a variety of possible so-called "next-step" ST facilities utilizing the compactness of high-performance ST plasmas. In the early part of the decade, a conceptual design activity was carried out for a 10 MA-class ST device [83, 84]. They were to be a follow-on device to NSTX to qualify the ST plasma performance needed for ST-FNSF devices, and thus minimize the physics risks. Those physics gaps for the ST-FNSF are now expected to be filled with NSTX-U and MAST-U as described in Sec. I.D. Here we present two examples of utilizing compact ST configurations, i.e., a plasma-material development facility and a fusion-fission transmutation facility.

Plasma material interface experiments – There is a general consensus in the community that the plasma material interface (PMI) is one of the greatest challenges in a fusion power plant. For example, if one were to expect a 2-3 GW fusion power plant of the size of ITER, the expected heat flux would be four to six times that of ITER for a much longer divertor component operation time. Similar PMI challenges are expected for an ST-based FNSF and DEMO/Power Plant. Satisfactory solutions are not available today, and clearly innovative solutions are needed due to the magnitude of the PMI challenge as discussed in Sec. VII. The FNSF facility, particularly in the shakedown phase, can be used to develop those PMI solutions. But since FNSF will be considered to be a nuclear facility, its construction approval may only come after satisfactory PMI solutions are available. The NSTX-U and MAST-U devices will be investigating innovative divertor/PMI solutions with DEMO/FNSF level divertor heat fluxes, but with limited plasma pulse lengths and duty factors. To address those PMI issues in an integrated facility, and taking advantage of high power density of an ST configuration, the National High Power Advanced Torus Experiment (NHTX) was proposed [85]. The basic device parameters are $R = 1m$, $P_{in} = 50\ MW$, $a = 0.55m$, $\kappa = 2.7 – 3.0$, $B_T = 2T$, and $I_p = 3 – 4\ MA$, with the goal of yielding very high power flux levels of P/S = 1.1 MW/m^2 and P/R = 50 MW/m for extended pulse durations. It uses steady-state, water-cooled, demountable copper coils for maximum flexibility and accessibility. The NHTX facility can accomplish its mission with relatively

modest confinement and beta parameters, and without the complexity of a nuclear environment as the facility is mostly operated with deuterium.

Fusion-Fission Transmutation System - Another ST application area is the fusion-fission transmutation system (FFTS), which has been examined recently with a replaceable compact ST fusion-core as shown in Fig. 37[86]. The basic aim of this facility is to use the high-energy spectrum of fusion neutrons from the ST-core to irradiate the spent fission-fuel-based blanket modules. This is believed to greatly enhance net-energy production, while eventually reducing the highly toxic long-lived actinide level in the spent fission fuel. The parameters of the proposed ST core of the Texas FFTS device are $R_0 = 135$ cm, $A = 1.8$, $\kappa = 3.0$, and $B_{T0} = 2.9$ T. With $I_p = 10 - 14$ MA, $\beta_N = 3.3$, and β_T of 15 – 18 %, 50 MW of auxiliary heating, there would be 0.9 MW /m^2 neutron wall loading. The FFTS neutron core is therefore similar to the 1 MW/m^2 version of the ORNL FNSF in terms of device size and plasma parameters. The device utilizes the super-x divertor configuration (to be tested on MAST-U) to handle the intense steady-state divertor heat flux.

D. ST Power Plants – In this section, we briefly describe the ST-based power plant studies. There are two main versions of the ST-power plant designs. One is based on the copper TF magnets. As shown in Fig. 32, copper magnets have the advantage of allowing more compact size reactors but requires larger recirculating power due to the resistive loss associated with copper [65, 87]. The copper TF center-post must also be refurbished periodically. Because of the large recirculating power, the fusion power output must be correspondingly larger and the required plasma parameters are well beyond what was achieved in the ST database and needed for an FNSF. The other class of ST power plants is the superconducting (SC) TF design being pursued in Japan [88] and Korea [89]. The size of the power plant is larger because of the thicker in-board neutron shield ($\Delta \sim 100$ cm) as shown in Fig. 32. The advantage of the SC-ST is that because of the neutron shield, the TF magnet is expected to last for the plant life, and it can also accommodate a modest OH solenoid for start-up. Because of lower fusion power (due to lower recirculating power) and larger size, the required plasma parameters are relatively modest, with β_N and β_T similar to that required for FNSF. The neutron wall loading and divertor heat flux would be correspondingly lower, further reducing the necessary technology

requirements. Due to the low-aspect-ratio geometry (the center-stack or the central post profile is relatively slender), all of the ST power plant designs achieve tritium self-sufficiency without requiring an inboard breeding blanket.

Copper-based ST Power Plant - Perhaps the most comprehensive study to date is the ARIES-ST study, which examined a 1000 MW electric fusion ST power plant conceptual design with $A = 1.6$, $R_0 = 3.2$ m, $\kappa = 3.4$, and $\delta = 0.74$ [65]. The normal conductor toroidal field coil magnet for an on-axis toroidal field of 2.1 T results in 329 MW of joule losses. The normal TF magnet design for this operational level is technically conservative, with $j_{TF} \sim 1$ kA/m^2 and low $B_{TF\text{-}MAX} \sim 7.4$ T. The PF coils are assumed to be superconducting to minimize the re-circulating power. The assumed ARIES-ST physics parameter range is quite aggressive however, with assumed limits to be 90% of the ideal MHD limits, namely, $\beta_T = 50\%$, $\beta_N = 7.4$, $\beta_P = 1.7$, $I_p = 28$ MA, and $f_{BS} = 0.96$. The fusion power of 2980 MW and the total thermal power of 3370 MW, with average neutron wall loading of 4.1 MW/m^2, are also rather high. The re-circulating power fraction of 0.34 is significant due to the TF-coil ohmic losses, assuming a net plant efficiency of 0.3. The power core uses an advanced 'dual-cooled' breeding blanket, with a flowing PbLi breeder material and He-cooled ferritic steel structures that can achieve a thermal conversion efficiency of ~ 45%. The possible advantages of the ARIES-ST power plant design is the ease of maintenance through vertical access as depicted in Fig. 38. This is quite similar in philosophy to that of the ST- FNSFs described in Sec. II-B. By lowering the entire plasma core, including blanket modules and plasma facing components, one can envision replacing the entire spent core with a new (or refurbished) one with a relatively short reactor down time. The removed spent core is to be refurbished during the period of power plant operation between core maintenance, which could be separated by a few years. In addition to the ARIES-ST study conducted in the US, there was an independent integrated modeling study at UK of important plasma physics issues related to the design of a steady-state spherical tokamak (ST) fusion power plant, similar to the ARIES-ST in plasma and device parameters [87].

Superconductor magnet-based ST power plant - The SC-ST design has the major advantage of potentially much lower recirculating power, which would reduce the fusion power output requirement by nearly 1 GW for a 1 GW-e power plant. Also, the SC magnet system could last

for the entire plant life with small re-circulating power; however, PFC and blanket module maintenance may require more complex horizontal access between the TF magnets, as with conventional aspect-ratio tokamak reactors. The SC-ST TF coils may provide larger horizontal access space because of the overall low toroidal field coil current, making the TF magnet outer leg less bulky. Because of the larger size and lower recirculating power, the plasma pressure for the SC-ST maybe significantly lower, i.e., $B_{T0}^2 \beta_T \sim 120$ instead of ~ 200. This could substantially relax plasma performance requirements. Here we introduce two SC-ST studies conducted in Japan and Korea.

Japanese SC-ST power plant studies - The superconductor (SC) magnet tokamak DEMO study in Japan has looked into the lower aspect ratio design VECTOR, with $A = 2.3$, $R = 3.2$ m, and a "Slim CS" with $A = 2.6$, $R = 5.5$ m to reduce the reactor size. More recently, an SC-ST power plant design called JUST was proposed, where $A = 1.8$, $R_0 = 4.5$ m, $B_{TF} = 2.36$ T, $\kappa = 2.5$, and $\delta = 0.35$. A JUST device schematic is shown in Fig. 39 [88]. The SC-TF is Ni_3Sn, and $B_{max} = 12.8$ T with $j_{TF} = 2800$ A/cm^2, which is well within present-day Ni_3Sn technology. The neutron shield is 80 cm thick for this design. The plasma operating parameters are $\beta_T = 22\%$, $\beta_N = 7.2$, $I_p = 18$ MA, and $f_{BS} \sim 1$ which is considerably less stringent than ARIES-ST with much lower I_p and β_T. The total fusion power is 2.2 GW for net 1 GW electric because of lower recirculating power. The plasma pressure $B_{T0}^2 \beta_T \sim 122$, which is low compared to the ~ 200 required for ARIES-ST. Further current ramp up is to be done by ECCD and bootstrap current overdrive. To alleviate the divertor heat load problem, the JUST design incorporates an innovative liquid lithium divertor. It should be noted that a new superconducting ST power plant study was conducted with conservative physics and technology assumptions, which still appears to give a competitive COE for electricity in Japan [89].

Korean SC-ST reactor studies - With availability of high-field high-temperature superconductor magnets in the recent years, a 1000 MWe-class SC-based ST power plant design with minimum re-circulating power was examined with a self-consistent system analysis code for A = 1.5 – 2.0 [90]. The high-temperature superconducting magnets with high critical current density opens up the possibility of a fusion power plant with compact size and small re-circulating power, simultaneously with low aspect ratio. A central ohmic start-up solenoid is envisioned. A model

of the radial build is shown in Fig. 40. As in all ST based systems, the tritium blanket is not placed in the inboard region. The use of WC (tungsten carbide) appears to be effective, since in addition to its good neutron shielding properties, it can reflect neutrons toward outboard tritium breeding blanket. This can help maximize the tritium breeding ratio (TBR), so tritium self-sufficiency therefore appears to be possible with only an outboard blanket.

III. Macrostability

A. Motivation for ST Research – The physics of macrostability has been a success story for the long history of tokamaks and STs. The ideal MHD model has been used successfully to predict plasma equilibrium and its stability properties for all types of tokamaks, large and small [21, 22]. Over the years, MHD stability codes have been improved to take into account various physical processes to support experiments. For example, the experimental quest for high beta regimes in NSTX has been guided by ideal and resistive MHD theory, and more recently, by theoretical kinetic MHD models using, for example, the MISK code which also include plasma rotation effects [91]. As noted in Sec. II, high β_T is needed for high fusion reactivity, and high β_N is needed for the high bootstrap current fraction required for non-inductive plasma sustainment. The highest β_T regime in the STs has been accessed with high values of I_p/aB_{T0} as shown in Fig 3 . The trend observed in tokamak experiments is also indicated in the figure. The slope is the $\beta_N \equiv \beta_T aB_{T0} / I_p$. The START device obtained high $\beta_T \leq 40$ %, which is consistent with theoretical expectations [92, 93]. NSTX was also able to achieve similar high β_T regime with $\beta_T \sim 35$ - 39% at $I_p \geq 1$ MA [94]. The ultra-low-aspect-ratio device PEGASUS has obtained the relatively high $\beta_T \sim 25$ % with Ohmic heating alone [6]. Ultra-high β_T was also obtained in a transient manner in the smaller TS-3 experiment [14], where merging ST plasmas inducing reconnection-based anomalous ion heating that resulted in transiently achieved ultra-high β_T (see Sec. IV.D). However, these very high β_T results were obtained by going to high I_p/aB_{T0} (at relatively lower β_N) which has only a small bootstrap current fraction. While it is important to demonstrate high β_T for high fusion power density for a given magnetic field, as discussed in Sec. II, it is critical to achieve high bootstrap current fraction f_{BS} for the fully non-inductive steady-state reactor operation needed for FNSF and a DEMO Power Plant. To achieve simultaneously high β_T and f_{BS} requires access to high β_N and high κ as shown by Eq. (3), i.e., $f_{BS} \propto A^{-0.5} (1+\kappa^2) \beta_N^2 / \beta_T$. Therefore, the quest to achieve stable high β_N and κ has become a central topic for ST macrostability research in recent years, which is similar to the goal for the advanced tokamak reactor concept [95]. One of the readily controllable plasma parameters is κ. Most future ST devices are designed with relatively high $\kappa \geq 2.5$ to generate significant bootstrap current. Figure 41 shows the equilibrium cross-section for such a discharge obtained in NSTX,

with $\kappa \sim 2.7$ at $\beta_N \sim 5.5$ maintained for 0.5 s or $\sim 2\tau_{CR}$ [96]. These discharges achieved high non-inductive current fractions, i.e., $f_{NI} \sim 65\%$ and $f_{BS} \sim 50\%$. Because of low ohmic flux consumption ($V_{loop} \sim 0.1 - 0.2$ V), the discharge duration of the high elongation discharges is now determined by the heating limits of the TF coils on NSTX. For β_T and β_N optimization, detailed macrostability or magneto-hydrodynamic (MHD) calculations were performed. They showed that with optimized plasma pressure and current profiles, it is indeed possible to produced reactor relevant plasmas with high β_T and high β_N values simultaneously. In order to reach high β_N, there are a number of obstacles, such as resistive wall modes (RWMs), as β passes through the so-called no-wall beta limit and approaches the so-called with-wall or ideal MHD beta limit as described in Sec. B. Neoclassical tearing modes (NTMs), which are considered to be a highly important research topic for tokamaks, turned out to be not as serious for STs due to its higher beta and higher q operations as discussed in Sec. C. In addition, the importance of error fields was recognized for MHD stability, particularly at high beta as described in Sec. D. ST MHD research also contributes strongly to the plasma disruption physics research discussed in Sec. E.

B. High β_N Regime – Because of its relevance to attractive reactors, recent ST MHD research has been focusing on access to the reactor-relevant high β_N regimes. As described in Sec. II, the high β_N regime is necessary for a steady-state tokamak reactor design with simultaneously high β_T and f_{BS}. One of the highly significant ST research accomplishments is the attainment of high β_N regimes near the ideal wall limit, through RWM stabilization and control as described in this section. In Ref. 59, it was shown theoretically that the high β_N regime for STs is indeed accessible through plasma shape and plasma profile control. Another insight for higher β_N can be seen in Fig. 4, where the achieved β_N is plotted as a function of plasma internal inductance l_i [48, 97. The l_i is a measure of plasma current profile where the broader plasma current profile, the lower the value of l_i. Lower values l_i for $\beta_N >$ 1-2 are not accessible since the plasma is generally more kink unstable. Yet, for high performance reactor operation, it is generally desirable to access high values of β_N/l_i. As one can see from Fig. 4, the NSTX database extends to $\beta_N \sim 7$ and $\beta_N/l_i \sim 13.5$, well above the normal expected tokamak beta limits of $\beta_N \sim 4$ and $\beta_N/l_i \sim 6$. The NSTX database now intercepts the higher l_i portion of the planned operational

ranges for ST-FNSF and ST pilot plants. It should also be noted that the achieved β_N now exceeds the computed β_N no-wall limit (shown by the blue line) or $\beta_{N\text{-}NW}$ by up to a factor of two. At lower $l_i \sim 0.38$, the plasma can reach the current-driven ideal kink stability limit, so that passive or active kink and resistive wall mode (RWM) stabilization is critical as discussed in the following sections. As mentioned in Sec. I, the plasma is not necessarily most unstable at highest beta values in NSTX [25]. Instead, disruptions occurred less frequently at high values of β_N/l_i, which is also supported by active MHD spectroscopy diagnostic measurements [26]. They show that resonant field amplification (RFA) (a measure of plasma going kink unstable) decreases at higher values of β_N/l_i as shown in Fig. 4. This favorable stability property at high values of β_N/l_i bodes well for the prospects for a ST-FNSF and ST-power plant.

C. Resistive Wall Modes (RWM) – As the plasma beta increases, ideal MHD instabilities such as internal pressure and current driven kink/ballooning instabilities set the β limit. A so-called 'no-wall' limit, $\beta_{N\text{-}NW}$, occurs in devices without a passive stabilizing conducting structure. The MAST device has a conducting structure, i.e., a vacuum vessel, relatively far away (see Fig. 12) so the limiting β_N is likely to be closer to the $\beta_{N\text{-}NW}$ limit. The NSTX device specifically installed a relatively thick closely-fitted copper passive stabilizing wall, and six ex-vessel control coils and related magnetic B_p and B_r sensors, as shown in Fig. 42 [98, 99]. They were used to investigate the RWM stabilization in order to exceed the $\beta_{N\text{-}NW}$ limit and approach the so-called 'with-wall" or ideal limit, $\beta_{N\text{-}WW}$. The global kink/ballooning MHD instabilities can be stabilized with the presence of a nearby conducting wall. In order for wall stability to be effective, the mode structure must allow coupling of the perturbed field to the conducting wall. The ST magnetic field geometry results in the MHD instability mode structures significantly different from those in advanced tokamaks. In Fig. 43(a), the DCON computed perturbed magnetic field normal to the outer most flux surface is shown [97]. The computation uses an EFIT experimental equilibrium reconstruction, and the illustration includes the sum of the n = 1–3 components scaled to the measured RWM sensor amplitudes and relative phases. The perturbed field amplitude shown has been scaled up by a factor of 10 to clarify the mode shape. Based on the measured field amplitudes for n = 1–3, an estimate of the real space displacement of the mode is about 3 cm at the outboard mid-plane. This is consistent with estimates of the mode amplitude based on fast visible light camera images, and electron temperature measurements from past experiments obtained by shifting relative timing of the two independent 30 Hz Nd:YAG lasers

used by the Thomson scattering diagnostic [100]. Figure 43 (*b*) shows the poloidal variation of the mode field perturbation at the plasma edge. Here, the poloidal angle θ is 0 at the outboard mid-plane and π at the inboard mid-plane. The mode has a strong ballooning character, being significantly larger on the outboard portion of the plasma.

RWM stabilization with plasma rotation – As the plasma approaches and exceeds the so-called no-wall beta limit, resistive wall modes (RWMs) (typically n=1, 2, and 3) can be excited as described above. The predominant mode is n=1, which is a kink-like mode with a particulary fast growth rate. The presence of a nearby conducting wall slows the mode growth. Earlier studies indicate that the mode growth can be suppressed if the plasma rotates sufficiently fast to make the nearby wall look like an ideal (superconductor-like) conductor for the growing modes. Plasma rotation frequencies normalized to the Alfvén frequency (ω_ϕ/ω_A) of a few per cent relative to the mode rotation frequency can passively stabilize the RWM in theory [101]. Rotational RWM wall stabilization has been extensively studied on tokamaks and STs with the NBI injection, which imparts significant momentum to spin the plasma. Early RWM stabilization models, which relied solely on plasma collisionality as a stabilizing energy dissipation mechanism was quite successful in explaining much of the RWM stabilization physics with plasma rotation. As shown in Fig. 44, RWM stabilization with a rotation frequency larger than $\Omega_{crit} \equiv \omega_A/(4q^2)$ is clearly demonstrated [96]. While this simple rotational RWM stabilization had many successes, it had a significant shortcoming. On NSTX, some RWMs are observed to be more unstable with higher rotation speed, contradicting the model as shown in Fig. 45 [102]. As shown in the figure, the RWM wall stabilization is not a simple function of the rotation speed. In addition, the RWM stabilization models which solely rely on plasma collisionality as a stabilizing energy dissipation mechanism predicts reduced stability at reduced collisionality, a concern for the future reduced collisionality plasmas. A breakthrough in the understanding of RWM physics was made through the inclusion of kinetic effects [103]. This kinetic model described below was successful in resolving the puzzling stability behavior with rotation observed in NSTX. But it also has important implications for next-step devices operating at reduced collisionality such as ITER/FNSF/DEMO.

Kinetic effects in RWM stabilization with plasma rotation and collisionality – The NSTX RWM research effort has established a new understanding of RWM stability by making quantitative correlations between experiments reaching the mode marginal stability point and kinetic RWM stabilization theory, which takes into account various plasma resonance frequencies [90, 104]. While the effects could be complex, some clarity has emerged on the role of resonance and off-resonance with collisionality as shown in Fig. 46 [105]. Figure 46 shows normalized growth rate vs. scaled experimental rotation for a given NSTX discharge. One can clearly see that a stabilizing resonance with the ion precession drift frequency occurs at low rotation ($0.2 < \omega_\phi/\omega_\phi^{exp} < 0.7$) and with bounce and transit frequencies at higher rotation ($\omega_\phi/\omega_\phi^{exp} > 1.6$), while in between these extremes there exists a narrow range of off-resonance rotation profiles with more unstable marginal stability ($1.3 < \omega_\phi/\omega_\phi^{exp} < 1.5$). In general, with other parameters equal, the reduced collisionality expected in future devices can enhance the RWM stability of on-resonance plasmas, while leaving the reduced stability of off-resonance plasmas roughly unchanged. This favorable collisionality behavior is in contrast to the predictions of previous fluid models [101], where decreased collisionality was thought to be universally destabilizing. In conjunction with kinetic resonances, collisions play a different role that can appear contradictory when compared to simpler models. This is because reduced collisions lower the collisional dissipation that is important when plasma rotational resonances are not present, but also decrease the damping of the competing resonant kinetic stabilizing effects, allowing them to be more powerful. The collisionality was varied in experiments that used $n = 1$ resonant field amplification to measure RWM stability [26]. They indicated the expected gradient in RWM stability for plasmas with high $5.5 < \beta_N/l_i < 13.5$ (as most are above the $n = 1$ ideal no-wall stability limit).

Active RWM stabilization at low plasma rotation – While the physics understanding of RWM passive stabilization has made impressive progress in the recent years, there is significant benefit to having active stabilization of RWMs, since they could still become unstable due to various kinetic effect as shown in the previous sections. For example, RWM active stabilization can be used when ω_ϕ passes through the unstable band of the off-resonance region, or for extremely low

plasma rotation operation expected for ITER and DEMO. Active stabilization is typically realized by a feedback control loop consisting of magnetic sensors capable of detecting low frequency (i.e., resistive wall time scale ~ $1/\tau_W$) modes, a set of control coils to provide magnetic fields in response to the detected modes (typically to try to cancel the dominant n=1 magnetic perturbation), and a control algorithm that determines the form of the response. On NSTX, active feedback control has been incorporated into routine high beta operations and has been steadily improved. The RWM sensor signal from poloidal and radial field RWM sensor arrays (48 coils in total shown in Fig. 42) were used to achieve feedback stabilization [97]. An example of RWM feedback stabilization of a low-rotation high-beta plasma is shown in Fig. 10 [34]. Both discharges are otherwise similar with constant P_b = 6.3 MW. The plasma without active stabilization has β_N = 4.1 as the rotation frequency $\omega_\phi/2\pi$ drops to below 4 kHz. At this time, RWM passive stabilization becomes insufficient, and the n = 1 RWM becomes unstable and β_N collapses. In contrast, the plasma with active stabilization does not suffer an unstable RWM, and continues to increase in β_N up to 5.6 and β_T up to 19.4% as ω_ϕ continues to decrease to $\omega_\phi/\Omega_{crit}$ = 0.2 near q = 2. The RWM is actively stabilized above $\beta_N^{no\text{-}wall}$ and below Ω_{crit} for significantly long durations exceeding $90/\gamma_{RWM}$ and seven τ_E, limited only by the toroidal field coil pulse length. The corresponding rotation profiles are shown in Fig. 47. Combined n = 1 RWM feedback control and β_N feedback control were used to generate more reliable high pulse-averaged β_N with low levels of fluctuation at various levels of plasma rotation. These active control system improvements have led to high success rates in stabilizing low l_i plasmas with near record ratios of β_N/l_i between 12 – 13.

More recently, an advanced RWM state space controller was implemented. It uses a reduced order model of the 3D conducting structure of NSTX (e.g., discrete passive conducting plates and a vacuum vessel including the large NBI port), and n = 1 ideal plasma instability eigenfunctions computed by the DCON MHD stability code, with variable phase to allow the controller to track mode rotation. Of particular interest is the predicted active control improvement for high beta operation with conducting structures (e.g., vacuum vessel in NSTX [106] and blanket in ITER [107]), using the advanced RWM state space controller. This ability is especially important for burning plasma devices, as it will be necessary to move such coils farther away from the plasma than in present experiments, and install shields to protect such coils

from neutron damage. Implementation of this system on NSTX and supporting studies have shown the advantage of the state derivative feedback approach [106]. The theoretical performance of the controller for plasmas with an insignificant level of passive stabilization is shown in Fig. 48. Using the plasma eigenfuction and wall response appropriate for an equilbrium near the no wall limit, the plasma can be controlled up to $\beta_N \sim 5.6$. Using input for an equilibrium near the with-wall β_N limit β_{NWW}, the plasma can be controlled up to $\beta_N \sim 6.7$ close to $\beta_{NWW} \sim 7.1$. In NSTX, plasmas limited only by coil heating constraints have exceeded $\beta_N = 6.4$, $\beta_N/l_i \sim 13$ using RWM space controller approaching its theoretical limit [26]. The advanced RWM state space controller is also predicted to significantly improve ITER performance [107]. Overall, the active n=1 RWM stabilization (plus other improvements) appears to be quite effective in maintaining high beta operation near the ideal MHD stability limit.

D. Neoclassical Tearing Modes **-** The Neoclassical Tearing Modes (NTMs) are magnetic islands at the resonant surfaces q = m/n, destabilized by a helically-perturbed bootstrap current [107]. Within the magnetic island, the plasma pressure tends to equilibrate, and the reduction of the pressure gradient reduces the bootstrap current within the island. The resulting magnetic perturbation term proportional to $A^{-1/2} \beta_p$ tends to cause the magnetic islands to further grow (i.e., become unstable) for positive values of magnetic shear length $L_q = q / (dq/dr)$, which applies to normal ST/tokamak operations. The NTMs are therefore usually stable for reversed magnetic shear and also for most stellarators. Since NTMs were observed at relatively low plasma beta in tokamaks and NTMs with growing magnetic islands degrade plasma confinement in present day tokamaks and possibly in ITER [108], exploring these modes and techniques for their suppression have been a high priority in conventional tokamaks. However, NTM research in STs has been relatively limited. Early NTM observations in MAST [109] and NSTX have been reported [110]. A computational study for ST (low-aspect ratio) equilibria showed stabilizing effects due to shaping / magnetic shear and curvature effects [111, 112]. The scarcity of NTM studies in STs is perhaps due to the fact that NTMs have thus far not played a significant role in determining high beta stability and confinement in ST experiments. This lack of NTM activity in STs may be due to the generally more stable characteristics of their plasmas, namely, strong shaping, high beta, and higher q operation, all of which tend to reduce the NTM drive as

expected theoretically and computationally. NTMs are stabilized by the so-called classical stability index Δ' (which is negative), and by good average magnetic field curvature which scales as $(q^2-1)\,\beta$, but destabilized by the helically perturbed bootstrap current term. A simplified NTM equation can be written as,

$$(\tau_R/r^2)\, dw/dt \sim \Delta' - 6.35\,(q^2-1)\,(L_q^2/rL_p)\,\beta/w + (L_q/L_{pe})\,(A^{-1/2}\,\beta_p)/w \qquad (5)$$

where $L_p = -\,p/(dp/dr)$ is the pressure scale length, and w is the characteristic island width [108]. The second curvature stabilizing term in Eq. (5) is usually not significant for conventional tokamaks, but can be important for STs with generally higher operating q and β. The third helically perturbed bootstrap current term in Eq. (5) is relatively insensitive to aspect ratio. Recently, a comparison experiment between NSTX and DIII-D indeed showed the magnetic curvature stabilizing term to be important for NSTX parameters [114]. Overall, NTMs in ST plasmas therefore appear to be more stable than in conventional tokamaks. Another important feature is the projected high f_{BS} ST reactor q profile [shown, for example, in Fig 30 (a)] that is monotonic and relatively high $q \geq 4$. The absence of low q resonances eliminates many of dominant resonance surfaces (i.e., magnetic islands) that are responsible for NTM drive. So, while we cannot completely rule out NTM-related issues for STs, the results thus far are quite encouraging in that NTMs may not be a serious obstruction for future ST facility operations. The longer-pulse, lower-collisionality discharges in NSTX-U and MAST-U will offer a good experimental test bed for the future NTM studies.

E. Effects of 3D Fields – The effect of 3-D fields has been an active area of research for both tokamaks and STs. In this section, the effects of non-axisymmetric fields on the ST plasma performance are discussed. The 3-D resonant magnetic perturbation on ELM control will be discussed in Sec. VI.D. A dramatic change in NSTX plasma performance was observed when machine improvements were made in 2002 as shown in Fig. 49 [115]. As seen in Fig. 49, the achieved peak β_T dramatically increased from the 20% range to the 35% range and β_N from the 4 range to 6, after poloidal field coil realignment and the installation of a bakeout system which generally improved vacuum condition. Prior to the machine improvements, the plasma beta limit was set primarily by confinement degradations associated with low n (n=1, 2) tearing mode

activity due to the poloidal coil misalignment. It should be noted that the n=1 error field reduction was also accompanied by high temperature bakeout during this period, so the operational limit improvements were attributed to both error field and vacuum condition. Additional error field compensation for the intrinsic n=3 fields generated by imperfections in the PF coils, and dynamic compensation for n=1 error fields arising from coil movement, resulted in further plasma performance improvements [116]. The dynamic error fields generated during plasma operation were detected by the error field sensors, and compensated by using the 3-D control coils shown in Fig. 42.

An important physics result associated with 3-D fields is the production of the neoclassical toroidal viscosity (NTV) [117]. The NTV is caused by the interaction of the plasma with 3D fields in a tokamak. The NTV magnetic braking, for example, can be a useful tool to control the toroidal rotation for MHD mode control. Comparison of the measured dissipation of plasma angular momentum caused by the externally applied n=3 non-resonant fields to the theoretical NTV torque profile is shown in Fig. 50 [118]. This good agreement was obtained when the effect of toroidally-trapped particles is included. The NTV with an applied n=2 non-resonant field was also investigated, and showed broader rotation damping profile than the n=3 case [119]. This is consistent with theoretical expectations. The observed increased plasma rotation damping rate with Ti during non-resonant magnetic braking is found follows theoretical prediction of $\tau_{NTV} \sim T_i^{5/2}$. To achieve a more precise picture of the NTV physics, including effects such as non-ambipolar transport, a new particle orbit code is being developed [120].

Another important advance in understanding the role of error fields was made with the new ideal perturbed equilibrium code (IPEC) [121], which can compute the 3-D perturbed tokamak plasma equilibrium with high resolution. IPEC can explain the successful cancellation of error fields by the relatively simple 3-D control coils in NSTX and DIII-D. This theoretical approach has also been applied to the understanding of NTV physics by including bounce and precession resonances and the use of the 3-D perturbed magnetic field lines [122]. Another example of the value of IPEC can be seen in Fig. 51, where the locking threshold values of the external error field currents (applied by the 3-D control coils) versus density for ohmic and NBI-heated high β plasma are plotted as a function of the plasma density [123]. As shown by Fig. 51(a), the usual linear density correlation can be seen for ohmic discharges, but it is no longer valid for high β

plasmas when the external measures are used. By using the total resonant fields calculated with IPEC instead of external currents or external fields, the linear correlation is regained for both ohmic and NBI-heated plasmas as shown in Fig. 51(b). This resolution comes from plasma amplifications by a factor of 2–3 in high density and high β plasmas.

F. Disruptions **-** Major disruptions have been identified as the most serious issue for the tokamak reactor approach. While not all of the major disruptions are triggered by MHD-related events, the vast majority of them are. In particular, the non-axisymmetic halo currents generated in the in-board (high field) side by a disruption are problematic for tokamak reactors due to the very large j x B force on PFCs and the first wall. For example, if a 2 MA halo-current (20% of total plasma current of 10 MA) is generated in the inner wall at a 10 T magnetic field, there will be about 2,000 tons/m of dynamic radial force imparted on the current carrying vacuum chamber wall and PFC components. If the force is non-axisymmetric, the resulting large localized stress could cause unacceptable reactor chamber wall failure. The large electric fields generated by disruptions can accelerate electrons to relativistic energies, and these electrons can also cause damage to the device PFCs [124]. A large database of disruption rate and disruptivity statistics spanning 2006 - 2010 of NSTX operation has been analyzed [25]. Figure 52 shows disruptivity as a function of β_N and q^*, pressure peaking factor $F_p \equiv p(0)/\langle p \rangle$, plasma shaping factor $S \equiv q_{95} I_p/aBT$, and l_i. Strikingly, and consistent with the dedicated stability experiments described above, no clear increase is found in disruptivity at increased β_N and $l_i < 0.8$. Significant increases in disruptivity are found for $q^* < 2.4$, at low plasma shaping, and at high values of F_p, and l_i, each of which are generally expected. Increased S, and decreased F_p typically beneficial for stability, are also shown to yield reduced disruptivity in this analysis. The disruptivity trend is quite encouraging, as future ST FNSF and Power Plant operating designs trend toward higher β_N, increased S, and decreased F_p and l_i.

An extensive NSTX database study has been conducted to determine the detectability of disruptions based on multiple-input criteria [125]. Quantitative evaluation of the levels of measured input, including low frequency $n = 1$ RWM amplitude, neutron emission compared to a computations from a rapidly-evaluated slowing-down model, ohmic current drive power, and plasma vertical motion (all able to be evaluated in real-time) are determined to maximize

disruption detectability, while minimizing false positives. A false positive occurs when the disruption alarm is declared more than 0.3 s in advance which is essentially a false warning. Results illustrate that no single diagnostic dominates the detection algorithm; a combination of signals is required. In total, 17 threshold tests are computed and a weighted sum is evaluated every 2 ms for ~1700 disruptive discharges tested. A flag noting that a disruption is imminent is set when the single weighted sum is sufficiently large. This approach has shown high success. Figure 53 illustrates a histogram of the warning times that this approach finds (with a reset time of 25 ms and eight points required for a positive flag). A total of 98% of the disruptions are flagged with at least 10 ms warning, with ~ 6% false positives. The majority of false positives are due to near-disruptive events. The number of missed warnings found is largely due to locked modes and RWMs. This multiple-input criteria approach is an innovative promising approach for maximizing the reliability of disruption detection for tokamaks and STs. Such a disruption avoidance system is planned for use in the upcoming operation of NSTX-U.

IV. Solenoid-free Start-up

***A. Motivation for ST Research*:** Because of the use of a minimally-shielded single turn copper TF center-post without a central solenoid for future compact ST devices such as FNSF, it is critically important to develop a reactor compatible solenoid-free plasma start-up and current ramp-up technique. A multi-turn ohmic solenoid with electrical insulating material without sufficient shielding, which is not possible for compact STs, is considered to be unacceptable for the fusion neutron environment. An inboard ohmic solenoid also occupies the very valuable central region of the device, and installing it would increase the inboard major radius of the plasma, thus proportionally increasing the overall ST device size. As noted in Sec. II, the inboard gap distance Δ is a particularly high-leverage parameter for compact ST-FNSF performance.

There are essentially four classes of solenoid-free start-up concepts which were pursued for STs. The first one is to utilize plasma waves such as electron cyclotron and electron Bernstein waves for heating and current drive, which will be described in Sec. IV B. The second approach is "helicity injection" or HI, which is essentially a direct injection of toroidal current via electrodes or electron guns (Sec. IV C). The third approach is to use merging-compression to create ST plasmas. This method has a possibility of heating ions rapidly due to the magnetic energy dissipated during the reconnection process, achieving very high beta ST plasmas as demonstrated in the TS-3 experiments (Sec. IV D). Finally, there are concepts developed for inductive flux-based start-up that includes the ohmic solenoid, but in a way to make it more reactor compatible (Sec. IV E). It should be noted that there is an informative recent tutorial article on tokamak / ST start-up including solenoid free start-up [126].

B. Plasma wave-based start-up: Electron cyclotron heating (ECH) is a commonly used technique to create an initial plasma discharge, since ECH at the electron cyclotron fundamental frequency ($\omega \sim \Omega_e$) could heat electrons essentially from zero temperature. At higher density, the electron cyclotron wave is expected to convert into the electron Bernstein wave (EBW) above the so-called electron cyclotron wave cut-off density. This condition is readily satisfied for ST plasmas due to their high plasma dielectric ($\omega_{pe} >> \omega_{ce}$) properties. The EBW physics for

current profile control in particular is discussed in Sec. IX. During the start-up, due to the low plasma density, the ECH condition is usually satisfied. The ECH start-up was previously investigated on CDX-U, where a toroidal current ~ 1 kA was generated with an ECH power of ~ 8 kW. In CDX-U, initially in an open field line configuration, toroidal plasma currents were generated by ECH owing to pressure driven currents such as the one associated with electron precessional drifts [127]. After closed flux surfaces are formed, pressure-driven "bootstrap" currents can be generated within the flux surfaces to maintain the plasma current [128].

The ECH/EBW start-up experiments have been performed in a number of ST devices in recent years: LATE [27, 129], TST-2 [130, 131], CPD [132], QUEST [133], and MAST [134]. An illustrative ECH/EBW start-up and ramp-up experiment was performed on the LATE device, which is shown in Fig. 20 [27]. The plasma current and applied vertical field are plotted in Fig. 54(a). When a 5 GHz microwave pulse is turned on, plasma breakdown takes place immediately along the external helical field lines, near the 2nd EC resonance layer at R ~ 27 cm as shown in Fig. 54(b) [27]. Then the plasma current spontaneously jumps up to 7 kA under the steady vertical field B_v and forms an initial closed field structure [Fig. 54(c)]. This current jump has been also observed in TST-2, CPD, and QUEST. This is the first stage denoted by (I) in Fig. 54(a). In the next stage (II), I_p ramps up with the ramping up of vertical magnetic fields B_v. At the final stage (III), even when the B_v ramp-up rate is set to be very low, I_p still ramps up at the same rate of ~ 260 kA/s as in the preceding stage (II). The I_p ramp occurs against the reverse loop voltage V_L which appears in this stage. The I_p finally reaches 20 kA at the end of microwave pulse, producing a low aspect ratio torus or an ST plasma [Fig. 54(d)].

Recent ECH start-up experiments on QUEST (see Fig. 17) have resulted in a plasma start-up current of up to 66 kA with $P_{rf} \leq 350$ kW, and a plasma duration of up to 10 minutes at ~ 20 kA was obtained [135]. On QUEST, ~ 55 kA of start-up current was obtained and maintained for ~ 1 s with 270 kW at 28 GHz [136]. The QUEST was able to handle the steady-state rf heat load with actively cooled tungsten limiters and PFCs. On the MAST device (see Fig. 12), ECH-assisted plasma current start-up has recently achieved a record I_p ~ 75 kA with only 75 kW of gyrotsource power, and without the use of solenoid flux [137, 138]. This is an intriguing and promising result for the future application of this technique for STs, as it may be able to have favorable current generation efficiency similar to that of lower hybrid current drive (LHCD) [139]. The current seems to increase with ~ P_{rf} rather than ~ $P_{rf}^{0.5}$ as expected for the pressure-

driven current approach. It is noted that the LHCD start-up is being investigated in TST-2 and generated a plasma current of 15 kA in low-density start-up plasmas [140].

C. DC-Helicity Injection based start-up - A DC-helicity injection (HI) based current start-up technique utilizes the magnetic poloidal flux injected into a torus by an injection of DC toroidal electric currents [141]. This method has been previously successfully used to create spheromaks [142]. A schematic of the coaxial helicity injection (CHI) set-up is shown in Fig. 55. The two sections (inboard and outboard) of the vacuum chamber serve as electrically-isolated forming electrodes. When bias voltage is applied, an electrical discharge is formed between the two electrodes. Due to the dominance of the toroidal field B_T during start-up, since the applied poloidal field B_p is very small compared to B_T (i.e., $B_T >> B_p$), the electrical discharge currents thus generated flow predominantly in the toroidal direction since the electrons tend to flow along the magnetic field lines. The toroidal current therefore multiplies by a so-called "stacking factor," which is essentially the number of toroidal transits around the torus before exiting. Typically, injected electrons can spiral around the torus several times before exiting, so one can obtain total toroidal current several times the injected electric current. There is a net force of j_{pol} x B_T on the injected current, which tends to push the current ring away from the injector region toward the main plasma as depicted in Fig. 55. The injected current ring being pulled away from the injector can be disconnected from the electrodes via magnetic reconnection. When the poloidal field generated by the injected toroidal current starts to dominate over the applied poloidal (vertical) field, a closed-flux (tokamak-like) configuration can be formed. Once the closed flux surface is formed, the physics changes dramatically and the so-called helicity injection (HI) current drive concept is introduced to explain this current drive mechanism. HI current drive is based on the conservation principle that magnetic field energy associated with the current tends to decay faster than the magnetic helicity K [142]. K represents a degree of linkage of toroidal magnetic flux with poloidal magnetic flux. It is given by $K = 2 \int \phi \, d\psi$, where ϕ is the toroidal flux inside a flux surface and ψ is the poloidal flux, defined to be zero at the wall.

The HI method was first tested in a tokamak/ST geometry in the CDX/CDX-U experiment, using a localized emissive cathode generating up to ~ 10 kA level toroidal current [143, 144]. The HI technique was further improved with the dedicated devices HIT and HIT-II, utilizing co-axial (or axi-symmetric) electrodes which extended the achievable plasma current to the ~ 100 - 150 kA

range [145, 146]. A schematic of the HIT-II device is shown in Fig. 16. A rotating n=1 distortion observed in the experiment is believed to facilitate current relaxation (and the reconnection process) or radial helicity transport. This technique, termed the coaxial helicity injection (CHI), was then transferred to the larger NSTX device. A toroidal current of 240 kA was generated flowing along open field lines with a current multiplication factor of 10 [147].

On HIT-II, a new type of CHI termed "transient CHI" was developed [148, 149], where, with the injector flux footprints sufficiently close together, the injector current is rapidly reduced to zero. This causes the oppositely directed field lines in the injector region to reconnect causing closed flux surfaces. In Fig. 56, transient CHI discharge traces in HIT-II are shown. One can see that the plasma current persists much longer than the injector current. In this way, closed flux surfaces were obtained as a plasma current of 40 kA decayed resistively. As can be seen in the figure, the radiative power becomes small once the injector current is turned off. This transient CHI was then tested on NSTX, which resulted in ~ 160 kA of total plasma current with closed flux surfaces as shown in Fig. 57 [150]. The plasma current amplification of as much as 100 was observed. As can be seen in Fig. 57 (a), the plasma current persists well after the injection current is completely turned off, and the plasma current decays resistively, indicative of a closed flux configuration consistent with EFIT reconstruction results shown in Fig. 57 (b). It was also shown that application of ohmic induction to a CHI-initiated discharge resulted in 1 MA H-mode plasmas with significantly reduced ohmic flux consumption [151, 152]. A CHI performance projection based on the HIT-II and NSTX results shows the possibility of driving as much as 0.5 - 1 MA of plasma current in NSTX-U and 2-3 MA for a FNSF-like device. It should be noted that the electrical insulation for CHI does not require high resistance, since the only requirement is its resistance to be well above the relatively small CHI discharge resistance. This gives a choice of CHI insulating material to minimize possible neutron damage. Also, the CHI insulator maybe placed behind a neutron shield to further reduce neutron damage.

Another significant development in HI-based start-up is the electron gun injection experiment on the PEGASUS device (see Fig. 14) [6]. While similar to the earlier CDX/CDX-U experiment in terms of injection configuration, the experiment utilizes electron guns or cold cathode instead of emissive cathodes as shown in Fig. 58 [52]. The PEGASUS experiment was able to produce up

to 160 kA of toroidal plasma current using this method [153]. The current multiplication factor can be quite high i.e., ~ 30. The PEGASUS gun approach is attractive for the portability of the plasma gun. For example, a plasma gun for NSTX-U is being developed to achieve 0.5 – 1.0 MA level of start-up current. For the FNSF, one can envision a scenario where the plasma gun is retracted to a safe location once the start-up is complete to avoid neutron damage.

D. Merging Start-Up - Pioneered in START, MAST has demonstrated a novel merging compression technique to form ST plasmas by only utilizing the poloidal field (PF) coils placed inside the vacuum vessel [29]. A schematic of the MAST cross section is shown in Fig. 12. By rapidly ramping down the current in the top and bottom PF coils, breakdown occurs around the PF coils, forming plasma rings with considerable toroidal currents. By programming the current waveforms, the plasma rings thus created can be "pinched" off from the PF coils, and merged into a single ST plasma which can then be compressed radially to further increase the plasma current. The visible fast camera picture of the plasma evolution is shown in Fig. 5. The merging-compression scheme is compared with the more conventional direct induction scheme in Fig. 59 [29]. In direct induction (solid curve), breakdown occurs in a poloidal field null, and the solenoid current is ramped down to give an initial loop voltage of 4 V, which produced a plasma current ramp of 9 MA/s. In a merging-compression discharge (dotted lines), the process produces 400 kA of plasma current very rapidly before the solenoid ramp begins; the low ramp rate associated $V_{loop} \sim 1$ V is sufficient to maintain the plasma current. By this method MAST was able to produce the plasma current of ~ 450 kA routinely without an ohmic solenoid. Because of the reconnection process, a high ion temperature was also observed [154].

In the smaller TS-3 device, a merging technique was pioneered to obtain various plasma configurations including high beta and medium beta STs. Instead of induction, electrodes were used to form the initial double spherical tokamak discharges as shown in Fig. 21 [14]. As shown in Fig. 60, the TS-3 ST plasma achieves ultra high beta with unity β_T and $\beta_N \sim 17$, maintained stably over 200 μs. The ultra-high beta ST plasma had the maximum pressure gradient and magnetic shear at the edge, which may have helped its MHD stability. Another variant of the merging technique is a repetitive injection of ST plasmas into the main plasma in the HIST device [155].

While the merging-compression method with internal coils works well on present devices, whether this method can be extended to ST reactors is a challenge. There, the internally placed PF coils are in contact with fusion plasmas and it maybe technically difficult to provide adequate shielding for the coils. To overcome this difficulty, the UTST device is constructed with all external PF coils as shown in Fig. 21 [15, 156]. The recently-completed VEST device (Fig. 22) also uses similar merging-compression techniques with all external PF coils [17, 157].

E. Inductive drive based start-up - A number of scenarios utilizing magnetic induction that includes a conventional central ohmic solenoid have been also investigated by the ST community. One variation of inductive plasma start-up uses vertical field coils with currents initially in the negative direction. This provides ohmic induction as the coil currents are swung down to zero. For this scheme to work, it is important to have sufficient pre-ionization due to the inherent "error" field in the applied vertical field, and the plasma is radially unstable. Using 100 kW of ECH power, 10 kA of plasma current was produced solely by the simple outer PF coil vertical field swing in TST-2 [12]. This technique was extended to an experiment on JT-60U, resulting in a non-inductively driven 600 kA high β_p plasma [158]. A refinement to the PF coil-only start-up is to create a multi-pole null region in the outer part of the plasma to reduce the error field, while retaining some of the poloidal flux needed for subsequent current ramp-up [159]. Recently, an all-metal iron-core transformer compatible with high neutron flux, that incorporates high-resistivity inserts, to break up eddy current patterns in the copper toroidal field coil design, has been proposed [160]. It should be also noted that for superconducting (SC) ST power plant designs, as with those based on tokamaks, neutron shielding is already available for the SC magnets. Because of this, an ohmic heating solenoid with a sufficient start-up capability can be incorporated into the design as mentioned in Sec. II.C. [88-90].

V. Transport and Turbulence.

A. Motivation for ST Research – A fundamental understanding of plasma transport physics is critical for designing future magnetic fusion devices. It is often quoted that the fusion energy gain factor Q scales as H^{5-7} where H is the confinement improvement factor compared to the standard H-mode. This would then imply that one would need to know the H-factor to within 10% in order to have sufficient confidence of predicting Q within a factor of two. As the operating parameters of future devices (including ITER) represent a considerable extrapolation from present day experiments, development of accurate confinement predictions is a key goal of present-day fusion energy research. Indeed, one of the key uncertainties of MA-class ST plasma performance has been the confinement quality of higher current, lower collisionality ST fusion plasmas. For example, ST plasmas, due to their large mirror ratio [$B_{Tmax}/B_{Tmini} \sim (A+1)/(A-1) = 2$ for $A = 3$, and $= 5$ *for* $A = 1.5$], can have a significant trapped particle population compared to tokamaks. How that can influence the anomalous transport is a natural question for ST plasmas as they enter the collisionless regime. Interestingly, as mentioned in the introductory section, observed MA-class ST plasma confinement actually showed an improving trend with reduced collisionality, i.e., $\tau_E \sim \nu^{*-1}$ as shown in Fig. 7. This is a somewhat surprising but very encouraging result, as the operating parameters of future devices are at least an order of magnitude lower in collisionality compared to present day experiments. It is generally agreed that plasma transport by so-called classical or neoclassical mechanisms such as collisional transport is relatively well understood. Therefore, the main focus of present-day transport research is on the less well understood plasma transport by plasma micro-turbulence, often termed "anomalous" transport. The generally high-beta nature of ST plasmas could host plasma turbulence with increasing electromagnetic character. This can potentially lead to greater anomalous transport, particularly for electrons. As illustrated in Fig. 61, the modes which are believed to be responsible for plasma transport include ion scale microturbulence (i.e., low-k_θ or $k_\theta\rho_s \sim 1$ where $\rho_s = C_s/\Omega i$). Examples are the ion temperature gradient (ITG) mode [161], trapped electron mode (TEM) [162], kinetic ballooning mode (KBM) [163], and micro-tearing (MT) mode [164]. Electron scale microturbulence (i.e., high-k_θ or $k_\theta\rho_s \sim 10$) includes electron temperature gradient (ETG) drift waves [165]. In addition, there

are energetic-particle-driven global and compressional Alfven eigenmodes (GAE and CAE), which can also affect power deposition and electron energy transport in the plasma core region [166]. In terms of drive and stabilization mechanisms, electron beta β_e and collisionality $\nu^{e/i}$ are important parameters as illustrated in Fig. 62 [167]. All of the ion scale ballooning-type drift waves (e.g., ITG, TEM, and KBM) tend to be stabilized by increasing $\nu^{e/i}$, while the ETG mode is insensitive to $\nu^{e/I}$, and the MT mode is often more unstable at higher $\nu^{e/i}$. The ETG and ITG/TEM modes are excited at low beta, and KBM and MT tend to become more important in high beta plasmas. Therefore, it is vital to understand the fundamental transport physics mechanisms (particularly that of the electron energy) based on micro-turbulence to gain sufficient confidence in predicting future ST performance, as the future reactor facilities including ITER represent significant capital investment. In addition to the benefits of predictive capability, if some tools to control plasma transport can be developed through better understanding of microturbulence driven transport, they can be utilized to achieve more optimum pressure and current profiles for reactor performance optimization [70].

Global scalings are discussed in Sec. B. However, it is crucial to understand fundamental transport mechanisms for each of the plasma quantities, including ion thermal energy, electron thermal energy, energetic particles (e.g., α–particles), toroidal momentum, and thermal particles including impurities. The ion transport physics is discussed in Sec. C. The electron transport physics is particularly important for burning plasma regimes, since fusion alpha particles predominantly heat electrons. The ETGs have been measured in NSTX for the first time, taking advantage of the large electron Larmor radius regime due to the high electron β, and first ever quantitative agreement was obtained with a gyro-kinetic transport modeling as discussed in Sec. D. The momentum transport is discussed in Sec. E. Finally, thermal particle transport physics, including impurity transport, is discussed in Sec. F. Energetic particle transport is discussed in the energetic particle section in Sec. VIII.

B. Global Confinement Scaling - Global confinement scaling has been actively pursued as a tool to quickly quantify the dependence of confinement on various plasma and device dimensional and non-dimensional parameters, and assess the plasma performance of present-day devices as well as predict the performance of future devices including ITER. Perhaps the most well-known

confinement scaling is the ITER98$_{pby,2}$ H-mode scaling [21], which is expressed in engineering variables as

$$\tau_{E,th} = 0.0562\, I_p^{0.93}\, B_T^{0.15}\, R_0^{1.97}\, \kappa^{0.78}\, n_e^{0.41}\, \mu^{0.19}\, P_L^{-0.69}\, A^{-0.58} \qquad (6)$$

There is a small adjustment for the average ion mass μ, giving a slight advantage for higher mass tritium-operation compared to that of hydrogen and/or deuterium. Here, the absorbed power P_L is defined as the total heating power into thermal plasma component, taking into account possible heating efficiency minus the change in the plasma stored energy dW_{th}/dt. The H-mode confinement scaling was derived by using the tokamak data base, so it is naturally of interest to see if this scaling actually applies to STs with much lower A and higher κ. For comparing the present-day tokamak experimental data base to ITER, the main extrapolating parameters are I_p, R_0, *and* P_L. For STs, the main extrapolation to future ST devices such as FNSF from NSTX/MAST experiments would be based on I_p, R_0, B_T, *and* P_L. If we were to compare ST and tokamak power plants with a given fusion power output, one might expect quite similar μ, n_e, and P_L. However, an ST power plant compared to that based on a tokamak may have ~ 2 x I_p and κ, but only ~ 1/2 x B_T, R_0, and A. Then, the $\tau_{E,Thermal}$ for the ST and tokamak plants as predicted by Eq. 6 would be essentially the same. The higher κ is desirable for the ST not only from the MHD and non-inductive operation point of view, as discussed in Sec. III, but also from the confinement scaling point of view if the tokamak scaling such as the one described by Eq. 6 holds true. The desirability of higher κ tends to drive the design point for future STs toward κ ~ 2.5 – 3.3.

The B_T and I_p confinement dependence observed in boronized + He GDC conditioned NSTX plasmas is shown in Fig. 63 [168]. The observed dependence $\tau_{E,th} \propto I_p^{\sim 0.4}\, B_T^{\sim 0.9}$ is clearly different from the tokamak scaling of $\tau_{E,th} \propto I_p^{0.93}\, B_T^{0.15}$. The MAST experiments also found a stronger than linear B_T dependence and weaker thank linear I_p dependence consistent with that of NSTX and in contrast with the conventional tokamak scaling [169]. For constant q (i.e., fixed B_T : I_p ratio) or $B_T \propto I_p$, the NSTX scaling then gives $\tau_{E,th} \propto I_p^{\sim 1.3}$, which is somewhat stronger than the tokamak scaling of $\tau_{E,th} \propto I_p^{\sim 1.1}$. This scaling trend in NSTX can be explained if the global confinement trend is dominated by electron energy transport, as the ion energy transport is close

to neoclassical as discussed in Sec. B. The recent experiments on NSTX with evaporated lithium wall conditioning, as described in more detail in Sec. VII, showed a strong I_p dependence however, and weak B_T dependence similar to that of the tokamak scaling in Eq. 6. The difference in the scaling with lithium and non-lithium PFCs presents a challenge for this type of scaling approach. It is found that collisionality unifies the lithium and non-lithium confinement results, as discussed below.

Another way of expressing the ITER98$_{y,2}$ H-mode confinement scaling is to use the dimensionless quantities or "physics variables" [21].

$$\tau_{E,th} \propto \tau_B \, \rho_*^{-0.70} \quad \beta^{0.90} \, \nu_*^{-0.01} \, M^{0.96} \, q_*^{-3.0} \, A^{-0.73} \, \kappa^{2.3} \qquad (7)$$

where τ_B is the Bohm time = a^2 B / T, ρ^* is the normalized toroidal Larmor radius ρ_L/a, q_* *is* cylindrical safety factor, and ν^* is the normalized collisionality. In this physics variable-based scaling, the extrapolation from present-day tokamaks to future devices would be mainly in ρ_* and ν_*. Since the ν_* dependence is so weak, the most important physics parameter for extrapolations is considered to be ρ_* for tokamaks. For STs on the other hand, there is relatively small variation in ρ_*, but the ν_* variation is quite large. Clearly if the ν_* dependence is indeed so weak as suggested by Eq. (7), then the confinement scaling for STs would be relatively simple. Another problem with the tokamak scaling suggested in Eq. (7) is the very strong beta degradation ($\beta^{0.90}$), which would be rather unfavorable for future higher beta reactor operation and generally higher beta STs. However, the confinement data from NSTX and MAST suggest a very different parameter scaling, showing improved confinement with reduced collisionality and essentially no beta dependence (or degradation), which is quite encouraging for future ST facilities. In Fig. 64, the collisionality dependence is shown for (a) NSTX [31, 168] and (b) MAST [170], where the confinement trend indicates improvement with reduced ν_* in both devices, i.e., $B\tau_{E,th} \propto \nu_*^{-0.79}$ for NSTX and $B\tau_{E,th} \propto \nu_*^{-0.82}$ for MAST. For NSTX, those discharges that used Li evaporation wall conditioning are in red, and those that used helium glow discharge cleaning (HeGDC) plus boronization conditioning are in blue [31]. It is seen in the plot that the Li evaporation discharges generally have lower collisionality and higher

confinement, extending the range of collisionality to lower values. Interestingly, this collisionality scaling appears to unify the confinement trends of these discharges, despite the different parametric dependences on engineering variables as noted above. The scaling exhibits a strongly favorable trend of increasing normalized confinement with decreasing collisionality, which bodes well for future lower collisionality STs. There has been a re-examination of the tokamak scaling utilizing improved regression techniques with the addition of NSTX and MAST data. This has yielded more collisionality dependence and much less beta degradation compared to the original ITER scaling (Eq. 7), which is now expressed as $B\tau_{E,th} \propto \rho_*^{-2.6} \beta^{-0.08} \nu_*^{-0.2}$ [22, 171]. Here, the collisionality and beta scalings are closer to that observed in NSTX and MAST. Also, in a review paper on the dimensional confinement analysis [172], it is pointed out that there is a significant ~ x3 variation in the ν_* trend among tokamak devices, which perhaps makes the correlation with ν_* less clear. The paper also points out a significant variation in the observed beta degradation even among tokamak experiments. It is encouraging to note that the beta degradation is weak for those devices reaching the highest values of β_N, including STs. This is particularly interesting, since the beta degradation is generally thought to depend on increased electromagnetic effects on turbulence as beta is increased. This makes the weakening of beta degradation at high beta counter-intuitive. Clearly, the device-to-device variations on dimensional confinement behavior suggests an acute need for more fundamental understanding of transport mechanisms if we are to develop a reliable predictive capability for future facilities. Indeed, extending the confinement data toward lower collisionality is one of the important missions for NSTX-U and MAST-U.

C. Ion Energy Transport - Due to stronger shaping and relatively low magnetic field, the ST configuration can create strong ExB sheared flow rates which can exceed that of the growth rate of ion transport relevant turbulence such as ITGs and TEMs. The resulting ExB shear stabilization of ITGs/TEMs makes the ion transport in STs near the neoclassical level for most of the plasma cross section [173]. Indeed, in NSTX and MAST H-mode discharges, the observed ion transport (from TRANSP analysis) is very close to the neoclassical level for much of the plasma profile, as shown in Fig. 6, while the electron energy transport remain anomalous. While close to neoclassical ion transport has been observed in tokamaks locally, this global close to neoclassical ion transport behavior appears to be a characteristic of ST H-mode plasmas. This

near neoclassical ion transport behavior is consistent with the observed weaker I_p dependence of the global confinement scaling in STs, as mentioned in Sec. B. Due to the good ion energy confinement, the NBI heated H-mode plasmas in NSTX and MAST generally have a higher ion temperature compared to the electron temperature, even though a higher fraction of the NBI power (~ 60 – 70 %) is estimated to flow into electrons. Also, the ion energy transport trend appeared to change as the collisionality is reduced in NSTX, as shown in Fig. 65, where the observed χ_i at mid-radius of r/a = 0.6 is plotted as a function of ν_e* [31]. As can be seen in the figure, the ion diffusivity χ_i is trending up well above the neoclassical values (i.e., $\chi_{i,neo}$) at lower collisionality regime. While the absolute level of χ_i may have a factor of two range of uncertainty, there is a clear trend of increasing χ_i from $\chi_i \sim \chi_{i,neo}$ to perhaps becoming four to five times more anomalous at lower collisionality. This is opposite the trend in electron transport, where χ_e is decreasing with reduced collisionliaty as discussed in Sections B. and D. While χ_e still dominates over χ_i in the present experiments, the trend indicates that it is essential to understand the behavior of both χ_e and χ_i in NSTX-U and MAST-U as much lower collisionality regimes are explored. Ion-scale turbulence research has made significant progress in recent years due to the implementation of the beam emission spectroscopy diagnostic (BES) on NSTX and MAST [174, 175]. One may note that because of the multiple possible ion transport relevant turbulence modes with a similar range of wavelength and frequency (i.e., ITG, TEM, and KBM), it is often difficult to clearly identify one particular mode responsible for the ion energy transport. In the core region of the MAST plasma, highly non-linear saturated "critically-balanced" turbulence behavior was observed [176]. Recently the ion-scale density turbulence measured by BES was compared with a non-linear, global, gyro-kinetic simulations [177]. The results indicate that while there are some degree of agreement seen in the mid-radius region, there is a significant shortfall, for example, in predicted fluctuation level and ion heat flux in the periopheral region. In the steep gradient region of the NSTX H-mode edge pedestal during ELM-free, MHD-quiescent periods, turbulence scaling consistent with TEM, KBM, or MT, but not with ITG, was observed perhaps due to the generally higher beta values for STs [178]. To further understand the ion transport physics, ion-scale turbulence diagnostics (e.g., BES) along with other turbulence diagnostics will be implemented on NSTX-U and MAST-U.

D. Electron Energy Transport – Electron energy transport is the most actively investigated transport physics topic in NSTX, since it is presently the dominant energy transport mechanism and the transport is clearly anomalous. The availability of the innovative high-k microwave tangential scattering diagnostic enabled, for the first time, measurement of radially resolved electron gyro-scale turbulence such as ETGs [179]. The physics of electron transport is likely to be also relevant in fusion reactors including ITER, as the plasma heating sources, such as negative ion neutral beams, ECH heating, and fusion-produced 3.5 MeV α-particles, all primarily heat electrons in the core. As expected, the electron transport physics is quite complex, and presently three main electron transport mechanisms have been reported for NSTX plasmas. The electrons, due to their very high mobility, can cause anomalous heat transport under a variety of conditions. The recent experiments on NSTX with evaporated lithium (Li) wall conditioning showed a clear indication of electron temperature profile broadening suggesting improved electron energy confinement in the edge region [180, 181]. A controlled lithium evaporation experiments showed that the main confinement improvement is indeed in the electron energy channel [182, 183]. The electron diffusivity at r/a = 0.7 showed continued reduction as a function of the Li deposition amount prior to the discharge up to the maximum Li deposition ~ 100 mg. The edge particle recycling was reduced from ~ 98% to ~ 90%. The reduced recycling resulted in the reduced edge density which together with generally higher electron temperature reduced the edge collisionality. The enhanced confinement with the Li deposition reducing edge collisionality is consistent with the inverse collisional scaling observed in NSTX shown in Fig. 64(a) [31]. The role of ETGs for electron energy transport is now emerging. In the collisional regime, the micro-tearing (MT) mode appears to be causing rapid electron transport through generation of stochastic magnetic fields. In strongly neutral beam heated plasmas, the excitation of Global Alfvén Eigenmodes (GAEs) with a large fluctuating magnetic field component (like MTs) were observed to cause strong electron energy transport in the core region of the plasma. This maybe again due to the generation of stochastic magnetic fields, producing a clamping of the central electron temperature even with a three-fold increase in NBI heating power. We shall now briefly describe the status of our understanding of these three electron energy transport mechanisms.

Electron energy transport associated with ETGs - The ETGs are the electron gyro-radius (ρ_e) scale turbulence known to cause electron transport in the presence of an electron temperature gradient [165]. The first definitive indications of ETGs was observed by taking advantage of the relatively large electron gyro-radius ρ_e scale length in NSTX due to high beta (i.e., high electron temperature per given magnetic field), using a radially-resolved tangential high-k scattering diagnostic on NSTX [179]. The system measures electron gyroscale fluctuations with $k_\perp \rho_e \leq 0.6$ and $k_\perp \leq 30$ cm^{-1}, with the radial and wave number resolutions of $\Delta R \sim +/- 2$ cm and $\Delta k \sim 1$ cm^{-1}, respectively. In NSTX L-mode plasmas, high-k fuctuation measurements revealed electron gyroscale fluctuations consistent with ETG turbulence. The high-k data also showed enhanced fluctuations when the electron temperature gradient exceeded the ETG linear critical gradient defined by,

$$(R/L_{Te})_{crit} = (1 + Z_{eff}\, T_e/T_i)\, (1.3 + 1.9\, s/q)\, (1 - 1.5\, \varepsilon) \qquad (8)$$

where Z_{eff} is the ionic effective charge (~ 2.5), q is the magnetic safety factor, $s = (r/q) \times (dq/dr)$ is the magnetic shear, and $\varepsilon = r/R$ is the inverse aspect ratio [184]. The ETGs indeed appear to play an effective role in regulating the electron temperature gradient near the ETG critical temperature gradient. In NSTX, HHFW core electron heating causes a very strong increase in the detected density fluctuations in the range of $k_\perp \rho_e = 0.2 - 0.4$ at R = 1. 2 m. In Fig. 66, two electron temperature profiles and corresponding measured spectral density of fluctuations are shown [185]. They indicate that the ETG scale fluctuations increase greatly when the temperature gradient exceeds the predicted ETG critical temperature gradients. This type of relatively clean ETG fluctuation measurement can be attributed to the lack of other possible modes in this frequency and wavelength range, which is not the case for the ion-scale turbulence as discussed in the previous section. It was also observed that electron gyro-scale fluctuations in NSTX H-mode plasmas with large toroidal rotation and, correspondingly, large E x B flow shear rates, increased when the electron temperature gradient is marginally stable with respect to the ETG linear critical gradient. The fluctuation amplitudes decreased when the E x B shearing rate exceeded the ETG linear growth rate [186]. The observations indicate that E x B flow shear can therefore be an effective suppression mechanism, even for ETG turbulence near marginal stability. A good agreement with the observed ETG-driven χ_e was obtained by a GTS (gyro-

kinetic) simulation code [187]. Another example of ETG physics came from the reversed magnetic shear regime, where the ETGs are predicted to be stabilized (see Eq. 8) and improved energy confinement has been observed on NSTX [188-190]. In Fig. 67, the electron temperature profiles (a) and associated q-profiles (b) are shown under condition of same HHFW electron heating power [189]. The variable here is the magnetic shear, where the reversed shear (RS) configuration represented by the red curves. One can see that a very steep electron temperature gradient (i.e., an electron temperature internal transform barrier) is developed at R = 1.2 m, where the high-k fluctuation is being monitored at the RS region as indicted by the yellow strip. In the discharge with normal magnetic shear, the electron temperature gradient relaxes to more typical profiles as represented by the blue curves. A comparison of the measured high-k fluctuations is shown in Fig. 67 (c) for those two cases. One can see that for the RS case, the ETG fluctuation is essentially stabilized and the same HHFW electron heating power significantly increases the central electron temperature. The bursts of ETGs appear to regulate the electron temperature gradient and maintain high core electron temperatures during the RS phase. The mechanism for the bursting of the ETGs is not fully understood, but the estimated enhanced transport appears to be sufficient to regulate the temperature gradient even though the bursts occur only about 1.6 % of the time [190]. A nonlinear ETG simulations of the NSTX RS plasma also showed ETG stabilization and corresponding reduction in the electron thermal diffusivity [191]. Another example is reflected in improved energy confinement associated with density gradients [192]. This has been observed for a long time in fusion research, as for example, in the peaked density profile of the TFTR super-shots [73]. The density gradient term alone, if large enough, could determine the ETG critical temperature gradient. This physics was investigated after the ELM event where the density gradient term a/L_{ne} in the pedestal region increased by a factor of five but a/L_{Te} remained constant (as did q, etc.) This resulted in ETG fluctuation reduction and a factor of two reduction in the transport coefficient in the density gradient region. All of these ETG experimental results appear to point to the basic validity of the ETG stability theory and its significant role in electron energy transport in ST plasmas. It should be also noted that while the ETGs were not directly observed in MAST, a nonlinear gyrokinetic flux-tube simulation showed that the ETG mode may be producing experimentally significant electron energy transport in MAST-like plasmas [193].

Electron transport due to micro-tearing modes – Micro-tearing modes (MTs) are small scale tearing modes with large toroidal (n) and poloidal (m) mode numbers, driven resistively unstable

and generating stochastic fields near the tokamak rational surfaces, q=m/n. As shown in Fig. 62, MTs may be particularly important for STs due to high β. Anomalous electron transport occurs when neighboring tearing mode-induced magnetic islands overlap. The approximate radial distance between two neighboring rational surfaces [m/n and (m+1)/n] is $\Delta r = 1 / (nq')$. With many toroidal modes present, the minimum distance between adjacent resonant surfaces is $\delta r = 1 / (n^2 q')$ [194]. A recent breakthrough in understanding anomalous electron thermal transport behavior with collisionality is the identification of the electromagnetic effects in causing electron thermal transport in the outer half of a set of NSTX high beta H-mode plasmas. This was achieved with state-of-art nonlinear gyrokinetic simulations as shown in Fig. 68 [195]. The microtearing mode-driven electron thermal transport is plotted as a function of normalized electron collision frequency. As can be seen in the figure, there is good qualitative agreement with the experimentally-observed values, including the observed reduced electron thermal diffusivity with reduced collisionality. The micro-tearing modes therefore may be avoided in future STs with higher toroidal magnetic field and much less collisional plasmas. On the other hand, as shown in Fig. 63, the KBM maybe excited instead as the collisionality is reduced.

Anomalous electron thermal energy transport by GAEs – With intense neutral beam injection, it was observed that core electron temperature, remain relatively constant (or even exhibit some reduction). This even holds when the NBI power is tripled in NSTX as shown in Fig. 69 (a) [167]. The radial electron temperature profile instead broadens with the NBI power, indicating greatly enhanced electron thermal diffusivity in the core with the applied NBI power as shown in Fig. 69 (b). The behavior is observed to correlate with the increased excitation of global Alfvén eigenmodes (GAEs) (see Sec. VIII). Recent measurements by high-k scattering and beam emission spectroscopy diagnostics showed an absence of any significant level of plasma turbulence, precluding normal turbulent transport in the region of active GAEs. Overlapping GAE modes can resonantly couple to the bulk thermal electrons and induce enhanced stochastic diffusion. The modeling work on GAE-driven electron transport appears to confirm this electron transport mechanism in the core of the NBI-heated plasmas. The proposed effect is potentially important for future STs as well as for any burning plasma where the fusion alphas could drive the GAEs.

E. Toroidal Momentum Transport – Plasma toroidal momentum transport is an active area of transport physics research for tokamaks and STs in recent years, due to its potential importance for future devices including ITER for macrostability and transport physics [21, 22]. The angular momentum balance equation is given by

$$m\,R\,\partial(n\,V\,P)/\partial t = \eta - (1/r)\,\partial(r\,\Gamma_\phi)/\partial r - (1/r)\,\partial(m\,r\,R\,V_\phi\,\Gamma_p)/\partial r \qquad (9)$$

where m is the ion mass, n is the ion density, η is the local torque density, Γ_p is the (radial) ion particle flux (which gives rise to a typically small convection of momentum), and Γ_ϕ is the (radial) angular momentum flux which can be written as $\Gamma_\phi = -m\,n\,R\,\chi_\phi\,\partial(V_\phi)/\partial r + m\,n\,R\,V^{Pinch} V_\phi$, including a radial momentum pinch term, V^{Pinch}. As can be given by Eq. 9, for a given local toroidal torque density η (both intrinsic and externally applied for example by NBI), the toroidal rotational profile is determined by the toroidal momentum transport or flux. As described in the RWM section (III.C), the plasma rotational profile is crucial for RWM stability in high beta operation for STs. The E x B shear produced by plasma rotation shear is believed to be partly responsible for the neoclassical level ion transport generally observed in NSTX and MAST as described in Sec. C. The anomalous momentum transport is believed to be driven by ion-scale micro-turbulence such as the ITG, TEM, and KBM, which can also drive anomalous ion energy transport. In Fig. 70, the measured ion thermal and momentum diffusivities in an NSTX H-mode plasma are plotted along with the corresponding neoclassical values computed by GTC-NEO [196]. As can be seen from the figure, unlike the relatively large neoclassical ion thermal diffusivities, the neoclassical momentum diffusivity is essentially zero. This presence of an anomalous effective momentum diffusivity may indicate the presence of residual ion scale turbulence not apparent in the ion energy transport due to the large neoclassical heat transport. In a perturbative experiment, it was also possible to deduce the radial momentum pinch term as well as the momentum diffusivity. A large inward V^{Pinch} of up to 40 m/s is observed between $0.6 < \rho < 0.8$ [197]. It is also noted that if the inward pinch is assumed to be zero, then the inferred effective momentum diffusivity is reduced by more than a factor of two. The momentum pinch drive may be caused by low-k turbulence, which theoretical models [198, 199] then predict a $V^{Pinch} \propto \chi_\Phi / R$, which appears to be consistent with the experimentally-observed trend. To further understand momentum transport, intrinsic plasma rotation (without any toroidal momentum injection) has been studied in tokamaks [200]. Intrinsic plasma rotation was also

investigated in MAST where the gas fueling location was found to be important for H-mode access [201]. Recently, in NSTX ohmic plasmas, the intrinsic rotation generated in the edge was found to be well correlated with change in the ion temperature gradient [202]. This observation is consistent with the theory of residual stress.

F. Particle and Impurity Transport - Particle transport physics is of importance because of fueling, impurity dilution, and accumulation issues. For example, if the particle confinement is too good, impurities, including fusion alpha particles, can accumulate in the plasma core. This could lead to not only fuel dilution, but also eventual radiative collapse of the main plasma as observed in long-pulse ELM-free H-mode plasmas. Nevertheless, particle transport physics is not as well investigated as energy transport physics, perhaps due to difficulties in measuring ion density profiles in any given experiment. Particle transport physics also requires tracking various ionization states, particularly for higher z impurity species. Also, from neoclassical theory, collisions among ion species could modify the neoclassical ion transport. Particle transport is therefore a complex coupled problem comprising all particle species, including electrons and ions. While particle neoclassical transport theory and modeling tools are well developed, anomalous particle transport mechanisms are not well understood either experimentally or theoretically. Impurity transport has been investigated in tokamaks and STs using controlled impurity injection techniques such as impurity gas and pellet injection. In CDX-U, impurity transport physics was investigated using VUV spectroscopic techniques. The measured core impurity diffusivity and inward pinch velocity are consistent with neoclassical analysis [203]. In NSTX, impurity transport physics was investigated using the tangential (scintillator based) multi-energy soft x-ray (SXR) array, which has identical groups of overlapping sightlines that view the same plasma volume through filters with different cutoff energies [204 - 206]. Earlier neon gas puff experiments in the NSTX L-mode showed close to neoclassical transport behavior, confirming the earlier CDX-U results [203]. The impurity transport in the H-mode also showed diffusivity levels consistent with neoclassical predictions [207]. The study also found that the plasma rotation can enhance diffusive and convective coefficients for heavy and not fully stripped impurities. For neon gas puff experiments in the H-mode, the time histories of the neon emissivity profiles after the injection were modeled using the one dimensional (radial) and time-dependent Multiple Ionization Stage Transport (MIST) code. The resulting neon diffusivity and convection velocity profiles are shown in Fig. 71 as

labeled [206]. There, the diffusivity is large (several m^2/s) at the outer radius ($r/a > 0.8$) while the core diffusivity is small (≤ 1 m^2/s). In the figure, the corresponding neoclassical values are calculated by NCLASS [207] and plotted, showing generally good agreement with the experimentally-observed values for the core region. Also, the effect of plasma rotation on impurity transport has been studied, which could explain an observed deviation from NCLASS without invoking anomalous transport. The comparison has been done for other ion species, and particle transport behavior in both L-mode and H-mode plasmas appears to be consistent with the NCLASS values in the NSTX core region.

VI. H-mode physics in STs

A. Motivation for ST Research - The so-called "high" confinement mode or H-mode has been a topic of intense tokamak research since its discovery in the early 1980's [208]. In tokamaks, the H-mode has been of interest particularly for its good (high) confinement and high pedestal pressure. The ITER design goal of fusion gain of Q =10 is based on H-mode access with a sufficient confinement H-factor of (i.e., H ~ 1) and pedestal height [21, 22]. As described in Sec. V, the Q depends very sensitively on H and it tends to increase with square of the pedestal pressure. H-mode access is also quite vital for compact ST reactors. A typical compact ST-based FNSF as discussed in Sec. II assumes relatively high confinement factors of up to H ~ 1.2-1.3. Importantly, the broader current and pressure profiles of H-modes are highly desirable for high bootstrap current fraction non-inductive operation as discussed in Sec. III. While H-mode research has a long history, many of the important physics insights are just starting to emerge in the recent years, owing to the newly available diagnostics and analysis tools. Since the H-mode "barrier" and resulting "pedestal" occur near the plasma edge region (where the plasma aspect ratio is the lowest), the relevant H-mode physics in STs takes place in a truly low-aspect-ratio regime (compared, for example, to the core transport physics which take place in the higher aspect-ratio region). The ST H-mode pedestal also generally occurs at higher plasma beta values compared to tokamaks. With accentuated pedestal parameters, H-mode studies in STs can therefore contribute substantially to on-gong worldwide H-mode research. Since global MHD stability and confinement properties of H-mode plasmas have been already discussed in Sections III and V, respectively, we will devote the present section to the H-mode-specific physics issues, pointing out some unique features for STs. In Sec. B, the H-mode transition and power threshold research for STs is discussed. In Sec. C, the H-mode pedestal stability and ELM physics is described, and in Sec. D, the ELM control tool development is summarized.

B. H-modes transition and power threshold – For STs, H-modes were first observed in START [207] and subsequently studied in NSTX and MAST, as its access was facilitated by auxiliary heating power and fine plasma divertor control [201, 210 - 227]. Recently, the H-mode was also observed in PEGASUS ohmic plasmas [228]. Overall, an H-mode in STs looks and behaves qualitatively similar to that in tokamaks. This observation reinforces the robustness of

fundamental H-mode physics for tokamaks and STs. In Fig. 72, typical H-mode plasma profiles measured in MAST are shown [211]. A strong density barrier is particularly evident near the edge, giving the well-known box-like profile ($t \geq 7$ ms) compared to the centrally peaked L-mode plasma prior to the H-mode transition ($t = 0$ ms). Density "ears" form at the plasma periphery due to impurity fueling, evolving over a time scale of ~ 20 ms (Fig. 72a). The change in T_e (Fig. 72b) is less pronounced. The pedestal pressure gradient (Fig. 72c) remains nearly constant throughout H-mode. These H-mode features are quite similar to those observed in NSTX and tokamaks in general.

One of the important questions that needs to answered is the H-mode power threshold for future STs and tokamaks including ITER. Since auxiliary heating power is quite expensive, it is highly desirable to achieve H-modes with minimum auxiliary heating power. The H-mode threshold power in STs is observed to vary greatly (by as much as an order of magnitude) with the vacuum/wall conditions and the plasma configurations. Once the vacuum and walls are well conditioned, the H-mode becomes accessible even with relatively modest sub-MW auxiliary heating power. With aggressive "boronization" and/or "lithiumization" as described in Sec. VII, the H-mode power threshold becomes quite low, enabling the H-mode access even in ohmic plasmas [201, 210, 229]. An in-board gas puff also reduces the H-mode power threshold. The benefit of in-board gas puff for H-mode access appears to be significant for STs compared to tokamaks [201, 209, 223]. The in-board gas puff has been therefore routinely used in MAST and NSTX, and it also enabled PEGASUS to achieve H-mode in ohmic plasmas [228]. With this inherent power threshold variability in mind, controlled H-mode threshold experiments were conducted on NSTX and MAST in well-conditioned plasmas [216, 217]. Since the non-activation phase of ITER is likely to use either hydrogen or helium plasmas, the H-mode power thresholds were compared for deuterium and helium plasmas. The results indicate that the L-H power threshold is approximately 20-40% greater in helium than in deuterium in NSTX [216] and about 40% in MAST [217]. These observations are similar to those in tokamaks except the power threshold is still a few times that of the scaling based on tokamaks [230]. Wall conditioning with lithium reduced the L-H power threshold in NSTX significantly, by as much as ~ 60% as shown in Fig. 73 [216]. Also in NSTX, the power threshold increases with increasing I_p and decreases with increasing R position of the x-point location as shown in Fig. 73 [216, 219]. Both trends are consistent with the increased threshold with toroidal magnetic field

at the x-point for a given q. This result is consistent with the prediction that the kinetic neoclassical transport, including ion orbit loss, sets the edge radial electric field and the ExB shear available to sustain the H-mode transport barrier. In MAST, the power threshold was investigated as a function of x-point height and κ. Both NSTX and MAST saw an increase in the H-mode power threshold with application of resonant magnetic perturbations (RMPs) [216, 217, 222]. This observation is similar to those from tokamaks and is somewhat expected since RMPs tend to degrade edge confinement (or change edge rotational shear.) There are some differences between MAST and NSTX, where in MAST, there is no obvious correlation with E_r shear profiles [217], but in NSTX, some dependence on the E_r shear was observed [216]. Also in MAST, there is no evidence for a critical T_e needed to access H-mode, but in NSTX, a critical T_e could explain the reduced threshold power with lithium which increased the edge T_e. Another notable observation is a strong minimum of the L-H power threshold at drsep ~ 0 (balanced double null configuration) [215, 220]. The effect observed in STs is much stronger than that observed at higher R/a. Overall, while there has been very good progress in obtaining an extensive H-mode experimental data base for STs and tokamaks, the fundamental understanding needed to explain the observed H-mode power threshold and develop an associated predictive capability is still lacking today.

C. H-mode pedestal and edge localized modes (ELMs) – Another active area of research involves H-mode pedestal and Edge Localized Modes (ELMs) physics. The ELMs are periodically-bursting modes occurring in the edge region of H-mode plasmas. They act as a regulating mechanism for the H-mode pedestal, and ELMs also facilitate the rapid expulsion of plasma both energy and particles from the pedestal region to outside the last closed flux surface (LCFS). The ST configuration readily allows global views of ELM activity as shown in Fig. 74, where the high-speed video images of MAST plasmas at the start of the ELM cycle show a global filament structure of $n \leq 10$ [226, 227]. In order to enhance the ELM image, the background plasma light from the preceding non-ELM frame has been subtracted. The time evolution of the edge density profile during ELM was captured by timing the four Nd-Yag lasers of the Thomson scattering diagnostic in MAST as shown in Fig. 75 (a). The laser timing is indicated in Fig. 75 (b): (1) The solid red circles and lines indicate ~50 μs before the ELM. (2) The open green circles and lines are ~100 μs after the start of the ELM. (3) The solid blue

squares and lines are ~250 μs after the start of the ELM, and (4) the open cyan squares and lines are ~400 μs after the start of the ELM. As shown in Fig. 75, the ELM event rapidly expels the plasma density from the pedestal.

There are a number of different types of ELMs observed in STs as shown in Fig. 76 [224]. The type I and III ELMs are regularly observed in tokamaks as well as in STs as shown in Fig. 76 (a) and (b), respectively. As shown in Fig. 76, the large Type I ELMs can produce 5-15% range stored energy reduction while the intermediate Type III can produce a 1-5% reduction. The Type V ELMs as shown in Fig. 76 (c) and (d) appear to be unique to NSTX [224, 225]. The Type V ELMs which occur at higher edge collisionality, are observed by several diagnostics but have no measurable impact on the stored energy. A high-speed camera image of the Type V ELMs shows that the global filament structure (usually one or two compared to multiple for Type I or III), is very narrow (~ 6 cm) and only lasts for a small fraction of the time of the larger ELM events. If the Type V ELMs can be extrapolated to future devices, it could be an attractive operating regime for next step fusion experiments including ITER.

The large Type I ELMs could introduce a high heat flux (predicted to be as high as 1 GW/m^2 for ITER-class plasmas) onto the divertor plates. This is due to the collapse of the H-mode pedestal, and could seriously damage the plasma-facing components in future large STs and tokamaks. Therefore, the stakes are extremely high for fully understanding H-mode pedestal physics, and developing satisfactory predictive capabilities to assure safe and acceptable H-mode operation. The H-mode pedestal stability and ELM excitation have been successfully described by the peeling-ballooning MHD stability model for tokamaks (included in the ELITE code) [231, 232]. According to this model, the H-mode pedestal stability is mainly determined by the current-driven kink-peeling modes and the pressure-driven ballooning modes as shown in Fig. 77. As also shown in the figure, the plasma shaping could expand the stable boundary. For STs, the strong shape-factor is therefore expected to play an important role in the pedestal stability. The peeling-ballooning stability diagram for the Type I ELM in NSTX is shown in Fig. 78 [233], and for a similar analysis performed for the MAST Type I ELM in Fig. 79 [234]. For NSTX, the ELMing discharges lie close to the peeling mode stability boundary, while for MAST, the experimental point appears to lie close to the tip of the peeling-ballooning stability boundary. We also note that the PEGASUS H-mode also appears to be inside the peeling mode stability boundary, perhaps due to the strong shape characteristic of the ultra-low aspect ratio geometry [235]. Due to generally higher ballooning limits for STs, the first access to the kink/peeling

branch is expected. The H-mode pedestal creates a strong pressure gradient which induces significant edge bootstrap currents, so the edge current and pressure are coupled. An observation which may illustrate the difference between STs and tokamaks is shown in Fig. 80, where the pedestal width is plotted as a function of the pedestal poloidal β [236]. The NSTX pedestal width follows a $\Delta = c(\beta_\theta^{ped})^1$ dependence, which is quite different from the $\Delta = c'(\beta_\theta^{ped})^{0.5}$ scaling for MAST [234] and DIII-D [237]. The ~ 1.0 exponent scaling observed for NSTX has been shown to be consistent with preliminary analyses using the ballooning critical technique (BCP) [238], which has yielded a 0.8 exponent scaling of the pedestal width as shown in Fig. 80. It should be noted that the BCP model shows a 0.5 exponent for standard aspect ratio tokamaks. This example shows the good progress being made in understanding of the pedestal physics.

D. ELM control – An important research area for ELMs is their control. If one can reliably stabilize ELMs or reduce their virulence, there will be a huge benefit for future tokamaks and STs including ITER. This is therefore a very active on-going research topic. Recently, ELMs were stabilized by the stochastic plasma boundary produced by a set of resonant magnetic perturbation (RMP) fields (n=3) on a tokamak [239]. The H mode transport barrier and core confinement were unaffected, despite a threefold drop in the toroidal rotation. Subsequent experiments on NSTX and MAST with similar RMP fields, however, resulted in varied effects on ELMs, even though a sufficiently stochastic boundary should have been created in the ST experiments. On MAST, RMP fields increased the ELM frequencies and reduced the amplitudes [240]. On NSTX, the application of RMP fields did not stabilize ELMs, but actually triggered ELMs in lithium-induced ELM-free plasmas as noted below [241-244]. Quite unexpectedly, lithium application in NSTX has resulted in a complete suppression of ELMs as shown in Fig. 81 [245, 246]. Plasmas previously exhibiting robust Type 1 ELMs gradually transformed into discharges with intermittent ELMs, and finally into continuously-evolving ELM-free discharges as the lithium evaporation rate is increased. The main change in the edge pedestal region is the reduction of density in the plasma scrape-off layer, and increased electron temperature in the pedestal region of the plasma as show in Fig. 82. Overall, however, the pedestal plasma pressure is much more enhanced for the lithium-stabilized ELM case. The increase in the pedestal pressure that appeared to result in ELM suppression seems contradictory at first. It should be pointed out however that while the H-mode pedestal pressure height is enhanced, the pedestal pressure gradient is not, i.e., the pedestal width increased dramatically. A detailed edge pedestal stability analysis using the ELITE code showed that the ELM-ing plasma started out to be near

the kink/peeling mode instability boundary (as shown in Fig. 78). It then moved well into the stable region as shown in Fig. 83, because of the inward shift of the pressure and edge current peak into the reduced magnetic shear region [245, 247].

On NSTX, ELM-free discharges exhibited impurity and radiation buildup, often leading to plasma disruptions. The application of a n=3 RMP field on NSTX was able to trigger the ELMs with relatively high reliability, as shown in Fig. 84 [241-243]. As shown in Fig. 84, by actively triggering the ELMs, the impurity accumulation was reduced sufficiently to prevent radiative collapse, but without degrading the plasma confinement in high performance discharges. Increasing the ELM triggering rate also reduced impurity levels and the ELM-triggered stored energy loss. The ELM triggering mechanism is being investigated with a 3-D MHD modeling [244]. It should be also noted that this ELM triggering is also known as the ELM pacing, and other techniques such as the repetitive lithium granular injection and vertical jogs have been successfully developed [248, 249].

VII. Boundary Physics

A. Motivation for ST Research - Boundary physics is arguably the most challenging area of research for developing an attractive magnetic fusion reactor design. Fusion reactors such as FNSF and Demo are envisioned to operate steady-state at much higher heat fluxes (2 – 3 x) than in present-day operating divertors, including conditions expected in ITER. The smaller major radius and higher power density of STs can produce very high divertor heat fluxes, so that measures of divertor heat load such as "P/R" can be correspondingly high. The peak divertor heat flux for presently-operating STs can regularly exceed 10 MW/m^2 [250] and transiently reach much larger values during ELMs and disruptions to approach values expected in ITER. The ST magnetic field pitch can be quite steep, with the pitch angles ~ 45° (or $B_T \sim B_P$) at the outboard mid-plane. This is nearly an order of magnitude larger than that of typical tokamaks as shown in Fig. 85 [251]. This sharp field pitch and small major radius makes the divertor connection length, i. e., the distance along the field line between the outer mid-plane and the divertor plate, to be relatively short. The heat from the core plasma is expected to flow out in the outer mid-plane region due to the unfavorable field line curvature, and the heat is readily exhausted along the field lines into the divertor region. Typically ~ 50% of the plasma heat is expected to reach the divertor plate, while the rest can be dissipated through various mechanisms including radiative losses. The short connection length of STs tends to make the peak heat flux high, since there may not be sufficient time for radial heat spreading via turbulence and other mechanisms. On the other hand, due to its relatively low toroidal field and smaller divertor major radius (i.e., strong toroidicity), cross-field "anomalous" transport can be greatly accentuated in STs. The large mirror ratio along the divertor field line could also affect the parallel heat transport [252]. In Sec. VII-B, divertor heat load and divertor configurations are described. We should note that the region we consider in this section is outside of the last closed flux surface. The H-mode and ELM effects were discussed in Sec. VI. In Sec VII-C, the edge turbulence and transport behavior is summarized. In Sec. VII-D, the plasma facing component (PFC) and divertor boundary research using lithium is described.

B. Divertor heat loads and their mitigation

Inboard/outboard divertor heat load asymmetry - The ST configuration, with small major radius and relatively short connection length, can produce very high divertor heat fluxes over 10 MW/m^2 even in present-day devices. On the MAST device, a strong asymmetry of power sharing between the inboard and outboard divertors was found as shown in Fig. 86 [253]. The shallow field line pitch for the inboard divertor in contrast to the strong outboard field line pitch can be seen in Fig. 85. The power flows predominantly (i. e., $P_{out}/P_{in} \sim 50$) to the outboard side, which is also the case during ELMs in that $P_{out}/P_{in} \sim 20$. Since it would be indeed technically challenging to handle the high heat flux for the inboard divertor due to the limited area and access, this very large power partition asymmetry toward outer divertor is quite favorable for the ST concept. Similar very low heat fluxes for the inner divertor was observed in NSTX plasmas [254, 255]. The inherently low heat flux enables the inner divertor to "detach," which further reduces the heat flux. Because of the very low power flux for the in-board divertor in STs, the main emphasis for diverter heat flux mitigation research has been focused on the outboard divertor for STs.

Heat flux mitigation by flux expansion - In NSTX, utilizing the high power neutral beam injection (NBI) system, a single null discharge with a moderate triangularity of 0.4 was observed to have a peak outer divertor heat flux during the H-mode that increased with NBI power, such that where the peak divertor heat flux, $q_{div,\,peak}$, reached as high as $\sim 10\ MW/m^2$ for $P_{NBI} \sim 5\ MW$ [250, 256]. This level of observed $q_{div,\,peak}$ on NSTX is similar to that expected for ITER. To develop a method to reduce $q_{div,\,peak}$, a number of experiments were performed on NSTX. One of the most reliable ways to reduce $q_{div,\,peak}$ is by the so-called the divertor flux expansion, f_{exp}. If the magnetic field flux from the mid-plane region can expand to a larger surface area, the peak heat flux is usually reduced accordingly. It is therefore instructive to look at the $q_{div,\,peak}$ on f_{exp}. In Fig. 87, the effects of the magnetic flux expansion on the peak divertor heat flux $q_{div,\,peak}$ is plotted as a function of flux expansion f_{exp} in highly shaped $(d \sim 0.8,\ k \sim 2.2 - 2.4)$, lower single null H-mode discharges with $I_p = 1.0 - 1.2\ MA$ and $P_{NBI} = 6\ MW$ in NSTX [256]. The $q_{div,\,peak}$ is reduced from $8\ MW/m^2$ to $2\ MW/m^2$ by increasing f_{exp} from 10 to 40. The ideas for divertor heat flux mitigation through expanding the divertor flux include the snow-flake divertor (SFD) [257] and the X-divertor [258, 259], which are based on additional field null points in close to the usual single null configuration of a conventional divertor. The multiple field nulls make the field null

size larger, and cause greater field null expansion in the null region. This type of multiple-null configuration was tested on NSTX, and shown to be quite effective in reducing the divertor heat flux. This configuration is illustrated in Figs. 8 and 88, and can result in a very large effective divertor flux expansion of ~ 50. As shown in Fig. 88, the SFD configuration resulted in a significant reduction of a factor of ~3 in the divertor heat flux [251]. It should be noted that the SFD configuration has a possibility of multiple heat flux channels [257]. The SFD configuration in NSTX can also be referenced to the x-divertor configuration. In terms of future possibilities, an innovative concept being considered is the super-X divertor (SXD) configuration [260]. By extending the outer divertor flux line to larger major radius, a large flux expansion is achieved that brings down the plasma temperature and creates a partially detached divertor condition. Another advantage of the SXD is that it significantly increases the divertor connection length, while increasing the divertor volume by expanding it into lower toroidal field region. The MAST device is upgrading its divertor to the SXD configuration as shown in Fig. 89. [261, 262]

Radiative cooling and other approaches to heat flux mitigation - In addition to the divertor flux expansion, there are other ways to reduce the divertor heat flux. It can be reduced in principle by a factor of two by going to a double null configuration, utilizing the upper and lower divertors for power exhaust. Further progress in reducing the peak flux in NSTX was demonstrated through the partially detached divertor (PDD) regime, resulting in a peak heat flux reduction of up to 60% [263, 264]. Deuterium gas puffing into the devertor area reduces the electron temperature to about a few eV in front of the divertor plate, which is sufficient to facilitate radiative cooling. The radiative cooling effect can be seen in the SFD configuration in Fig. 88. (b), where radiative cooling can cause partial divertor detachment and further reduces the heat flux by about a factor of three [251]. The combination of the SFD and radiative cooling can reduce the heat flux by an order of magnitude. It maybe noted that the SFD configuration can increase the volume of the field null region and significantly increase the divertor connection length which tend to enhance the radiative cooling [257]. While radiative cooling and partial divertor detachment together form a powerful tool for reducing the divertor heat flux, a potential weakness of this approach is that it is highly non-linear. A heat pulse caused by an ELM, for example, can often reduce the effectiveness of radiative cooling. The resulting rise in electron

temperature can result in reduced radiation, unless some seed ions of heavier impurities such as argon are introduced. The heavier impurity seeding could result in plasma performance degradation and core impurity accumulation as observed in tokamak experiments.

Heat flux mitigation by lithium – A potentially important observation for divertor heat flux mitigation is the divertor heat flux reduction accompanying the Li coating of divertor surfaces in NSTX [265]. As shown in Fig 91, the measurements showed a ~ 50% reduction in peak heat load on the divertor strike point surfaces with only a modest amount of Li (~ 300 mg) evaporation prior to the discharge compared to 150 mg evaporation. It is estimated that < 10 % of the evaporated Li is deposited over the LLD surfaces. The heat flux reduction is accompanied by an increase in the localized radiation measured by bolometers from the region above the inner and outer strike points. Motivated by this observation, a liquid lithium (LL) based radiative divertor concept termed the RLLD (radiative liquid lithium divertor), has been proposed [264]. The evaporated or injected Li is readily ionized by the plasma due to its low ionization energy, and the poor Li particle confinement near the divertor plate enables ionized Li ions to radiate strongly, resulting in a significant reduction in the divertor heat flux. This radiative process has the desired effect of spreading the localized divertor heat load to the rest of the divertor chamber wall surfaces, facilitating divertor heat removal while maintaining low recycling for improved plasma performance. The modeling results indicated that the Li radiation can be quite strong and explains the NSTX Li results. The same model predicts that only a small amount of Li (~ a few moles/sec) is needed to significantly reduce the divertor peak heat flux for typical (1 GW-electric) fusion reactor parameters.

Effects of 3-D fields - With the utilization of 3-D fields for various purposes (see Sec. III), the effects of 3-D fields on the divertor heat flux have been also investigated in NSTX [267] and MAST [268]. The main effect of the 3-D fields is to cause toroidal and poloidal variations in the divertor heat flux. This effectively increases the peak heat flux locally, since the heat flux can no longer be toroidally uniform. In Fig. 91, the divertor heat flux is shown in red for a detached divertor plasma with light gas puffing [267]. As the 3-D (n=3) fields is applied, one can see multiple heat flux peaks appear in blue at the locations where the increased heat flux peaks are apparent. At this point, the divertor is back to the attached regime as evident from the increased

heat flux. Finally, the heat flux increase associated with ELMs, as indicated by the green trace, can cause reattachment.

C. Boundary Turbulence & Transport **–** As the plasma heat comes out of the core plasma (presumably predominantly from the outer mid-plane region where there is unfavorable curvature), an important research topic is how the heat (or energy) and particles diffuse out radially (and poloidally) while flowing toward the divertor region (i. e., outside the last closed flux surface) via parallel transport. The radial (turbulent) heat transport could largely determine the peak divertor plate heat flux, which then determines the divertor heat handling design requirements for future devices including ITER. It is therefore of critical importance that a predictive (theoretical) capability is developed to be able to quantify the radial transport. This area of research is actively pursued for tokamaks and STs for its obvious importance. For example, there is a multi-device study that reveals a notable trend in the divertor heat flux. This is shown in Fig. 92, where the power fall-off length l_q at the mid-plane is plotted as a function of the poloidal magnetic field at the outer mid-plane for various tokamak/ST devices [268]. This is an unfavorable trend, as the $l_q \sim B_{pol}^{-1}$ dependence would predict even higher peak fluxes for the higher B_{pol} (and I_p) operation expected for future devices including ITER and FNSF. As can be seen from the figure, the NSTX and MAST contributions to this database are represented in the lower B_{pol} part of parameter space. This trend can be tested in NSTX-U and MAST-U with the doubling of B_{pol} from NSTX and MAST. This observed trend is consistent in absolute magnitude with the predictions of a recently formulated heuristic drift-based model, assuming non-turbulent particle transport coupled with anomalous electron thermal transport [270].

Edge Turbulence Study **–** In order to develop a physics-based understanding of the radial transport of heat and particles, there have been extensive edge turbulence transport studies in many fusion devices utilizing primarily visible fast cameras [271], gas-puff-imaging (GPI) measurements [272], edge probes [273, 274], beam emission spectroscopy (BES) [175, 176] together with theory and modeling [275 – 278]. The region of interest is outside of the last-closed-flux-surface (LCFS), and it is in the open field line region. It is therefore not so surprising that the observed edge turbulence in STs is similar to the edge turbulence in large and small tokamaks, stellarators, and RFPs [279]. This is apparently due to the generic drift wave and nonlinear "blob" or "filamentation" formation mechanisms in all (open field line)

toroidal plamas [275, 276]. The advantage of the ST geometry is illustrated in Fig. 93 where the fast camera images of edge turbulence can be obtained for the entire plasma [280, 281]. The full view turbulence images of (a) inter-ELM, (b) L-mode, and (c) ELM phases from the same discharge are shown, and (*d*) the corresponding intensity traces normalized to the peak ELM amplitude are shown for the three cases. The number of filaments per fixed toroidal angle $\Delta\varphi$, which is indicative of the quasi-toroidal mode number, is the largest for the L-mode phase, followed by the inter-ELM, and lastly the ELM phase. The edge turbulence appears predominantly to assume filament-like structures. The inter-ELM and L-mode filaments are observed to move radially with a constant speed, consistent with the E x B motion. However, the ELM filaments can often accelerate presumably driven by the free energy generated by the H-mode pedestal collapse, as discussed in Sec. VI.

A GPI diagnostic was developed to obtain more detailed local turbulence information and to develop new further insights into the physics of scrape-off-layer (SOL) transport [282, 283]. A puff of neutral gas is injected toward the core from a port in the outboard wall of the machine. Collisions with plasma electrons stimulate atomic emission from the neutrals and the radiation is captured on a fast camera. Its fast camera views along a local magnetic field line, where the 2-D (radial and poloidal) time evolution of plasma edge fluctuation images are enhanced by a localized D_2 gas puff. Except for the modest amount of gas introduced in the region to illuminate the edge turbulence, the GPI is considered to be non-perturbing diagnostic; in contrast, edge probes could be perturbing. The resulting images (an exposure time of 3 ms / frame at 64x64 pixel resolution) are shown in Fig. 94 for an L-mode (left) and H-mode (right), where highly non-linear regions of strong localized light emission, known as 'blobs' (which are equivalent to the filaments on MAST) are seen in the L-mode frame [283]. The blobs appear in nearly all discharges (even in an H-mode but with much less frequency and intensity), typically having cm-like radial scale lengths and moving both poloidally and radially in NSTX. The blobs are ubiquitous hotter and denser "plasmoids," as they are expelled from the inner hotter and denser birth zone, i. e., near the separatrix (last closed flux surface) where $\sim$ Max $[-\nabla \ln p]$, to the outer colder scrape-off layer. The blobs are highly elongated along the field line, i. e., are filamentary in structure (as shown in Fig. 94), owing to the rapid parallel heat conduction. The blobs appear to regulate the radial power transport in the separatrix region by the frequency of their occurrence rather than their magnitude. A cross machine comparison was also made

between NSTX and Alcator C-Mod [284]. A similar study has been done on the MAST device [285]. Very good progress has been made through the comparison of various models (both electrostatic and electromagnetic) with experiment to understand the physics of blobs [277, 278, 286]. The 2D scrape-off layer turbulence (SOLT) code simulates turbulence driven by magnetic curvature and drift-wave effects in a 2D plane normal to the magnetic field **B**. The simulation domain is the outer mid-plane of the tokamak, encompassing both the edge and SOL regions. The model includes the effects of wave-phase directionality (drift waves and background flows), curvature drive, radial transport (turbulent Reynolds stress and blobs), sheared flows, and dissipation (sheath loss and friction). A GPI frame showing a typical blob from NSTX and one from a SOLT simulation are shown in Fig. 95 [286]. Note that the simulation blob is smooth and poloidally elongated, whereas the experimental blob is smaller and more circular in shape. Factor-of-two agreement between the simulated and experimental number of blobs and size distributions were obtained for the best-case simulations. Blob characteristics such as the blob size and radial velocity have thus far been explained relatively well with the electrostatic-based model. The role of the blobs on energy and particle transport and on the divertor heat and particle flux is under active investigation.

D. Plasma facing material and lithium research - The low aspect ratio and high power densities in STs provide unique opportunities and challenges for plasma-facing components (PFCs). While large P/R values make special demands on PFCs for high-performance ST plasmas, ST experiments initially used PFC materials that were common to conventional tokamaks. As mentioned earlier, the first ST in the United States was CDX-U. As with all tokamaks, impurity influx from PFCs limited plasmas performance. The CDX-U vacuum vessel was primarily stainless steel, and the main impurities were oxygen and carbon. Titanium gettering was used to reduce their content in CDX-U plasmas [203].

Larger STs, like most conventional tokamaks, have used graphite as the primary PFC material, and share common conditioning approaches. In NSTX, for example, the vacuum vessel walls were subject before plasma operations to prolonged bakeout at 350°C to remove water from the PFCs, and boronization to control oxygen [287]. Helium glow discharge cleaning (GDC) has also been performed between discharges to remove deuterium in the PFCs, following the prescription for improved plasma performance in earlier tokamaks like TFTR [288]. The TFTR

experiments also included the earliest demonstration of lithium coatings as an effective PFC conditioning technique, and the highest plasma stored energy was achieved with its application [289].

The effect of lithium PFC coatings on ST plasmas was investigated extensively on NSTX. The compact geometry of the ST makes it amenable not only to imaging plasmas in the main vacuum chamber, but also in the divertor region. Such imaging is important because of the toroidal and poloidal asymmetries in the divertor heat flux that occur naturally and are introduced with 3-D fields as discussed earlier. To this end, two fast visible cameras were absolutely calibrated and installed on NSTX-U, with views that covered the entire lower divertor. A coherent fiber optic bundle coupled the light from the viewports to the cameras, and narrow bandpass filters for carbon and lithium lines and the CD band in a filter wheel between the focusing and collimating lenses allowed spatially-resolved measurements of the impurity emission [290]. Divertor surface temperatures were obtained with a two-color IR camera. The image was split and passed through filter with bandpasses of 4-6 μm and 7-10μm. This removed any uncertainties introduced by assumptions about the surface emissivity. The IR camera has good sensitivity over a temperature range from 100 to 700C, and can acquire images with a time resolution of less than a millisecond [291].

The first apparatus used to introduce lithium into NSTX were the lithium pellet injector (LPI) and lithium evaporator (LITERs) [180]. Lithium was injected into NSTX discharges with the LPI, and the LITERs consisted of lithium-filled ovens with apertures that directed lithium vapor toward the lower NSTX divertor region. Both techniques resulted in the enhanced absorption of deuterium by the NSTX walls. In particular, the improved confinement using the LITERs was the first demonstration of the efficacy of the approach for divertor H-mode plasmas as well as limiter discharges as in TFTR, where the value of lithium PFC coatings was initially shown. The empirically observed effectiveness of lithium-coated graphite to absorb deuterium is unexpected from stoichiometry of lithium and carbon. It predicts the formation of lithium carbide, which is unable to bind additional deuterium. Quantum-classical atomistic simulations have shown, however, that in the presence of oxygen, the deuterium can be bound in a lithium-carbon-oxygen-deuterium system. This has been supported by laboratory experiments that investigated the effect of oxygen on deuterium uptake in lithium-coated graphite samples [292].

Salient characteristics of the H-mode plasmas achieved with lithium PFC coatings, as described earlier, include enhanced pedestal temperatures and stabilization of ELMs. While the latter is attractive as it reduces heat loads on PFCs, it has also been associated with the accumulation of carbon in the core plasma. Among the unexpected results from experiments with lithium evaporation on NSTX PFC surfaces is the amount of lithium relative to carbon in the plasma core [293]. Analysis of impurity transport indicated that ELM suppression and changes in neo-classical transport can lead to the observed carbon accumulation, and that high core carbon concentrations enhance neoclassical lithium particle diffusivities [294]. This mechanism alone is not sufficient for low core lithium concentrations, and further research into a more complete explanation will be conducted in NSTX-U.

The core carbon accumulation limits discharge duration, so a means by which the carbon can be reduced through controlled ELM destabilization ("ELM pacing") is desirable. A technique for ELM pacing is the injection of lithium granules ("micropellets") at a controlled frequency into the discharge. An oscillating piezoelectric disk causes submillimeter-sized granules to fall through a hole in its center, and they are subsequently propelled into the plasma by a set of rotating blades. The system was originally designed to another approach for lithium wall conditioning in NSTX, but its potential for ELM pacing as well was demonstrated on EAST [248].

Solid PFC coatings that result from techniques like lithium evaporation are difficult to extrapolate to long-pulse applications. The availability of lithium only on the PFC surface limits the amount of deuterium it can bind, and any solid PFC is subject to long-term damage in a fusion reactor environment [293]. The alternative is to investigate the feasibility of liquid metal PFCs, and the ST has features that make it a convenient test-bed. The first studies of large area, free-surface liquid lithium PFC were conducted on CDX-U (Fig. 96). Its vacuum chamber was a large cylinder, with a center stack occupying a relative small volume. Its low toroidal field (TF) compared to conventional tokamaks of similar plasma size (e. g., CDX-U has the same 22 cm minor radius as Alcator C-Mod) permits the TF coils to have a relatively small cross section. The large space between them provides good access to the vacuum chamber, which allowed a fully-toroidal liquid lithium limiter to be easily inserted and assembled within it. The result was a 2000 cm^2 free surface of liquid lithium that formed a limiter for CDX-U plasmas. When CDX-U PFCs were also evaporatively coated with lithium, the resulting reuction in recycling led to

global energy confinement that exceeded scaling predictions for Ohmic ST plasmas by a factor of six [7, 296]. The next step beyond the toroidal liquid lithium limiter was to create a low-recycling lithium PFC that fully encloses the plasma. This has been achieved in the Lithium Tokamak Experiment (LTX), which was constructed by replacing the original lithium limiter with a conducting shell inside the CDX-U vacuum vessel. The shell consists of 1 cm-thick copper with an explosively-bonded 1.5 mm stainless steel liner as the PFC. The stainless steel keeps the copper from reacting with the lithium, and the copper maintains a uniform PFC temperature up to and above the point where the lithium liquefies [297, 298].

The same basic design is found in the Liquid Lithium Divertor (LLD) for NSTX (Fig. 97). The goal of the LLD was to extend the capability of the divertor to bind lithium beyond the amount that a solid surface would provide. Unlike the LTX shell, however, a 0.25 mm stainless steel liner was braised to 2.2 cm copper [299]. The heat loads to the NSTX divertor were considerably higher compared to LTX PFCs, so the thickness of the liner was greatly reduced to insure that the thermal response was determined by the copper. The stainless steel surface was plasma-sprayed with molybdenum (Mo) create a 0.17 mm-thick layer with 45% porosity. A plasma-sprayed Mo coating was also applied to a second LTX shell, to be installed after experiments with the original uncoated shell were completed. It was decided to use a Mo coating on the LLD from the start, as sputtering is more of a concern in the NSTX divertor. The porous Mo surface would also help restrain the lithium against potentially large electromagnetic forces that could expel the liquid lithium [300].

Experiments were performed in NSTX that included placing a strike point of lower-single-null plasmas on the LLD. The LLD was loaded with lithium by evaporation from the LITERs, and the ability of its surface to retain the lithium was demonstrated by the absence of any spectroscopic evidence for Mo in NSTX discharges [301]. Examination of the LLD surface after plasma operations did not reveal any damage, and this was consistent with test stand exposures of an LLD sample to heat loads of 1 to 2 MW/m^2 for up to three seconds with a diagnostic neutral beam [302]. The LLD performance also demonstrated the efficacy of Mo as a substrate for lithium coatings. Future plans for NSTX-U PFCs include the phased replacement of graphite tiles with Mo tiles, and studies where lithium-coated Mo samples are exposed to discharges that simulate NSTX-U divertor plasmas are in progress [303].

Any effects specifically attributable to the LLD on NSTX plasma performance were less clear. For example, the fueling required to achieve and maintain stable discharges was comparable to what was needed when graphite PFCs were coated with solid lithium [299, 304]. There is also no significant change in the confinement time over the run year over during which NSTX plasmas were exposed to the LLD, as shown in Fig. 98 [300]. The suspicion is that the LLD surface is contaminated by compounds like lithium hydroxide that are formed when its static lithium coating interacts with the partial pressure of water in the NSTX vacuum vessel [305]. Lithium hydroxide, for example, liquefies at a temperature over twice as high as that for lithium. The contaminated LLD thus could have remained solid even if the lithium beneath it melted, and this was observed during test stand exposures of LLD samples [302]. The lithium PFC coating with the LITERs will continue on NSTX-U, and various additional lithium capabilities such as upward flash lithium evaporators and a lithium granule injector will be also implemented. For a longer term, the NSTX-U PFC will evolve toward increasing coverage with high-Z PFCs. A liquid lithium loop system is also being developed for NSTX-U.

A possible solution is to have a flowing liquid lithium divertor, and a special ST has been dedicated to its development. The Kazakhstan Tokamak for Material testing (KTM) has a vacuum vessel with a volume of 12.3 cubic meters, and it has a divertor consisting of mounted plates on a rotary table that can also be moved vertically . This provides KTM with the unique capability of replacing the plates without venting the vacuum vessel, and the compact divertor geometry the ST provides makes the concept feasible. The first lithium divertor module on KTM is a plate with a capillary porous surface, fed by liquid lithium feeding volume behind it [304]. The idea of individual test divertor modules prototypes the approach other devices will take in developing flowing liquid lithium divertor concepts.

VIII. Energetic Particles

A. Motivation for ST Research **-** The fusion alpha heating in reacting plasmas makes energetic particle (EP) physics an integral part of magnetic fusion research. Since fusion plasmas are in the regime where the 3.5 MeV alpha particle velocity usually exceeds the Alfvén velocity (V_A) (i.e., the super-Alfvénic regime) in magnetically confinement fusion reactors including ITER, the physics of the super-Alfvénic regime is particularly of interest [21, 22]. The EPs generated during MeV-class neutral beam injection (NBI) and ICRF heating and current drive can also excite Alfvénic modes, which can influence their heating and current drive efficiency. The Alfvénic mode excitation could become even more significant in ITER with auxiliary heating such as NBI and ICRF in addition to the alpha heating [307, 308]. Super-Alfvénic fusion alpha particles are particularly energetically favorable for exciting a number of Alfvénic modes, which tend to occur when fast ion velocity (V_{Fast}) is resonant with V_A, i.e., $V_{Fast} \sim V_A$. Those excited Alfvénic modes can cause "anomalous" particle slowing-down as well as radial transport. In some cases, the Alfvénic mode excitation can lead to a rapid loss of EPs directly to the plasma edge and the first wall. This EP transport and losses could reduce the effectiveness of alpha heating (which is a primary means of maintaining the burning plasma condition), but also could cause serious damage to the plasma facing components. The Alfvénic mode excitation could also cause deterioration of electron energy confinement, and thus the fusion plasma performance (as discussed in Sec. V). Utilizing high-energy NBI as the source of fast particles, the NSTX/MAST experiments can access a wide range of Alfvén Mach number $M_A \equiv V_{fast}/V_A$ and normalized fast ion pressure β_{fast}/β_{tot}, overlapping and extending beyond tokamaks and ITER as shown in Fig. 9. NSTX-U and MAST-U will encompass an even broader parameter space, and will more closely approach those expected for future STs (Fig. 9.) The capability of spanning a much broader range of parameters for EP physics studies than conventional tokamaks provides an important opportunity for advancement of predictive capabilities to burning plasma regimes. In this section, we will focus on ST EP research which is unique or complementary to that on tokamaks. We will therefore focus on the EP modes discovered in STs, and the energetic ion transport/loss mechanisms, which are driven by the excited EP modes.

The EP research on STs began with the mode identification as described in Sec. B. This has expanded to the investigation of EP transport and resulting losses as described in Sec. C. More

recently, due to improved EP-related diagnostics and theoretical modeling tools, some successes in reproducing the observed EP transport and losses by the EP induced modes were achieved, and they will be discussed in Sec. D. The EP research is now entering the era of theory/modeling validation of simulation based on non-linear mode overlapping and the resulting EP transport, to improve the predictive capability needed for ITER and future STs.

B. Energetic-Particle-Driven Modes – The most commonly observed and investigated EP driven phenomena are Alfvén waves. The Alfvén wave phase velocity is approximately $V_A \equiv c\,\Omega_i / \omega_{pi} = B/(4\pi n_i m_i)^{1/2} \propto B/n_i^{1/2}$. The Alfvén wave excitation by EP tends to occur for $V_{Fast} \sim V_A$. The toroidal Alfvén eigenmode (TAE) is a naturally occurring Alfvén wave in tokamak geometry, where the effective wavelength is given by $\lambda_{II} \sim 4\,\pi q R_0$ which is the nominal length of the lowest eigenmode in the flux tube. Therefore, $\omega_{TAE} = k_{II}\, V_A = V_A / (2qR_0)$ is a nominal TAE frequency. The typical TAE frequency range is 50 – 200 kHz in MAST and NSTX. In STs, a variety of TAE-type modes have been easily excited, as shown in Fig. 99 [309]. There are TAEs which have stationary mode frequencies [Fig. 99 (a)] and downward (b) and upward (c) chirping modes. Some modes are simultaneously upward and downward chirping, and are often called "angel fish" or "hole-clump" modes [310]. A theoretical analysis for the hole-clump mode has been performed, and has been shown to be caused by a distortion (s) in the energetic ion velocity distribution [311]. There is a class of Alfvén eigenmodes (AEs) which exist near the minimum q (q-min) in reversed-shear (rs) discharges termed the rs-AE. In an evolving discharge, q-min tends to decrease in a current relaxation time scale so the rs-AE tends to rise in frequency and is also called the Alfvén cascading (AC) mode. Perhaps the most notable contribution of STs for understanding TAEs is in the effects of plasma beta values on TAEs. The wave dispersion relation for the rs-AE or AC is essentially that of a shear Alfvén wave, including plasma pressure or acoustic term as given by

$$\omega_{AC}^2 = [k_{II}^2\, V_A^2 + (1+7T_i/4T_e)\,(2Cs^2/R_0^2)], \qquad k_{II} = (m-nq_{min})/q_{min}R \qquad (10)$$

where m and n are the poloidal and toroidal mode numbers, respectively [311]. In this equation, the coupling to the geodesic acoustic mode (GAM) or β-induced Alfvén eigenmode (BAE) is included. This is related to the fact that as the plasma β approaches ~ 1, V_A approaches Cs which facilitates coupling. The acoustic term can become dominant at high β, and when $m \sim$

nq_{min} making $k_{II} \sim 0$. It should be noted that the TAE frequency detected by a magnetic probe has a Doppler shifted frequency component for a rotating plasma which has to be taken into account. In MAST, a stabilizing trend in the TAE-type modes was observed with increasing beta, where the TAEs were stabilized for the beta above ~ 15% for the NBI beam energy of 45 kV [312]. Figure 101 presents statistics on the maximum amplitudes of chirping modes plotted as a function of β in several similar NBI discharges on MAST. A clear decrease in the amplitude with the β-value is seen, with the mode amplitudes close to zero at $\beta = 15\%$. Such a decrease in the chirping mode amplitude may be associated with a significant increase in the thermal ion Landau damping, as V_A slows down toward V_{Ti} with increasing β.

However, on NSTX with higher 90 kV energy beams, the Alfvén Mach number and therefore the drive can be considerably higher than in the MAST case. The higher beta regime in NSTX was accessed with higher density, which slows the Alfvén velocity and therefore increases the Alfvén Mach number further, resulting in higher drive. In NSTX, as the β is increased, the cascading behavior transitions to a pure TAE mode with flat frequency at the TAE gap frequency. This is shown in the early phase of the discharge in Fig. 101. As the β is increased further (in this case with time), the TAEs evolve toward bursting-type TAE modes. This is also shown in Fig. 101 where the plasma is just above the threshold beta of disappearance of the AC [313]. Here $\beta_e \sim 7\%$ (with a total $\beta \sim 20\ \%$) at $R = 1.2$ m. The flat mode frequency is an indication of the acoustic term becoming dominant in Eq. 10. The n=3 (green) and n=4 (blue) TAEs appear and disappear as, presumably, the q_{min} passes through and between low order rationals. In a higher $\beta > 20$ % NSTX plasma, a new class of global MHD eigenmodes termed beta-induced Alfvén–acoustic eigenmodes (BAAEs) has been observed [314]. The modes with n=1, 2, and 3 arise in the gaps in the low frequency Alfvén-acoustic continuum below the GAM frequency. These modes also exhibit a bursting or avalanche behavior, with similar levels of neutron drops and EP loss as in the case of the TAE avalanche. This will be discussed more in the next section related to the EP loss. Another low frequency EP mode is the so-called fishbone instability which is an n=1 precessional drift resonant mode discovered in PDX [315], and since then observed in virtually all NBI driven tokamaks. Fishbones are also seen in NSTX and MAST, but they have not been studied as a high priority since their physics is relatively well understood. Some fishbones observed in NSTX have higher n numbers (i.e., n = 2, 3) and they are conjectured to be driven by trapped-ion resonances [316].

Two new types of high frequency EP modes first discovered in STs are Compressional Alfvén Eigenmodes (CAEs) and Global Alfvénic Eigenmodes (GAEs), as shown in Fig. 102 [317]. As can be seen from the figure, the CAEs [318 - 320] and GAEs [321] exist at higher frequency ranges, well above the TAEs, rsAEs, and other modes thus far discussed. The CAEs and GAEs appear in a broad spectrum of nearly equally spaced peaks in the frequency range from ~ 0.2 Ω_i to ~ 1.2 Ω_i (or 500 kHz to a few MHz) in NSTX [318]. The CAEs are compressional Alfvén waves which can exist above and below the ion cyclotron frequency, and GAEs represent the shear Alfvén wave roots that exist below the ion cyclotron frequency (f_{ci} ~ 3 MHz for this case). The CAE dispersion relation is $\omega_{CAE} = k\ V_A$, where k is mainly defined by the radial wave number. The GAEs are well described by Eq. 10, and can occur at high frequency compared to TAEs because of negative higher n values (e.g., n = - 4 and m = 2). The beam-induced GAEs are believed to be responsible for the possible rapid electron energy loss in the core region of the NSTX NBI heated plasma as discussed in Sec. V.C [166]. As can be see from Fig. 102, a variety of EP modes can be excited simultaneously and their behavior is highly time-varying, particularly during the initial current ramp-up phase where the plasma parameters are rapidly changing. In addition to the magnetic pick-up loops, there are various techniques such as microwave reflectometry [322] and beam emission spectroscopy (BES) [174, 175] that can be used to measure the EP mode amplitudes. The observed EP modes were compared with theoretical models and show generally good agreement with linear theory. A quantitative comparison of the measured TAE mode structure with theory has been successfully made with the NOVA-K Toroidal Alfvén Eigenmode code [323] for STs [317, 324] and tokamaks [21-22].

C. Energetic particle transport/losses **-** EP transport and losses have been investigated actively on STs and tokamaks due to their importance for ITER and future burning plasma devices. Here we shall focus on plasma mode-driven transport but not include classical and neoclassical processes (such as ripple transport), since they were actively investigated in tokamaks and relatively well understood [21, 22]. For STs, because of the strong EP drive as shown in Fig. 9 (i.e., super-Alfvénic conditions and high normalized fast ion β), significant EP transport processes by various EP modes have been observed. Utilizing EP and current profile diagnostics, significant EP radial transport and prompt losses have been measured on NSTX. The prompt losses were observed particularly when multiple over-lapping modes or "avalanches"

were simultaneously excited. The TAE (Toroidal Alfvén Eigenmode) avalanche is the most commonly observed avalanche process, involving a simultaneous excitation of multiple TAE modes in NSTX [317, 325]. In Fig. 103 (a), a TAE avalanche is shown where the magnetic pickup coil frequency spectrogram with toroidal mode numbers 1 through 4 appear together in an avalanche on an expanded time scale [325]. A total neutron rate drop of ~ 13% is shown in Fig. 103 (b). Since there is no significant change in the bulk plasma parameters, the neutron drop is interpreted as an outward transport of fast ions due to the avalanche. The total detected fast particle loss flux by a scintillator fast ion loss probe (s-FLIP) [326], located at the outer mid-plane edge, is shown as a function of time in Fig. 103 (c) [325]. As can be seen, the fast ion loss comes in a rapid short burst coinciding with the avalanche. It should be noted that the neutron drop is usually observed during a TAE avalanche but the fast ion loss is not always observed, indicating that fast ion transport during an avalanche does not necessarily lead to fast ion loss. In Fig. 104, the brightest of the s-FLIP frames with a superimposed interpretation grid for the gyro-radius and pitch angle of the lost particles is shown. The relatively wide bright spot size indicates that the loss is relatively broad in pitch angle but within a narrow range of gyroradius (~ 17 cm) which corresponds to ions near the injected NBI energy of 90 keV. This observation therefore shows that the TAE avalanche can produce highly focused lost ions at maximum energy in a very narrow time frame. This very rapid and focused fast ion loss could cause damage to PFCs in ITER and future reactors. Another fast ion diagnostic, the Fast Ion D-α (FIDA) system [327] also measured a level of core fast ion density decrease similar to that deduced from the neutron rate drop as shown in Fig. 105 [328]. The fast ion transport due to the TAE avalanche and its effect on the NBI driven current has also been investigated [329]. In this study, an upper bound on the fast-ion diffusivity of ~ 0.5 – 1 m^2/s^{-1} is found. This level of fast ion diffusivity can significantly broaden the NBI driven current profile, which can be beneficial from the plasma stability point of view but can also lead to a loss of current drive efficiency. Another type of avalanche process was found with lower frequency modes consistent with the BAAE avalanche with n= 1, 2, and 3 [330]. The total neutron rate drop is ~ 13% as with the TAE avalanche, and the rapid fast ion particle loss with a wide pitch angle range but relatively close to the injected energy of 90 keV is again quite similar to the TAE avalanche. Another avalanche process is observed for the higher frequency GAE, where the GAE avalanche of n = -7 to -10 can trigger the TAE avalanche of n=1 through 6 [331]. While not an EP mode, low

frequency (f = 5 - 8 kHz) continuous n=1 MHD modes can also transport EPs and significantly modify the NBI current drive profiles [332]. One modeling calculation shows that the fast ion diffusivity of 20 m^2/s^{-1} within the region of mode activity of $r/a < 0.45$ is required to match the measured neutron drop. It should be also noted that an application of n = 3 fields has altered the dynamics of high-frequency bursting energetic-ion-driven Alfven modes [333]. Calculations indicate that the 3D perturbation affects the orbits of fast ions that resonate with the bursting modes. The fast ion transport effects on the NBI current drive will be discussed more in Section X.

D. Theory / modeling validation – It is clearly vital to develop a predictive capability for EP mode excitation, particularly the avalanches and their consequences in terms of EP transport and losses. A major advance in recent years is in improved diagnostics (as described above) and simulation/modeling capabilities for explaining their observations [317, 324, 325]. The simulations usually involve multiple steps. First, the mode amplitude profiles are needed. Once good mode identification is made, the NOVA-K code is used to provide the corresponding TAE structures. The NOVA-K generated eigenmodes are then scaled to an overall amplitude that produced the best fit to the displacements measured, for example, by the microwave reflectometer system. This is done for the entire plasma volume, since the measured profiles are available at only specific and limited locations. Then the selected eigenmodes are used in the ORBIT code [334] to simulate the fast-ion loss. In Fig. 106, the calculated net neutron rate drop in ORBIT simulations (red squares), the neutron drop due to lost beam ions (blue circles), and the neutron drop in the confined beam ion population due to fast ion redistribution and loss of energy to the TAE are shown [317]. It should be noted that the neutron drop from redistribution and energy loss occurs well before the fast ions are lost from the plasma. There is an apparent threshold for energy loss in the fast ion population at a normalized mode amplitude of ≈ 0.4, and the threshold for fast ion loss onset occurs at a normalized mode amplitude of ≈ 1. Therefore it appears that there is good agreement between the measured neutron rate drop and that predicted at the measured mode amplitude. With the simplifying assumptions used in the modeling, it is surprising that the agreement is as good as it is. The use of the ideal eigenmodes, with unphysical interactions with the continuum, the use of the unperturbed fast ion distributions in the presence of multiple Alfvénic instabilities, the use of a guiding center code in a situation with

large Larmor radii, together with the general uncertainties in equilibrium reconstruction, could all potentially contribute to large uncertainties in the simulations. The NOVA-K is a linear mode modeling code, so a non-linear model is needed to fully describe the highly non-linear nature of the TAE avalanches. In the experimental area, continued improvement in measurements of the EP population and excited modes are needed.

IX. Plasma waves for heating and current drive

A. Motivation for ST Research **-** Efficient heating and current drive are essential for the success of the ST/tokamak fusion reactor concept. In present day ST experiments, neutral beam injection (NBI) is a reliable and established method for heating and current drive. At the same time, it is highly desirable to develop radio-frequency (RF) wave based heating and current drive since the NBI-based approach tends to be technically challenging for reactor applications in terms of beam penetration and compatibility with the fusion reactor neutron environment. For developing attractive RF heating and current drive methods, ST plasmas present a special challenge due to being in the so-called "over-dense" regime [i.e., $(\omega_{pe}/\omega_{ce})^2 >> 1$ where ω_{pe} and ω_{ce} are the electron plasma and electron cyclotron frequencies, respectively.] For a typical tokamak plasma, $(\omega_{pe}/\omega_{ce})^2 \sim 1$ - 2 in the plasma core while for STs, it can be $(\omega_{pe}/\omega_{ce})^2 \sim 10$ - 20 due to a factor of ~ 3 – 4 lower magnetic field. The over-dense condition makes some of the conventional radio-frequency wave heating and current drive concepts such as Electron Cyclotron wave Heating (ECH) and Lower Hybrid wave Current Drive (LHCD) not practical due to the severe wave accessibility limits imposed by the over-dense condition [335]. For this reason, RF heating and current drive research in STs has thus far focused on the High Harmonic Fast Wave (HHFW) and Electron Bernstein Wave (EBW) approaches as described in Sec. B and C.

B. High harmonic fast wave for electron heating and current drive **-** The High Harmonic Fast Wave (HHFW) heating and current drive was proposed for its promise to heat electrons in high beta and over-dense conditions for STs [336]. The HHFW is in the compressional Alfvén wave branch (i.e., same branch as the conventional ion cyclotron range of frequency or ICRF heating in tokamaks) but at higher ion cyclotron harmonic frequencies (~ 10 times greater). The wave perpendicular phase velocity is approximately the Alfvén speed or $\omega/k_\perp \sim V_A \equiv c\,\Omega_i / \omega_{pi} = B/(4\pi n_i m_i)^{1/2} \propto B/n_i^{1/2}$. It can be also shown that the Alfvén speed slows down as the ion plasma beta is increased, approaching $\omega/k_\perp \sim V_A \sim V_{Ti}$ at the unity ion beta. The HHFW starts to take on the whistler-like characteristics, and electron damping via magnetic pumping as well as the usual electron Landau damping becomes significant [316]. For NSTX plasma parameters, the electron damping was predicted to be strong enough to attain single-pass absorption at high β, with some possibility for localized off-axis heating and current drive.

Initial HHFW physics experiments were performed in the Current Drive Experiment- Upgrade (CDX-U) with a rotatable dual strap antenna system [337]. The HHFW physics was also investigated in TST-2 initially using a six-element combline antenna at lower power (1 kW) where high efficient wave lunching qualitatively consistent with modeling was observed [10]. A two-strap antenna was later employed on TST-2 at higher injected power of ~ 240 kW where parametric decay instabilities (PDI) were investigated [338]. The HHFW high power heating experiment on NSTX has been conducted utilizing a 12 strap antenna system powered by six 30 MHz high power rf transmitters (~ 1 MW each) with real time phase control [339]. The NSTX 12 strap antenna array is shown in Fig. 107. Efficient electron heating by HHFW has been confirmed on NSTX [338, 339]. As we can see in Fig. 108, application of ~ 3 MW of HHFW power resulted in the production of plasmas from an initial Ohmic temperature of a few hundred eV to a central electron temperature $T_{e0} \sim 6.2\ keV$ in helium and $T_{e0} \sim 5.2\ keV$ in deuterium at central electron density of ~ 1.5 x 10^{13} cm^{-3} [340]. These temperatures are particularly impressive for NSTX, which operated at a maximum axial toroidal field of only 0.55 T. The electron temperature is typically very peaked during RF heating but in deuterium, it is broader with a steeper T_e gradient, giving the appearance of internal transport barrier (ITB) formation. While we shall use the word "ITB" for the steep T_e gradient region, it is not fully resolved at the present time that the appearance of the ITB-like steep temperature gradient is due to the formation of a transport barrier or the improved core heating efficiency due to the higher electron temperature. It is instructive to look at the time evolution of HHFW as shown in Fig. 109 [341]. An overlay of the time evolution of T_{e0} and the central ion temperature T_{i0} from the x-ray crystal spectrometer [342] is shown. We see that T_{e0} gradually increases to a peak of ~ 4 keV over ~ 200 ms, which is much longer than the electron energy confinement time of ~ 30 ms; T_{i0} also increases, with some delay, to 2 keV before dropping to near 1 keV. An MHD reconnection event occurs at 0.22 s. As shown in the figure, the central temperature rise is very gradual considering the constant applied RF power. Assuming constant heating efficiency, TRANSP analysis for this plasma shows that the core electron heat diffusivity goes down by a factor of 10. The TRANSP calculations also suggest that the q profile is weakly reversed, as a result of the bootstrap current generated in the core region which could be causing the core electron confinement improvement. It could be noted that the HHFW heating efficiency may be improving in time as the electron temperature increases.

The magnitude of current driven in initial HHFW current drive experiments, inferred from the magnetic measurements, is ~ 50 - 100 kA and roughly consistent with theoretical estimates [343 - 346]. The loop voltage was close to zero as shown in Fig. 110, and there was a calculated f_{NI} =

0.7 – 1 [346] . The H-mode starts around t = 0.22 s, and an "ITB" at r/a ~ 0.4 is formed at t = 0.38 s. The calculated bootstrap current oscillates between 100 and 230 kA. These large fluctuations in bootstrap current result from plasma pressure profile changes near the end of the RF power ramp-up (at 0.26 s), at the formation of the ITB (at 0.3 s), and inside the ITB (at 0.38 s) as indicated in Fig. 110. Three-quarters of the non-inductive current was estimated to be generated inside the ITB. This suggests that the HHFW is a promising tool for current ramp-up. A strong modeling effort utilizing advanced computational tools is also being pursued [347].

Although HHFW absorption by the bulk ions is estimated to be negligible, some ion cyclotron harmonic interactions are expected with the NBI fast ions [336]. In NSTX, there are indications of NBI fast ion acceleration by HHFW and an associated neutron increase [348]. Simulations based on the higher toroidal fields expected in NSTX-U suggest that some bulk thermal ion cyclotron harmonic heating may be possible for the first time by the fast waves [347].

Lithium coatings of plasma facing components (PFCs), which reduced the edge density and collisionality, also helped to improve the HHFW heating efficiency, particularly in deuterium plasmas. The heating efficiency dropped off sharply with higher wave phase velocity. To understand the sources of HHFW inefficiency, various possible mechanisms were investigated. One of the most significant effects affecting the HHFW heating efficiency was found to be the edge density profile [349]. The heating efficiency was shown to depend strongly on the "onset" density at which the HHFW starts to propagate as shown in Fig. 111. A sequence of RF pulses was applied with k_φ= 14 m^{-1} and -8m^{-1}, respectively. As can be seen in Fig. 111(a), the first pulse has poor heating efficiency compared to the subsequent pulses, particularly for the longer wavelength case where k_φ= -8m^{-1}. One important variable was the edge density as shown in Fig. 111(b) where the density must be lower than the so-called "onset" density. The onset density is defined as the density at which the HHFW waves start to propagate, i.e.,

$$n_e\left(10^9\, cm^{-3}\right) = (5.0Z/\mu)(n+1)B_T^2(n_{||}^2-1) \quad (11)$$

where Z is the ion charge, μ is the ion mass, n is the ion cyclotron harmonic number, $n_{||} \equiv k_{||}\, c/\omega$ is the launched wave number, and B_T is the local magnetic field. If the edge density is above the onset density and the HHFW wave is propagating, a significant loss of RF power could occur before reaching the main plasma through various wave dissipation processes, including collisional damping as well as by means of parametric decay instabilities. Since the

onset density is lower for longer wavelength, the onset condition becomes more challenging to avoid for lower $n_{//}$. This explains why the HHFW heating efficiency tends to be lower for lower $n_{//}$, and improves with lithium application to PFCs, which reduces the edge plasma density. It also explains why a higher toroidal field and $n_{//}$ tend to lead to better HHFW heating efficiency, since the onset condition is easier to avoid.

The HHFW edge power loss mechanisms have been investigated in NSTX. A significant fraction of the HHFW power can be lost to the scrape-off layer (SOL) and deposited in bright spirals on the divertor [350]. The dependence of the edge RF power deposition on the onset density relative to the antenna location suggests that edge density control is quite important for efficient HHFW heating and current drive, and this edge interaction maybe also relevant for ITER ICRF [351]. The parasitic effects are likely to be reduced with higher magnetic field for NSTX-U [347]. Another possible mechanism investigated is the PDI, i.e., a three wave coupling process where the launched HHFW wave, for example, can decay into an ion Bernstein wave (IBW) and an ion quasi-mode (IQM) with matching wave frequencies and wave numbers [352]. In TST-2, the PDI processes were investigated using probes and reflectometer, where the decay waves were found to be consistent with HHFW or IBW for the lower side band and IQM for the lower frequency mode [338]. On NSTX, such an instability was indeed observed to cause strong ion heating at the plasma edge [353].

C. Electron Bernstein waves for localized current drive

In ST or tokamak reactors, non-inductive plasma current profile control is an important research topic, as the achievable beta limit is sensitively dependent on the plasma current profile. For this reason, a technique for driving the plasma current at a desired location (often in the mid-to-outer region r/a $\geq$ 0.5) even at a few % level is highly desirable. The conventional Fisch-Boozer current drive becomes inefficient for r/a > 0.5 due to trapped particles [354]. On the other hand, the so-called Ohkawa current can be driven efficiently, even in the outer region, by moving electrons from barely passing into trapped orbits via electron cyclotron harmonic heating. Indeed, numerical modeling of electron Bernstein wave current drive (EBWCD) for a $\beta = 40\%$ ST plasma predicts efficient, off-axis Ohkawa EBWCD. The calculated normalized current drive efficiency increases with r/a, and is a factor of 2 higher at $r/a = 0.7$ than has been obtained with electron cyclotron current drive near the axis of large aspect ratio tokamaks [355].

The Electron Bernstein Wave (EBW) is an electrostatic short wavelength wave, which exists due to finite electron gyro radius (i.e., finite electron temperature) effects. It can propagate in the over-dense conditions of STs, and due to its electrostatic nature, can be strongly absorbed locally near the electron cyclotron layer and the locations of its harmonics. It is therefore well suited to heat and drive plasma currents when good localization is desired, for example, for the current profile control needed for high performance ST operations. This conclusion is based on EBW modeling calculations for localized current drive [356]. However, since the EBW is a finite electron temperature plasma mode, it must be coupled from an external launcher which is typically designed for conventional electromagnetic electron cyclotron extraordinary X mode and/or ordinary O mode launching. The X mode can couple to EBWs in the vicinity of the upper hybrid resonance (UHR) (i.e., the B-X process), and the O mode can couple first to the slow X mode, which subsequently mode converts to EBWs near the UHR (i.e., B-X-O process). An informative review of EBW for heating and plasma diagnostic for fusion devices can be found in Ref. 357.

EBW Experiments –In the hot over dense electron core of ST plasmas, the EBWs are naturally excited by the optically thick plasmas near the electron cyclotron harmonic layers, and this easily satisfies the EBW blackbody condition. This makes the EBW an attractive electron temperature diagnostic technique for STs [357]. The EBW mode conversion analysis predicts that the EBW mode conversion efficiency is reversible (i.e., the mode conversion efficiency is the same for EBW to X/O modes and X/O modes to EBW) [358]. The first B-X EBWE was measured on CDX-U by comparing the EBWE T_e with Thomson scattering T_e measurements, where near 100% conversion efficiency occurred with ~ 50 eV electron temperature ST plasmas [359]. The first series of EBWE experiment on NSTX showed an efficient EBW coupling (~ 0.8 +-0.2) in L-mode plasmas, in good agreement with the numerical EBW modeling prediction of 0.65 [360]. Simulations show that indeed 80% of the EBW energy could be dissipated by collisions in the edge plasma. However, application of lithium as a PFC coating greatly improved the EBWE coupling to ~ 60 - 70% even in H-mode plasmas, as shown in Fig. 112 (a) [361]. The lithium PFC coating reduced the scrape-off-layer density as shown in Fig. 112 (b). As in the case of HHFW, edge conditioning has proved to be highly important for efficient EBW coupling in H-mode. Another application of the EBWE is innovative measurements of plasma parameters such

as magnetic field pitch and plasma rotation at the plasma edge being developed on MAST [362, 363].

X. Integrated Scenarios

A. Motivation for ST Research **-** In order to establish a sufficient database for designing future STs facilities, it is essential to perform experiments in present ST facilities to test integrated scenarios that can be scaled to match the performance of future ST devices [366, 366]. The key goal of integrated scenario development is to test properly-scaled device and plasma parameters that match as many key dimensionless parameters as possible for future STs under conditions required for steady-state non-inductive operations. The main key dimensionless device and plasma parameters include A (aspect-ratio), κ (elongation), δ (triangularity), ρ^* (rho-star or gyro-radius normalized by plasma minor radius), ν^* (plasma collisionality), q^* (cylindrical safety factor), q_{95} (edge safety factor), β_N (normalized beta), β_T (torodidal beta), β_P (poloidal beta), f_{BS} (bootstrap current fraction), HH (H-mode confinement enhancement factor), and N_G (Greenwald density fraction). The target device and plasma dimensionless design parameters for various future devices are shown in Table III in Sec. II.

One of the key device/plasma control parameters is the plasma elongation κ, since it is an externally-controllable parameter which potentially has a major impact on the plasma performance, particularly for non-inductive operation as discussed in Sec. II and III. The plasma elongation achieved in NSTX and target range for future devices are illustrated in Fig. 113 [329]. As can be seen in the figure, NSTX was able to scan a relatively wide range of A. In the inset, the $\kappa = 3$ plasma equilibrium achieve in NSTX is shown. For NSTX and NSTX-U, the plasma height is limited by the vacuum vessel to be about 3 m. Therefore, the plasma height limitation tends to limit the achievable κ to ~ 3.0. For FNSF, $\kappa \sim 3.0$ might be satisfactory but for high f_{bs} devices such as pilot and ARIES-ST, higher κ values of 3.3 – 3.4 is desired. As noted in Sec. II, one can relax physics parameters such as κ, q^*, and β_T toward a more FNSF-like range if the copper TF magnet is replace by a superconducting magnet, due to greatly reduced recirculating power. The superconducting device size increases, however, to $R_0 \sim 4.5$ m due to the additional magnet shielding needed, while larger values of β_N and f_{BS} are still required to minimize the necessary non-inductive current drive.

Clearly, there are still a number of physics issues one needs to address. At the present time, experimental research has been mostly carried out in individual topical areas to develop the

necessary tools as discussed in the previous sections. The tools developed in those topical areas then must work together in an integrated manner before we have sufficient confidence to design and build future devices that can operate in steady-state reliably with the projected plasma performance. Once those tools become available, their integration can take place relatively quickly in devices like NSTX-U and MAST-U.

While tokamaks have been working for some years on integrated scenario development aimed for the ITER operations, for FNSF, integration scenario development has just begun. A question commonly asked is whether or not it is possible to achieve reliable steady-state (i.e., non-inductive) plasma operation with all the projected plasma parameters as indicated in Table III. In Sec X.B, we shall discuss the importance of plasma optimization for plasma performance particularly toward achieving non-inductive operations. There are many aspect of plasma optimization, and we shall attempt to cover only the main ones. In Sec. X.C, we will summarize the progress being made toward non-inductive operation and the prospects for full non-inductive operation in the upgraded ST facilities.

B. Plasma Optimization – Plasma optimization is an important part of integrated scenario development, and is made challenging since there are many parameters to optimize. While a particular set of plasma parameters is chosen for a design point, there maybe other parameters which are easier to achieve while satisfying the same facility operational goals. For example, as noted in Table III, there are three FNSF design points with relatively large device and plasma parameter variations, but are still aiming for the same goal of steady-state 1 MW/m^2 neutron wall loading. Also, certain plasma parameters are coupled so one cannot arbitrarily choose those parameters independently. If the confinement is not sufficient, the target plasma parameters may not be reached with the available heating power. In Fig. 114, the achieved β_N and figure of merit for f_{bs} $<0.5\varepsilon^{0.5}\beta_p>$, chosen from the entire NSTX discharge data base, are plotted as a function of the achieved pulse duration [367]. It should be noted for NSTX, because of the limited inductive volt-second availability (~ 0.6 V-sec), a typical ohmic discharge would only last for ≤ 0.5 sec. The larger the non-inductive current fraction, the lower the loop voltage becomes. This enables the discharge to extend well beyond ~ 0.5 sec possible by available inductive drive as illustrated in Fig. 114 (b). The benefit of the shape factor $S \equiv q_{95}I_p/aB_T$ is also apparent in achieving both high β_N and f_{NI}, as shown in Fig. 114. We should also note that in Sec. III.F, we discussed major

disruptions, and in Fig. 52, depicted the disruptivity dependence of β_N, and q^*, pressure peaking factor $F_p \equiv p(0)/\langle p \rangle$, S, and internal inductance factor l_i for NSTX [25]. The disruptivity trend we saw in Fig. 52 is actually encouraging, as future ST FNSF and power plant designs trend toward higher β_N and S and lower F_p and l_i, in the direction of reduced disruptivity. Disruptivity diagrams such as Fig. 52 are quite informative in determining not only if the target operational plasma parameters are realistically achievable, but also a safe path to reach the target parameters without suffering a disruption. Indeed, the observed disruptivity tends to be reduced for high β_N in the $q^* = 3 - 4$ range. This is where most of the future device design points lie as shown in Table III. We now comment briefly on the plasma performance dependence on some of the key plasma and device parameters:

Aspect-ratio Scaling - The aspect ratio A is important as it distinguishes STs from conventional tokamaks. Most of the ST devices operating today are indeed operating in the projected ST future device range of $A \sim 1.5 - 1.7$. In the present-day experimental data base, plasmas with a wide aspect ratio range of $A \sim 1.2$ - 1.7 have been investigated; for example, Pegasus, TS-3-4, UTST, VEST, and HIST are in the ultra-low-A range of ≤ 1.4, and other ST devices, i.e., NSTX, MAST, GLOBUS-M, and QUEST, etc., are in the mid-range of $A \sim 1.4 - 1.7$. The aspect-ratio scaling of MHD stability has been investigated based on modeling and experimental [66, 67]. Thus far, while there are some observable trends as described in Sec. III and V, there have been no dramatic qualitative changes observed in the MHD stability and confinement properties with A for ST regimes. This observation does give some flexibility for choosing an optimum aspect ratio in the range of $A \leq 1.7$, depending on the design objectives of future STs.

Plasma equilibrium and shape control - Plasma equilibrium and control are the fundamental part of to integrated scenario development. A comprehensive description of plasma equilibrium reconstruction has been provided in [368] and real time reconstruction developed for plasma control in tokamaks [369] applied to STs is described in Ref. 368. For beta control, the real time control system is also applied to the NBI heating system [370]. While a high plasma shaping factor is quite important as noted in Fig. 114, κ is probably the most important in terms of plasma performance. As described in previous chapters, higher κ helps achieve higher I_p, β, and f_{bs}, all of which are highly important for fusion reactor performance. Here we show an example of the plasma elongation research conducted in NSTX [248]. As shown in Fig. 115, the achieved "sustained beta" parameter $\varepsilon^{1/2}\beta_p\beta_T$ (i.e., a figure of merit of non-inductive operation $\propto f_{bs}\beta_T$) is

plotted as a function of the elongation factor $1+\kappa^2$. The red points cover a period of NSTX operation where the plasma control system is not adequate to control high elongation discharges. They show mainly the $\kappa \leq 2$ regime, which is considered to be "naturally" stable for STs and thus not needing fast feedback control as described in Sec. III. The green points were obtained once an adequate (i.e., sufficiently fast) plasma control system was implemented in NSTX to control higher elongation ($\kappa \geq 2.5$) discharges. The higher elongation resulted in a higher sustained beta parameter as shown in Fig. 115 [250]. This example illustrates the importance of plasma elongation, and adequate control capability to achieve the desired plasma parameters in a stable fashion. That is the reason for the choice of relatively high κ values (≥ 3) for all of the future ST devices shown Table III. Utilizing the updated plasma control system, stable control of high elongation discharges $\kappa \sim 3$ was demonstrated as shown in the inset in Fig. 113 [96]. While κ confinement scaling is not yet established for STs, a favorable confinement trend has been observed for a conventional tokamak [372]. The triangularity δ is considered to be also important for MHD stability, pedestal, and ELM behavior, and divertor performance. High-triangularity high performace discharges with $\delta \sim 0.8$ have been demonstrated on NSTX. However, given the limited number of in-board PF coils, high $\delta \sim 0.8$ plasmas may not be accessible, and it is thus unclear what would be the optimum δ for future STs. This is reflected in the relatively modest range of $\delta \leq 0.64$ chosen for ST-based fusion systems as shown in Table III (Sec. II). There is an additional shape factor called "squareness," but its precise benefit is not well established at the present time, due mainly to the lack of experimental data. The squareness was also scanned in a set of recent experiments in NSTX [373] but no strong plasma performance dependence has been thus far found.

ρ^* and ν^* scaling – The ρ^* (ratio of ion gyro-radius to plasma minor radius) is considered to be an important parameter for tokamaks for NTMs and possibly energetic particle instabilities. Since ρ^* is expected to decrease by an order of magnitude for future machines such as ITER compared to present day tokamak experiments, ρ^* scaling is an important research topic for tokamaks [172]. For STs, the ρ^* is expected to remain relatively unchanged from present-day STs to future STs including the ST Demo, perhaps varying by a factor of two. While the ρ^* variation maybe modest for STs, the confinement projection can be significantly influenced, for example, by whether ρ^* scaling is Bohm-like or gyro-Bohm-like for STs. This area of research

still remains to be an important future research topic for STs. On the other hand, the ν^* *(collisionality)* for the present-day STs are one to two orders of magnitude higher than what is anticipated in future STs. The ν^* can, for example, influence ELM behavior, transport physics, bootstrap current generation, and boundary physics as described in the previous sections. On NSTX and MAST, the plasma confinement (mainly in the electron channel) shows a strong dependence of ν^{*-1} as discussed in Sec. V. If this trend holds true, then future STs maybe able to achieve even better confinement due to much lower ν^*. The ν^* scaling is therefore viewed as a particularly important dimensionless parameter for STs, and thus is one of the high-priority research areas for NSTX-U and MAST-U.

Plasma beta scaling – As discussed in Sec. III, the plasma betas are crucial parameters for fusion power production (β_T) as well as plasma maintenance with high bootstrap current fraction (β_N). The present-day experiments achieved beta parameters closer to that needed for the ST-FNSFs (i.e., $\beta_T \leq 20\%$ and $\beta_N \leq 5.0$) as shown in Fig. 114 and 115. It is also quite fortunate that the high β_N regime exhibits relatively stable MHD behavior and good confinement up to the highest $\beta_N \sim 6$ achieved thus far. The achievement of ST-FNSF-like beta regimes with a significant off-axis bootstrap current fraction would likely require advanced MHD control, such as an active RWM control system. This is because of the relatively low internal inductance expected in these plasmas, which makes them prone to the n=1 kink/RWM instability as described in Sec. III. The bootstrap current fraction is at the 50-60 % level in present high-performance H-mode ST plasmas, which is sufficient for the ST-FNSF but not at the ultra-high ~ 90 – 95 % level envisioned for ST power plants.

Current and plasma profile control – Current and plasma profile control is one of the desired features for future STs particularly for the ST Power Plant to achieve the near-perfect current and pressure profile alignment needed for the high β_N and f_{BS} regime. This is also the case for advanced tokamak operational scenarios. If one were to use NBI as a non-inductive current drive tool, for example, as envisioned in the FNSF, then off-axis NBI current drive is a promising tool for current profile control in future STs. Off-axis NBI was investigated on MAST by shifting the magnetic axis of the plasma far off the mid-plane ($Z_{mag} = 0.35$m) as shown in Fig. 116 [374]. The MAST results indicates that broadening the fast ion deposition profile by off-axis neutral beam (NB) injection helps to avoid harmful plasma instabilities, and significantly extends the operational window of MAST. Long pulse (>0.65 s) H-mode plasmas

were achieved with plasma durations limited only by present machine and NBI engineering limits as shown in Fig. 116 (a). As shown in the figure, about 1/3 of the plasma current is driven by NBICD with a small incremental fraction by j_{bs}. In order to match the experimentally observed neutron rate and stored energy, however, a low level of anomalous fast ion diffusion ($D_b \sim 0.5 - 1.0$ m^2 s^{-1}) is required. This anomalous diffusion with incremental reduction in current drive efficiency is attributable to n=1 fish-bone-like MHD activity. The introduction of the fast ion diffusion broadens the neutral beam current drive profile and degrades the relative contribution of NB-driven current from ~40% to ~30%. This so-called anomalous fast ion diffusion was also observed previously on NSTX due to a rotating n=1 MHD kink/tearing mode [332]. As shown in Fig. 117, the NBI current drive radial diffusion was deduced from the observed neutron rate as shown in Fig. 117(a). The observed calculated neutron rates agree well until the on-set of the n=1 mode around 1.05 sec. Then a significant deviation develops suggesting anomalous fast particle diffusion/confinement. Two examples of diffusion profiles (high central diffusivity in red and lower broader diffusivity in black) are shown. As shown in Fig. 117(b), the NBICD profile (green) is dramatically broadened by diffusion. The broadened NBICD profile tends to make the plasma more MHD stable, which could enable stationary plasma operation. However, the large core n=1 mode reduced the plasma rotation, and degraded confinement and performance significantly. The NBI ion transport due to TAE was described in Sec. VIII.C, and this type of current diffusion can be relatively benign in terms of its effects on plasma performance [328, 329]. The NBI on-axis/off-axis current drive will therefore require consideration of possible instability-driven (anomalous) radial transport, which could broaden the driven current with the benefit of making the plasma more MHD-stable but could also reduce the current drive efficiency. The use of EBW off-axis current drive for current profile control has also received some attention as described in Sec. IX.C. Off-axis current drive physics will be further investigated in NSTX-U and MAST-U, where significant off-axis current drive capabilities will be implemented [24, 25, 375]. As for plasma profile control, the profiles are largely determined by the confinement properties of the plasma. The H-mode produces much broader plasma pressure profiles, which enabled NSTX and MAST to explore high beta / performance regimes. The plasma rotation profiles are also determined by the momentum transport, but the application of a 3-D field enables some control of the rotation speed and profile.

C. Prospects for steady-state high performance discharges – All of the future ST devices listed in Table III are designed to run essentially steady-state. Since it is highly challenging and costly to actually run an experimental research facility truly steady-state, the experimental goal for present-day STs is to reach a condition which is termed "physics steady-state." Here we are not addressing the engineering or technology steady-state conditions, such as wall-particle interaction time scales which could be hours or even longer. The longer time scale non-inductive ST operation is the goal of the QUEST device [135]. The physics steady-state conditions would be the time for the plasma to be maintained for much longer than a certain physics driven time constant such as the energy, particle, and momentum confinement time, and the current diffusion time τ_{CD} for current profile stationary conditions. Since the τ_{CD} is usually the longest physics time constant, the physics steady-state can be effectively defined as a plasma discharge time duration 2-3 τ_{CD}. The long pulse experiments that have been performed on NSTX were mainly possible due to discharges with relatively high bootstrap current fractions of ~ 50 – 60%. The discharges had a non-inductive current fraction of ~ 70%, with very limited available OH flux of only ~ 0.6 V-S. An example of such a discharge is shown in Fig. 118, where the pulse length is sufficiently long to reach some degree of stationary conditions as evident by the nearly flat q_0 and l_i evolution as shown in Fig. 118(a) [367]. The $\beta_N \sim 5$ is well above the no-wall limit, and even the with-wall (or ideal) limit is approached, with f_{BS} well over 50% and f_{NI} reaching ~ 70%. We note that these parameters reflect the conditions for FNSF.

As we prepare for fully non-inductive operation on NSTX-U and MAST-U, it is natural to ask how the present NSTX results could extrapolate to NSTX-U. With near doubling of B_T and lower collisionality, one could expect significantly higher T_e and T_i. In Fig. 119 (a), the discharge shown in Fig. 118 is indicated as the leftmost point at a temperature multiplier TM of one [367]. The points for TM > 1 were obtained using TRANSP to increase TM and iterating until the current profile reached a stationary state while the input power, field, current, and the boundary shape were held fixed. With increased TM, the f_{NI} rises and crosses 1 to reach a fully non-inductive state at TM ~ 1.4 (or a 40% higher temperature). The required confinement enhancement was 1.5 and $\beta_N \sim 6.5$. The q_0 is raised from 1 to 1.45, and the mid-radius $\nu*$ is reduced by ~ 50% from 0.17 to 0.09. The current and q profiles are shown for the end points (TM = 1 and 1.4) in Fig. 119 (b). On both NSTX-U and MAST-U, the available B_T enhancement should be nearly a factor of 2, with considerably more off-axis beam power for current profile

control. Generally higher temperature and reduced collisionality increases both bootstrap current and NBICD. If the confinement enhancement is not sufficient, one could introduce additional NBI power, which also increases the current through NBICD. It is also quite possible that the MHD (both low frequency n=1 and higher frequency TAE avalanche) instabilities could affect the NBICD performance through anomalous particle diffusions, as noted above and also in Sec. VIII.C. Some moderate fast ion diffusion ~ $1 m^2 s^{-1}$ can actually be beneficial for MHD stability by reducing the pressure peaking and raising the q_{min} with somewhat elevated confinement requirement [375].

XI. Conclusions and Outstanding Challenges

The spherical tokamak (ST) is a class of tokamak confinement devices that has numerous features that make it unique for fundamental studies in plasma physics and plasma-surface interactions, and attractive as a fusion reactor concept. The increase in the ideal tokamak β and sustainable current with low aspect ratio, together with natural plasma elongation, enable high performance plasmas to be achieved in a compact geometry. These features are being exploited in more than sixteen ST research facilities around the world, including two megampere-scale facilities, NSTX in the United States and MAST in the United Kingdom. Both NSTX and MAST are undergoing upgrades that include higher neutral beam powers, increased pulse lengths, and field coil modifications to allow greater flexibility in magnetic topology.

Future research in the role of ST in fusion energy development will focus on two main areas. The first is directed toward a Fusion Neutron Science Facility (FNSF). The development of reliable fusion tritium breeding blanket modules and plasma facing components under reactor neutron environment is a major technological obstacles before one can design an attractive DEMO. The compact nature of the ST offers an economical approach to the high fluence volumetric neutron source (VNS) required for the development. The second is the development of fusion power plant, and two approaches will continue to be investigated. The copper-based ST power plant has been the focus of the ARIES-ST study in the US. It has the advantage of allowing a more compact-sized reactor, but the higher resistivity of the copper means larger recirculating power. The physics feasibility of such a facility has not yet been established. The superconducting toroidal field (TF) magnet approach pursued in Japan and Korea results in a larger sze power plant because of the neutron shielding requirements, but it also means that the TF magnet is expected to last for the lifetime of the plant. The physics requirements are less stringent and close to those already achieved.

The achievement of high beta values has been a salient characteristic of STs, and it has been successfully understood in terms ideal and resistive MHD models, and more

recently, kinetic MHD theory. As in all tokamaks, non-axisymmetric effects are important for STs. Performance improvements have been achieved in NSTX, for example, by correcting for poloidal field coil asymmetries and applying 3-D control coils, and a major effort will be devoted to the further development of active control systems. Disruptions are a major issue for tokamaks, and the consequences of non-axisymmetric halo currents induced in the inboard ("high-field") side when they occur are a particular concern. Techniques for detecting the onset of disruptions have been tested using an extensive database of NSTX plasmas, and will be the basis of a future disruption avoidance system.

Tokamaks have historically relied on an ohmic solenoid in the center of the device for starting up the discharge and ramping up the plasma current. Such a solenoid, however, increases the dimensions of ST reactors due to the space required for coil itself and the neutron shielding that must be supplied. Approaches presently under investigation include RF heating and current drive, helicity injection, and merging-compression. Startup with magnetic induction is also under consideration, as there are ST power plant designs that can accommodate shielding for ohmic solenoids within the requirements of protecting superconducting magnetics. Because of their importance, the development of start-up techniques will continue to be a key element of future ST research. The emphasis will be shifted toward plasma current ramp-up as the longer-pulse ST facilities. A fully solenoid-free operation (start-up, ramp-up, and maintenance) is one of the highest research goals for NSTX-U, MAST-U, and QUEST as the facilities are being commissioned with higher power current drive tools.

As with magnetic fusion devices in general, a fundamental understanding of plasma transport physics is critical for the proper interpretation of present-day ST results and extrapolating them to future STs. A particular area of interest is the confinement quality of fusion plasmas in the higher current and lower collisionality regime for STs. Global scaling trends indicate that confinement improves with decreasing collisionality, but the underlying mechanism for anomalous transport is not as well understood as the basis for classical or neoclassical transport. Improved modeling of driving mechanisms like

electron temperature gradient instabilities will continue to be an important research focus, along with innovative diagnostics for measuring their characteristics in STs.

Operation in the "high" confinement mode or H-mode have been the primary means of obtaining high performance plasmas in present day tokamaks, and the success of ITER is predicated on H-mode achievement for high fusion gain. Access to the H-mode is also critical for ST reactors, where the broader current and pressure profiles of H-mode plasmas are advantageous for non-inductive operation with high bootstrap current fractions. As with large aspect ratio tokamaks, there is an incentive to minimize the heating power threshold needed to achieve H-modes. A ubiquitous characteristic of H-modes is the presence of Edge Localized Modes (ELMs). The detailed physics of the H-mode power threshold and ELM dependence on pedestal parameters, however, is still not well understood. The ST will continue to provide a unique configuration for addressing such questions, as the pedestal dependence of the H-mode means that it can be studied in a region that is most sensitive to the effects of low aspect ratio.

The compact configuration of STs allows very high divertor heat loads. The flexibility of the ST geometry also makes it amenable to test methods for mitigating the effects of high heat loads, and developing them remains a challenge. Complementing the need for heat load mitigation techniques, an understanding is also required of the physics underlying transport of heat and particles in the plasma edge, and this merits further investigation such as the observed $1/B_p$ scaling for divertor heat flux width. NSTX-U and MAST-U will explore high heat flux expansion concepts such as snow-flake and super-x divertor configurations, respectively. High heat fluxes in STs also provide a strong incentive to develop PFCs for handling them. Novel concepts such as liquid lithium PFCs have been explored on CDX-U, LTX, and NSTX, and the KTM program is presently focused on flowing liquid lithium divertors. The development of innovative PFCs is expected to continue as an active area of ST research in the future.

The study of energetic particle (EP) physics is a key element of magnetic fusion research, due to the importance of alpha heating in fusion reactor plasmas. An understanding of the

super-Alfvénic regime is of special interest, since the alpha particle velocity typically exceeds the Alfvén velocity in ITER and future magnetic fusion reactors. Super-Alfvénic fusion alpha particles and EPs driven with auxiliary heating can excite Alfvénic modes, which can cause an "anomalous" slowing down of particles as well as radial transport. . In ST plasmas, because of $V_{Alf} \sim \beta^{-0.5} Cs$ scaling, the high beta ST can readily access super-Alfvénic regimes with the NBI injection. Substantial progress has been made in simulating such phenomena, but non-linear models still need development for the predictive capability required for ITER and future STs. Improvements in diagnostics are also planned to better characterize Alfvénic modes and EP populations in STs.

Neutral beam injection (NBI) has been shown to be an effective means for heating and current drive in ST plasmas. However, limitations in beam penetration and the need to shield large complex structures close to the plasma chamber constrain the practicality of NBI for fusion reactors. Radiofrequency (RF) waves are an alternative for heating and current drive. The ST presents a special challenge compared to conventional tokamaks, because its plasmas operate in the over-dense regime for ECH and LHCD. While RF power sources can be readily isolated from the plasma chamber, much work remains to be done in developing launching structures compatible with the high heat and particle fluxes that future ST PFCs must handle.

The success of future STs depends on the understanding gained from integrated scenario development in current STs. This involves operating them in ways that match as many key dimensionless parameters as possible. The actual steady-state conditions expected in a reactor are not yet achieved in present STs. However, they are able to operate with plasma durations that are long compared to the time scales of key physics parameters, including the energy, particle, and momentum confinement times, and the current diffusion time required to achieve steady-state current profiles. In NSTX, for example, plasmas were achieved with β_N above the no-wall limit and relatively high bootstrap current values ~ 50% that are characteristic of FNSF conditions. These parameter ranges can be further explored when the NSTX-U and MAST-U devices become operational.

The ST builds on the success of the tokamak approach to achieve high-performance plasmas. At the same time, STs are able to reach parameters that are attractive for FNSF and fusion power plants, but are not as readily accessible at larger aspect ratio. Significant challenges remain, however, and they are being addressed through the on-going facility upgrades and extensive efforts of the international ST community.

APPENDIX A: Basic characteristics of tokamaks

The basic tokamak configuration is depicted in Fig. 120. A detailed description of tokamaks is provided, for example, in Wesson's book "Tokamaks" [20]. A comparison of tokamak and ST plasmas is described in Sec. II and depicted in Fig. 27. The essential ingredient of a tokamak configuration is the toroidal magnetic field $B_{TF} \propto 1/R$, where R_0 is the major radius. This is generated by toroidal field coils, usually consisting of a number of coils placed uniformly around the torus. Their purpose is to generate a nearly axi-symmetric toroidal field, with minimal toroidal field ripple between the coils. The toroidally-flowing plasma current I_p creates the poloidal field B_{PP} (Fig. 120). Additional poloidal fields B_{PF}, generated by a number of externally-placed circular polodal field coils around the plasma with their current in the toroidal direction, maintain the desired plasma equilibrium. The B_{PP}, together with B_{TF} and B_{PF}, generate "nested" toroidal flux surfaces for confining a stable toroidal plasma. The so-called equilibrium poloidal field coils shown in Fig. 120 have their coil current direction opposing the plasma current. This applies essentially a vertical field B_{PF} to exert a radially-inward force $\propto I_p \, x \, B_{PF}$, to hold the outwardly expanding plasma current ring. There are other poloidal field coils (not shown) for plasma shape control and divertor x-point creation. In general, a tokamak facility typically has a central ohmic heating solenoid (not shown) to induce plasma current by induction. The tokamak configuration is ideally an axi-symmetric system, although the study of 3-D fields is an active research topic as described in Sec. III. The world-wide effort in tokamak research has led to the International Thermonuclear Experimental Reactor (ITER). The ITER device is presently under construction, and is intended to demonstrate burning fusion plasmas. The ITER Physics Requirement Documents [21, 22] also provide a good summary of the status of tokamak research until the time of its publication (1999 and updated in 2007.)

The definitions for often used parameters are as follows [59]:

$a \equiv$ *plasma horizontal minor radius at the mid-plane*

$b \equiv$ *plasma vertical minor radius*

$\kappa \equiv b/a \equiv$ *plasma elongation*

$R_0 \equiv$ *plasma major radius*

$A \equiv R_0/a \equiv$ *plasma aspect ratio*

$I_P \equiv$ *plasma toroidal current*

$L_P \equiv$ *effective plasma minor circumference* $\sim 2\,\pi\, a[(1 + k^2)/2]^{1/2}$

$B_p \equiv$ *poloidal magnetic field* $\equiv \mu_0 I_P / L_P$

$q^* \equiv$ *cylindrical kink (MHD) safety factor* $\equiv L_p B_{T0} / 2\pi R_0 B_p$

$B_{TF} \equiv$ *toroidal magnetic field* $\propto 1/R$

$\beta_{TF} \equiv$ *toroidal beta* $\equiv 2\,\mu_0 \langle p \rangle / B_{T0}^2$

$\beta_N \equiv$ *normalized beta* $\equiv 40\,\pi\,\beta_T\, a\, B_{T0} / \mu_0\, I_P$

Appendix B: Brief background for STs and tokamaks

The tokamak configuration is the most developed concept within magnetic confinement fusion research with a history of over 50 years [20 - 23]. A brief description of tokamaks and the definitions of their key parameters are given in Appendix A. With the confirmation of a high plasma electron temperature of ~ 1 keV in the 1960's in Russia, tokamak research expanded rapidly worldwide. Soon after the demonstration of good energy confinement in the tokamak configuration, interest in high plasma beta (β) naturally developed for economical tokamak reactor designs. The β is the ratio of plasma pressure to the applied toroidal magnetic pressure, and the thermo-nuclear fusion power produced roughly scales as β^2 for a given toroidal magnetic field. Ideal tokamak MHD calculations were carried out in the 1970's, when numerical tokamak stability codes were developed for the first time. It was recognized quite early (i.e., well before the availability of experimental data) that high-n ballooning and lower-n kink modes were the main beta-limiting ideal MHD instabilities for tokamaks [376 - 378]. In Ref. 377, for example, it was predicted that the tokamak β limit increases as the inverse of the tokamak aspect ratio $A \equiv R_0/a$, where R_0 is the tokamak plasma major radius and a is the minor radius, (i.e., $\beta \propto 1/A$). Therefore one may note that because of its favorable beta limit, the potential attractiveness of the low-aspect-ratio regime was appreciated fairly early in the history of tokamaks. This led to a number of proposals to build low aspect ratio tokamak facilities. In 1977, for example, an idea was put forth for a small aspect-ratio tokamak ("SMARTOR"), shown in Fig. 121, to demonstrate thermonuclear ignition in a compact tokamak [379]. In the 1980's, the tokamak experimental database and theoretical calculations were used to formulate the well-known Tryon scaling [380], as described by Eq. (1) in Sec. I.

Appendix C : Relationship of STs with other magnetic confinement concepts

While the ST is a tokamak concept, ST research has significant overlap with other alternate magnetic confinement concepts, and has been influenced by them. The stellarator configuration is similar to that of a tokamak, in that the plasma confinement and MHD stability is provided by nested poloidal magnetic surfaces with a dominant toroidal field but the confining fields are generated mainly by external coils. Unlike tokamaks, stellarators do not require plasma currents to be driven and thus have the advantage of even lower recirculating power. Because of their complicated 3-D coil structures, the stellarator is inherently high aspect-ratio (A ~ 8-12). Even the lowest aspect ratio stellarator reactor design (ARIES-CS) has an effective aspect ratio of ~ 4.5, and the achievable plasma beta is similar to that of a tokamak, i. e., ~ 5% [381]. Prior to the start of ST experiments, the spheromak concept was actively investigated as a possible attractive reactor concept. This is because its fusion blanket module does not link the magnetic field coils, and thus greatly simplifies reactor engineering. The main issue for spheromaks, as it turned out, is magnetic stability and confinement. A spheromak plasma, for example, is found to be tilt-unstable. One of the ways to stabilize this tilt instability is to insert a toroidal field (B_{TF}) coil rod through the center of the plasma. The application of a B_{TF} of sufficient magnitude could make a spheromak into a spherical torus plasma. While this insertion of a TF rod has been discussed by the spheromak community, it was not implemented in major spheromak experiments [140, 382]. This is perhaps because such a linked coil addition would eliminate the spheromak's reactor advantage. Smaller spheromak facilities, including TS-3/4 and HIST, are now capable of operating as STs with the installation of a TF coil rod. The Coaxial Helicity Injection (CHI) plasma start-up concept, developed on HIT / HIT-II and implemented on NSTX, is a direct application of an approach developed through spheromak research. (See Sec. IV.C) The merging-compression start-up being developed on MAST was also utilized for spheromak/ST start-up in TS-3/4. (See Sec. IV.D) The PEGASUS facility, with an ultra-low-aspect-ratio configuration, is exploring the boundary between STs and spheromaks. An RFP (MST) has demonstrated the dramatic benefit of current profile control on MHD stability and plasma confinement [383]. Current profile control is also an important long term goal of STs and advanced tokamaks. Another RFP (RFX) has demonstrated the feedback stabilization of MHD

modes, which has some commonality with RWM feedback stabilization research in STs and tokamaks [384]. The copper TF magnet approach for STs is also similar to other high-beta based magnetic confinement concepts, such as RFPs [383, 384] and FRCs [385]. This is because the power loss to the magnetic field coils can be made manageably small, due to the relatively modest requirements from the point of view of the reactor recirculating power. A major perceived advantage of STs over other high beta systems at the present time is the existence of possible steady-state operating scenarios, with high bootstrap current fractions and good tokamak confinement.

Acknowledgements: This work was supported by DoE Contract No. DE-AC02-09CH11466. Valuable comments on the manuscript by Drs. B. Lloyd, S. Kaye and J. Menard are greatly appreciated. Helpful comments on the topical sections by Drs. G.D. Gates, D. E. Fredrickson, S. Gerhardt, N. Gorelenkov, W. Guttenfelder, R. Maingi, R. Raman, Y. Ren, V. Soukhanovoskii, G. Taylor are also very much appreciated.

References:

1. M. Ono, S.M. Kaye, Y.-K.M. Peng, et al., *Nucl. Fusion* **40**, 557 (2000).
2. S.M. Kaye *et al*., *Fusion Technol*. **36**, 16 (1999).
3. A. C. Darke *et al*., *Nucl. Fusion* **1**, 799 (1995).
4. Q.W. Morris *et al*., Proc. Int. Workshop on ST, St. Petersburg, (1997) Vol. 1, 290, Ioffe Inst. St. Petersburg.
5. V.K. Gusev, S.E. Aleksandrov, V/ Kh Alimov, et al., *Nucl. Fusion* **49,** 104021 (2009).
6. G.D. Garstka, S.J. Diem, R. J. Fonck, et al., *Phys. Plasmas* **10,** 1705 (2003).
7. R. Majeski, R. Doerner, T. Gray, et al., *Phys. Rev. Lett.* **97**, 075002 (2006).
8. R. Majeski, L. Berzak, T. Gray, et al., *Nucl. Fusion* **49**, 055014 (2009).
9. A.J. Redd, B.A. Nelson, T. R. Jarboe, et al., Physics of Plasmas **9**, 2006 (2002)
10. K. Hanada, K.N. Sato, H. Zushi, et al., *IAEA Fusion Energy Conference*, FT/P3-25, 2008.
11. Y. Takase, A. Ejiri, N. Kasuya, et al., *Nucl. Fusion* **41,** 1543 (2001).
12. Y. Takase, A. Ejiri, S. Shiraiwa, et al., *Nucl. Fusion* **46**, S598 (2006).
13. T. Maekawa, Y. Terumichi, H. Tanaka, et al., *Nucl. Fusion* **45**, 1439 (2005).
14. Y. Ono, T. Kimura. E. Kawamori, et al., *Nucl. Fusion* **43**, 789 (2003).
15. Y. Ono, R. Imazawa, H. Imanaka et al*., IAEA Fusion Energy Conference,* EX/P9-4, 2008.
16. M. Nagata et al., *Phys. Plasmas* **10,** 2932 (2003).
17. K.J. Chung, Y.H. An, B.K. Jung et al., *Plasma Science and Technology* **15**, 244 (2013).
18. W. H. Wang, Y.H. He, Z. Gao et al., *Plasma Phys. Control. Fusion* **47,** 1 (2005).
19. G.O. Ludwig, E. Del Bosco, and J.G. Ferreira, *Nucl. Fusion* **45**, 675 (2005).
20. J. Wesson, *Tokamaks* (Oxford University Press, New York, 2004).
21. ITER Physics Basis, *Nucl. Fusion* **39,** 2175 (1999).
22. Progress in the ITER Physics Basis, *Nucl. Fusion* **47**, S1 (2007).
23. J.E. Menard, S. Gerhardt, M. Bell et al., *Nucl. Fusion* **52,** 083015 (2012).
24. D. Stork, H. Meyer, R. Akers, *et al.*, *IAEA Fusion Energy Conference*, ICC/P5-06, 2010.
25. S.P. Gerhardt, R.E. Bell, A. Diallo, et al., *Nucl. Fusion* **53**, 043020 (2013).
26. J.W. Berkery, S.A. Sabbagh, A. Balbaky, *et al.*, *IAEA Fusion Energy Conference*, EX/P8-07, 2012.
27. M. Uchida, T. Yoshinaga, H. Tanaka, and T. Maekawa, *Phys. Rev. Lett.* 104, 065001 (2010).
28. R. Raman, B.A. Nelson, M.G. Bell, et al., *Phys. Rev. Lett.* **97**, 175002 (2006).
29. A. Sykes, R.J. Akers, L.C. Appel, E.R. Arends, et al., Nucl. Fusion **41**, 1423 (2001).
30. Y. Ren et al., http://meetings.aps.org/link/BAPS.2011.DPP.TI2.2.
31. S. Kaye, S. Gerhardt, W. Guttenfelder, et al., Nucl. Fusion **53,** 063005 (2013).
32. V. A. Soukhanovskii1, J.-W. Ahn, R. E. Bell, et al., Nuclear Fusion **51** 012001 (2011).
33. N.N. Gorelenkov, S.D. Pinches, K. Toi, "Energetic particle physics in fusion research in preparation for burning plasma experiments", *Nucl. Fusion* (2014).
34. S. A. Sabbagh, R. E. Bell, J. E. Menard, et al., *Phys. Rev. Lett.* **97**, 045004 (2006).
35. A. Sykes, Plasma Phys. Contr. Fusion **36,** B93 (1994).
36. Y-K.M. Peng, Physics of Plasmas **7**, 1681 (2000).
37. M. Ono, M.G. Bell, R.E. Bell, et al., *Nucl. Fusion* 41, 1435 (2001).
38. E.J. Synakowski, M.G. Bell, R.E. Bell, et al., *Nucl. Fusion* **43**, 1653 (2003).
39. B. Lloyd, J-W Ahn, R.J. Akers, et al., *Nucl. Fusion* **43**, 1665 (2003)
40. S.M. Kaye, M.G. Bell, R.E. Bell, et al., *Nucl. Fusion* **45**, S168 (2005).

41. G.F. Councell, R.J. Akers, L.C. Appel, et al., *Nucl. Fusion* **45**, S157 (2005).
42. J.E. Menard, M.G. Bell, R.E. Bell,et al., *Nucl. Fusion* **47**, S645 (2007).
43. B. Lloyd, R.J. Akers, F. Alladio, et al., *Nucl. Fusion* **47**, S658 (2007).
44. D.A. Gates, J. Ahn, J. Allain, et al., *Nucl. Fusion* **49**, 104016 (2009).
45. H. Meyer, R.J. Akers, F. Alladio, et al., *Nucl. Fusion* **49**, 104017 (2009).
46. R. Raman, J.-W. Ahn, J. Allain, et al., **51**, 094011 *Nucl. Fusion* (2011).
47. B. Lloyd, R.J. Akers, F. Alladio, et al. **51**, 094013 *Nucl. Fusion* (2011).
48. S.Sabbagh. J.-W. Ahn. J. Allain, et al., *Nucl. Fusion* **53,** 104007 (2013).
49. H. Meyer, I.G. Abel, R.J. Akers, et al., *Nucl. Fusion* **53,** 104008 (2013).
50. V.K. Gusev, E.A. Azizov, A.B. Alekseev, et al., *Nucl. Fusion* **53,** 093013 (2013).
51. A.C. Sontag, S.J. Diem, R.J. Fonck, et al., *Nucl. Fusion* **48,** 095006 (2008).
52. D.J. Battaglia, M.W. Bongard, R.J. Fonck, A.J. Redd, and A.C. Sontag, *Phys. Rev. Lett.* **102**, 225003 (2009).
53. K. Yamazaki, Y. Taira, T. Oishi, et al., *J. Plasma Fusion Res.* **8** 1044 (2009).
54. F. Alladio, P. Costa, A. Mancuso, et al., *Nucl. Fusion* **46,** S613 (2006).
55. L. Dudek, J. Chrzanowski, P. Heitzenroeder, et al., *Fusion Engineering and Design* **87**, 1515 (2012).
56. J. Milnes, T. Barrett, G. Cunningham, et al., "MAST Upgrade – Progress and Engineering challenges", Conference Proceedings, SOFE (2013).
57. Y-K.M. Peng, D.J. Strickler, *Nucl. Fusion* **26**, 769 (1986).
58. M. Roberto and R.M. O. Galvao, *Nuclear Fusion Letters* **32**, 1666 (1992).
59. J.E. Menard, S.C. Jardin, S.M. Kaye, C.E. Kessel, and J. Manickarn, Nuclear Fusion **37,** 595 (1997).
60. R.L. Miller *et al.*, Phys. Plasmas **4**, 1062 (1997).
61. R.D. Stambaugh, V.S. Chan, R.L. Miller, et al., Development path of low aspect ratio tokamak power plants, Fusion Eng. Des. **41**, 385 (1998).
62. T.C. Hender *et al.*, *Phys. Plasmas* **6**, 1958 (1999).
63. S. C. Jardin, et al., *Fusion Science and Technology* **43**, 161 (2003)
64. Y-K.M. Peng, J. Galambos, P. Shipe, *Fusion Technology* **21**, 1729 (1992).
65. F. Najmabadi, M. Billone, L. Bromberg, et al., *Fusion Engineering and Design* **65**, 143 (2003).
66. J. E. Menard, M. G. Bell, R. E. Bell, et al., PPPL-3779 (2003).
67. J. E. Menard, M. G. Bell, R. E. Bell, et al., *Phys. Plasmas* **11**, 639 (2004).
68. M.C. Zarnstorff, M. G. Bell, M. Bitter, et al., *Phys. Rev. Letters* **60,** 1306 (1988).
69. M. Kikuchi, M. Azumi, S. Tsuji, et al., *Nucl. Fusion* **30**, 343 (1990).
70. M. Ono, R. Bell, C.S. Chang, et al., Plasma Physics and Controlled Fusion, Vol. 39, A361-A369 (1997).
71. M.A. Abdou, S.E. Berk, A. Ying, et al., *Fusion Technol.* 29 (1996).
72. E.T. Cheng, Y.K. M. Peng, R. Cerbone, et al., *Fusion Engineering and Design* **38**, 219 (1998).
73. J.D. Strachan, et al., *Phys. Rev. Letters* **72,** 3526 (1994).
74. D.H. Start, et al., *Phys. Rev. Letters* **80,** 4681 (1998).
75. Y-K.M. Peng, J.M. Canik, S. J. Diem, et al., *Fusion Sci. Technol.* **60,** 441 (2011).
76. J.E. Menard, T. Brown, J. Canik et al., *IAEA Fusion Energy Conference,* FTP/3-4, 2012.
77. G.M. Vossa, S. Davisa, A. Dnestrovskijb, et al., *Fusion Engineering and Design* **83**, 1648 (2008).
78. J.E. Menard, L. Bromberg, T. Brown, et al., *Nucl. Fusion* **51**, 103014 (2011).
79. Y-K.M. Peng, P.J. Fogarty, T.W. Burgess, et al., *Plasma Phys. Control. Fusion* **47,** B263 (2005).
80. Y-K.M. Peng, T.W. Burgess, A. J. Carroll, et al., *Fusion Sci. Technol.* **56**, 957 (2009).
81. A. Sykes, et al., *IEEE Transactions Plasma Science* **40**, 715 (2012).
82. A. Lumsdaine, J. Tipton, M. Peng, et al., *Fusion Engineering and Design* **87**, 1190 (2012).
83. Y-K.M. Peng, W. Reierson, S.M. Kaye, et al., *Nucl. Fusion* **40**, 583 (2000)
84. M. Ono, M. Peng, C. Kessel, C. Neumeyer, et al., *Nucl. Fusion* **44**, 452 (2004).

85. R.J. Goldston, J.E. Menard, J.P. Allain, et al., *IAEA Fusion Energy Conference,* FT/P3-12, 2008.
86. M. Kotschenreuther. P.M. Valanju, S.M. Mahajan, E.A. Schneider, *Fusion Engineering and Design* **84**, 83 (2009).
87. H. R. Wilson, J-W. Ahn, R.J. Akers, *et al., Nucl. Fusion* **44** 917 (2004).
88. Y. Nagayama et al., *IEEJ Trans. F&M* **132**, 555(2012).
89. K. Gi, Y. Ono, M. Nakamura, et al., *IAEA Fusion Energy Conference,* FIP/P7-15-12, 2014.
90. B.G. Hong, Y.S. Hwang, J.S. Kang, et al., *Nucl. Fusion* **51**, 113013 (2011).
91. B. Hu, R. Betti, J. Manickam, et al., *Phys. Plasmas* **12**, 057301 (2005).
92. M. Gryaznevich, R. Akers, P.G. Carolan, et al., *Phys. Rev. Letters* **80**, 3972 (1998).
93. A. Sykes, et al., *Nuclear Fusion* **39**, 1271 (1999).
94. D.A. Gates, et al., *Phys. Plasmas* **10**, 1659 (2003).
95. F. Najmabadi, et al., *Fusion Engineering and Design* **80**, 3-23 (2006).
96. D.A. Gates, J. Menard, R. Maingi, et al., *Nucl. Fusion* **47**, 1376 (2007).
97. S. A. Sabbagh, A. C. Sontag, J.M. Bialek, et al., *Nucl. Fusion* **46**, 635 (2006).
98. A.C. Sontag, S.A. Sabbagh, W. Zhu, *et al., Phys. Plasmas* **12** 056112 (2005).
99. A. C. Sontag, S. A. Sabbagh, W. Zhu, et al., *Nucl. Fusion* **47**, 1005 (2007).
100. S. A. Sabbagh, J.M. Bialek, R.E. Bell, et al., *Nucl. Fusion* **44**, 560 (2004).
101. A. Bondeson and M.S. Chu, *Phys. Plasmas* **3** 3013 (2001996).
102. J. W. Berkery, S.A. Sabbagh, H. Reimerdes, et al., *Phys. Plasmas* **17** 082504 (2010).
103. J. W. Berkery, S.A. Sabbagh, R. Betti, et al., *Phys. Rev. Letters* **104**, 035003 (2010).
104. I. Chapman et al., *Plasma Phys. Controlled Fusion* **51**, 055015 (2009)
105. J. W. Berkery, S.A. Sabbagh, R. Betti, et al., *Phys. Rev. Letters* **106**, 075004 (2011).
106. S. A. Sabbagh, J. W. Berkery, R.E. Bell, et al., *Nucl. Fusion* **50**, 025020 (2010).
107. O. Katsuro-Hopkins, et al., *Nucl. Fusion* **47**, 1157 (2007).
108. R.J. La Haye, *Phys. Plasmas* **13** 055501 (2006).
109. T.C. Hender, *et al., Nucl. Fusion* **47** S128 (2007).
110. R. J. Buttery, O. Sauter, R. Akers, et al., *Phys. Rev. Lett.* **88** 125005 (2002).
111. E. Fredrickson, J. Menard, K. Triz, et al., Bull. Am. Phys. Soc.**49**, 68 (2004).
112. S. Kruger, C.C. Hegna and J.D. Callen, *Phys. Plasmas,* **5** 455 (1998).
113. C.C. Hegna, *Phys. Plasmas,* **6** 3980 (1999).
114. R.J. La Haye, R.J. Buttery, S.P. Gerhardt, et al., *Phys. Plasmas,* **19** 062506 (2012).
115. J. E. Menard, M.G. Bell, R.E. Bell, et al., *Nuclear Fusion* **43**, 330 (2003).
116. J. E. Menard, R.E. Bell, D.A. Gates, et al., *Nuclear Fusion* **50**, 045008 (2010).
117. K.C. Shaing, et al., *Phys. Rev. Letters* **80**, 5353 (1998).
118. W. Zhu, S.A. Sabbagh, R.E. Bell et al., et al., *Phys. Rev. Letters* **96**, 225002 (2006).
119. S.A. Sabbagh, J.W. Berkery, T.E. Bell, et al., *Nuclear Fusion* **50**, 025020 (2010).
120. K. Kim, J.-K. Park, A.H. Boozer and K. Kramer, *Phys. Plasmas,* **19** 082503 (2012).
121. J.K. Park, A.H. Boozer, A.H. Glasser, *Phys. Plasmas* **14** 052110 (2007).
122. J.-K. Park et al., *Phys. Rev. Letters* **102**, 065002 (2009).
123. J.-K.Park, J. E. Menard, S.P. Gerhardt, et al., Nuclar Fusion **52**, 023004 (2012).
124. M.N. Rosenbluth and S.V. Putvinski, *Nucl. Fusion* **37** 1335 (1997).
125. S.P. Gerhardt, D.S. Darrow, R.E. Bell, et al., *Nucl. Fusion* **53**, 063021 (2013).
126. D. Muller, *Phys. Plasmas,* **20** 058101 (2013).
127. C.B. Forest, Y.S. Hwang, M. Ono and D. S. Darrow *Phys. Rev. Lett.* **68** 3559 (1992).
128. Y.S. Hwang, C.B. Forest, M. Ono and D. S. Darrow *Phys. Rev. Lett.* **77** 3811 (1996).
129. T. Yoshinaga, M. Uchida, H. Tanaka, and T. Maekawa, *Phys. Rev. Lett.* 96, 125005 (2006).
130. A. Ejiri, Y. Takase, H. Kasahara, T. Yamada, et al, *Nucl. Fusion* **46** 709 (2006).
131. A. Ejiri, Y. Takase, T. Oosako, T. Yamaguchi, et al, *Nucl. Fusion* **49** 065010 (2009).
132. T. Kikukawa et al., *Plasma Fusion Res.* **3** 010 (2008).
133. M. Ishiguro, K. Hanada, H. Liu et al. *Phys. Plasmas.* **19** 062508 (2012).
134. M. Gryaznevich, V. Shevchenko and A. Sykes *Nucl. Fusion* **46** S573 (2006).

135. K. Hanada, H. Zushi, H. Idei, et al., *Plasma Science and Technology* **13** 307 (2011).
136. H. Idei, et al., IAEA Fusion Energy Conference, EX/P1-38 (2014).
137. V.F. Shevchenko, M.R. O'Brien, D. Taylor, et al., *Nucl. Fusion* **50** 022004 (2010).
138. T.S. Bigelow, et al, http://meetings.aps.org/Meeting/DPP13/Event/199947.
139. N.J. Fisch, *Phys. Rev. Lett.* **41**, 873 (1978).
140. Y. Takase, A. Ejiri, H. Kakuda, et al., *Nucl. Fusion* 53 (6), 063006 (2013).
141. T.R. Jarboe, *Fusion Technol.* **15** 7 (1989).
142. T.R. Jarboe, I. Henins, A.R. Sherwood et al., *Phys. Rev. Lett.* **51**, 39 (1983).
143. M. Ono, G.J. Greene, D.S. Darrow, C. Forest, et al., *Phys. Rev. Lett.* **59,** 2165 (1987).
144. D.S. Darrow, M. Ono, C.B. Forest, G.J. Greene, et al., *Phys. Fluids* **B 2**, 1415 (1990).
145. B. Nelson, T. R. Jarboe, D.J. Orvis, L.A. McCullough, et al., *Phys. Rev. Lett.* **72**. 3666 (1994)
146. T.R. Jarboe, P. Gu, V.A. Izzo, et al., *Nucl. Fusion* **41**, 679 (2001).
147. R. Raman, T. R. Jarboe, D. Mueller, et al., *Nucl. Fusion* **41**, 1081 (2001)
148. R. Raman, T. R. Jarboe, B.A. Nelson, et al., *Phys. Rev. Lett.* **90**, 0750005-1 (2003).
149. R. Raman, T. R. Jarboe, B.A. Nelson, et al., *Phys. Plasmas* **11,** 2565 (2004).
150. R. Raman, B.A. Nelson, M.G. Bell et al., *Phys. Rev. Lett.* **97**, 175002 (2006).
151. R. Raman, D. Mueller, B.A. Nelson, T.R. Jarboe, et al., *Phys. Rev. Lett.* **104**, 095003 (2010).
152. B. Nelson, T. R. Jarboe, D. Mueller, et al., *Nucl. Fusion* **51**, 063008 (2011).
153. D.J. Battaglia, M.W. Bongard, R.J. Fonck, and A.J. Redd, *Nucl. Fusion* **51**, 073029 (2011).
154. Y. Ono, H. Tanabe, T. Yamada, et al., *Plasma Phys. Controlled Fusion* **54**, 124039 (2012).
155. M. Nagao, T. Higashi, M. Ishihara, et al., IAEA Fusion Energy Conference, ICC/1-1Rb, 2012.
156. T. Yamada, R. Imazawa, S. Kamio, et al., IAEA Fusion Energy Conference, EXSP2-19 (2011).
157. K.J. Chung, Y.H. An, B.K. Jung et al., *Fusion Engineering and Design* **88**, 787 (2013).
158. M. Ushigome, S. Ide, S. Itoh, et al., *Nucl. Fusion* **46** 207 (2006).
159. W. Choe, J. Kim, M. Ono, *Nucl. Fusion* **45**, 1463 (2005).
160. D. A. Gates, C. Jun, I. Zatz, A. Zolfaghari, *Fusion Engineering and Design* **86**, 41(2011).
161. B. Coppi and F. Pegoraro, *Nucl. Fusion* **17**, 969 (1977).
162. B.B. Kadomtsev and O.P. Pogutse, *Nucl. Fusion* **11**, 67 (1971).
163. W.M. Tang, J.M. Connor, and R.J. Hastie, *Nucl. Fusion* **20**, 1439 (1980).
164. R.D. Hazeltime, D. Dobrott, and T.S. Wang, *Phys. Fluids* **18**, 1778 (1975).
165. Y.C. Lee, et al., *Phys. Plasmas,* **30**, 1331 (1987).
166. D. Stutman, L. Delgado-Aparicio, N. Gorelenkov, et al., *Phys. Rev. Lett.* **102**, 115002 (2009).
167. W. Guttenfelder, J.L. Peterson, J. Candy, et al., *Nucl. Fusion* **53**, 093022 (2013).
168. S.M. Kaye, F.M. Levinton, D. Stutman, et al., *Nucl. Fusion* **47** 499 (2007).
169. M. Valovic, R. Akers, M. de Bock, et al., *Nucl. Fusion* **49** 075016 (2009).
170. M. Valovic, R. Akers, M. de Bock, et al., *Nucl. Fusion* **51** 073045 (2011).
171. G. Cordey, K. Tomsen, A. Chudnovskiy, et al., *Nucl. Fusion* **45**, 1078 (2005).
172. C.C. Petty, *Phys. Plasmas* 15, 080501 (2008).
173. E.J. Synakowski, M.G. Bell, R.E. Bell, et al., *Plasma Phys. Controlled Fusion* **44**, A165 (2002).
174. D. R. Smith, H. Feder, R. Feder, et al., *Rev. Sci. Instrum*. **81**, 10D717 (2010).
175. A. R. Field, D. Dunai, R. Gaffka et al., *Rev. Sci. Instrum*. **83**, 13508 (2012).
176. Y.-c. Ghim, A.A. Schekochihin, A.R. Field, et al., *Phys. Rev. Lett.* **110**, 145002 (2013).
177. A. R. Field, D. Dunai, Y.-c. Ghim, et al., *Plasma Phys. Controlled Fusion* **56**, 025012 (2014).
178. D. R. Smith, S.E. Parker, W. Wan, et al., *Nucl. Fusion* **53**, 113029 (2013).
179. D. R. Smith et al., Rev. Sci. Instrum. **79**, 123501 (2008).
180. H. Kugel *et al., Phys. Plasmas* **15**, 056118 (2008).
181. M.G. Bell et al *Plasma Phys. Controlled Fusion* **51**, 124056 (2009).
182. R. Maingi, S.K. Kaye, S.H. Skinner, et al., *Phys. Rev. Lett.* **107**, 145004 (2011).
183. R. Maingi, D.P. Boyle, J.M. Canik, et al., *Phys. Plasmas* **52,** 083001 (2012).
184. F. Jenko, W. Dorland, and G.W. Hammett, *Phys. Plasmas* **8**, 4096 (2001).
185. E. Mazzucato, R. E. Bell, S. Ethier, et al., *Nucl. Fusion* **49** 055001 (2009).

186. D. R. Smith, S.M. Kaye, W. Lee, et al., *Phys. Rev. Lett.* **102**, 225005 (2009).
187. S. Ethier, W.X. Wang, F. Poli, et al., *IAEA Fusion Energy Conference,* TH/P4-08, 2010.
188. F.M. Levinton, H. Yuh, M.G. Bell, et al., *Phys. Plasmas* **14** 056119 (2007).
189. H.Y. Yuh, F. M. Levinton, R.E. Bell et al., *Phys. Plasmas* **16** 056120 (2009).
190. H.Y. Yuh, S.M. Kaye, F. M. Levinton, et al., *Phys. Rev. Lett.* **106**, 055003 (2011).
191. J.L. Peterson, R. Bell, J. Candy, et al., *Phys. Plasmas* **19** 056120 (2011).
192. Y. Ren, S. Kaye, E. Mazzucato, et al., *Phys. Rev. Lett.* **106** 165005 (2011).
193. N. Joiner, D. Applegate, S.C. Cowley, et al., *Plasma Phys. Controlled Fusion* **48** 685 (2006).
194. K.L. Wong, S. Kaye, D.R. Mikkelsen et al., *Phys. Rev. Lett.* **99** 135003 (2007).
195. W. Guttenfelder, J. Candy, S.M. Kaye, et al., *Phys. Plasmas* **19**, 056119 (2012).
196. S.M. Kaye, W.M. Solomon, R.E. Bell, et al., *Nucl. Fusion* **49** 045010 (2009).
197. W.M. Solomon, S.M. Kaye, R.E. Bell, et al., *Phys. Rev. Lett.* **101** 065004 (2008).
198. T.S. Hahm, P.H. Diamond, O.D. Gurcan, and G. Rewoldt, *Phys. Plasmas* **14**, 072302 (2007).
199. A.G. Peeters, C. Angioni, and D. Strintzi, *Phys. Rev. Lett.* **98** 265003 (2007).
200. E.J. Doyle, W.A. Houlberg, Y. Kamada, et al., *Nucl. Fusion* **47** S18 (2007).
201. A.R. Field, P.G. Carolan, .J. Conway, et al., *Plasma Phys. Controlled Fusion* **46**, 981 (2004).
202. J.-K. Park, R.E. Bell, S.M. Kaye, et al., *Nucl. Fusion* **53** 063012 (2013).
203. V.A. Soukhanovskii, M. Finkenthal, H.W. Moos, et al., *Plasma Phys. Controlled Fusion* **44**, 2339 (2002).
204. D. Stutman, M. Finkenthal, and R.E. Bell, et al., *Phys. Plasmas* **10** 4387 (2003).
205. L. Delgado-Aparicio, D. Stutman, K. Tritz, et al., *Nucl. Fusion* **49** 085028 (2009).
206. D.J. Clayton, K. Tritz, D. Stutman, et al., *Plasma Phys. Controlled Fusion* **54**, 105022 (2012).
207. W.A. Houlberg, K.C. Shaing, S.P. Hirshman, and M.C. Zarnstorff, *Phys. Plasmas* **4** 3230 (1997).
208. F. Wagner *et al*., *Phys. Rev. Lett.* **49**, 1408 (1982).
209. A. Sykes, R. J. Akers, L. C. Appel, *et al., Phys. Rev. Lett.* **84**, 495 (2000).
210. A. Sykes, J.-W. Ahn, R. Akers, *et al., Phys. Plasmas* **8**, 2101 (2001).
211. R. J. Akers, G. F. Counsell,1 A. Sykes,1 et al., *Phys. Rev. Lett.* **88**, 035002 (2002).
212. R. J. Akers, J.-W. Ahn, L. C. Appel, *et al., Phys. Plasmas* **9**, 3919 (2002).
213. R. Maingi, M.G. Bell, R.E. Bell, et al., *Phys. Rev. Lett.* **88**, 035003 (2002).
214. C. E. Bush, M. G. Bell, R. E. Bell, *Phys. Plasmas* **10**, 1755 (2003).
215. H. Meyer, P.G. Carolan, G.D. Conway, *et al Nucl. Fusion* **46,** 64 (2006).
216. S.M. Kaye, R. Maingi, D. Battaglia, et al., *Nucl. Fusion* **51,** 113019 (2011).
217. H. Meyer, M.F.M. De Bock, N.J. Conway, et al., *Nucl. Fusion* **51,** 113011 (2011).
218. Y.R. Martin, T. Takizuka, and the ITPA CDBM H-Mode Threshold Working Group 2008 *J. Phys.: Conf. Ser.* **123** 012033.
219. D. Battaglia, C.S. Chang, S.M. Kaye, et al., *Nucl. Fusion* **53,** 113032 (2013).
220. R. Maingi, S. M. Kaye, R.E. Bell, et al., *Nucl. Fusion* **50**, 064010 (2010).
221. R. Maingi, R. E. Bell, J. M. Canik, et al., *Phys. Rev. Lett.* **105**, 135004 (2010).
222. A. Kirk, Y. Liu, E. Nardon, et al., *Plasma Phys. Controlled Fusion* **53**, 065011 (2011).
223. R. Maingi, C. S. Chang, S. Ku, et al., *Plasma Phys. Controlled Fusion* **46**, A305 (2004).
224. R. Maingi, S.A. Sabbagh, C.E. Bush, et al., *J. Nucl. Materials* **337-339** 727 (2005).
225. R. Maingi, M.G. Bell, E.D. Fredrickson,et al.., *Phys. Plasmas* **13**, 092510 (2006).
226. A. Kirk, H. R. Wilson, R. Akers et al., *Plasma Phys. Controlled Fusion* **47**, 315 (2005).
227. A. Kirk, B. Koch, R. Scannel, et al., *Phys. Rev. Lett.* **96**, 185001 (2006).
228. K. E. Thome, et al., http://meetings.aps.org/Meeting/DPP13/Event/200451
229. C.E. Bush *et al*., *Proc. 10th US–EU TTF Workshop (Varenna, Italy, 6–9 September 2004)*.
230. Martin Y.R., Takizuka T. and the ITPA CDBM H-Mode Threshold Working Group 2008 *J. Phys.: Conf. Ser.* **123** 012033.
231. H.R. Wilson, P.B. Snyder, G.T.A. Huysmans, and R.L. Miller, *Phys. Plasmas* **9**, 2037 (2002).
232. P.B. Snyder, H.R. Wilson, J.R. Ferron, et al., *Phys. Plasmas* **9**, 2037 (2002).
233. A.C. Sontag, J.M. Canik, R. Maingi, *Nucl. Fusion* **51**, 103022 (2011).

234. A. Kirk, T.O'Gorman, S. Saarelma, et al., *Plasma Phys. Controlled Fusion* **51**, 065016 (2009).
235. M.W. Bongard, et al., http://meetings.aps.org/Meeting/DPP13/Event/201226
236. A. Diallo, J. Canik, T. Goerler, et al., *Nucl. Fusion* **53**, 093026 (2013).
237. R. Groebner *et al*., *Nucl*. *Fusion* **49** 085037 (2009).
238. P.B. Snyder, et al., *Nucl*. *Fusion* **51** 103016 (2011).
239. T. E. Evans, R. A. Moyer, P. R. Thomas, et al., *Phys. Rev. Lett.* **92**, 235003-1 (2004).
240. E. Nardon, A. Kirk, R. Akers, et al., *Plasma Phys. Controlled Fusion* **51**, 124010 (2009).
241. J. M. Canik, R. Maingi, T. E. Evans, et al., *Phys. Rev. Lett.* **104**, 045001 (2010).
242. J. M. Canik, R. Maingi, T. E. Evans, et al., *Nucl. Fusion* **50**, 034012 (2010).
243. J. M. Canik, A.C. Sontag, R. Mangi, et al., *Nucl. Fusion* **50**, 064016 (2010).
244. J. M. Canik, S.O. Hirshman, R. Sanchez, et al., *Nucl. Fusion* **52**, 054004 (2012).
245. R. Maingi, T.H. Osborne, B. P. LeBlanc, et al., *Phys. Rev. Lett.* **103**, 075001 (2009).
246. D.K. Mansfield, H.W. Kugel, R. Maingi, et al., Journal of Nuclear Materials **390–391,** 764 (2009).
247. D.P. Boyle, R. Maingi, P.B. Snyder, et al., *Plasma Phys. Controlled Fusion* **53**, 105011 (2011).
248. D. Mansfield et al., *Nucl. Fusion* **53**, 113023 (2013).
249. S.P. Gerhardt, J.-W. Ahn, J.M. Canik, et al., *Nucl. Fusion* **50**, 064015 (2010).
250. D. A. Gates, R. Maingi, J. Menard, et al., *Phys. Plasmas* **13**, 056122 (2006).
251. V. A. Soukhanovskii, R.E. Bell, A. Diallo, et al., *Phys. Plasmas* **19**, 082504 (2012).
252. A. Kirk, W. Fundamenski, J-W. Ahn, et al., *Plasma Phys. Controlled Fusion* **45**, 1445 (2003).
253. G.F. Counsell, A. Kirk, J-W. Ahn et al., *Plasma Phys. Controlled Fusion* **44**, 827 (2002).
254. R. Maingi, H.W. Kugel, C.J. Lasnier, et al., *J. Nucl. Materials* **313-316**, 1005 (2003).
255. V.A. Soukhanovskii, et al., *J. Nucl. Materials* **337** 475 (2005).
256. T.K. Gray, R. Maingi, V.A. Soukhanovskii, et al., *J. Nucl. Materials* **415** S360 (2011).
257. D. Ryutov, et al., *Phys. Plasmas* **14**, 064502 (2007).
258. H. Takase, *J. Phys. Soc. Japan* **70** 609 (2001).
259. M. Kotschenreuther, P. Valanju, S. Mahajan, et al., *Phys. Plasmas* **14**, 72502 (2007).
260. P.M. Valanju, M. Kotschenreuther, S.M. Mahajan, et al., *Phys. Plasmas* **16**, 056110 (2009).
261. E. Havlickova, et al., *J. Nucl. Materials* **438**, S545 (2013).
262. V. Rozhansky, *Plasma Phys. Controlled Fusion* **55**, 035005 (2013).
263. V.A. Soukhanovskii, R. Maingi, D.A. Gates, et al., *Phys. Plasmas* **16**, 02501 (2009).
264. V.A. Soukhanovskii, R. Maingi, D.A. Gates, et al., *Nucl. Fusion* **49**, 095025 (2009).
265. T.K. Gray, J.M. Canik, R. Maingi, et al., *Nucl. Fusion* **54**, 023001 (2014).
266. M. Ono, M.A. Jaworski, R. Kaita, et al., *Nucl. Fusion* **53**, 113030 (2013).
267. J-W. Ahn, *Phys. Plasmas* **18** 056108 (2011).
268. P. Cahyna, M. Oeterka, A. Kirk, et al, *J. Nucl. Materials* **438**, S326 (2013).
269. T. Eich, A.W. Leonard, R.A. Pitts, et al., *Nucl. Fusion* **53**, 093031 (2013).
270. R.J. Goldston, *Nucl. Fusion* **52**, 013009 (2012).
271. A. Kirt, N. Ben Ayed, G. Counsell, et al., *Plasma Phys. Controlled Fusion* **48**, B433 (2006).
272. S.J. Zweben, R.J. Maqueda, D.P. Stotler, et al., *Nucl. Fusion* **44**, 134 (2004).
273. B.D. Dudson, R.O. Dendy, A. Kirk, et al., *Plasma Phys. Controlled Fusion* **47**, 885 (2005).
274. J.A. Boedo, R. Crocker, L. Chousal, et al., *Rev. Sci. Instrum.* **80** 123506 (2009).
275. S. I. Krasheninnikov, *Phys. Lett. A* 2**83**, 368 (2001).
276. D.A. D'Ippolito, J. R. Myra, and S. I. Krasheninnikov, *Phys. Plasmas* **9**, 222 (2002).
277. J.R. Myra, W.M. Davis, D.A. D'Ippolito, et al., *Nucl. Fusion* **53**, 073013 (2013).
278. D.A. D'Ippolite, J.R. Myra, and S.J. Zweben, et al., *Phys. Plasmas* **18**, 060501 (2011).
279. S.J. Zweben, J.A. Boedo, O. Grulke, et al., *Plasma Phys. Controlled Fusion* **49**, S1 (2007).
280. B.D. Dudson, N. Ben Ayed, A. Kirk, et al., *Plasma Phys. Controlled Fusion* **50**, 1240122 (2008).
281. N. Ben Ayed, A. Kirt, B. Dudson, et al., *Plasma Phys. Controlled Fusion* **51**, 035016 (2009).
282. R.J. Maqueda, R. Maingi, et al., *Phys. Plasmas* **16,** 056117 (2009).
283. S.J. Zweben, R.J. Maqueda, R. Hager, et al., *Phys. Plasmas* **17,** 102502 (2010).
284. S.J. Zweben, R.J. Maqueda, J.L. Terry, et al., *Phys. Plasmas* **13,** 056114 (2006).

285. F. Militello, P. Tamain, W. Fundamenski, et al., *Plasma Phys. Controlled Fusion* **55**, 025005 (2013).
286. D.A. Russell, J. R. Myra, A. D'Ippolito, et al., *Phys. Plasmas* **18**, 022306 (2011).
287. H. Kugel *et al*., J. Nucl. Materials **337–339**, 495 (2005).
288. J. Strachan *et al., Plasma Phys. Control. Fusion* **44**, 2339 (2002).
289. D. Mansfield *et al., Nucl. Fusion* **41**, 1823 (2001).
290. F. Scotti *et al., Rev. Sci. Instrum.* **83**, 10E532 (2012).
291. A. McLean *et al., Rev. Sci. Instrum*. **83**, 053706 (2012).
292. P. Krstic *et al., Phys. Rev. Lett.* **110**, 105001 (2013).
293. M. Podesta *et al., Nucl. Fusion* **52**, 033008 (2012).
294. F. Scotti *et al.,* Nucl. Fusion **53**, 083001 (2013).
295. M. Abdou *et al., Fus. Eng. Design* **54**, 181 (2001)
296. R. Kaita *et al., Phys. Plasmas* **14**, 056111 (2007).
297. R. Kaita *et al., Fus. Eng. Design* **85**, 874 (2010).
298. R. Majeski *et al., Phys. Plasmas* **20**, 056103 (2013).
299. H. Kugel *et al., Fus. Eng. Design* **87**, 1724 (2012).
300. M. Jaworski *et al.,* Nucl. Fusion **53**, 083032 (2013).
301. V.A. Soukhanovskii, A.L. Roquemore, R.E. Bell, et al., *Rev. Sci. Instrum*. **81,** 10D723 (2010).
302. T. Abrams *et al., J. Nucl. Materials* **438**, S313 (2013).
303. De Temmerman *Fus. Eng. Design* in press (2013).
304. R. Kaita *et al., J. Nucl. Materials* **438**, S488 (2013).
305. C. Skinner *et al*., J. Nucl. Materials **438**, S647 (2013).
306. I. Lyublinski *et al., Fus. Eng. Design* **87**, 1719 (2012).
307. N.N. Gorelenkov et al., Nucl. Fusion **43**, 594 (2003).
308. N.N. Gorelenkov, H.L. Berk and R.V. Budny, Nucl. Fusion **45**, 226 (2005).
309. M. Gryaznevich, V. Shevchenko and A. Sykes *Nucl. Fusion* **46** S942 (2006).
310. R.G.L. Vann, R.O. Dendy, and M.P. Gryaznevich, *Phys. Plasmas* **12**, 032501 (2005).
311. B. N. Breizman, M. S. Pekker, and S. E. Sharapov, *Phys. Plasmas* **12**, 112506 (2005)
312. M.P. Gryaznevich and S.E. Sharapov, *Plasma Phys. Controlled Fusion* **46**, S15 (2004).
313. E. D. Fredrickson, N.A. Crocker, N. Gorelenkov, et al., *Phys. Plasmas* **14**, 102510 (2007).
314. N.N. Gorelenkov, H.L. Berk, N.A. Crocker, et al., *Plasma Phys. Controlled Fusion* **49**, B317 (2007).
315. K. McGuire, et al., *Phys. Rev. Lett.* **50** 891 (1983).
316. E. D. Fredrickson, L. Chen, and R. Whilte, *Nucl. Fusion* **43** 1258 (2003).
317. E. D. Fredrickson, N.A. Crocker, D.S. Darrow, et al., *Nucl. Fusion* **53** 013006 (2013).
318. E. D. Fredrickson, N. Gorelenkov, C. Z. Cheng, et al., *Phys. Rev. Lett.* **87**, 145001-1 (2001).
319. N.N. Gorelenkov, C.Z. Cheng, and E. Fredrickson, *Nucl. Fusion* **42**, 977 (2002).
320. L.C. Appel, T. Fulop, M. J. Hole, et al., *Plasma Physics and Controlled Fusion* **50**, 115011 (2008).
321. N.N. Gorelenkov, E. Belova, H.L. Berk, et al., *Phys. Plasmas* **11**, 2586 (2004).
322. N.A. Crocker, W.A. Peebles, S. Kubota, et al., *Phys. Rev. Lett.* **97**, 045002 (2006).
323. C.Z. Cheng Phys. Rep. **211** 1-51(1992).
324. M. Podestà, N.N. Gorelenkov, R.B. White, et al., *Phys. Plasmas* **20,** 082502 (2013).
325. D.S. Darrow, N. Crocker, E.D. Fredrickson, et al., *Nucl. Fusion* **53** 013009 (2013).
326. D.S. Darrow, *Rev. Sci. Instrum*. **79** 023502 (2008).
327. M. Podestà, et al., *Rev. Sci. Instrum*. **79,** 10e521 (2008).
328. M. Podestà, W.W. Heidbrink, D. Liu, et al., *Phys. Plasmas* **16,** 056104 (2009).
329. S.P. Gerhardt *Nucl. Fusion* **51** 033004 (2011).
330. D.S. Darrow, E.D. Fredrickson, N.N. Gorelenkov, et al., **48**, 084004 (2008).
331. E. D. Fredrickson, N.N. Gorelenkov, E. Belova, et al., *Nucl. Fusion* **52** 043001 (2012).
332. J. E. Menard, R. E. Bell, D. A. Gates, et al., *Phys. Rev. Lett.* **97**, 095002 (2006).

333. A. Bortolon, W.W. Heidbrink, G.J. Kramer et al., *Phys. Rev. Lett.* **110**, 265008 (2013).
334. R.B. White, and M.S. Chance, *Phys. Fluids* **27** 2455 (1984).
335. T.H. Stix, *Waves in Plasmas* (American Institute of Physics, New York, 1992).
336. M. Ono, Physics of Plasmas **2**, 4075 (1995).
337. J.E. Menard, R. Majeski, R. Kaita, et al., *Phys. Plasmas* **6**, 2002 (1999).
338. T. Oosako, Y. Takase, A. Ejiri, Y. Nagashima, et al., *Nucl. Fusion* 49, 065020 (2009).
339. P.M. Ryan, J.R. Wilson, D.W. Swain, Fusion Engineering and Design 56, 569 (2001).
340. G. Taylor, R. E. Bell, J. C. Hosea, B. P. LeBlanc, et al., *Phys. Plasmas* **17**, 056114 (2010).
341. B.P. LeBlanc, R.E. Bell1, S.M. Kaye1, D. Stutman, et al., Nucl. Fusion 44, 513 (2004).
342. M. Bitter, K.W. Hill, A.L. Roquemore, et al., 1999 *Rev. Sci. Instrum.* **70** 292 (1999).
343. P. Ryan, et al., in Proceedings of the 19th IAEA Fusion Energy Conference, Lyon, 2002, edited by M. Spak, IAEA, Vienna, 2003, Paper No. EX/P2-13.
344. R. Wilson, R. E. Bell, S. Bernabei, M. Bitter,et al., *Phys. Plasmas* **10** 1733(2003).
345. C.K. Phillips, R. E. Bell, L.A. Berry, et al., *Nucl. Fusion* **49,** 075015 (2009).
346. G. Taylor, J.C. Hosea, C.E. Kessel, et al., *Phys. Plasmas* **19**, 042501 (2012).
347. N. Bertelli, E.F. Jaeger, L. Berry, et al., "Fast wave heating in the NSTX-Upgrade device" to be published in *Proceedings of the 20th Topical Conference on Applications of Radio-Frequency Power to Plasmas* (AIP, New York, 2013).
348. A. L. Rosenberg, J. E. Menard, J. R. Wilson, et al., *Phys. Plasmas* **11**, 2441 (2004).
349. J. Hosea, E. R. Bell, B. P. LeBlanc, et al., *Phys. Plasmas* **15**, 056104 (2008).
350. R. J. Perkins, J.C. Hose, G.J. Kramer, et al., *Phys. Rev. Lett.* **109** 045001 (2012).
351. E.F. Jaeger, et al., *Phys. Plasmas* **15** 72513 (2008).
352. F. Skiff, M. Ono, and K.L. Wong, *Phys. Fluids* **27** 1051 (1984).
353. T. M. Biewer, R. E. Bell, S. J. Diem, et al., *Phys. Plasmas* **12**, 056108 (2005).
354. N.J. Fisch and A.H. Boozer, *Phys. Rev. Lett.* **45** 720 (1980).
355. G. Taylor, P.C. Efthimion, C.E. Kessel, et al., *Phys. Plasmas* **11,** 4733 (2004).
356. P. C. Efthimion, G. Taylor, B. Jones *et al.*, *Proceedings of the 19th IAEAFusion Energy Conference* (International Atomic Energy Agency, Vienna, 2002), paper IAEA-CN-94/EX/P2-12.
357. H.P. Lagua, *Plasma Phys. Controlled Fusion* **49**, R1 (2007).
358. A.K. Ram and A. Bers, *Nucl. Fusion* **43**, 1305 (2003).
359. B. Jones, P. C. Efthimion, G. Taylor et al., *Phys. Rev. Lett.* **90**, 165001-1 (2003).
360. G. Taylor, P.C. Efthimion, B.P. LeBlanc, et al**.,** *Phys. Plasmas* **12,** 052511(2005).
361. S. J. Diem, G. Taylor, J. B. Caughman, et al., *Phys. Rev. Lett.* **103**, 015002 (2009).
362. V. Shevchenko, R.G.L. Vann, S.J. Freethy, and B.K. Huang, *J. Instrum.* **7** P10016 (2012).
363. S.J. Freethy, B.K. Huang, V.F. Shevchenko, and R.G.L. Vann, *Plasma Phys. Controlled Fusion* **55**, 124010 (2013).
364. S. Shiraiwa, H. Hanada, M. Hasegawa, et al., *Phys. Rev. Lett.* **96**, 185003 (2006).
365. V. Shevchenko, G. Cunningham, A. Gurchenko, et al., *Fusion Sci. and Tech.* **52** 202 (2007).
366. C. E. Kessel, R. E. Bell, M. G. Bell, et al., *Phys. Plasmas* **13**, 056108 (2006).
367. S.P. Gerhardt, D.A. Gates, S.M. Kaye, et al., *Nucl. Fusion* **51** 073031 (2011).
368. S.A. Sabbagh, S.M. Kaye, J. Menard, et al., *Nucl. Fusion* **41** 1601 (2001).
369. J.R. Ferron, *et al., Nucl. Fusion* **38** 1055(1998).
370. D. A. Gates, J.R. Ferron, M. Bell, et al., *Nucl. Fusion* **46**, 17 (2006).
371. S.P. Gerhardt, D. Mastrovito, M.G. Bell, et al., *Fusion Sci. and Tech.* **61** 1 (2012).
372. C. Holland, L. Schmitz, T.L. Rhodes, et al., *Phys. Plasmas* **18**, 056113 (2011).
373. E. Kolemen, D. A. Gates, S. Gerhardt, et al., *Nucl. Fusion* **51**, 113024 (2011).
374. M. Turnyanskiy, D. L. Keeling, R.J. Akers, et al., *Nucl. Fusion* **49,** 065002 (2009).
375. S. P. Gerhardt, R. Andre, and J.E. Menard, *Nucl. Fusion* **52,** 083020 (2012).
376. D. Dobrott, D. B. Nelson, J.M. Greene et al., *Phys. Rev. Lett.* **39,** 943 (1977).
377. A.M.M. Todd, M.S. Chance, J.M. Greene, et al., *Phys. Rev. Lett.* **38**, 826 (1977).

378. A. Sykes, J.A. Wesson, S. J. Cox, *Phys. Rev. Lett.* **39,** 757 (1977).
379. D. L. Jassby, IAEA-TC-**145/9**, 119 (1977).
380. F. Troyon, R. Gruber, H. Saurenmann, et al., *Plasma Phys. Controlled Fusion* **26**, 209 (1984).
381. F. Najmabadi, et al, Physics of Plasmas **13**, 056123-1 (2006).
382. M. Yamada, R.A. Ellis, Jr., A. Janos, et al., *IAEA Fusion Energy Conference,* CN-59/C-4-3 (1988).
383. J. Sarff, A. Almagri, J. Anderson, et al., *Nucl. Fusion* **43** 1684 (2003).
384. P. Martin, *Fusion Sci. and Tech.* **59** 602 (2011).
385. M. Tuszewski, *Nucl. Fusion* **28**, 2033 (198

Tables:

	R_0 (m)	A_{min}	κ	I_p (MA)	B_T (T)	t_{TF} (s)	NBI (MW)	f_{NI}, f_{BS} (%) @1MA
NSTX	0.854	1.28	2.8	1	0.55	1	7	<70, <60
NSTX-U	0.934	1.5	2.8	2	1	6.5	14	≤100, ≤80

Table I. NSTX and NSTX U Parameters

	R_0 (m)	A_{min}	κ	I_p (MA)	I_{TF} (MA)	t_{TF} (s)	NBI (MW)	f_{NI}, f_{BS} (%)@1MA
MAST	0.85	1.32	2.5	1.5	2.0	1	3.8	<30, <30
MAST-U*	0.85	1.32	2.5	2	3.2	6.5	7.5	≤100, ≤40

Table II. MAST and the phase 1 MAST-U parameters.

Parameters	**FNSF-I**	**FNSF-II**	**FNSF-III**	**Pilot**	**ARIES-ST**
R_0 **(m)**	1.3	1.0	0.85	2.2	3.2
A	1.7	1.7	1.55	1.7	1.6
B_T**(T)**	2.9	3.0	2.5	2.4	2.1
I_p **(MA)**	6.7	7.5	6.5	18.0	29.0
κ	3.1	3.0	2.4	3.3	3.4
δ	0.5	0.5	0.4	0.5	0.64
q^*	4.1	3.5	2.3	3.0	2.9
q_{95}	10	7.3	6.6	7.3	9.0
β_N	3.3	4.6	3.5	5.3	7.4
β_T**(%)**	10.1	19.5	16.6	31	50
f_{BS}	0.45	0.8	0.4	0.86	0.96
H	≤ 1.25	1.2	1.3	1.34	1.47
N_G	0.4	0.8	0.59	0.70	0.6
P_{Fusion}**(MW)**	76	60	35	645	2980
W_L **(MWm^{-2})**	1	1	1	2.0	4.1

Table III. Device and plasma parameters of future ST facilities.

Figure Captions:

Fig. 1. MA-Class STs : (a) NSTX and (b) MAST devices. © EURATOM/CCFE.

Fig. 2. Medium to smaller ST facilities around the world.

Fig. 3. Experimentally achieved plasma beta values for STs ($R/a \leq 2.0$) and conventional tokamak ($R/a \geq 2.5$). The ITER and FNSF beta regimes are indicated.

Fig. 4. High β_N, low l_i operational space in NSTX. Red/cyan points indicate plasmas with/without n=1 active RWM control. Blue circles indicate stable long pulse plasmas with active RWM control; yellow indicates disruptions. Reprinted with permission from S. A. Sabbagh et al., *Nucl. Fusion* **53,** 104007 (2013). Copyright (2013) Institute of Physics.

Fig. 5. Solenoid-free ST start-up concepts. Pictures are initial open field line phase at the top and the final closed flux ST formation phase at the bottom. (a) RF heating and current drive start-up (LATE). Reprinted with permission from M. Uchida et al., *Phys. Rev. Lett.* 104, 065001 (2010). Copyright (2010) American Physical Society. (b) Helicity injection start-up (NSTX). Reprinted with permission from R. Raman, et al., *Phys. Rev. Lett.* **97**, 175002 (2006), Copyright (2006) American Physical Society. (c)Merging ST start-up (MAST). Reprinted with permission from A. Sykes et al., Nucl. Fusion **41**, 1423 (2001). Copyright (2001) Institute of Physics.

Fig. 6. Electron and ion thermal energy diffusivity profiles in NSTX H-mode plasmas. The ion neoclassical (NCLASS) value is shown. Reprinted with permission from Y. Ren.

Fig. 7. Energy confinement time vs. electron collisionality with and without lithium wall conditioning. Reprinted with permission from J.E. Menard et al., *Nucl. Fusion* **52**, 083015 (2012). Copyright (2012) Institute of Physics.

Fig. 8. Snow-flake divertor configuration (above) and measured divertor flux comparison with standard configuration. Reprinted with permission from A. Soukhanovskii1 et al., Nuclear Fusion **51** 012001 (2011). Copyright (2011) Institute of Physics.

Fig. 9. Energetic particle parameter space with normalize velocity and beta values. Reprinted with permission from E. D. Fredrickson.

Fig. 10. RWM stabilization at low rotation. (a) β_N evoluation, (b) rotation, (c) RWM/EF coil current, and (d) n=1 mode amplitude.
Reprinted with permission from S. A. Sabbagh et al., *Phys. Rev. Lett.* **97**, 045004 (2006). Copyright (2006) American Physical Society.

Fig. 11. (a) Schematic of NSTX device cross-section and (b) interior view.

Fig. 12. (a) Schematic of MAST device cross-section and (b) interior view. © EURATOM/CCFE.

Fig. 13. Globus-M Device areal view. Reprinted with permission from V.K. Gusev.

Fig. 14. Schematic of PEGASUS device. Reprinted with permission from R.J. Fonck.

Fig. 15. Schematic of LTX device.

Fig. 16. Schematic of HIT-II device. Reprinted with permission from T. R. Jarboe.

Fig. 17. Schematic of QUEST device. Reprinted with permission from K. Hanada.

Fig. 18. Inside view of the TST-2 device. Reprinted with permission from Y. Yakase.

Fig. 19. The LATE device cross section schematic. Reprinted with permission from T. Maekawa.

Fig. 20. Schematic of TS-3 device cross section. Reprinted with permission from Y. Ono.

Fig. 21. Schematic of UTST. Reprinted with permission from Y. Ono.

Fig. 22. Schematic of VEST device. Reprinted with permission from Y-S. Hwang.

Fig. 23. NSTX and NSTX-U center stack schematics and the TF coil cross sections.

Fig. 24. Top view of the NSTX-U with the 2nd tangential NBI.

Fig. 25. The MAST-U divertor configuration with conventional and Super-X configurations. © EURATOM/CCFE.

Fig. 26. The double beam box NBI configuration for off-axis current drive in MAST-U. © EURATOM/CCFE.

Fig. 27. Natural cross-sections of a spherical tokamak (R/a ~ 1.5) and a high-aspect-ratio tokamak without active shaping

Fig. 28. Copper based ST cross section with toroidal magnet and shielding gap Δ defined as gap between inner plasma edge and in-board TF magnet radius R_{TF}, where $B_T = B_{T(Max)}$.

Fig. 29. (a) Toroidal beta, (b) plasma elongation, and (c) normalized beta values versus aspect ratio for wall-stabilized fully self-sustained equilibria. Reprinted with permission from J. E. Menard, et al., PPPL-3779 (2003).

Fig. 30. (a) q (safety factor) profiles, (b) normalized pressure profiles, (c) normalized current density profiles, and (d) kink marginally-stable wall position divided by plasma minor radius for the A=1.6 and A=3.3 equilibria shown in Fig. 34. Reprinted with permission from J. E. Menard, et al., PPPL-3779 (2003).

Fig. 31. Plasma pressure dependence with the gap distance as a function of the device major radius R_0 for FNSF-like parameters;

Fig. 32. Operating points depicted by circles for ST DEMOs. I. ARIES-like copper TF reactor with B_{max} = 7T at operating point of R_0 = 3.2m. II. Super-conducting ST with shielding distance of Δ = 1 m and B_{max} = 12T at operating point of R_0 = 4.4 m.

Fig. 33. Three representative FNSF design studies. (a) Culham compact design with R_0 = 85cm. Reprinted with permission from G.M. Voss et al., *Fusion Engineering and Design* **83**, 1648 (2008). Copyright (2008) Elsevier. (b) ORNL medium size design with R_0 = 130 cm. Reprinted with permission from Y-K.M. Peng et al., *Fusion Sci. Technol.* **60,** 441 (2011). Copyright (2011) American Nuclear Society. (c) PPPL pilot design with R_0 = 220 cm. Reprinted with permission from J.E. Menard et al., *Nucl. Fusion* **51**, 103014 (2011). Copyright (2011) Institute of Physics.

Fig. 34. Culham design of center rod cross section at mid-plane. Reprinted with permission from G.M. Voss et al., *Fusion Engineering and Design* **83**, 1648 (2008). Copyright (2008) Elsevier

Fig. 35. ORNL vertical remote handling concept. Reprinted with permission from Y-K.M. Peng et al., *Fusion Sci. Technol.* **56,** 957 (2009). Copyright (2006) American Nuclear Society.

.

Fig. 36. PPPL ST pilot plant vertical maintenance scheme. Reprinted with permission from J.E. Menard et al., *Nucl. Fusion* **51**, 103014 (2011). Copyright (2011) Institute of Physics.

.

Fig. 37. 2D schematic of a ST-based fusion-fission hybrid with super-x divertor. Reprinted with permission from M. Kotschenreuther et al., *Fusion Engineering and Design* **84**, 83 (2009). Copyright (2009) Elsevier

Fig. 38. Vertical maintenance scheme of ARIES-ST power core. Reprinted with permission from F. Najmabadi et al., *Fusion Engineering and Design* **65**, 143 (2003). Copyright (2003) Elsevier.

Fig. 39. Schematic of JUST device with liquid lithium divertor. Reprinted with permission from Y. Nagayama et al., *IEEJ Trans. F&M* **132**, 555(2012). Copyright (2012) IEEJ.

Fig. 40. Radial build of a compact superconducting coil ST reactor. Reprinted with permission from B.G. Hong, et al., *Nucl. Fusion* **51**, 113013 (2011). Copyright (2011) Institute of Physics.

Fig. 41. Reconstruction of a typical high $\kappa \sim 2.8$, high $\beta_p \sim 1.8$ equilibrium. Reprinted with permission from D.A. Gates et al., *Nucl. Fusion* **47**, 1376 (2007). Copyright (2007) Institute of Physics.

Fig. 42**.** Diagram of NSTX showing internal *B*r and *B*p sensors, passive stabilizing plates and ex-vessel 3-D control coils. Reprinted with permission from S. Sabbagh et al.

Fig. 43. NSTX RWM Structure. (a) DCON computer normal perturbed field for unstable RWM. (b) Theoretical computed poloidal variation of the n=1 RWM field at the plasma boundary as a function of poloidal angle. Reprinted with permission from S. A. Sabbagh et al., *Nucl. Fusion* **46**, 635 (2006). Copyright (2006) Institute of Physics.

Fig. 44. Observed kink/RWM stability versus local ω_w/ω_A, parametrized by local q value. Ω_{crit} is well defined by the Bondeson–Chu expression $\omega_A/(4q^2)$. Reprinted with permission from S. A. Sabbagh et al., *Nucl. Fusion* **46**, 635 (2006). Copyright (2006) Institute of Physics.

Fig. 45. Toroidal plasma rotation profiles for NSTX, showing a high rotation stable case, an intermediate rotation unstable case, and a low rotation stable case. Reprinted with permission from J. W. Berkery, et al., *Phys. Plasmas* **17** 082504 (2010). Copyright (2010) American Institute of Physics.

Fig. 46. MISK computed kinetic RWM n = 1 stability vs. plasma rotation at various levels of scaled collisionality. Reprinted with permission from J. W. Berkery, et al., *Phys. Rev. Letters* **106**, 075004 (2011). Copyright (2011) American Physical Society.

Fig. 47. Actively stabilized plasma equilibrium and rotation profiles. Shown are ω_w/ω_A vs. R for plasmas that are rotationally stabilized, at critical rotation profile, and actively stabilized below Ω_{crit}. Reprinted with permission from S. A. Sabbagh, et al., *Phys. Rev. Lett.* **97**, 045004 (2006). Copyright (2006) American Physical Society.

Fig. 48. Experimental β_N reached with $n = 1$ active control (shaded region) compared with theoretical feedback control performance using proportional gain and with an advanced state-space controller. Reprinted with permission from S. A. Sabbagh, et al., *Nucl. Fusion* **50**, 025020 (2010). Copyright (2010) Institute of Physics.

Fig. 49. Database plot of β_t vs. $I_p/(aB_{t0})$, showing that the data are bound by a line with slope β_N □ 6.0–6.5 in NSTX. Discharges are divided into experimental data in 2002 (red) vs earlier results (black). Reprinted with permission from J. E. Menard, et al., *Nuclear Fusion* **43**, 330 (2003). Copyright (2003) Institute of Physics.

Fig. 50. Comparison of measured $d(I\Omega_\phi)/dt$ profile to theoretical integrated NTV torque for an $n = 3$ applied field configuration. Reprinted with permission from W. Zhu, et al., *Phys. Rev. Letters* **96**, 225002 (2006). Copyright (2006) American Physical Society.

Figure 51. (a) Summary of locking threshold measurements in external currents versus density for NBI-heated high β cases (red circles) as well as ohmic plasma cases (black diamonds). (b) Revision of (a) using total resonant fields at the q = 2/1 surface utilizing IPEC. Reprinted with permission from J.-K.Park et al., Nuclar Fusion **52**, 023004 (2012). Copyright (2012) Institute of Physics.

Fig. 52. Disruptivity as a function of β_N and a) q^*, b) shape factor, c) pressure peaking, and d) l_i. Reprinted with permission from S.P. Gerhardt et al., *Nucl. Fusion* **53**, 043020 (2013). Copyright (2013) Institute of Physics.

Fig. 53. Histogram of warning times computed for 1700 disruption discharges. Reprinted with permission from S. P. Gerhardt.

Fig. 54. A 20 kA current ramp-up discharge in LATE. (a) plasma current and B_v; (b), (c), and (d) field lines and plasma images at the breakdown, initial closed field formation, and final low aspect ratio torus formation, respectively. Reprinted with permission from M. Uchida, et al., *Phys. Rev. Lett.* 104, 065001 (2010). Copyright (2010) American Physical Society.

Fig. 55. CHI schematic drawing of the NSTX including the location of the insulating gaps between the divertor plates. Reprinted with permission from R. Raman et al., *Phys. Rev. Lett.* **97**, 175002 (2006). Copyright (2006) American Physical Society.

Fig. 56. CHI only discharge in HIT-II: Injector current, CHI-produced plasma current, and radiated power signal from a wide-angle bolometer. Reprinted with permission from R. Raman et al., *Phys. Rev. Lett.* **90**, 0750005-1 (2003). Copyright (2003) American Physical Society.

Fig. 57. (a) Discharge evolution of 160 kA closed flux current produced by CHI alone in NSTX. Discharges in 2006 operated at higher toroidal field and injector flux. (b) Equilibrium reconstructions show the shape evolution of the CHI produced plasma in response to decaying current. EFIT analysis is possible when no injector current is present. Reprinted with permission from R. Raman et al., *Phys. Rev. Lett.* **97**, 175002 (2006). Copyright (2006) American Physical Society.

Fig. 58. Localized plasma gun start-up in PEGASUS (a) – (d) Time wave forms for plasma current, bias voltage and total injected current, current multiplication, and plasma major radius and inverse aspect ratio, respectively. (e) An experimental set up schematic of plasma gun start-up. Magnetic equilibrium reconstruction of poloidal flux surfaces at t = 28 ms. Reprinted with permission from D.J. Battaglia *PRL* **102**, 225003 (2009). Copyright (2009) American Physical Society.

Fig. 59. Direct induction (solid curves) and merging-compression dotted curves) schemes for MAST discharges. Reprinted with permission from A. Sykes et al., Nucl. Fusion **41**, 1423 (2001). Copyright (2001) Institute of Physics.

Fig. 60**.** Toroidal betas β_T of single low-beta STs (no merging) and high-beta STs produced by mergings as a function of I/aB_T in TS-3. Reprinted with permission from Y. Ono, et al., *Nucl. Fusion* **43**, 789 (2003). Copyright (2003) Institute of Physics.

Fig. 61. Illustration of wave number range for various microturbulence as labeled in NSTX parameter range. Reprinted with permission from S. M. Kaye.

Fig. 62. Local values of β_e and $\nu^{e/i}$ (r/a = 0.6 – 0.7) for various H-mode discharges. The colored regions illustrate where various microinstabilities are generally predicted to occur. Reprinted with permission from W. Guttenfelder, et al., *Nucl. Fusion* **53**, 093022 (2013) Copyright (2013) Institute of Physics.

Fig. 63. Total and thermal energy confinement times vs. (a) B_T at constant I_p, n_e, and P_L, and (b) I_p at constant B_T, n_e, and P_L . Reprinted with permission from S.M. Kaye et al., *Nucl. Fusion* **47** 499 (2007). Copyright (2007) Institute of Physics.

Fig. 64. (a) Normalized confinement time as a function of collisionality at mid-radius in NSTX. Blue points are from discharges that used HeGDC+B wall conditioning, while red points are from discharges that used Li. Reprinted with permission from S.M. Kaye et al., *Nucl. Fusion* **53** 063005 (2013). Copyright (2013). Institute of Physics. (b) Collisionality scan of thermal energy confinement time in MAST. Reprinted with permission from M. Valovic et al., *Nucl. Fusion* **51** 073045 (2011). Copyright (2011) Institute of Physics.

Fig. 65. Ion thermal diffusivity, χ_i normalized to the neoclassical ion thermal diffusivity as determined by NCLASS as a function of ν_e* at r/a =0.6. Values from both the collisionality (Nu) scan (blue) and Li scans (red) are shown. Reprinted with permission from S.M. Kaye et al., *Nucl. Fusion* **53** 063005 (2013). Copyright (2013). Institute of Physics.

Fig. 66. Temperature profiles (top) and spectral density of fluctuations (bottom) at 0.3 s (red) and 0.43 s (black). The blue stripe indicates the location of measurement where L_{Te} is 15 cm and 50 cm, respectively. Negative frequencies (bottom) correspond to Doppler shifted frequency spectrum due to wave propagation in the electron diamagnetic direction. Reprinted with permission from E. Mazzucato et al., *Nucl. Fusion* **49** 055001 (2009). Copyright (2009). Institute of Physics.

Fig. 67. Comparison between a case with an e-ITB and strongly negative magnetic shear (red) vs. a zero reversed shear case (blue). (a) Electron temperature profiles. (b) q-profiles. Shaded region indicates the high-k measurement region. (c) High-k microwave scattering fluctuation power spectra. Reprinted with permission from H.Y. Yuh et al., *Phys. Plasmas.* **16**, 056120 (2009). Copyright (2006) American Institute of Physics.

Fig. 68. Normalized electron thermal diffusivity vs. normalized electron collision frequency. The shaded square shows the experimental values with uncertainties. All calculations are based on an NSTX H-mode plasma using the GYRO code. Reprinted with permission from W. Guttenfelder, et al., *Phys. Plasmas* **19**, 056119 (2012). Copyright (2012) American Institute of Physics.

Fig. 69. (a) T_e profiles with P_{NBI} = 2, 4, and 6 MW NSTX H-modes. (b) TRANSP computed χ_e profiles in the same plasmas. Also shown are the χ_i and NCLASS ion thermal diffusivity for the 6 MW case and the measured neon diffusivity. Reprinted with permission from D. Stutman et al., *Phys. Rev. Lett.* **102**, 115002 (2009). Copyright (2009) American Physical Society.

Fig. 70. Experimentally inferred values of χ_i and χ_* compared with the neoclassical values computed by GTC-NEO for an NSTX H-mode plasma. Reprinted with permission from S.M. Kaye et al., *Nucl. Fusion* **49** 045010 (2009). Copyright (2009). Institute of Physics.

Fig. 71. (a) The resulting diffusion profile (b) and convection profile for the I_p = 1.1 MA, B_T = 0.55 T NSTX H-mode case. The shaded region represents the results from NCLASS neoclassical transport calculations. Reprinted with permission from D.J. Clayton, et al., *Plasma Phys. Controlled Fusion* **54**, 105022 (2012). Copyright (2012) Institute of Physics.

Fig. 72. Evolution of the thermal electron radial profile vs normalized poloidal flux: (a) density, (b) temperature, and (c) pressure. Reprinted with permission from R. J. Akers, et al., *Phys. Rev. Lett.* **88**, 035002 (2002). Copyright (2002) American Physical Society.

Fig. 73. Density-normalized loss power as a function of X-point radius for two different lithium evaporation rates. The solid symbols denote discharges that have transitioned into the H-mode at that loss power, while the open symbols denote those that remain in the L-mode. Reprinted with permission from S.M. Kaye et al., *Nucl. Fusion* **51,** 113019 (2011). Copyright (2011). Institute of Physics.

Fig. 74. High-speed video images of MAST plasmas with an ELM event, showing evidence of a filamentary structure. Reprinted with permission from A. Kirk et al., *Plasma Phys. Controlled Fusion* **47**, 315 (2005) . Copyright (2005) Institute of Physics.

Fig. 75. (a) The time evolution of the edge density profile for a single ELM. (b) The target D_α signal with the measurement times as indicated. Reprinted with permission from A. Kirk, et al., *Plasma Phys. Controlled Fusion* **47**, 315 (2005). Copyright (2005) Institute of Physics.

Fig. 76. Examples of different ELM types in NSTX: (*a*) large, Type I in DN configuration, (*b*) medium Type III in configurations close to DN, (*c*) small, Type V in

LSN configuration and (*d*) mixed Type I/Type V in LSN configuration. Reprinted with permission from R. Maingi.

Fig. 77. Schematic diagram of the peeling–ballooning stability limit for different shaped discharges as a function of edge current and pressure gradient. Reprinted with permission from P.B. Snyder et al., *Phys. Plasmas* **9**, 2037 (2002). Copyright (2002) American Institute of Physics.

Fig. 78. Peeling–ballooning stability diagram as calculated by the ELITE code for NSTX H-mode during the type-I ELMy phase. Reprinted with permission from A.C. Sontag et al., *Nucl. Fusion* **51**, 103022 (2011) . Copyright (2011). Institute of Physics.

Fig. 79. Stability diagram plots from ELITE showing edge current density versus normalized pressure gradient for Type I ELM in MAST. Reprinted with permission from A. Kirk, et al., *Plasma Phys. Controlled Fusion* **51**, 065016 (2009). Copyright (2009) Institute of Physics.

Fig. 80. The pedestal width (in ψ_n) scaling with $(\beta_q^{ped})^{1/2}$. This width scaling effectively provides a relation between the width and the height of the pedestal. The best fit for NSTX width is $(\beta_q^{ped})^{1.05}$. A theoretical model applied to NSTX data using BCP shows a $(\beta_q^{ped})^{0.8}$ scaling. Reprinted with permission from A. Diallo et al., *Nucl. Fusion* **53**, 093026 (2013). Copyright (2013). Institute of Physics.

Fig. 81. Temporal edge D-alpha signal for various lithium deposition rate. The regularly occurring spikes represents the Edge Localized Modes (ELMs). Reprinted with permission from D.K. Mansfield.

Fig. 82. Profiles for n_e and T_e for pre- and post lithium discharges (black and red lines, respectively). Reprinted with permission from R. Maingi.

Fig. 83. Stability boundary (blue to orange color transition) from ELITE code with fixed boundary kinetic EFITs for post-lithium discharge. Reprinted with permission from D.P. Boyle.

Fig. 84. Comparison of discharges with lithium conditioning only (black line) and with combined lithium and 3D field-induced ELMs (red and blue or gray lines): (a) stored energy, (b) n_e^{ave}, (c) P_{rad}, and (d)–(f) I_{RWM-5} and D_a emission. Reprinted with permission from J. M. Canik et al., *Phys. Rev. Lett.* **104**, 045001 (2010). Copyright (2010) American Physical Society.

Fig. 85. Visualization of the field line on the flux surface $y_N = 1.005$ in the NSTX standard divertor. Reprinted with permission from V.A. Soukhanovskii.

Fig. 86. Total power to the outboard and inboard targets (summing contributions from the upper and lower targets in each case) for an L-mode phase in MAST, with all strike points fully attached. More than 98% of power arriving at the targets is detected at the

outboard side. Reprinted with permission from G.F. Counsell et al., *Plasma Phys. Controlled Fusion* **44**, 827 (2002). Copyright (2002) Institute of Physics.

Fig. 87. Effect of f_{exp} as measured at the outer strike point in NSTX. (a) Reduction in $q_{div,\ peak}$ as f_{exp} is increased. (b) Broadening of the heat flux profile, l_q^{div} as f_{exp} is increased. Reprinted with permission from T.K. Gray et al., *J. Nucl. Materials* **415** S360 (2011). Copyright (2011) Elsevier.

Fig. 88. Heat flux profile during the SFD discharge as labeled. Reprinted with permission from V. A. Soukhanovskii et al., *Phys. Plasmas* **19**, 082504 (2012). Copyright (2012) American Institute of Physics.

Fig. 89. Super-x divertor configuration compared to the conventional divertor planned in MAST-U. © EURATOM/CCFE.

Fig. 90. Divertor surface temperature and corresponding heat flux as a function of Li evaporation for otherwise similar NBI heated H-mode discharges. Pre-discharge Li evaporation of 150 mg shown as blue solid lines and 300 mg as red dashed lines. Reprinted with permission from T.K. Gray, et al., *Nucl. Fusion* **54**, 023001 (2014). Copyright (2014) Institute of Physics.

Fig. 91. Measured heat flux profiles with and without the 3-D field application, as labeled, for the detached divertor plasma with lower gas puffing.
Reprinted with permission from J-W. Ahn et al., *Phys. Plasmas* **18** 056108 (2011). Copyright (2011) American Institute of Physics.

Fig. 92. Power fall-off length λ_q at the mid-plane versus the poloidal magnetic field at the outer mid-plane. Reprinted with permission from T. Eich et al., *Nucl. Fusion* **53**, 093031 (2013). Copyright (2013) Institute of Physics.

Figure 93. Full view camera images of edge filaments for (*a*) inter-ELM, (*b*) L-mode and (*c*) ELM periods within the same discharge (shot #15586), and (*d*) the intensity traces are superposed normalized to the peak ELM intensity showing the contrast in measured intensities across the three phases. Reprinted with permission from N. Ben Ayed et al., *Plasma Phys. Controlled Fusion* **51**, 035016 (2009). Copyright (2009) Institute of Physics.

Fig. 94. Typical GPI images of the light emission in the NSTX L-mode and H-mode. Also shown is the best estimate for the separatrix location (dashed line) and the shadow of the rf antenna/limiter location (dotted line.) Reprinted with permission from S.J. Zweben et al., *Phys. Plasmas* **17,** 102502 (2010). Copyright (2010) American Institute of Physics.

Fig. 95. (a) Actual NSTX, shot no. 112825 and (b) synthetic SOLT GPI intensity images. The magnetic separatrix is at r = 0 in the NSTX shot. Intensities are normalized by their

respective global maxima over the frame. Reprinted with permission from D.A. Russel et al., *Phys. Plasmas* **18**, 022306 (2011). Copyright (2011) American Institute of Physics.

Fig. 96. Liquid lithium divertor tray inside CDX-U vacuum vessel. One-foot (30.48 cm) ruler in foreground provides scale. Heat shield with titanium carbide coating protects center stack. White cables emerging from tray provide power to heaters.

Fig. 97. Interior of NSTX vacuum vessel. LLD appears as light-colored sections surrounding the center stack. Darker areas are graphite tiles constitute bulk of PFCs. RF antennas, ports for diagnostics, and neutral beam armor are main features in NSTX mid-plane.

Fig. 98. Selected entries from the LLD experimental database. Run day is the number of days since the beginning of the 2010 experimental campaign, Li Total is the integrated amount of lithium evaporated into the vessel, W_{MHD} is the plasma stored energy, τ_{MHD} is the energy confinement time, and H_{97L} is the H-factor compared to the ITER 97L global confinement scaling. The values of W_{MHD}, τ_{MHD}, and H_{97L} are averages taken between 400–600 ms. Reprinted with permission from M. Jaworski *et al.,* Nucl. Fusion **53**, 083032 (2013) . Copyright (2013) Institute of Physics.

Fig. 99. Examples of TAEs observed in NB heated discharges on MAST (*a*) long-lasting TAE mode with quasi-stationary frequency at the center of the TAE gap; (*b*) chirping-down modes; (*c*) chirping-up modes; (*d*) hole–clump mode with starting frequency at the TAE gap center. Reprinted with permission from M. Gryaznevich, et al., *Nucl. Fusion* **46** S942 (2006). Copyright (2006) Institute of Physics.

Fig. 100. Dependence on β of the maximum amplitude in a single burst of chirping modes, which start in the TAE-gap, in NBI discharges on MAST. Reprinted with permission from M.P. Gryaznevich and S.E. Sharapov, *Plasma Phys. Controlled Fusion* **46**, S15 (2004). Copyright (2004) Institute of Physics.

Fig. 101. Color Spectrogram of Mirnov coil from discharge at the threshold beta below which Alfvén cascades are seen. Frequency sweeping is largely absent. Reprinted with permission from E. D. Fredrickson, et al., *Phys. Plasmas* **14**, 102510 (2007) . Copyright (2007) American Institute of Physics.

Fig. 102. (*a*) Spectrogram of EP induced magnetic fluctuations in NSTX, (*b*) plasma current and neutral beam power evolution. Reprinted with permission from E. D. Fredrickson et al., *Nucl. Fusion* **53** 013006 (2013). Copyright (2013) Institute of Physics.

Fig. 103. (*a*) Magnetic pickup coil frequency spectrogram during a TAE avalanche on an expanded time scale, (*b*) neutron rate, and (*c*) total fast ion loss rate measured by the sFLIP detector. Reprinted with permission from D.S. Darrow et al., *Nucl. Fusion* **53** 013009 (2013). Copyright (2013) Institute of Physics.

Fig. 104. sFLIP detector camera frame at time of peak loss with interpretive grid defining the gyroradius centroid and pitch angle of the lost particles. Based upon the EFIT magnetic field at the detector location, 90 keV D ions should have a gyroradius of 17 cm. Reprinted with permission from D.S. Darrow et al., *Nucl. Fusion* **53** 013009 (2013). Copyright (2013) Institute of Physics.

Fig. 105. Color Measured evolution of the fast-ion profile in NSTX by FIDA. The decrease after t=280 ms, following a TAE avalanche, is detailed in the inset. Reprinted with permission from of M. Podestà et al., *Phys. Plasmas* **16,** 056104 (2009). Copyright (2009) American Institute of Physics.

Fig. 106. Simulated neutron rate drop due to TAE avalanche (red), neutron rate drop resulting from lost beam ions (blue) and neutron rate drop in confined beam ion population from energy loss (green). Reprinted with permission from E. D. Fredrickson et al., *Nucl. Fusion* **53** 013006 (2013). Copyright (2013) Institute of Physics.

Fig. 107. NSTX HHFW antenna array.

Fig. 108. (a) $T_e(R)$ immediately prior to HHFW heating t = 0.198 s (dashed line) and during 2.7 MW of $k_\varphi = -8$ m^{-1} heating t = 0.298 s (solid line) of a helium plasma. (b) $T_e(R)$ immediately prior to rf heating t = 0.148 s (dashed line) and during 3.1 MW of $k_\varphi = -8$ m^{-1} heating t =0.248 s (solid line) of a deuterium plasma. Reprinted with permission from of Taylor et al., *Phys. Plasmas* **17**, 056114 (2010) . Copyright (2010) American Institute of Physics.

Fig. 109. Central temperatures T_{i0} and T_{e0} as a function of time. Reprinted with permission from B.P. LeBlanc et al., Nucl. Fusion 44, 513 (2004). Copyright (2004) Institute of Physics.

Fig. 110. Time evolution of an I_p = 300 kA HHFW-generated H-mode plasma. (a) Line integrated density (n_eL), central electron temperature ($T_e(0)$ and total plasma stored energy (W_{tot}). (b) Outer gap between the last closed flux surface and the front of the HHFW antenna on the mid-plane and RF power. (c) The measured loop voltage. Reprinted with permission from of G. Taylor et al., *Phys. Plasmas* **19**, 042501 (2012). Copyright (2012) American Institute of Physics.

Fig. 111. (a) Electron stored energy evolution with modulated HHFW power of 2 MW with k_φ = 14 m^{-1} and -8m^{-1}, respectively. (b) Edge electron density (2 cm in front of Faraday shield) vs. time. The onset density for perpendicular propagation is indicated by the horizontal dashed lines for k_φ = 14 m^{-1} and -8m^{-1} as marked. Reprinted with permission from of J. Hosea et al., *Phys. Plasmas* **15**, 056104 (2008). Copyright (2008) American Institute of Physics.

Fig. 112. (a) The EBW coupling efficiency in H-mode with and without lithium in the scrape-off-layer. (b) The Thomsons scattering n_e profiles with and without lithium in the

scrape-off-layer for H-mode. Reprinted with permission S. J. Diem et al., *Phys. Rev. Lett.* **103**, 015002 (2009). Copyright (2009) American Physical Society.

Fig. 113. Plot of elongation versus aspect ratio for NSTX discharges. The black line encloses the historical NSTX operating space for discharges with flat-top duration exceeding 0.5 s, and specific high-performance discharges are indicated in blue. The points collected in the high aspect-ratio experiment are indicated in red. The approximate future device operating space is as labeled. Inset shows $\kappa = 3$ NSTX equilibrium. Reprinted with permission from S.P. Gerhardt et al., *Nucl. Fusion* **51** 033004 (2011). Copyright (2011) Institute of Physics.

Fig. 114. Flat-top average of global performance parameters plotted against the I_p flat-top duration. The colors represent different values of the shape parameter. The symbols are indicative of the year when the discharge was taken, as indicated in the legend. The quantities shown are (*a*) β_N and (*b*) $0.5\ \sqrt{\varepsilon}\beta_P$. Reprinted with permission from S.P. Gerhardt et al., *Nucl. Fusion* **51** 073031 (2011). Copyright (2011) Institute of Physics.

Fig. 115. The quantity $\varepsilon^{1/2}\beta_p\beta_t$ averaged over the plasma current flattop is plotted against $1+\kappa^2$, also averaged over the current flattop. The straight line in the figure is meant to guide the eye. Reprinted with permission from D. A. Gates.

Fig. 116. (a) TRANSP simulated distribution of the total plasma current, I_p, between Ohmic, bootstrap and neutral beam driven components for $D_b = 0.5\text{m}^2\ \text{s}^{-1}$. (b) Experimentally observed neutron yield is compared with TRANSP simulations for $D_b = 0$ and $0.5\text{m}^2\ \text{s}^{-1}$. Reprinted with permission from M. Turnyanskiy et al., *Nucl. Fusion* **49,** 065002 (2009). Copyright (2009) Institute of Physics.

Fig. 117. (a) Measured (blue line) and calculated neutron rates (x 0.9) and (b) comparison of reconstructed (gray) and calculated (black) total parallel current density profile for t = 1.2–1.35 s for the best-fit fast-ion diffusivity model. NBICD profiles for the diffusivities of (a) are also shown. Reprinted with permission J. E. Menard et al., *Phys. Rev. Lett.* **97**, 095002 (2006). Copyright (2006) American Physical Society.

Fig. 118. A high-β_P (0.7MA and 0.48 T) scenario NSTX discharge with lower-l_i and higher pressure peaking. (a) The plasma current, internal inductance and central safety factor as labeled. (b) The normalized β, pressure peaking factor and no- and with-wall stability limits. Reprinted with permission from of S.P. Gerhardt, et al., *Nucl. Fusion* **51** 073031 (2011) . Copyright (2011) Institute of Physics

Fig. 119. (a) Dependence of the confinement time, pressure-driven current fraction, beam current drive fraction, total non-inductive fraction and β_N on the temperature multiplier in the TRANSP simulations, and (*b*) profiles for the base configuration (solid) and fully non-inductive configuration (dashed). Reprinted with permission from of S.P. Gerhardt, et al., *Nucl. Fusion* **51** 073031 (2011) . Copyright (2011) Institute of Physics.

Fig. 120. Basic characteristic of a simple circuler tokamak

Fig. 121. Elevation view of illustration design for SMARTOR (Small-Aspect-Ratio Torus). EF coil positions are schematic only. B_{TF} = 11 T at R = 0.9m. Reprinted with permission from D.L. Jassby.

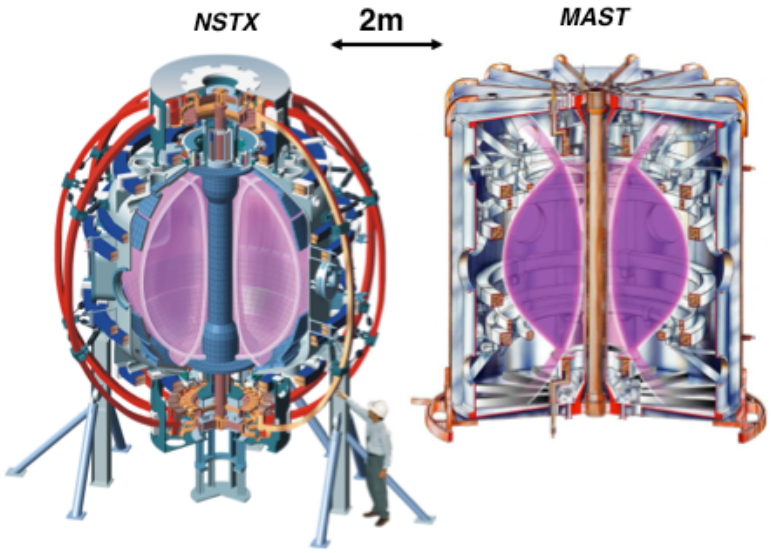

Fig. 1. MA-Class STs : (a) NSTX and (b) MAST devices. © EURATOM/CCFE.

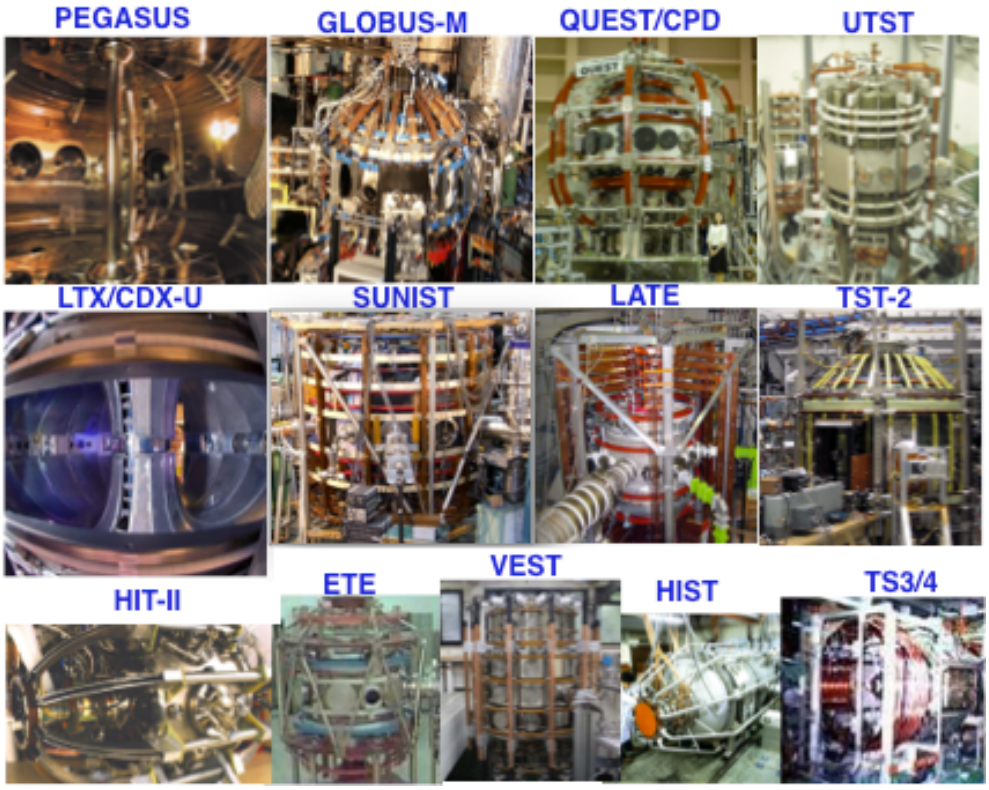

Fig. 2. Medium to smaller ST facilities around the world.

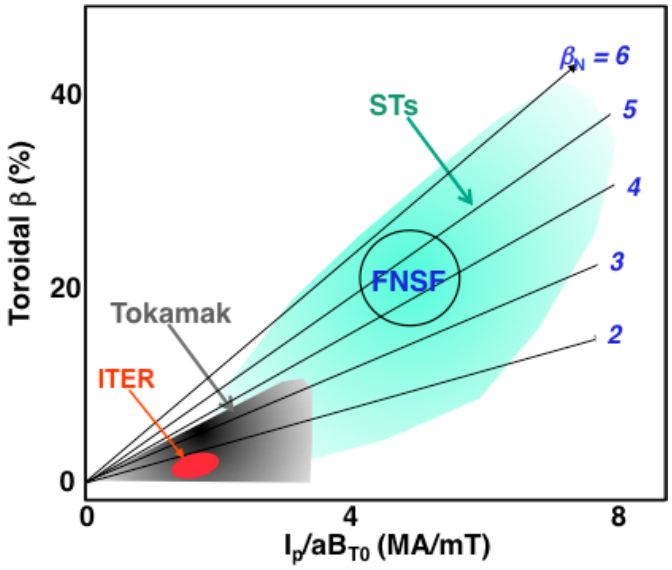

Fig. 3. Experimentally achieved plasma beta values for STs (R/a ≤ 2.0) and conventional tokamak (R/a ≥ 2.5). The ITER and FNSF beta regimes are indicated.

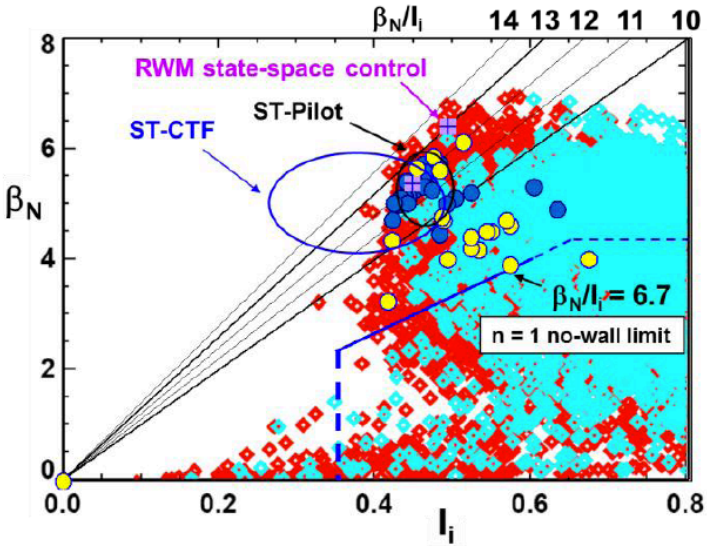

Fig. 4. High β_N, low l_i operational space in NSTX. Red/ cyan points indicate plasmas with/without n=1 active RWM control. Blue circles indicate stable long pulse plasmas with active RWM control; yellow indicates disruptions. Reprinted with permission from S. A. Sabbagh et al., *Nucl. Fusion* **53,** 104007 (2013). Copyright (2013) Institute of Physics.

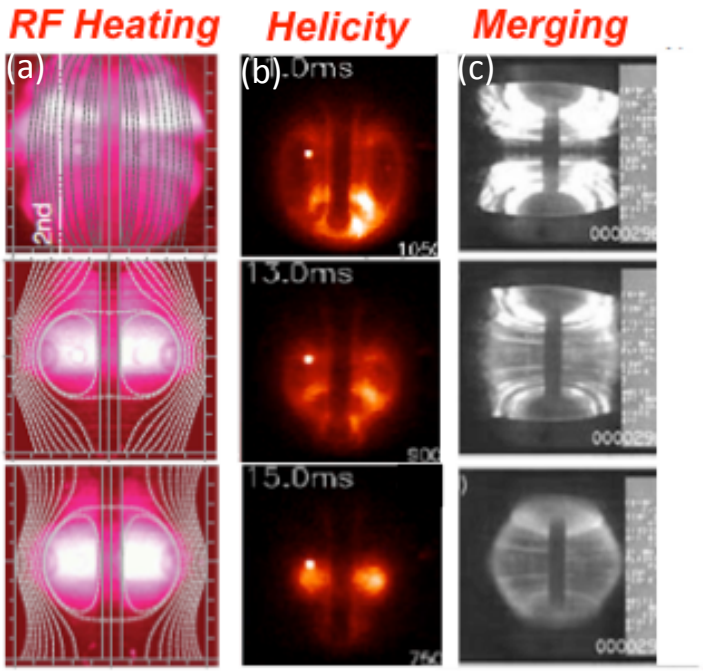

Fig. 5. Solenoid-free ST start-up concepts. Pictures are initial open field line phase at the top and the final closed flux ST formation phase at the bottom. (a) RF heating and current drive start-up (LATE). Reprinted with permission from M. Uchida et al., *Phys. Rev. Lett.* 104, 065001 (2010). Copyright (2010) American Physical Society. (b) Helicity injection start-up (NSTX). Reprinted with permission from R. Raman, et al., *Phys. Rev. Lett.* **97**, 175002 (2006), Copyright (2006) American Physical Society. (c)Merging ST start-up (MAST). Reprinted with permission from A. Sykes et al., Nucl. Fusion **41**, 1423 (2001). Copyright (2001) Institute of Physics.

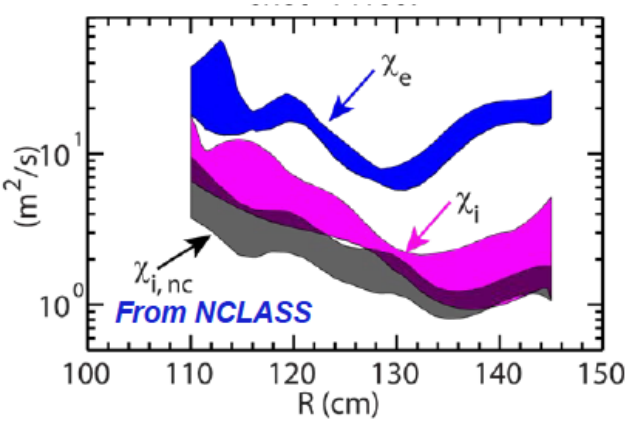

Fig. 6. Electron and ion thermal energy diffusivity profiles in NSTX H-mode plasmas. The ion neoclassical (NCLASS) value is shown. Reprinted with permission from Y. Ren.

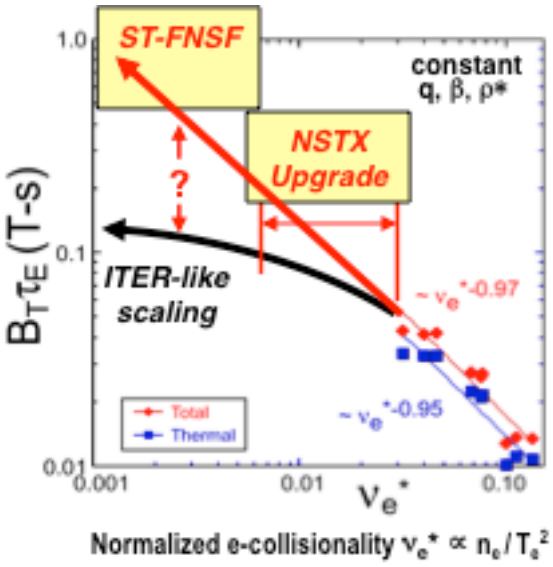

Fig. 7. Energy confinement time vs. electron collisionality with and without lithium wall conditioning. Reprinted with permission from J.E. Menard et al., *Nucl. Fusion* **52**, 083015 (2012). Copyright (2012) Institute of Physics.

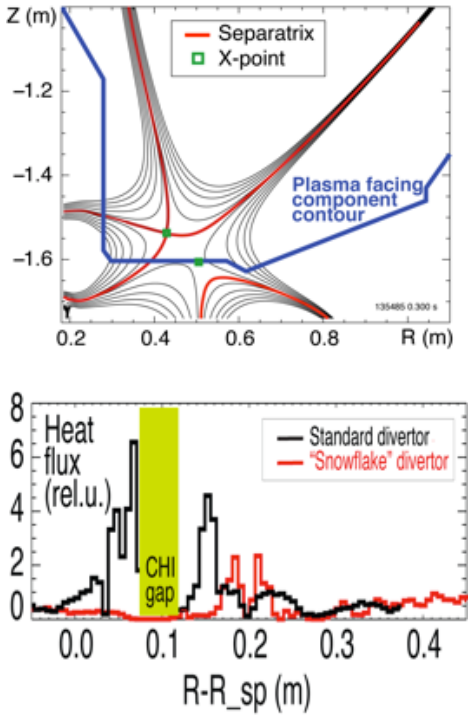

Fig. 8. Snow-flake divertor configuration (above) and measured divertor flux comparison with standard configuration. Reprinted with permission from A. Soukhanovskii1 et al., Nuclear Fusion **51** 012001 (2011). Copyright (2011) Institute of Physics.

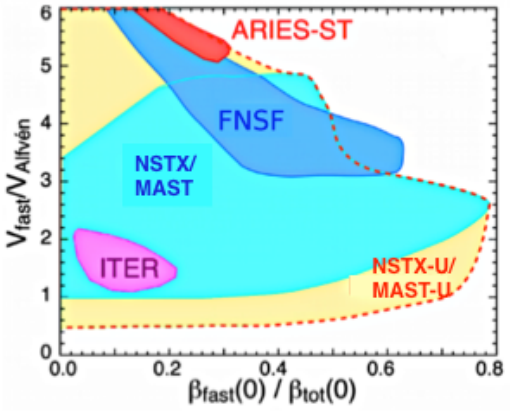

Fig. 9. Energetic particle parameter space with normalize velocity and beta values. Reprinted with permission from E. D. Fredrickson.

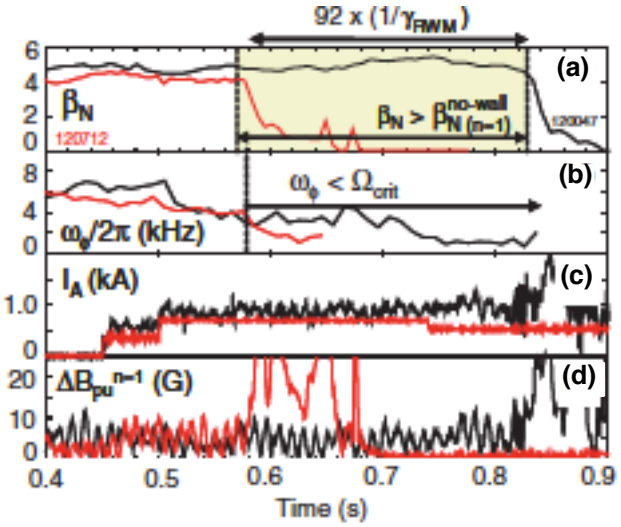

Fig. 10. RWM stabilization at low rotation. (a) β_N evoluation, (b) rotation, (c) RWM/EF coil current, and (d) n=1 mode amplitude. Reprinted with permission from S. A. Sabbagh et al., *Phys. Rev. Lett.* **97**, 045004 (2006). Copyright (2006) American Physical Society.

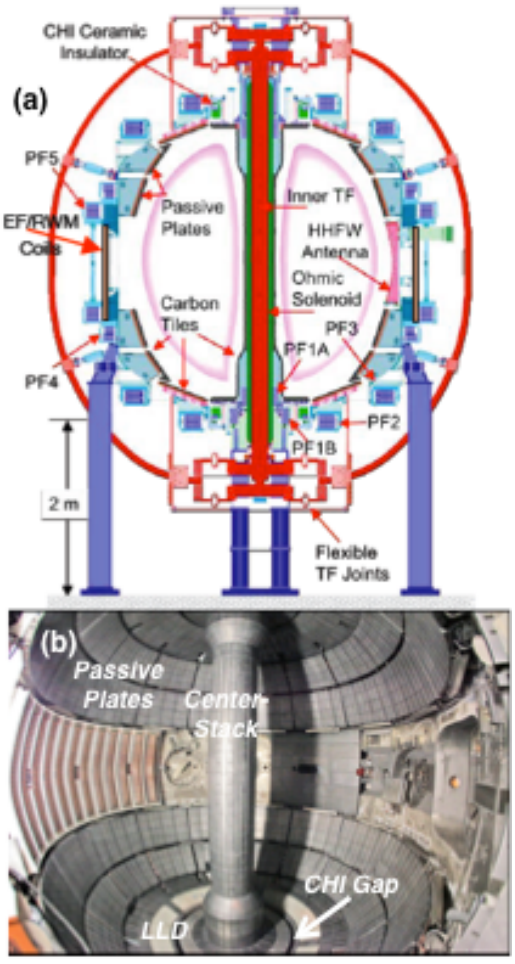

Fig. 11. (a) Schematic of NSTX device cross-section and (b) interior view.

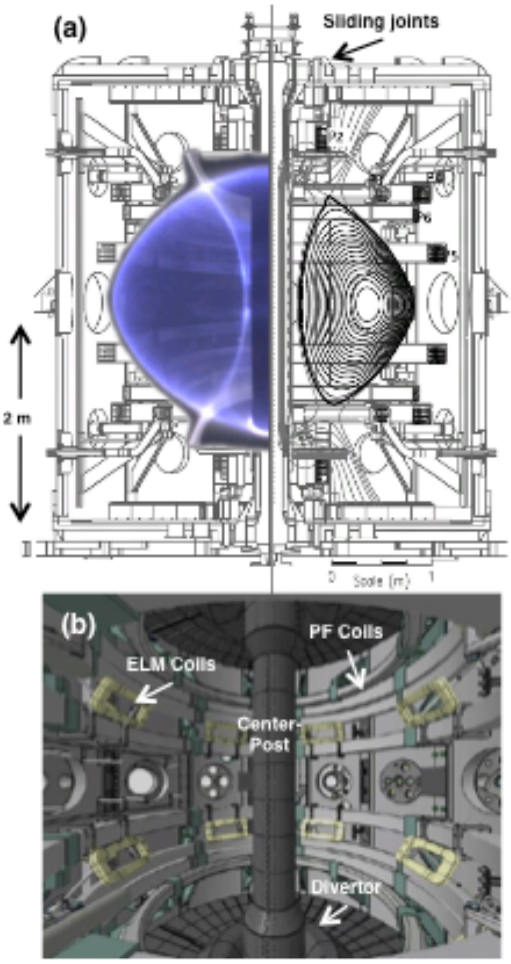

Fig. 12. (a) Schematic of MAST device cross-section and (b) interior view. © EURATOM/CCFE.

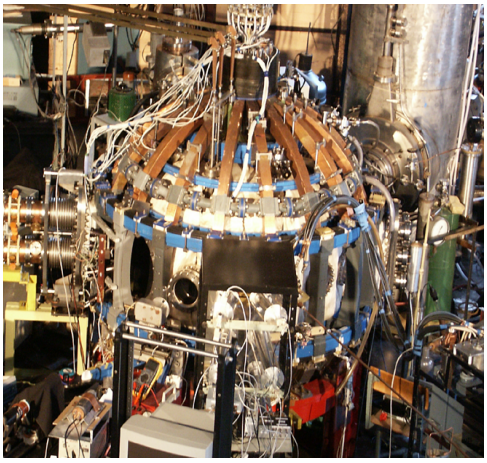

Fig. 13. Globus-M Device areal view. Reprinted with permission from V.K. Gusev.

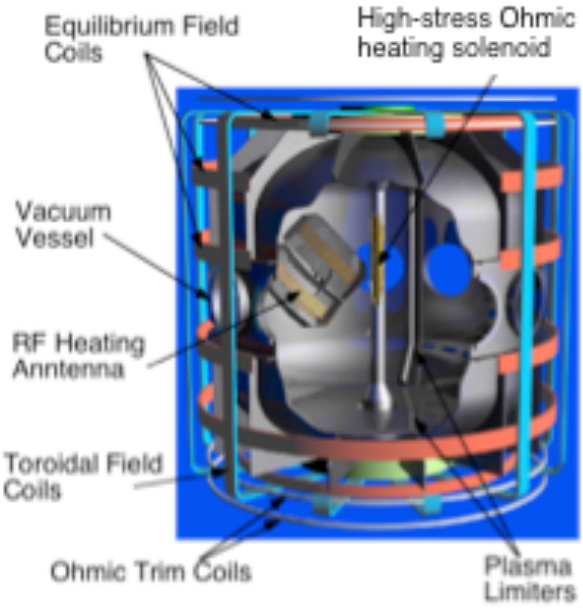

Fig. 14. Schematic of PEGASUS device. Reprinted with permission from R.J. Fonck.

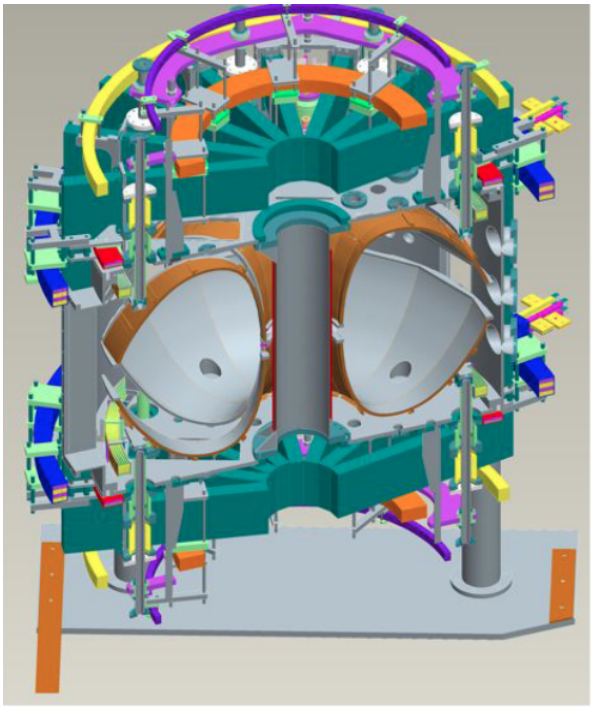

Fig. 15. Schematic of LTX device.

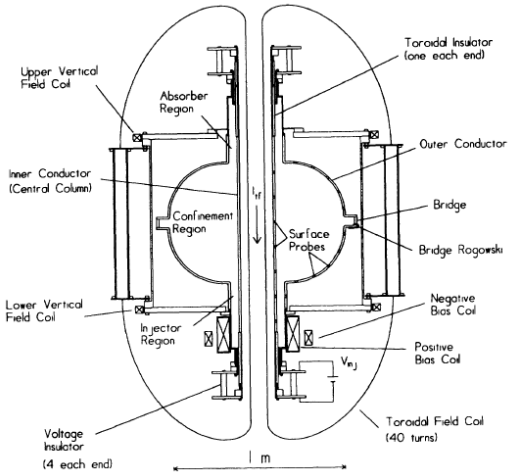

Fig. 16. Schematic of HIT-II device. Reprinted with permission from T. R. Jarboe.

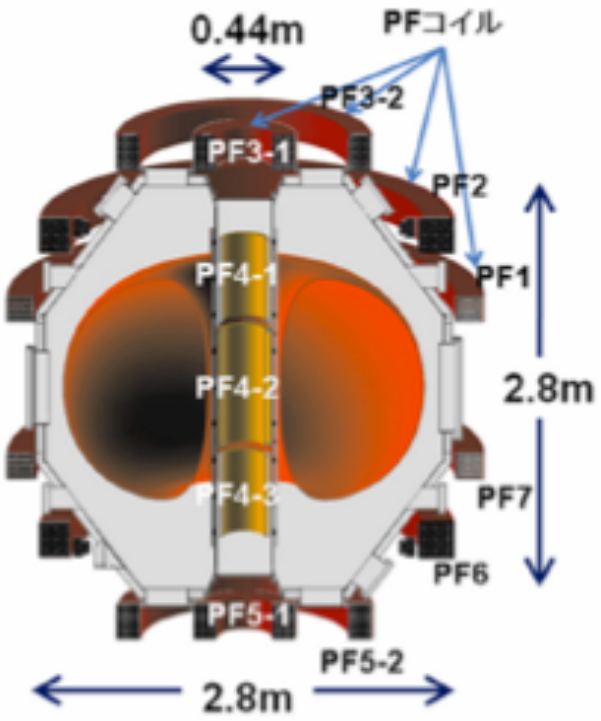

Fig. 17. Schematic of QUEST device. Reprinted with permission from K. Hanada.

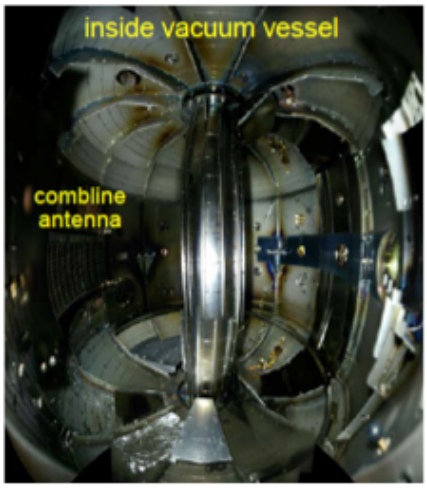

Fig. 18. Inside view of the TST-2 device. Reprinted with permission from Y. Yakase.

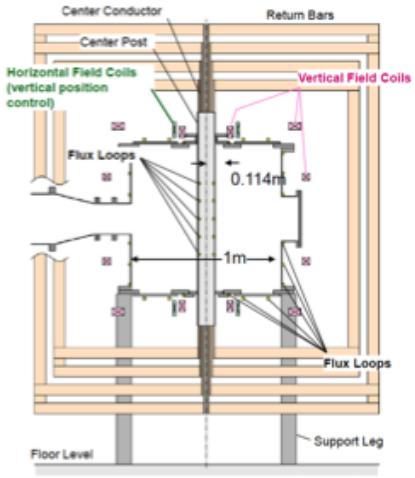

Fig. 19. The LATE device cross section schematic. Reprinted with permission from T. Maekawa.

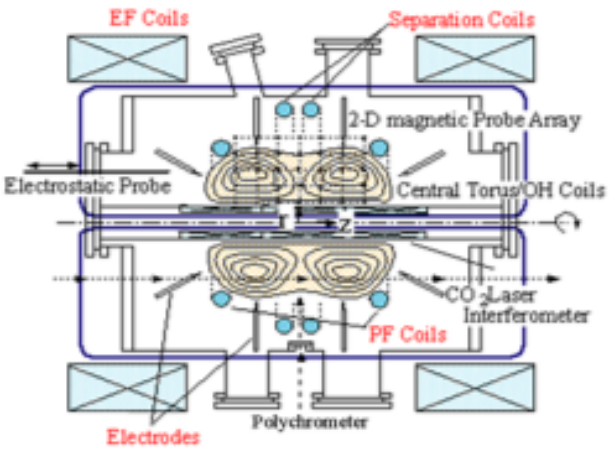

Fig. 20. Schematic of TS-3 device cross section. Reprinted with permission from Y. Ono.

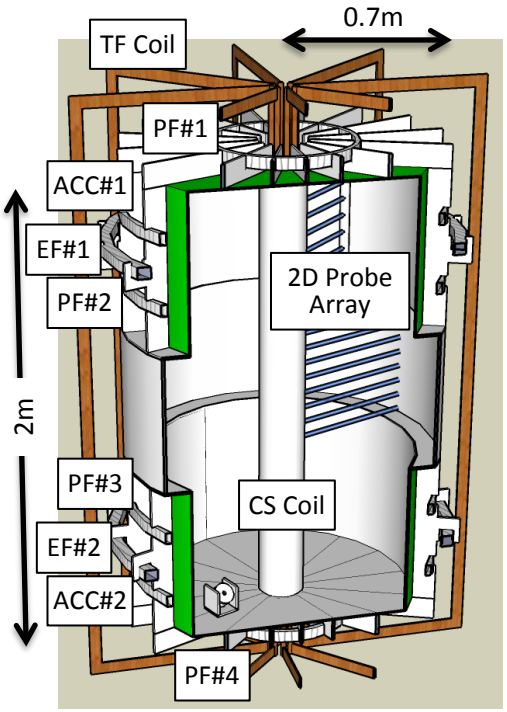

Fig. 21. Schematic of UTST. Reprinted with permission from Y. Ono.

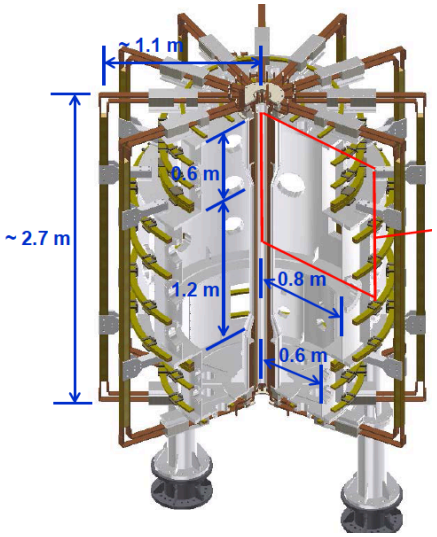

Fig. 22. Schematic of VEST device. Reprinted with permission from Y-S. Hwang.

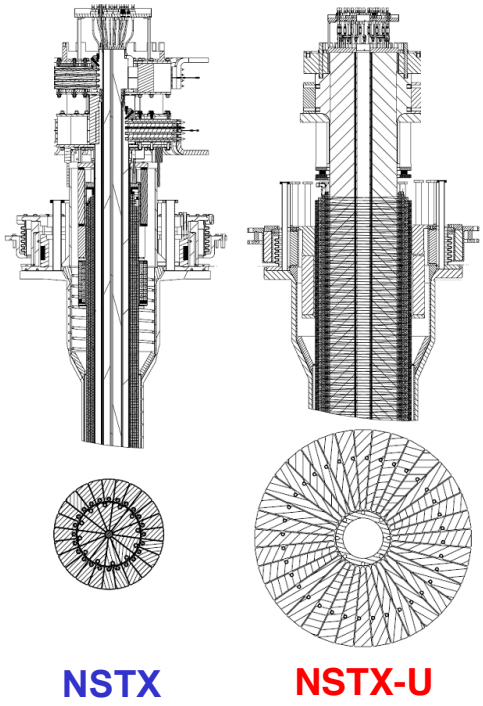

Fig. 23. NSTX and NSTX-U center stack schematics and the TF coil cross sections.

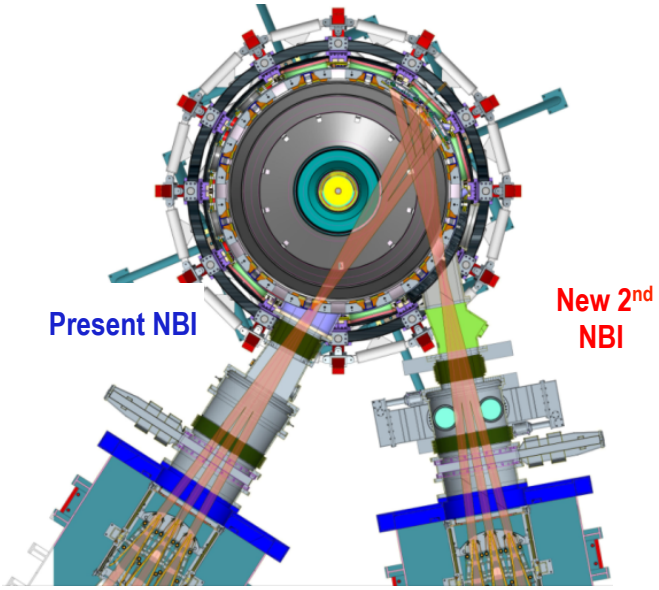

Fig. 24. Top view of the NSTX-U with the 2nd tangential NBI.

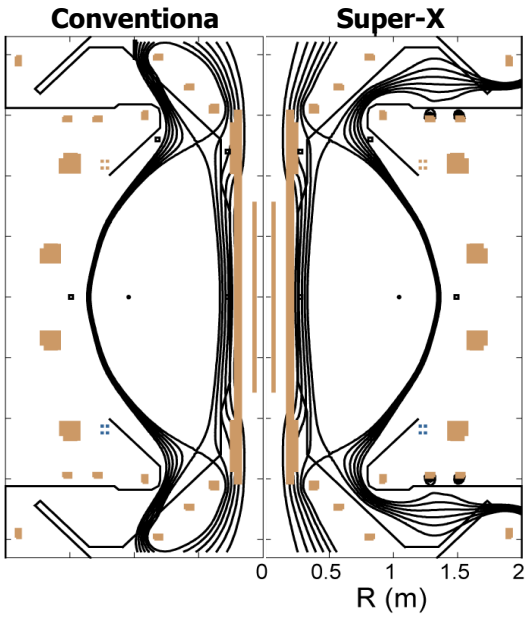

Fig. 25. The MAST-U divertor configuration with conventional and Super-X configurations. © EURATOM/ CCFE.

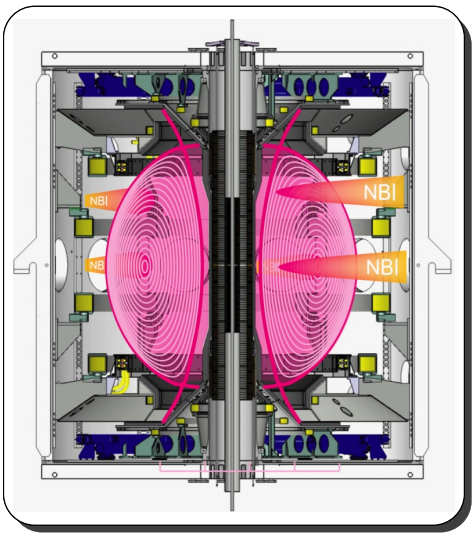

Fig. 26. The double beam box NBI configuration for off-axis current drive in MAST-U. © EURATOM/ CCFE

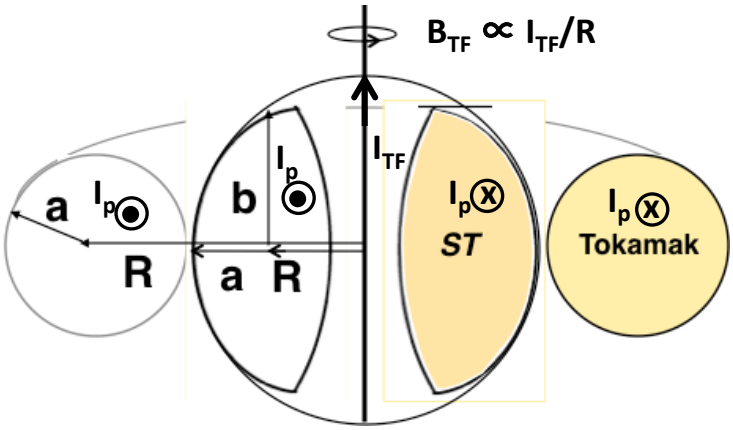

Fig. 27. Natural cross-sections of a basic spherical tokamak (R/a = 1.5) and a conventional high aspect ratio tokamak without active shaping

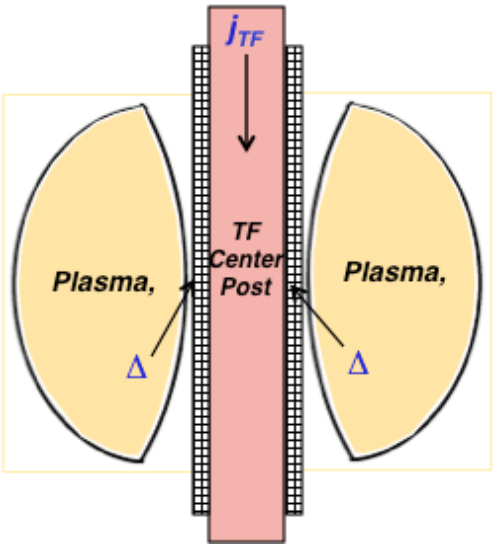

Fig. 28. Copper based ST cross section with toroidal magnet and shielding gap Δ defined as gap between inner plasma edge and in-board TF magnet radius R_{TF}, where $B_T = B_T(Max)$.

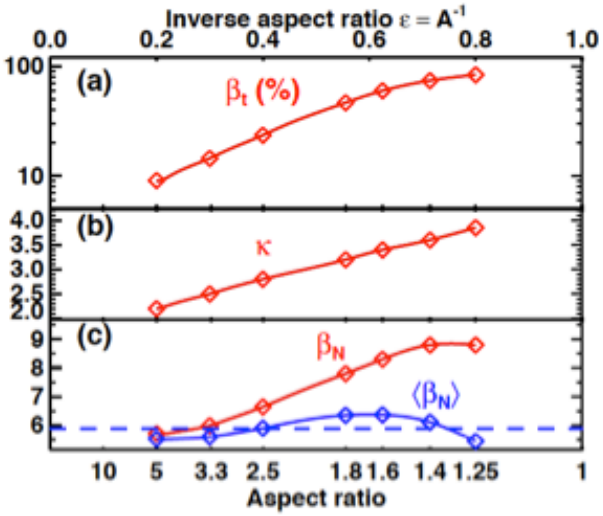

Fig. 29. (a) Toroidal beta, (b) plasma elongation, and (c) normalized beta values versus aspect ratio for wall-stabilized fully self-sustained equilibria. Reprinted with permission from J. E. Menard, et al., PPPL-3779 (2003).

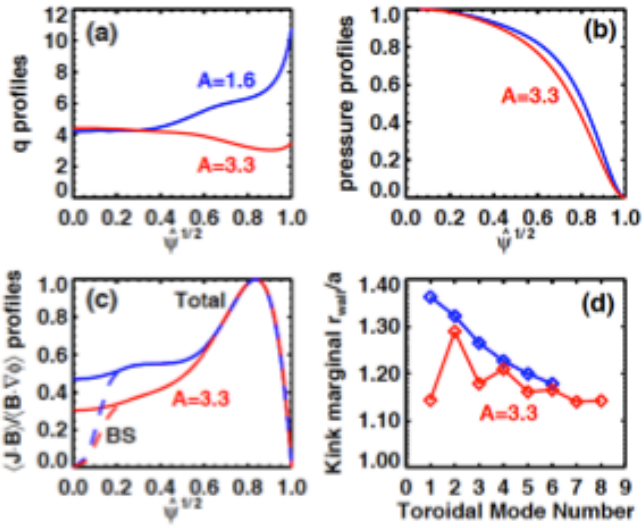

Fig. 30. (a) q (safety factor) profiles, (b) normalized pressure profiles, (c) normalized current density profiles, and (d) kink marginally-stable wall position divided by plasma minor radius for the A=1.6 and A=3.3 equilibria shown in Fig. 34. Reprinted with permission from J. E. Menard, et al., PPPL-3779 (2003).

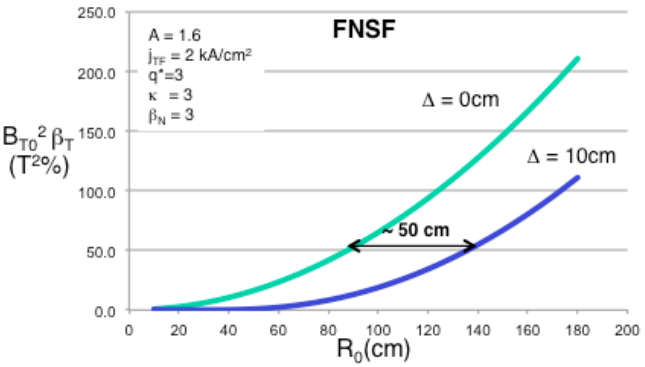

Fig. 31. Plasma pressure dependence with the gap distance as a function of the device major radius R_0 for FNSF-like parameters;

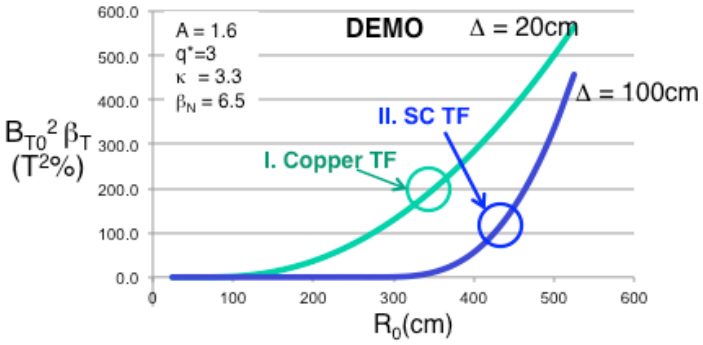

Fig. 32. Operating points depicted by circles for ST DEMOs. I. ARIES-like copper TF reactor with B_{max} = 7T at operating point of R_0 = 3.2m. II. Super-conducting ST with shielding distance of Δ = 1 m and B_{max} = 12T at operating point of R_0 = 4.4 m.

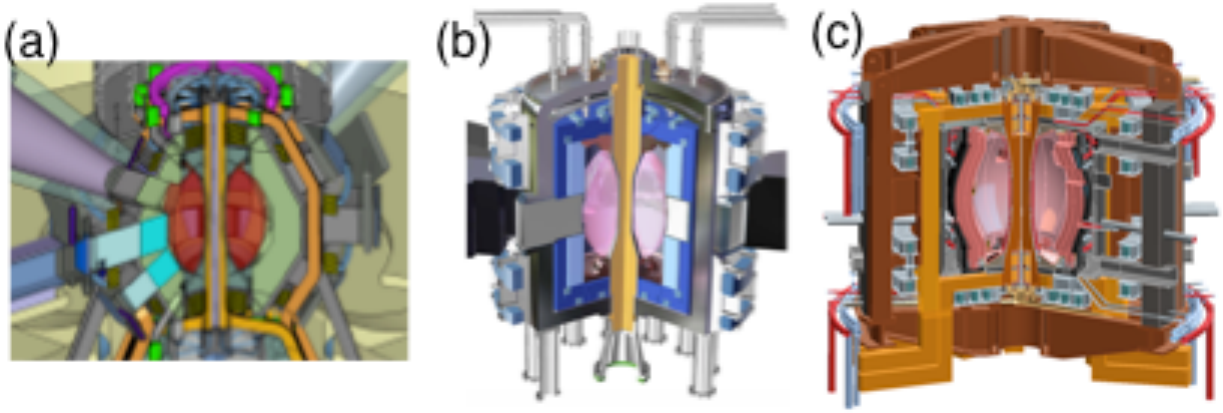

Fig. 33. Three representative FNSF design studies. (a) Culham compact design with R_0 = 85cm. Reprinted with permission from G.M. Voss et al., *Fusion Engineering and Design* **83**, 1648 (2008). Copyright (2008) Elsevier. (b) ORNL medium size design with R_0 = 130 cm. Reprinted with permission from Y-K.M. Peng et al., *Fusion Sci. Technol.* **60,** 441 (2011). Copyright (2011) American Nuclear Society. (c) PPPL pilot design with R_0 = 220 cm. Reprinted with permission from J.E. Menard et al., *Nucl. Fusion* **51**, 103014 (2011). Copyright (2011) Institute of Physics.

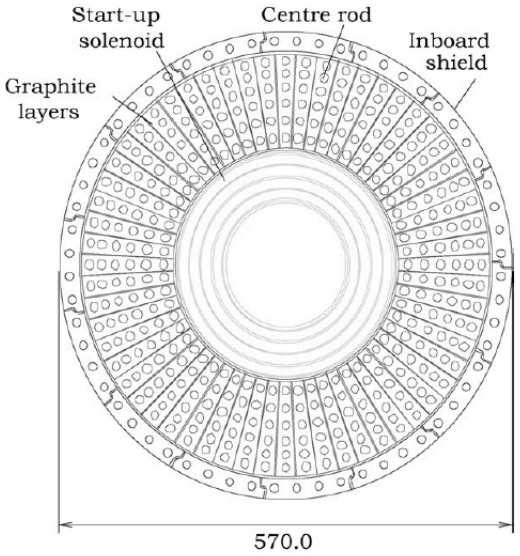

Fig. 34. Culham design of center rod cross section at mid-plane. Reprinted with permission from G.M. Voss et al., *Fusion Engineering and Design* **83**, 1648 (2008). Copyright (2008) Elsevier

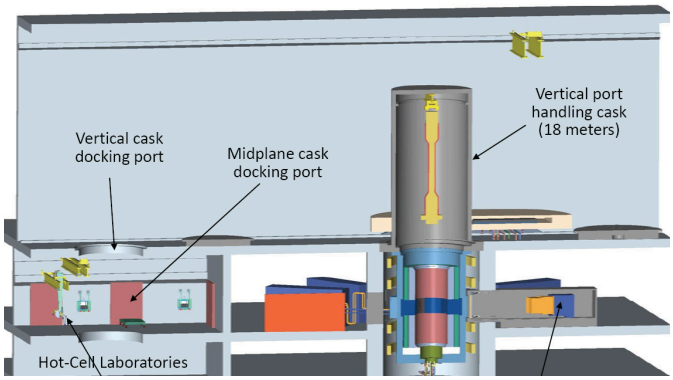

Fig. 35. ORNL vertical remote handling concept. Reprinted with permission from Y-K.M. Peng et al., *Fusion Sci. Technol.* **56,** 957 (2009). Copyright (2006) American Nuclear Society.

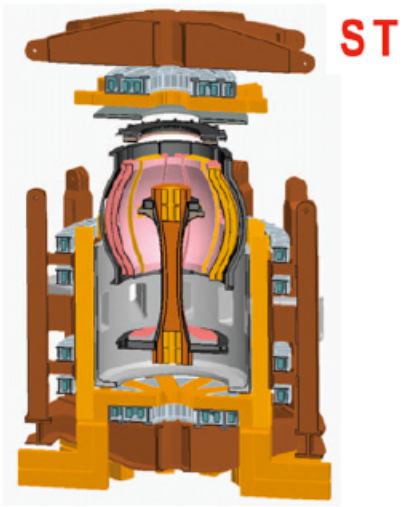

Fig. 36. PPPL ST pilot plant vertical maintenance scheme. Reprinted with permission from J.E. Menard et al., *Nucl. Fusion* **51**, 103014 (2011). Copyright (2011) Institute of Physics.

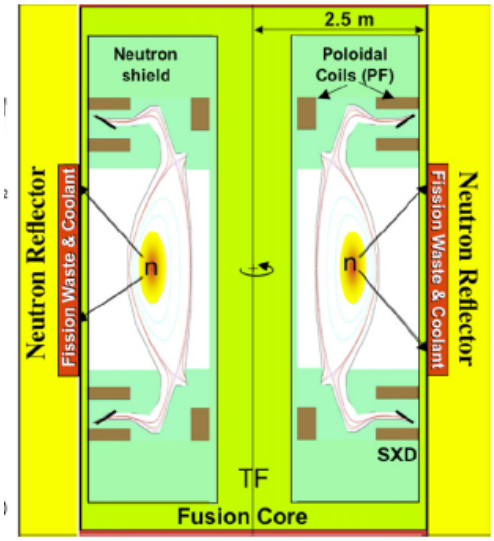

Fig. 37. 2D schematic of a ST-based fusion-fission hybrid with super-x divertor. Reprinted with permission from M. Kotschenreuther et al., *Fusion Engineering and Design* **84**, 83 (2009). Copyright (2009) Elsevier

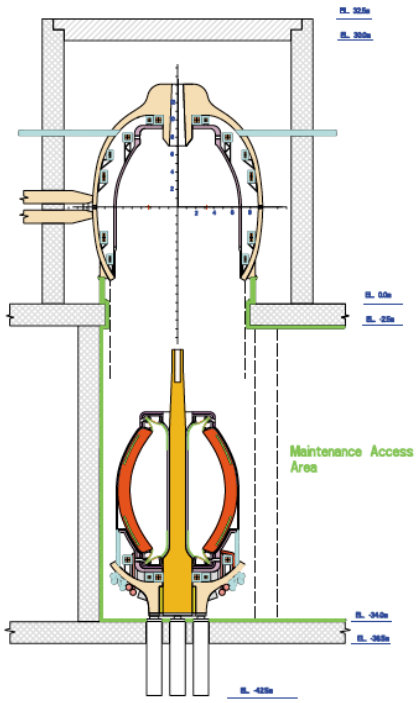

Fig. 38. Vertical maintenance scheme of ARIES-ST power core. Reprinted with permission from F. Najmabadi et al., *Fusion Engineering and Design* **65**, 143 (2003). Copyright (2003) Elsevier.

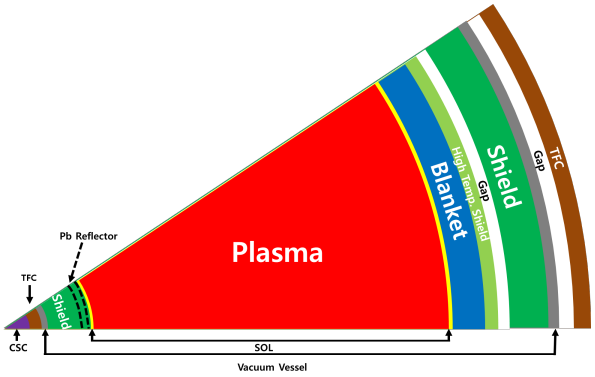

Fig. 40. Radial build of a compact superconducting coil ST reactor. Reprinted with permission from B.G. Hong, et al., *Nucl. Fusion* **51**, 113013 (2011). Copyright (2011) Institute of Physics.

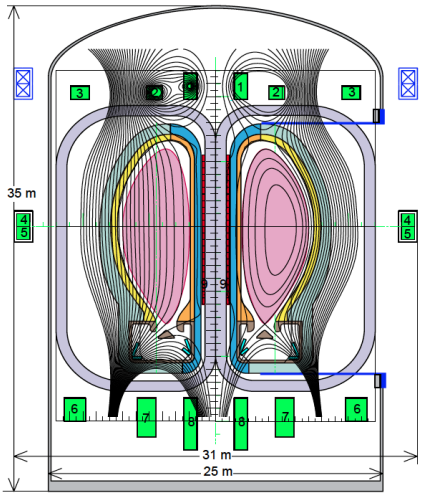

Fig. 39. Schematic of JUST device with liquid lithium divertor. Reprinted with permission from Y. Nagayama et al., *IEEJ Trans. F&M* **132**, 555(2012). Copyright (2012) IEEJ.

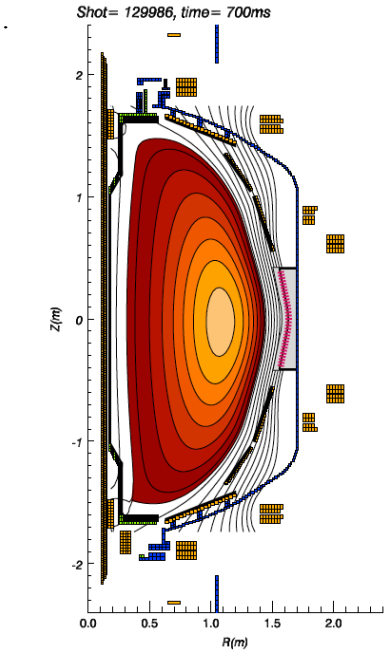

Figure 41. Reconstruction of a typical high $\kappa \sim 2.8$, high $\beta_p \sim 1.8$ equilibrium. Reprinted with permission from D.A. Gates et al., *Nucl. Fusion* **47**, 1376 (2007). Copyright (2007) Institute of Physics.

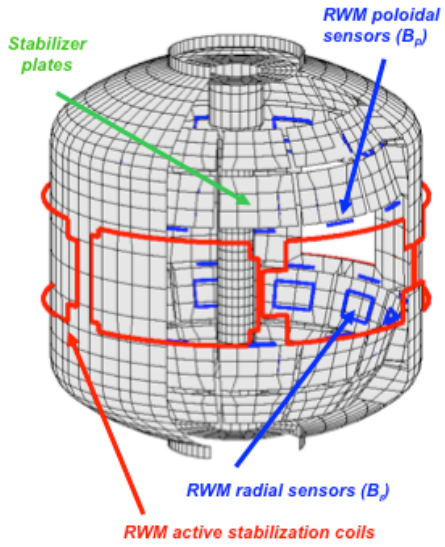

Fig. 42**.** Diagram of NSTX showing internal *B*r and *B*p sensors, passive stabilizing plates and ex-vessel 3-D control coils. Reprinted with permission from S. Sabbagh et al.

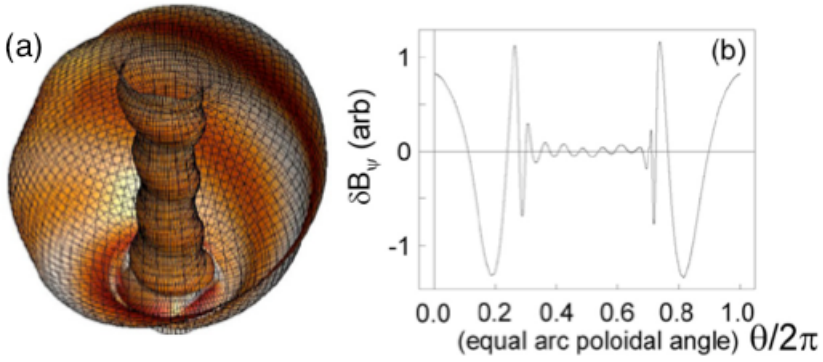

Fig. 43. NSTX RWM Structure. (a) DCON computer normal perturbed field for unstable RWM. (b) Theoretical computed poloidal variation of the n=1 RWM field at the plasma boundary as a function of poloidal angle. Reprinted with permission from S. A. Sabbagh et al., *Nucl. Fusion* **46**, 635 (2006). Copyright (2006) Institute of Physics.

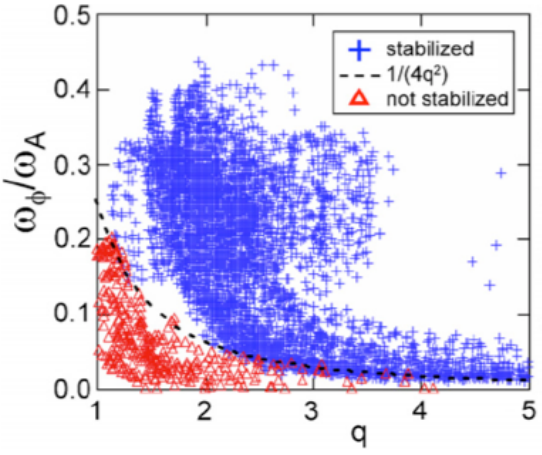

Fig. 44. Observed kink/RWM stability versus local ω_ϕ/ω_A, parametrized by local q value. Ω_{crit} is well defined by the Bondeson–Chu expression $\omega_A/(4q^2)$. Reprinted with permission from S. A. Sabbagh et al., *Nucl. Fusion* **46**, 635 (2006). Copyright (2006) Institute of Physics.

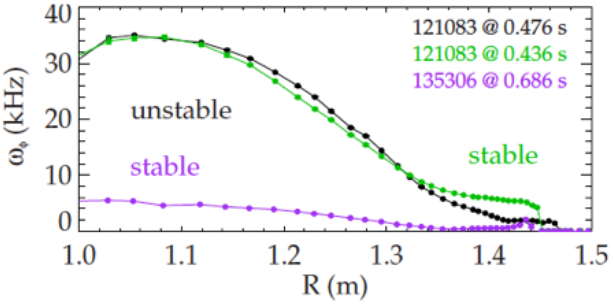

Fig. 45. Toroidal plasma rotation profiles for NSTX, showing a high rotation stable case, an intermediate rotation unstable case, and a low rotation stable case. Reprinted with permission from J. W. Berkery, et al., *Phys. Plasmas* **17** 082504 (2010). Copyright (2010) American Institute of Physics.

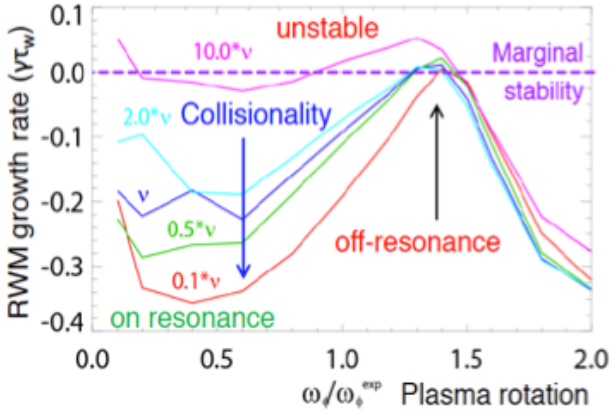

Fig. 46. MISK computed kinetic RWM n = 1 stability vs. plasma rotation at various levels of scaled collisionality. Reprinted with permission from J. W. Berkery, et al., *Phys. Rev. Letters* **106**, 075004 (2011). Copyright (2011) American Physical Society.

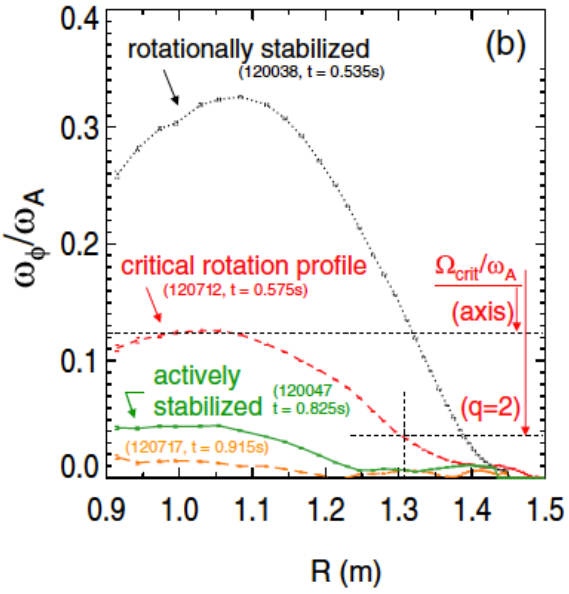

Fig. 47. Actively stabilized plasma equilibrium and rotation profiles. Shown are ω_Φ/ω_A vs. R for plasmas that are rotationally stabilized, at critical rotation profile, and actively stabilized below Ω_{crit}. Reprinted with permission from S. A. Sabbagh, et al., *Phys. Rev. Lett.* **97**, 045004 (2006). Copyright (2006) American Physical Society.

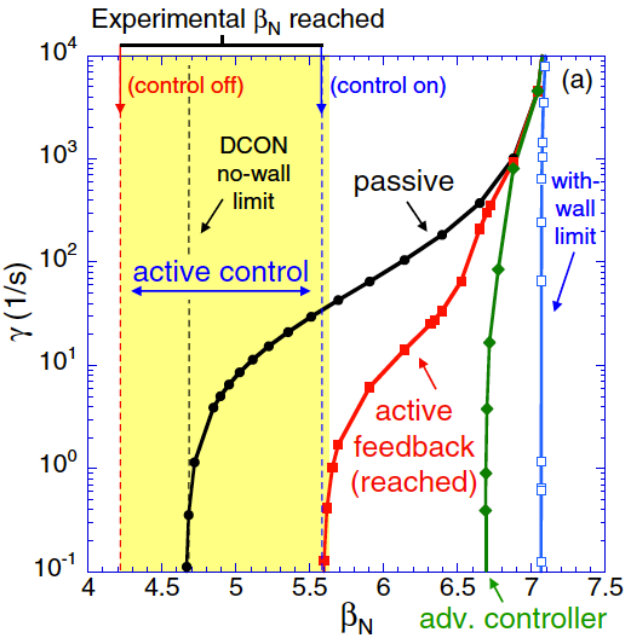

Fig. 48. Experimental β_N reached with $n = 1$ active control (shaded region) compared with theoretical feedback control performance using proportional gain and with an advanced state-space controller. Reprinted with permission from S. A. Sabbagh, et al., *Nucl. Fusion* **50**, 025020 (2010). Copyright (2010) Institute of Physics.

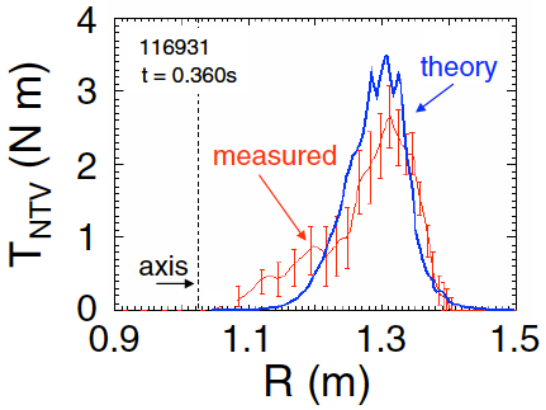

Fig. 50. Comparison of measured $d(I\Omega_\phi)/dt$ profile to theoretical integrated NTV torque for an $n = 3$ applied field configuration. Reprinted with permission from W. Zhu, et al., *Phys. Rev. Letters* **96**, 225002 (2006). Copyright (2006) American Physical Society.

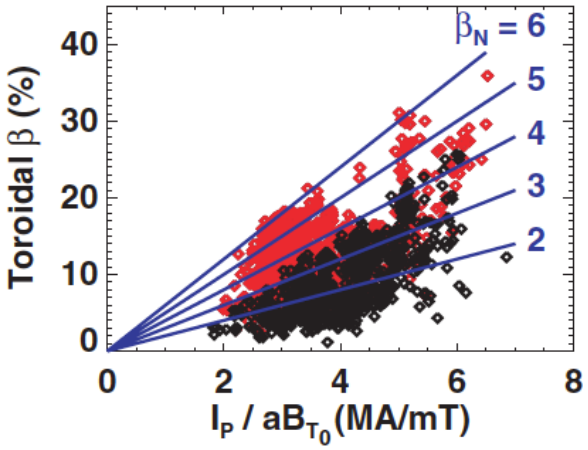

Fig. 49. Database plot of β_t vs. $I_p/(aB_{t0})$, showing that the data are bound by a line with slope β_N ~ 6.0–6.5 in NSTX. Discharges are divided into experimental data in 2002 (red) vs earlier results (black). Reprinted with permission from J. E. Menard, et al., *Nuclear Fusion* **43**, 330 (2003). Copyright (2003) Institute of Physics.

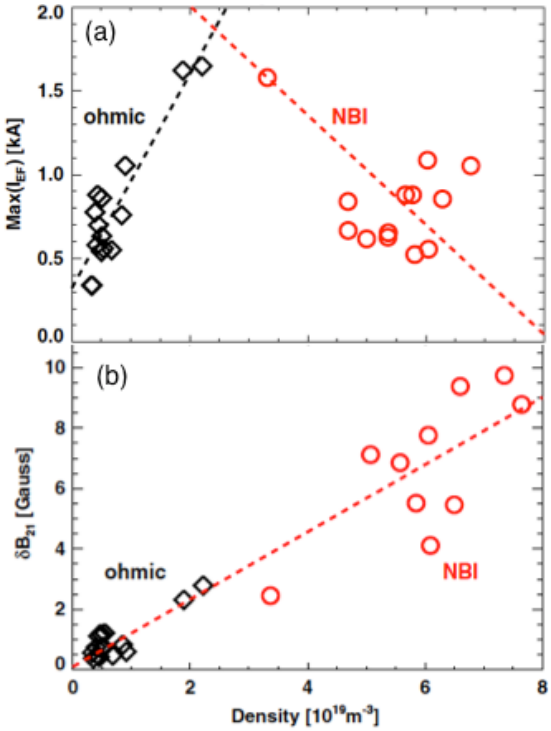

Figure 51 (a) Summary of locking threshold measurements in external currents versus density for NBI-heated high β cases (red circles) as well as ohmic plasma cases (black diamonds). (b) Revision of (a) using total resonant fields at the q = 2/1 surface utilizing IPEC. Reprinted with permission from J.-K.Park et al., Nuclar Fusion **52**, 023004 (2012). Copyright (2012) Institute of Physics.

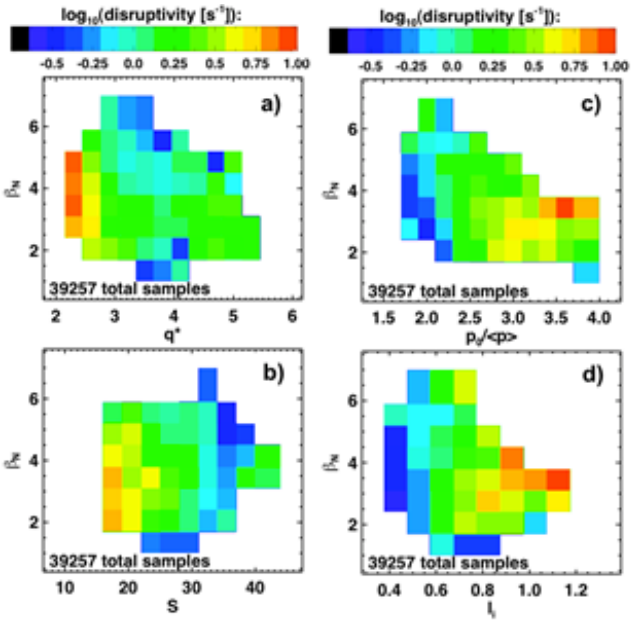

Fig. 52. Disruptivity as a function of β_N and a) q*, b) shape factor, c) pressure peaking, and d) l_i. Reprinted with permission from S.P. Gerhardt et al., *Nucl. Fusion* **53**, 043020 (2013). Copyright (2013) Institute of Physics.

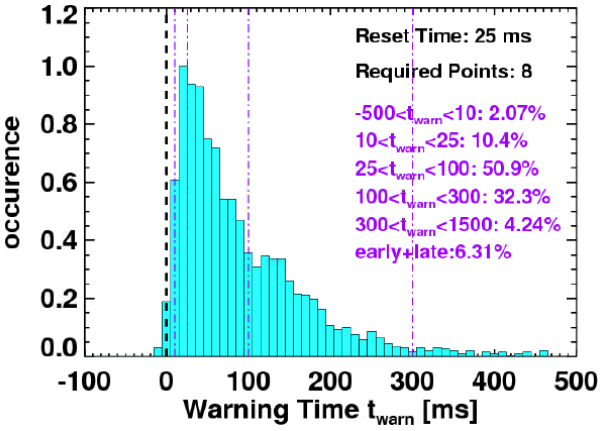

Fig. 53. Histogram of warning times computed for 1700 disruption discharges. Reprinted with permission from S. P. Gerhardt.

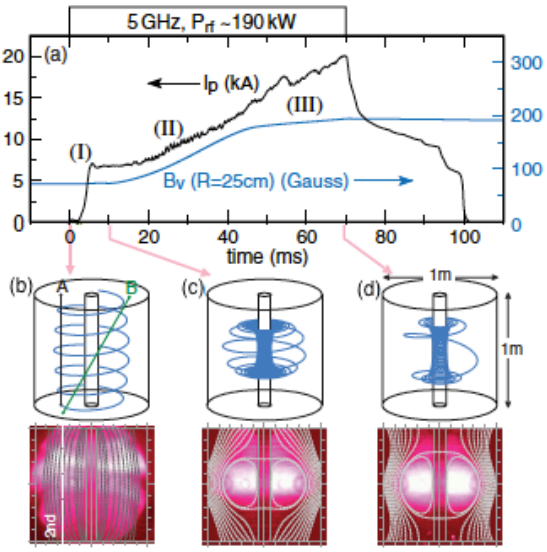

FIG. 54. A 20 kA current ramp-up discharge in LATE. (a) plasma current and B_v; (b), (c), and (d) field lines and plasma images at the breakdown, initial closed field formation, and final low aspect ratio torus formation, respectively. Reprinted with permission from M. Uchida, et al., *Phys. Rev. Lett.* 104, 065001 (2010). Copyright (2010) American Physical Society.

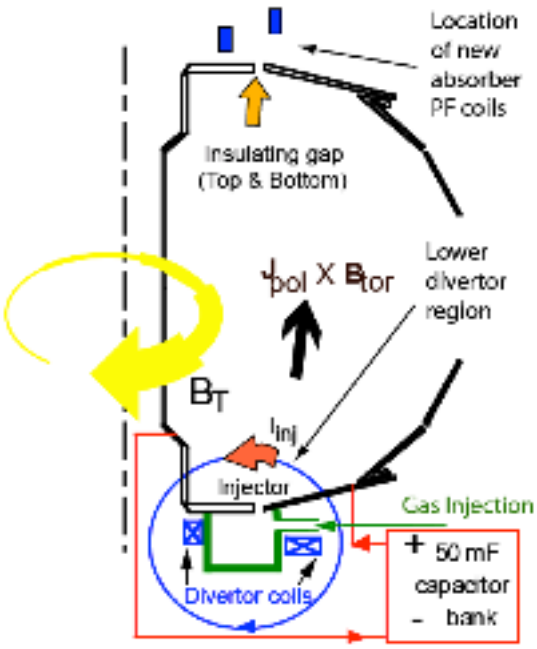

Fig. 55. CHI schematic drawing of the NSTX including the location of the insulating gaps between the divertor plates. Reprinted with permission from R. Raman et al., *Phys. Rev. Lett.* **97**, 175002 (2006). Copyright (2006) American Physical Society.

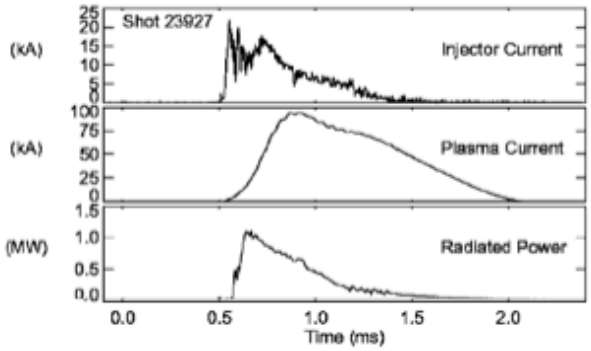

Fig. 56. CHI only discharge in HIT-II: Injector current, CHI-produced plasma current, and radiated power signal from a wide-angle bolometer. Reprinted with permission from R. Raman et al., *Phys. Rev. Lett.* **90**, 0750005-1 (2003). Copyright (2003) American Physical Society.

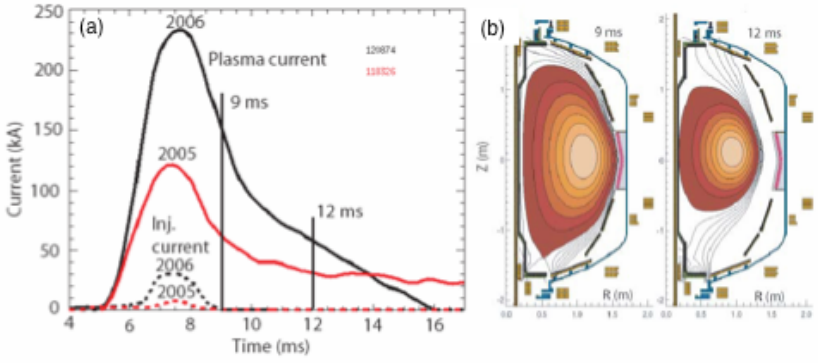

Fig. 57. (a) Discharge evolution of 160 kA closed flux current produced by CHI alone in NSTX. Discharges in 2006 operated at higher toroidal field and injector flux. (b) Equilibrium reconstructions show the shape evolution of the CHI produced plasma in response to decaying current. EFIT analysis is possible when no injector current is present. Reprinted with permission from R. Raman et al., *Phys. Rev. Lett.* **97**, 175002 (2006). Copyright (2006) American Physical Society.

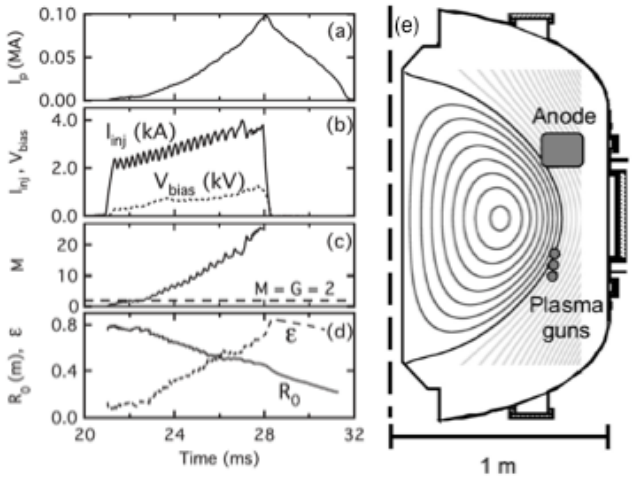

Fig. 58. Localized plasma gun start-up in PEGASUS (a) – (d) Time wave forms for plasma current, bias voltage and total injected current, current multiplication, and plasma major radius and inverse aspect ratio, respectively. (e) An experimental set up schematic of plasma gun start-up. Magnetic equilibrium reconstruction of poloidal flux surfaces at t = 28 ms. Reprinted with permission from D.J. Battaglia *PRL* **102**, 225003 (2009). Copyright (2009) American Physical Society.

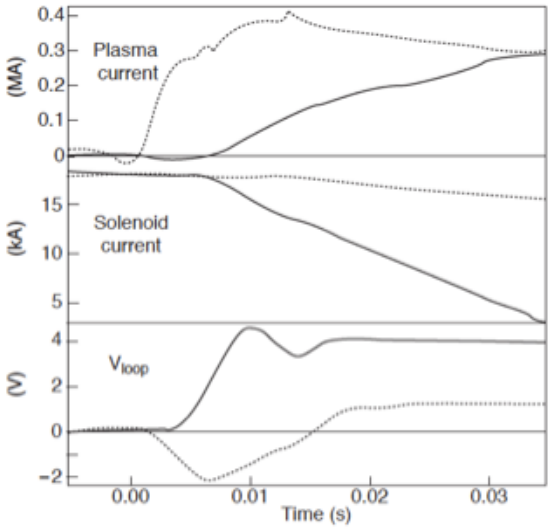

Fig. 59. Direct induction (solid curves) and merging-compression dotted curves) schemes for MAST discharges. Reprinted with permission from A. Sykes et al., Nucl. Fusion **41**, 1423 (2001). Copyright (2001) Institute of Physics.

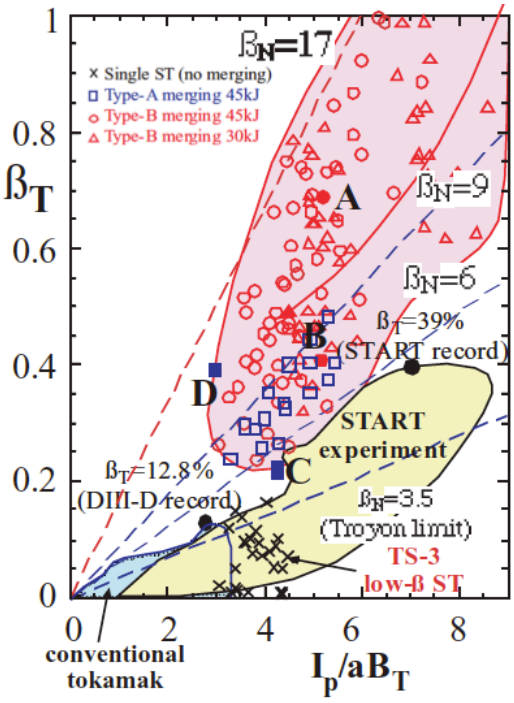

Fig. 60**.** Toroidal betas β_T of single low-beta STs (no merging) and high-beta STs produced by mergings as a function of I/aB_T in TS-3. Reprinted with permission from Y. Ono, et al., *Nucl. Fusion* **43**, 789 (2003). Copyright (2003) Institute of Physics.

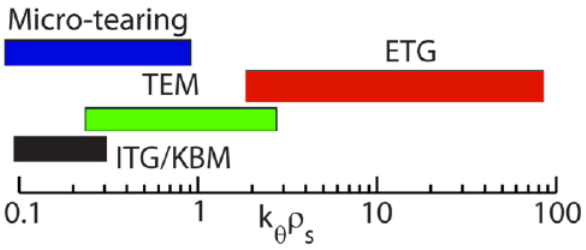

Fig. 61. Illustration of wave number range for various microturbulence as labeled in NSTX parameter range. Reprinted with permission from S. M. Kaye.

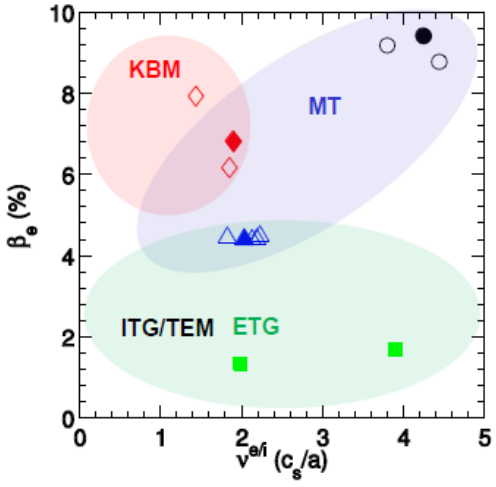

Fig. 62. Local values of β_e and $\nu^{e/i}$ (r/a = 0.6 – 0.7) for various H-mode discharges. The colored regions illustrate where various microinstabilities are generally predicted to occur. Reprinted with permission from W. Guttenfelder, et al., *Nucl. Fusion* **53**, 093022 (2013) Copyright (2013) Institute of Physics.

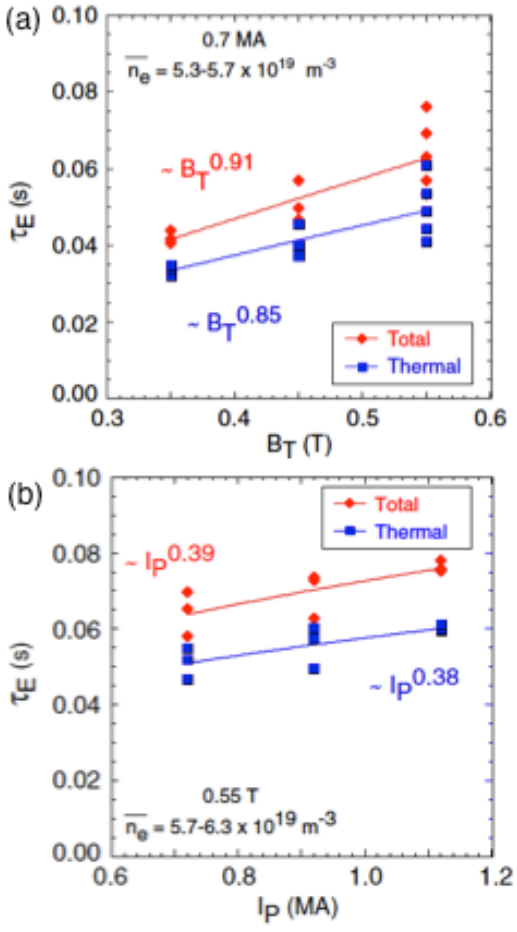

Fig. 63. Total (red) and thermal (blue) energy confinement times vs. (a) B_T at constant I_p, n_e, and P_L, and (b) I_p at constant B_T, n_e, and P_L . Reprinted with permission from S.M. Kaye et al., *Nucl. Fusion* **47** 499 (2007). Copyright (2007) Institute of Physics.

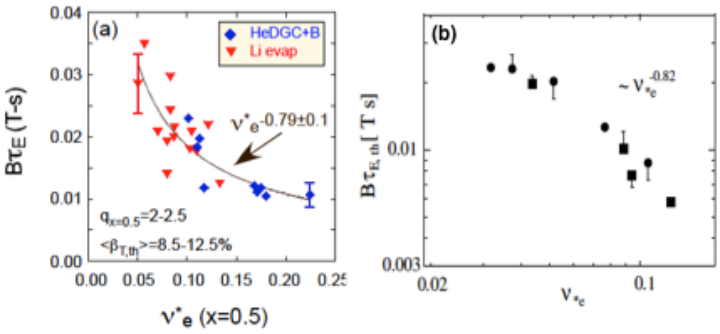

Fig. 64. (a) Normalized confinement time as a function of collisionality at mid-radius in NSTX. Blue points are from discharges that used HeGDC+B wall conditioning, while red points are from discharges that used Li. Reprinted with permission from S.M. Kaye et al., *Nucl. Fusion* **53** 063005 (2013). Copyright (2013). Institute of Physics. (b) Collisionality scan of thermal energy confinement time in MAST. Reprinted with permission from M. Valovic et al., *Nucl. Fusion* **51** 073045 (2011). Copyright (2011) Institute of Physics.

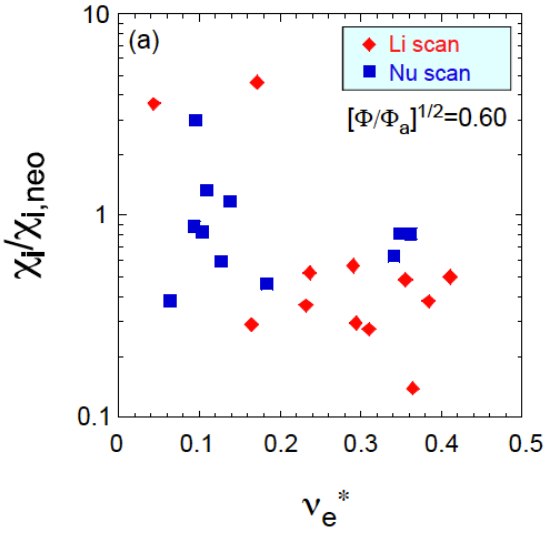

Fig. 65. Ion thermal diffusivity, χ_i normalized to the neoclassical ion thermal diffusivity as determined by NCLASS as a function of ν_e^* at r/a =0.6. Values from both the collisionality (Nu) scan (blue) and Li scans (red) are shown. Reprinted with permission from S.M. Kaye et al., *Nucl. Fusion* **53** 063005 (2013). Copyright (2013). Institute of Physics.

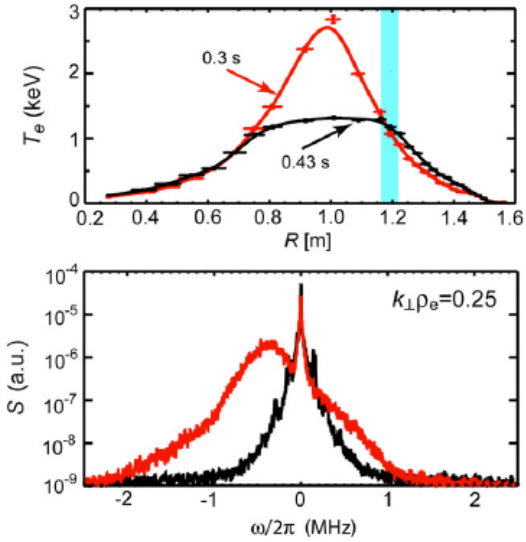

Fig. 66. Temperature profiles (top) and spectral density of fluctuations (bottom) at 0.3 s (red) and 0.43 s (black). The blue stripe indicates the location of measurement where L_{Te} is 15 cm and 50 cm, respectively. Negative frequencies (bottom) correspond to Doppler shifted frequency spectrum due to wave propagation in the electron diamagnetic direction. Reprinted with permission from E. Mazzucato et al., *Nucl. Fusion* **49** 055001 (2009). Copyright (2009). Institute of Physics.

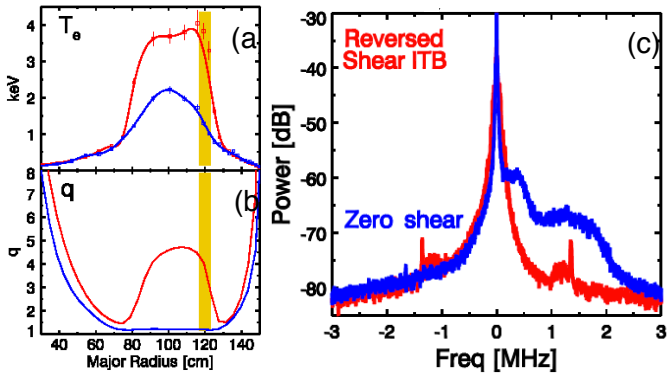

Fig. 67. Comparison between a case with an e-ITB and strongly negative magnetic shear (red) vs. a zero reversed shear case (blue). (a) Electron temperature profiles. (b) q-profiles. Shaded region indicates the high-k measurement region. (c) High-k microwave scattering fluctuation power spectra. Reprinted with permission from H.Y. Yuh et al., *Phys. Plasmas.* **16**, 056120 (2009). Copyright (2006) American Institute of Physics.

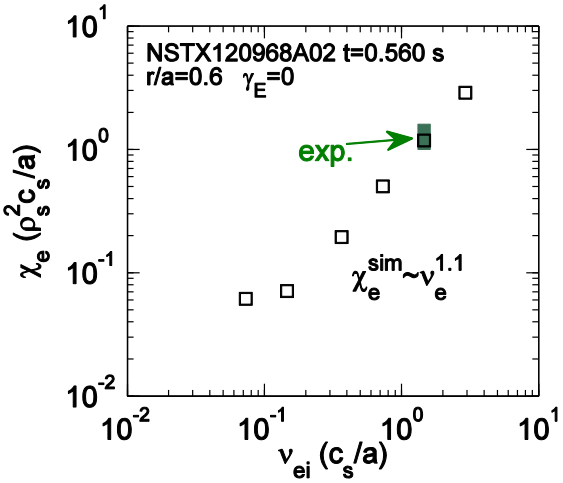

Fig. 68. Normalized electron thermal diffusivity vs. normalized electron collision frequency. The shaded square shows the experimental values with uncertainties. All calculations are based on an NSTX H-mode plasma using the GYRO code. Reprinted with permission from W. Guttenfelder, et al., *Phys. Plasmas* **19**, 056119 (2012). Copyright (2012) American Institute of Physics.

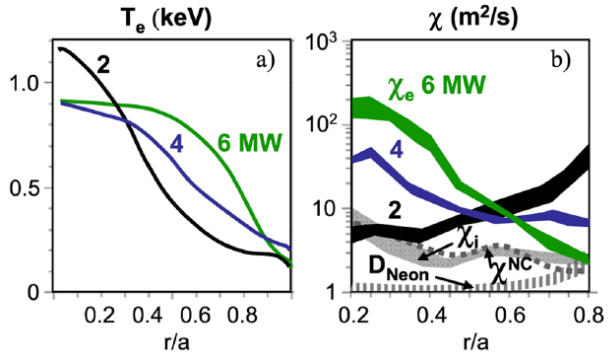

Fig. 69. (a) T_e profiles with P_{NBI} = 2, 4, and 6 MW NSTX H-modes. (b) TRANSP computed χ_e profiles in the same plasmas. Also shown are the χ_i and NCLASS ion thermal diffusivity for the 6 MW case and the measured neon diffusivity. Reprinted with permission from D. Stutman et al., *Phys. Rev. Lett.* **102**, 115002 (2009). Copyright (2009) American Physical Society.

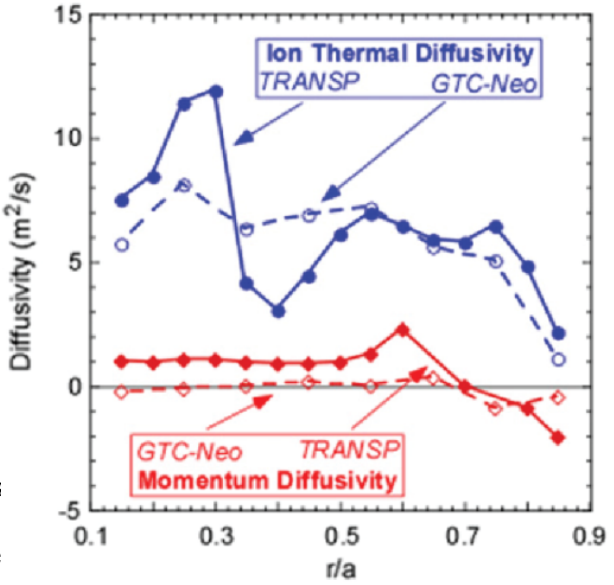

Fig. 70. Experimentally inferred values of χ_i and χ_ϕ compared with the neoclassical values computed by GTC-NEO for an NSTX H-mode plasma. Reprinted with permission from S.M. Kaye et al., *Nucl. Fusion* **49** 045010 (2009). Copyright (2009). Institute of Physics.

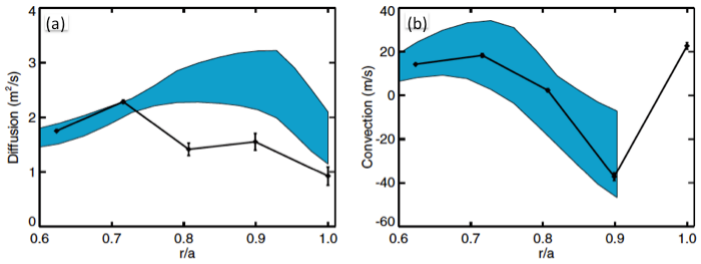

Fig. 71. (a) The resulting diffusion profile (b) and convection profile for the I_p = 1.1 MA, B_T = 0.55 T NSTX H-mode case. The shaded region represents the results from NCLASS neoclassical transport calculations. Reprinted with permission from D.J. Clayton, et al., *Plasma Phys. Controlled Fusion* **54**, 105022 (2012). Copyright (2012) Institute of Physics.

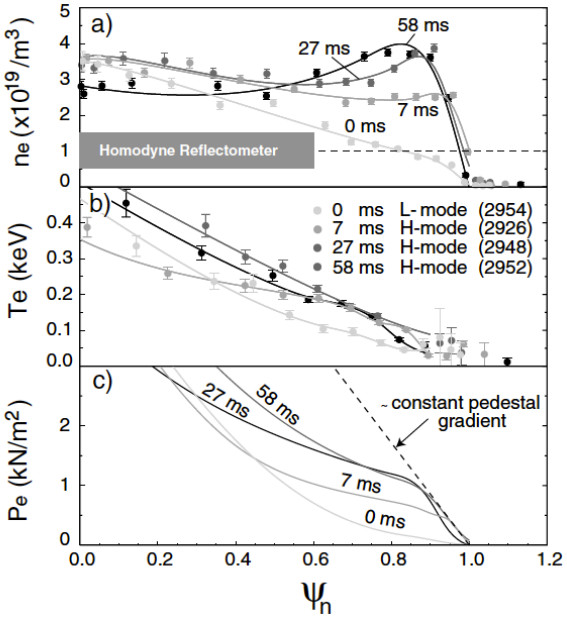

Fig. 72. Evolution of the thermal electron radial profile vs normalized poloidal flux: (a) density, (b) temperature, and (c) pressure. Reprinted with permission from R. J. Akers, et al., *Phys. Rev. Lett.* **88**, 035002 (2002). Copyright (2002) American Physical Society.

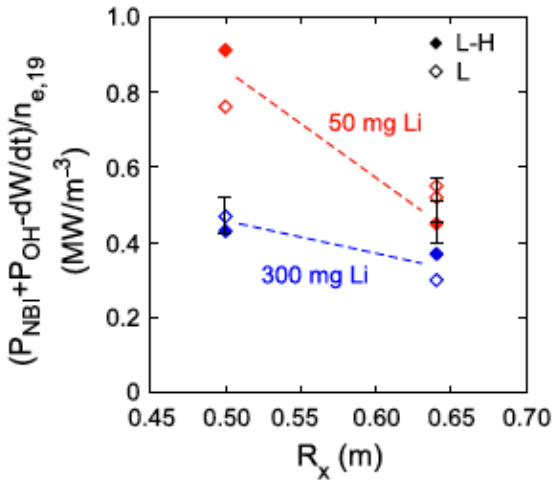

Fig. 73. Density-normalized loss power as a function of X-point radius for two different lithium evaporation rates. The solid symbols denote discharges that have transitioned into the H-mode at that loss power, while the open symbols denote those that remain in the L-mode. Reprinted with permission from S.M. Kaye et al., *Nucl. Fusion* **51,** 113019 (2011). Copyright (2011). Institute of Physics.

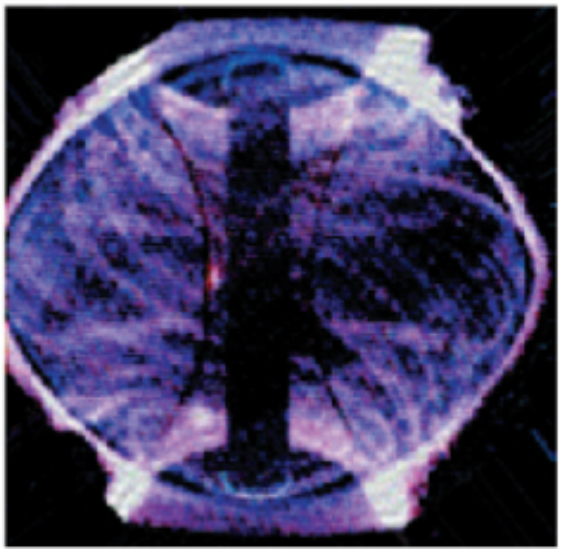

Fig. 74. High-speed video images of MAST plasmas with an ELM event, showing evidence of a filamentary structure. Reprinted with permission from A. Kirk et al., *Plasma Phys. Controlled Fusion* **47**, 315 (2005) . Copyright (2005) Institute of Physics.

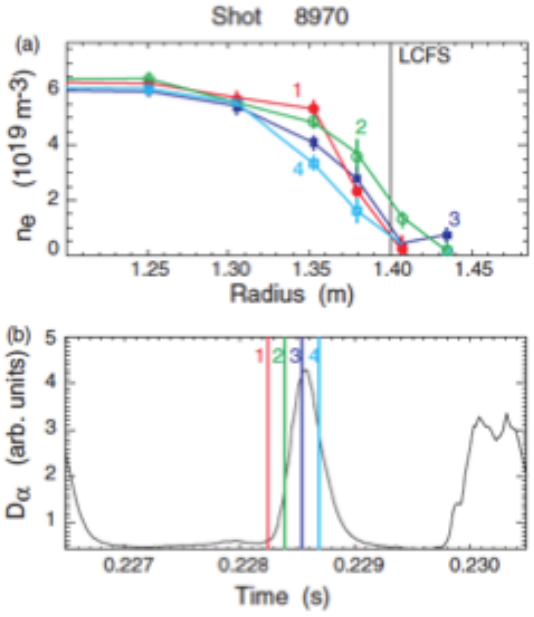

Fig. 75. (a) The time evolution of the edge density profile for a single ELM. (b) The target D_α signal with the measurement times as indicated. Reprinted with permission from A. Kirk, et al., *Plasma Phys. Controlled Fusion* **47**, 315 (2005). Copyright (2005) Institute of Physics.

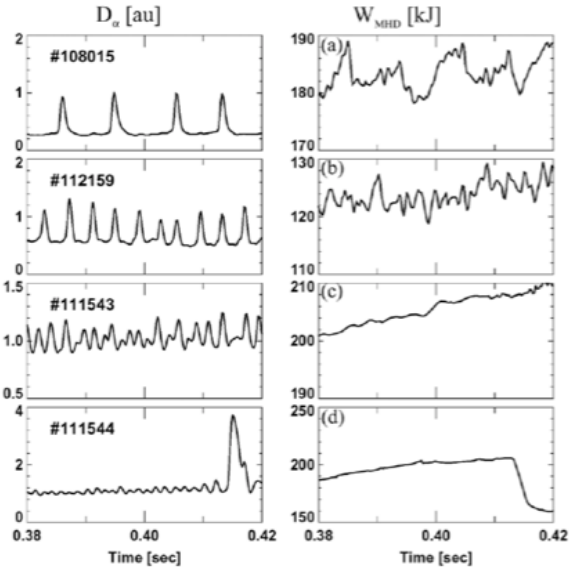

Fig. 76. Examples of different ELM types in NSTX: (*a*) large, Type I in DN configuration, (*b*) medium Type III in configurations close to DN, (*c*) small, Type V in LSN configuration and (*d*) mixed Type I/Type V in LSN configuration. Reprinted with permission from R. Maingi.

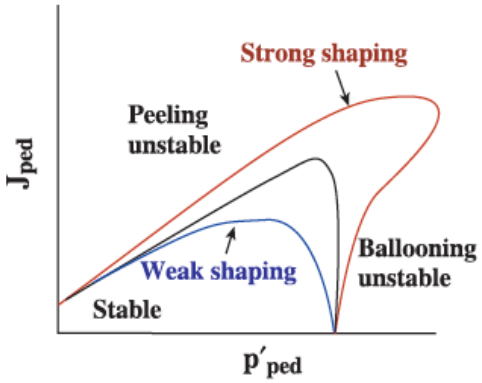

Fig. 77. Schematic diagram of the peeling–ballooning stability limit for different shaped discharges as a function of edge current and pressure gradient. Reprinted with permission from P.B. Snyder et al., *Phys. Plasmas* **9**, 2037 (2002). Copyright (2002) American Institute of Physics.

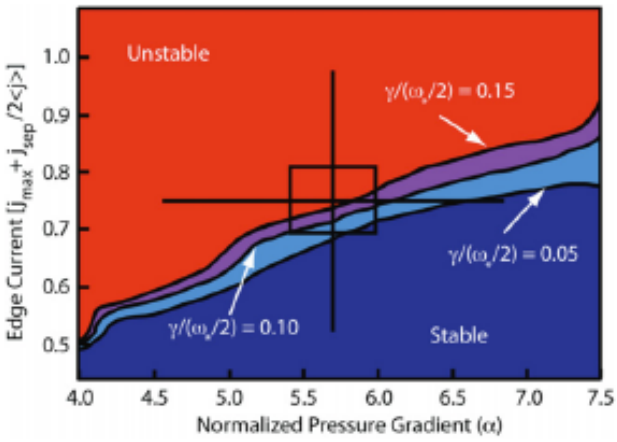

Fig. 78. Peeling–ballooning stability diagram as calculated by the ELITE code for NSTX H-mode during the type-I ELMy phase. Reprinted with permission from A.C. Sontag et al., *Nucl. Fusion* **51**, 103022 (2011) . Copyright (2011). Institute of Physics.

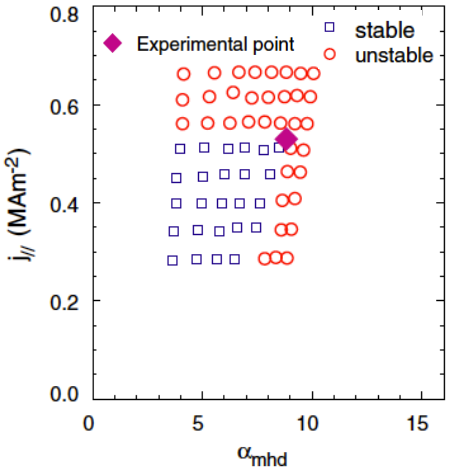

Fig. 79. Stability diagram plots from ELITE showing edge current density versus normalized pressure gradient for Type I ELM in MAST. Reprinted with permission from A. Kirk, et al., *Plasma Phys. Controlled Fusion* **51**, 065016 (2009). Copyright (2009) Institute of Physics.

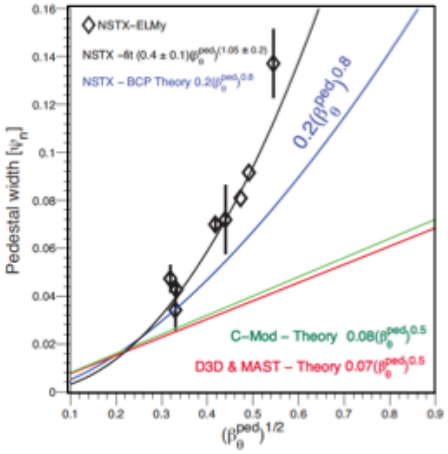

Fig. 80. The pedestal width (in ψ_n) scaling with $(\beta_q^{ped})^{1/2}$. This width scaling effectively provides a relation between the width and the height of the pedestal. The best fit for NSTX width is $(\beta_q^{ped})^{1.05}$. A theoretical model applied to NSTX data using BCP shows a $(\beta_q^{ped})^{0.8}$ scaling. Reprinted with permission from A. Diallo et al., *Nucl. Fusion* **53**, 093026 (2013). Copyright (2013). Institute of Physics.

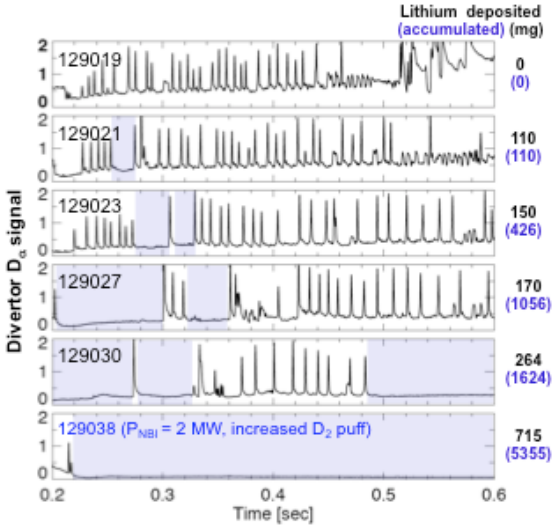

Fig. 81. Temporal edge D-alpha signal for various lithium deposition rate. The regularly occurring spikes represents the Edge Localized Modes (ELMs). Reprinted with permission from D.K. Mansfield.

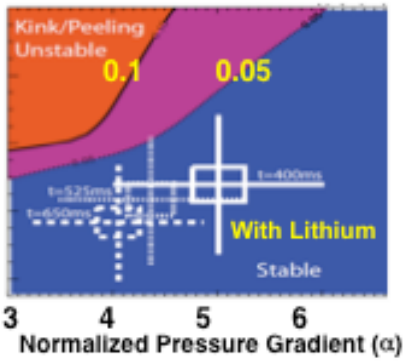

Fig. 83. Stability boundary (blue to orange color transition) from ELITE code with fixed boundary kinetic EFITs for post-lithium discharge. Reprinted with permission from D.P. Boyle.

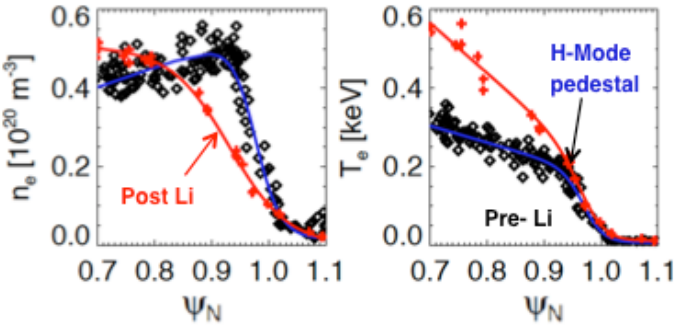

Fig. 82. Profiles for n_e and T_e for pre- and post lithium discharges (black and red lines, respectively). Reprinted with permission from R. Maingi.

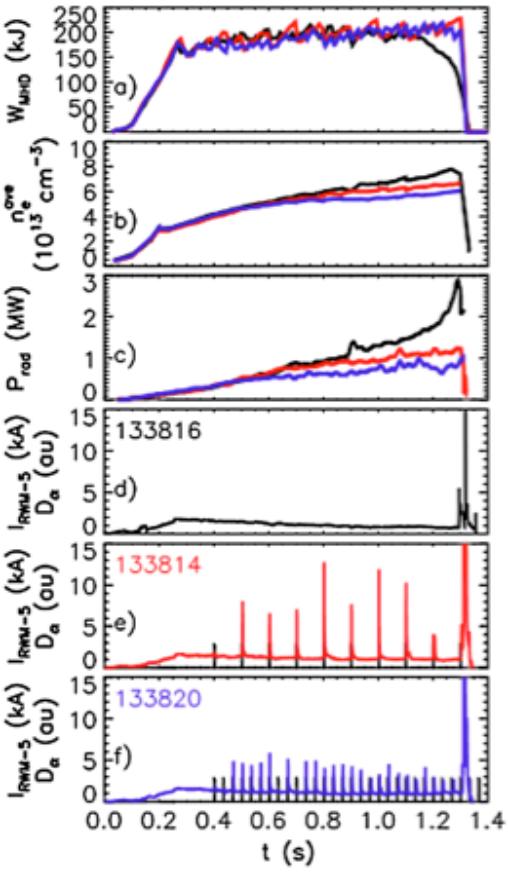

Fig. 84. Comparison of discharges with lithium conditioning only (black line) and with combined lithium and 3D field-induced ELMs (red and blue or gray lines): (a) stored energy, (b) n_e^{ave}, (c) P_{rad}, and (d)–(f) I_{RWM-5} and D_a emission. Reprinted with permission from J. M. Canik et al., *Phys. Rev. Lett.* **104**, 045001 (2010). Copyright (2010) American Physical Society.

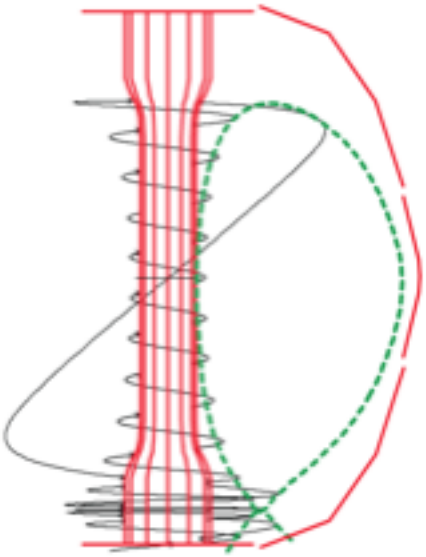

Fig. 85. Visualization of the field line on the flux surface $y_N = 1.005$ in the NSTX standard divertor. Reprinted with permission from V.A. Soukhanovskii.

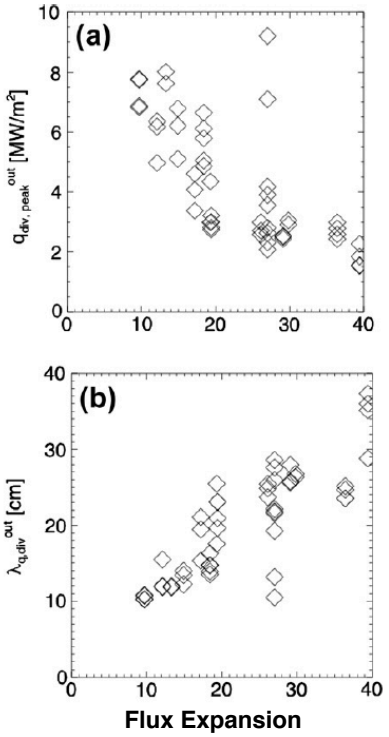

Fig. 87. Effect of f_{exp} as measured at the outer strike point in NSTX. (a) Reduction in $q_{div, peak}$ as f_{exp} is increased. (b) Broadening of the heat flux profile, λ_q^{div} as f_{exp} is increased. Reprinted with permission from T.K. Gray et al., *J. Nucl. Materials* **415** S360 (2011). Copyright (2011) Elsevier.

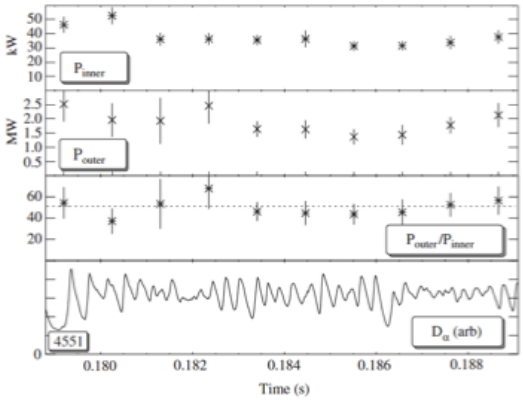

Fig. 86. Total power to the outboard and inboard targets (summing contributions from the upper and lower targets in each case) for an L-mode phase in MAST, with all strike points fully attached. More than 98% of power arriving at the targets is detected at the outboard side. Reprinted with permission from G.F. Counsell et al., *Plasma Phys. Controlled Fusion* **44**, 827 (2002). Copyright (2002) Institute of Physics.

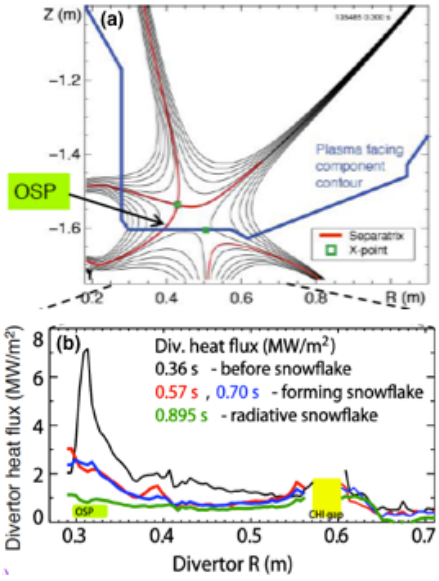

Fig. 88. (a) Poloidal flux contours for the asymmetric SFD. (b) Heat flux profile during the SFD discharge as labeled. Reprinted with permission from V. A. Soukhanovskii et al., *Phys. Plasmas* **19**, 082504 (2012). Copyright (2012) American Institute of Physics.

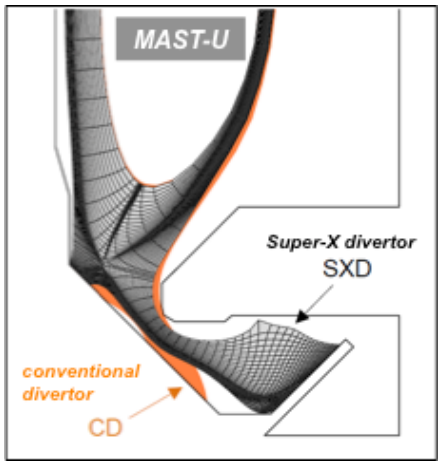

Fig. 89. Super-x divertor configuration compared to the conventional divertor planned in MAST-U. © EURATOM/CCFE.

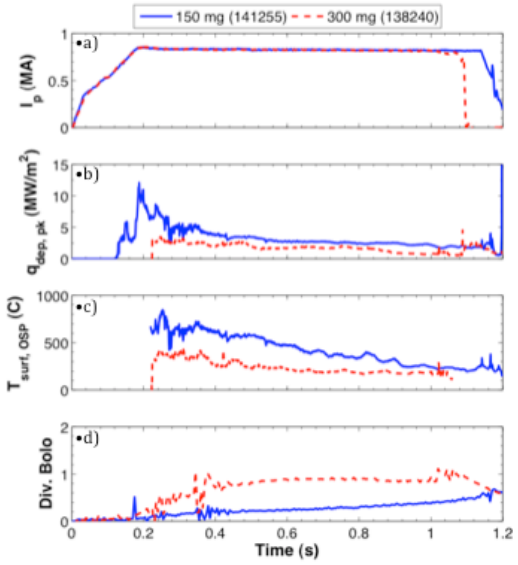

Fig. 90. Divertor surface temperature and corresponding heat flux as a function of Li evaporation for otherwise similar NBI heated H-mode discharges. Pre-discharge Li evaporation of 150 mg shown as blue solid lines and 300 mg as red dashed lines. Reprinted with permission from T.K. Gray, et al., *Nucl. Fusion* **54**, 023001 (2014). Copyright (2014) Institute of Physics.

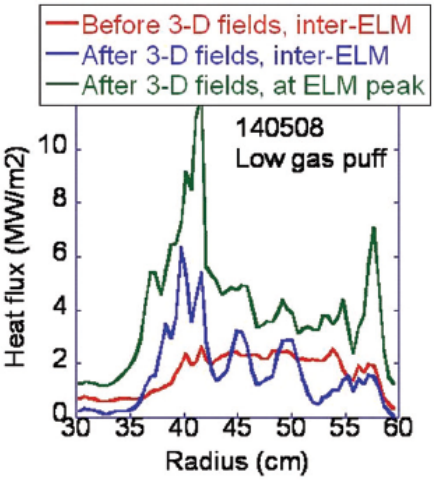

Fig. 91. Measured heat flux profiles with and without the 3-D field application, as labeled, for the detached divertor plasma with lower gas puffing. Reprinted with permission from J-W. Ahn et al., *Phys. Plasmas* **18** 056108 (2011). Copyright (2011) American Institute of Physics.

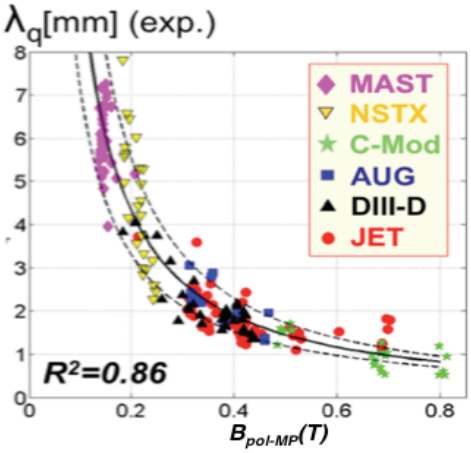

Fig. 92. Power fall-off length λ_q at the mid-plane versus the poloidal magnetic field at the outer mid-plane. Reprinted with permission from T. Eich et al., *Nucl. Fusion* **53**, 093031 (2013). Copyright (2013) Institute of Physics.

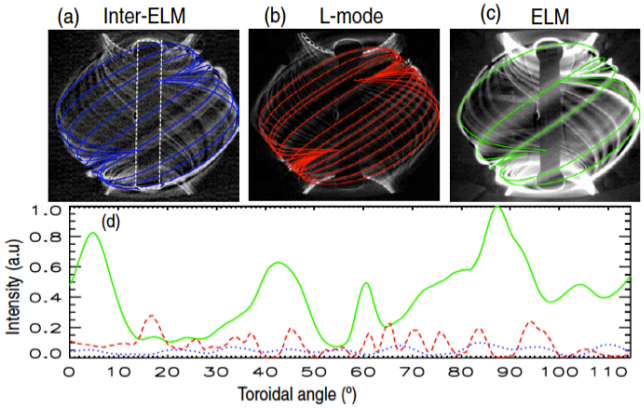

Figure 93. Full view camera images of edge filaments for (*a*) inter-ELM, (*b*) L-mode and (*c*) ELM periods within the same discharge (shot #15586), and (*d*) the intensity traces are superposed normalized to the peak ELM intensity showing the contrast in measured intensities across the three phases. Reprinted with permission from N. Ben Ayed et al., *Plasma Phys. Controlled Fusion* **51**, 035016 (2009). Copyright (2009) Institute of Physics.

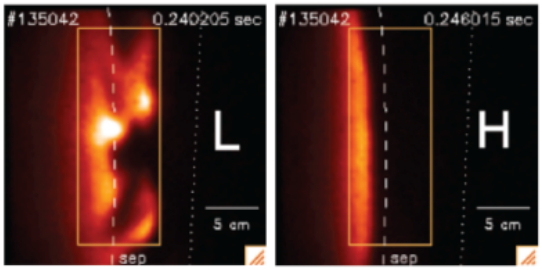

Fig. 94. Typical GPI images of the light emission in the NSTX L-mode and H-mode. Also shown is the best estimate for the separatrix location (dashed line) and the shadow of the rf antenna/limiter location (dotted line.) Reprinted with permission from S.J. Zweben et al., *Phys. Plasmas* **17,** 102502 (2010). Copyright (2010) American Institute of Physics.

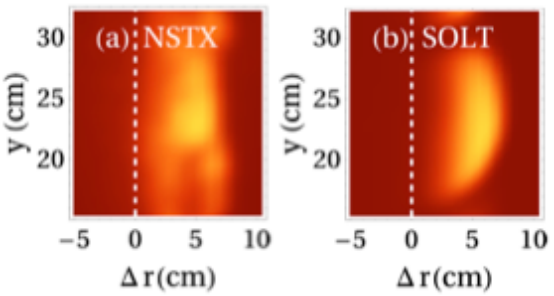

Fig. 95. (a) Actual NSTX, shot no. 112825 and (b) synthetic SOLT GPI intensity images. The magnetic separatrix is at r = 0 in the NSTX shot. Intensities are normalized by their respective global maxima over the frame. Reprinted with permission from D.A. Russel et al., *Phys. Plasmas* **18**, 022306 (2011). Copyright (2011) American Institute of Physics.

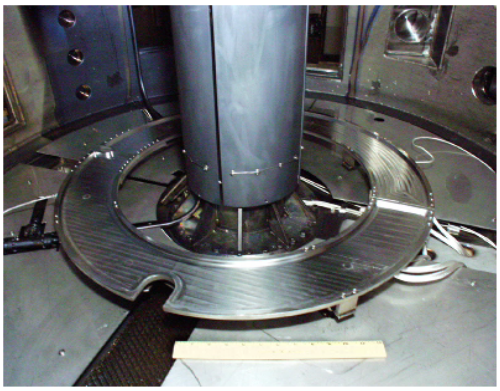

Fig. 96. Liquid lithium divertor tray inside CDX-U vacuum vessel. One-foot (30.48 cm) ruler in foreground provides scale. Heat shield with titanium carbide coating protects center stack. White cables emerging from tray provide power to heaters.

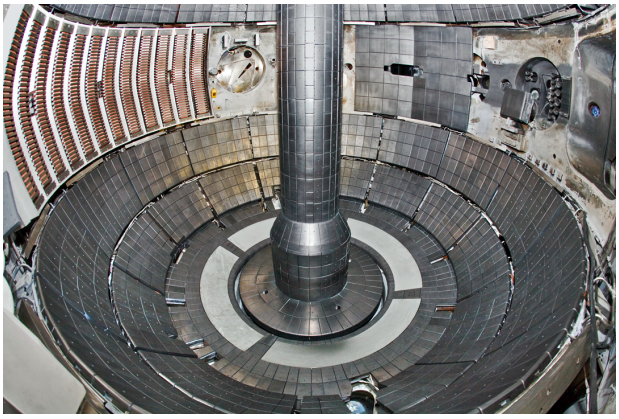

Fig. 97. Interior of NSTX vacuum vessel. LLD appears as light-colored sections surrounding the center stack. Darker areas are graphite tiles constitute bulk of PFCs. RF antennas, ports for diagnostics, and neutral beam armor are main features in NSTX mid-plane.

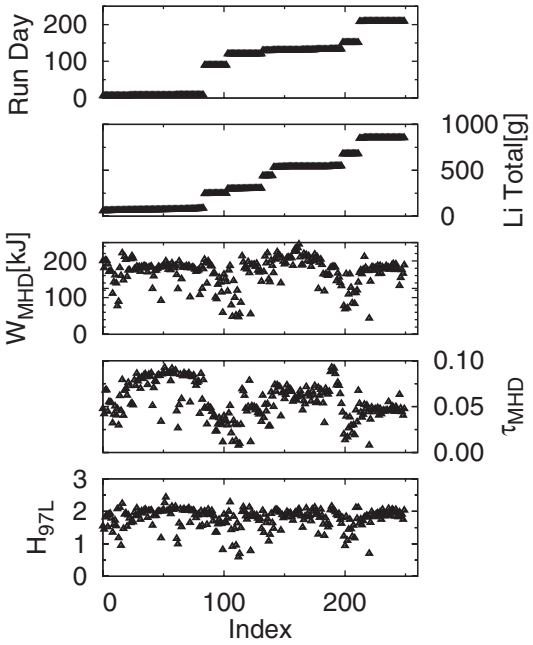

Fig. 98. Selected entries from the LLD experimental database. Run day is the number of days since the beginning of the 2010 experimental campaign, Li Total is the integrated amount of lithium evaporated into the vessel, W_{MHD} is the plasma stored energy, τ_{MHD} is the energy confinement time, and H_{97L} is the H-factor compared to the ITER 97L global confinement scaling. The values of W_{MHD}, τ_{MHD}, and H_{97L} are averages taken between 400–600 ms. Reprinted with permission from M. Jaworski *et al.*, Nucl. Fusion **53**, 083032 (2013) . Copyright (2013) Institute of Physics.

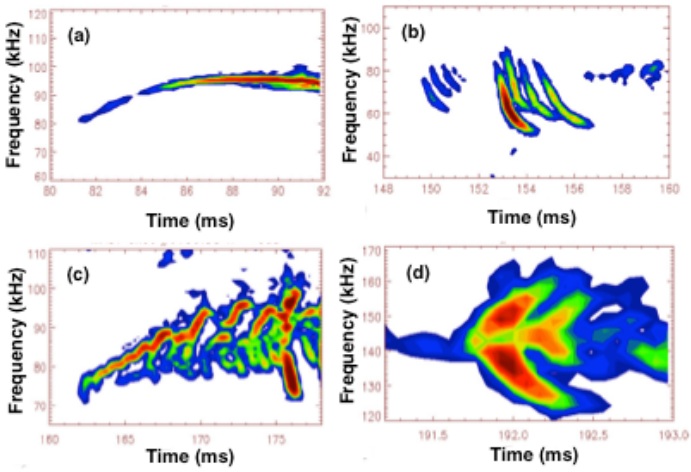

Fig. 99. Examples of TAEs observed in NB heated discharges on MAST (*a*) long-lasting TAE mode with quasi-stationary frequency at the center of the TAE gap; (*b*) chirping-down modes; (*c*) chirping-up modes; (*d*) hole–clump mode with starting frequency at the TAE gap center. Reprinted with permission from M. Gryaznevich, et al., *Nucl. Fusion* **46** S942 (2006). Copyright (2006) Institute of Physics.

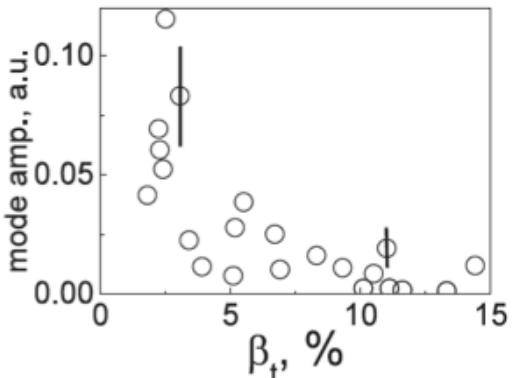

Fig. 100. Dependence on β of the maximum amplitude in a single burst of chirping modes, which start in the TAE-gap, in NBI discharges on MAST. Reprinted with permission from M.P. Gryaznevich and S.E. Sharapov, *Plasma Phys. Controlled Fusion* **46**, S15 (2004). Copyright (2004) Institute of Physics.

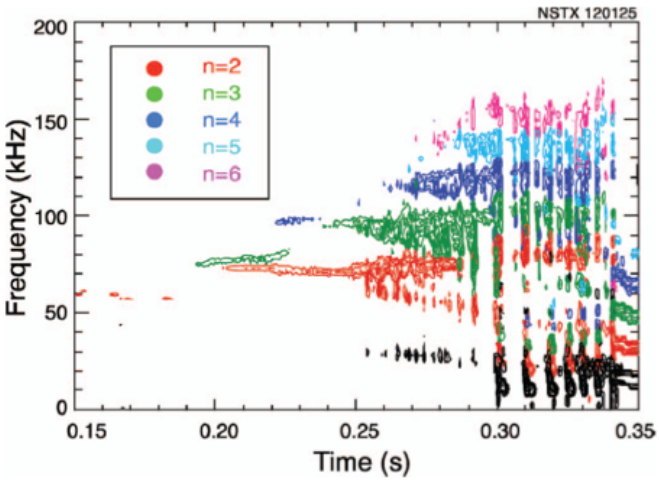

Fig. 101. Color Spectrogram of Mirnov coil from discharge at the threshold beta below which Alfvén cascades are seen. Frequency sweeping is largely absent. Reprinted with permission from E. D. Fredrickson, et al., *Phys. Plasmas* **14**, 102510 (2007) . Copyright (2007) American Institute of Physics.

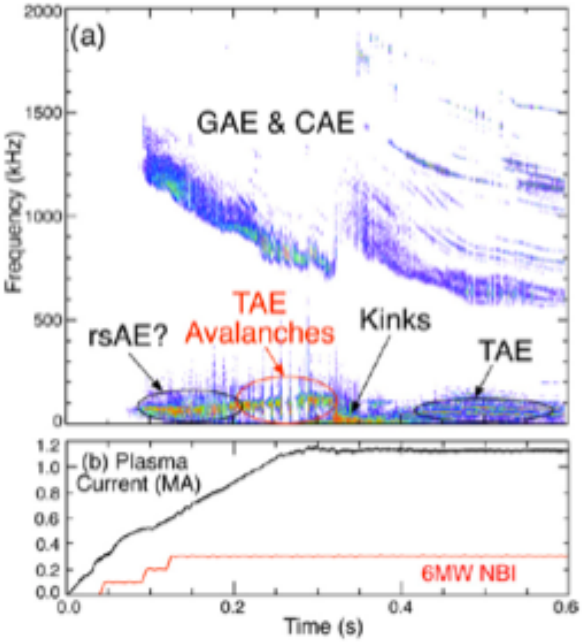

Fig. 102. (*a*) Spectrogram of EP induced magnetic fluctuations in NSTX, (*b*) plasma current and neutral beam power evolution. Reprinted with permission from E. D. Fredrickson et al., *Nucl. Fusion* **53** 013006 (2013). Copyright (2013) Institute of Physics.

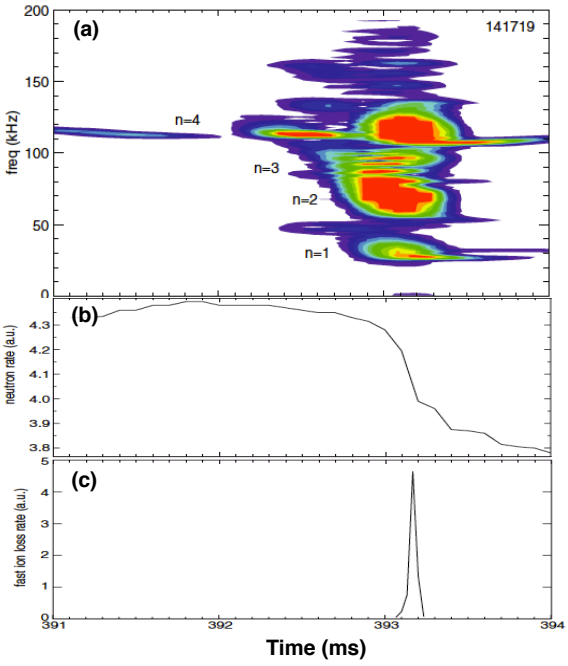

Fig. 103. (*a*) Magnetic pickup coil frequency spectrogram during a TAE avalanche on an expanded time scale, (*b*) neutron rate, and (*c*) total fast ion loss rate measured by the sFLIP detector. Reprinted with permission from D.S. Darrow et al., *Nucl. Fusion* **53** 013009 (2013). Copyright (2013) Institute of Physics.

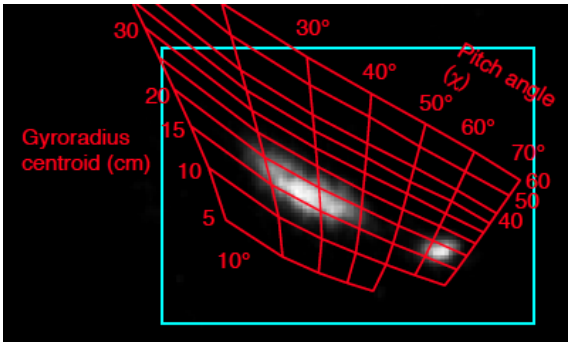

Fig. 104. sFLIP detector camera frame at time of peak loss with interpretive grid defining the gyroradius centroid and pitch angle of the lost particles. Based upon the EFIT magnetic field at the detector location, 90 keV D ions should have a gyroradius of 17 cm. Reprinted with permission from D.S. Darrow et al., *Nucl. Fusion* **53** 013009 (2013). Copyright (2013) Institute of Physics.

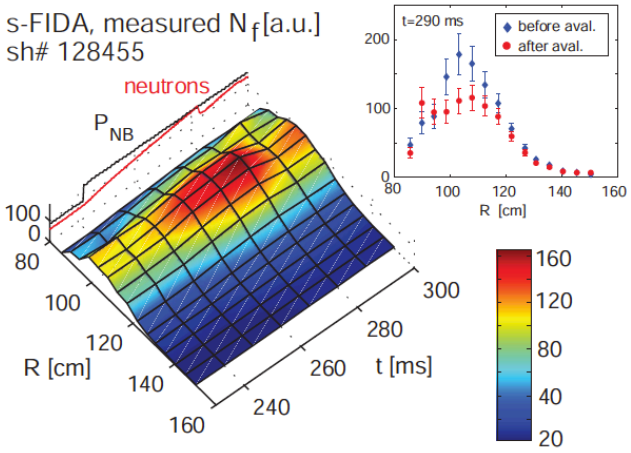

Fig. 105. Color Measured evolution of the fast-ion profile in NSTX by FIDA. The decrease after t=280 ms, following a TAE avalanche, is detailed in the inset. Reprinted with permission from of M. Podestà et al., *Phys. Plasmas* **16,** 056104 (2009). Copyright (2009) American Institute of Physics.

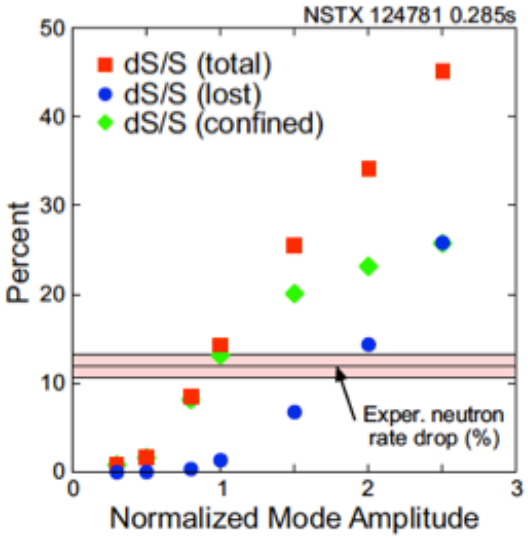

Fig. 106. Simulated neutron rate drop due to TAE avalanche (red), neutron rate drop resulting from lost beam ions (blue) and neutron rate drop in confined beam ion population from energy loss (green). Reprinted with permission from E. D. Fredrickson et al., *Nucl. Fusion* **53** 013006 (2013). Copyright (2013) Institute of Physics.

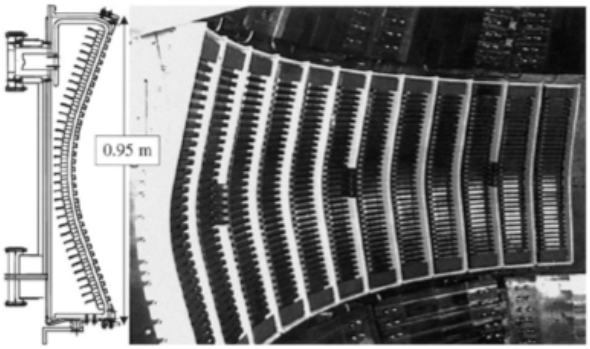

Fig. 107. NSTX HHFW antenna array.

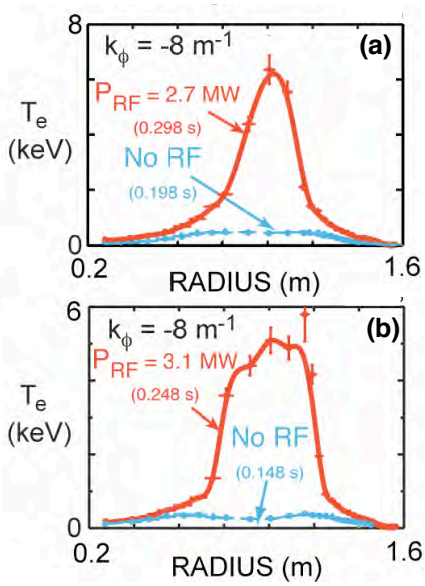

Fig. 108. (a) $T_e(R)$ immediately prior to HHFW heating t = 0.198 s (dashed line) and during 2.7 MW of k_ϕ =−8 m $^{-1}$ heating t = 0.298 s (solid line) of a helium plasma. (b) $T_e(R)$ immediately prior to rf heating t = 0.148 s (dashed line) and during 3.1 MW of k_ϕ =−8 m^{-1} heating t =0.248 s (solid line) of a deuterium plasma. Reprinted with permission from of Taylor et al., *Phys. Plasmas* **17**, 056114 (2010) . Copyright (2010) American Institute of Physics.

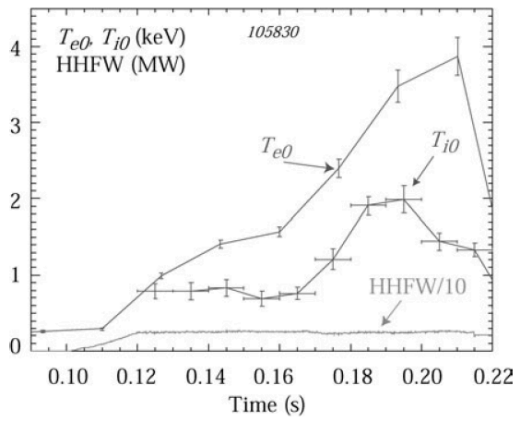

Fig. 109. Central temperatures T_{i0} and T_{e0} as a function of time. Reprinted with permission from B.P. LeBlanc et al., Nucl. Fusion 44, 513 (2004). Copyright (2004) Institute of Physics.

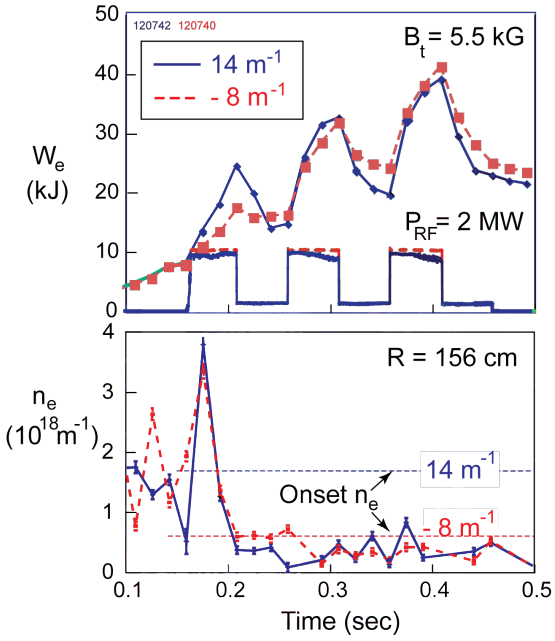

Fig. 111. (a) Electron stored energy evolution with modulated HHFW power of 2 MW with k_ϕ = 14 m^{-1} and -8m^{-1}, respectively. (b) Edge electron density (2 cm in front of Faraday shield) vs. time. The onset density for perpendicular propagation is indicated by the horizontal dashed lines for k_ϕ = 14 m^{-1} and -8m^{-1} as marked. Reprinted with permission from of J. Hosea et al., *Phys. Plasmas* **15**, 056104 (2008). Copyright (2008) American Institute of Physics.

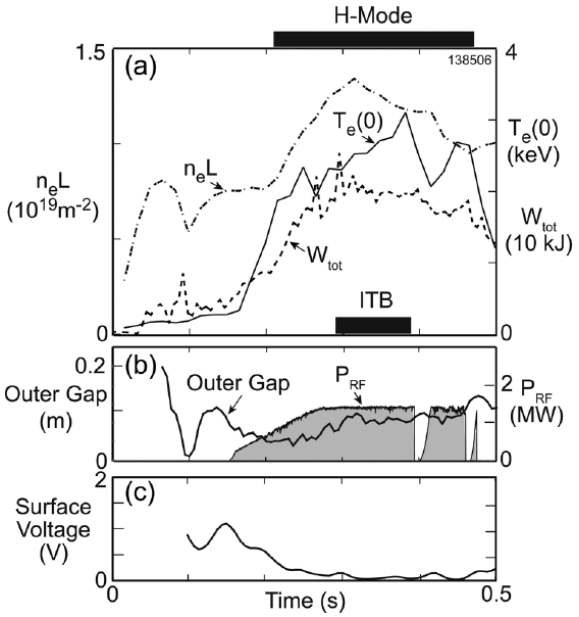

Fig. 110. Time evolution of an I_p = 300 kA HHFW-generated H-mode plasma. (a) Line integrated density (n_eL), central electron temperature ($T_e(0)$) and total plasma stored energy (W_{tot}). (b) Outer gap between the last closed flux surface and the front of the HHFW antenna on the mid-plane and RF power. (c) The measured loop voltage. Reprinted with permission from of G. Taylor et al., *Phys. Plasmas* **19**, 042501 (2012). Copyright (2012) American Institute of Physics.

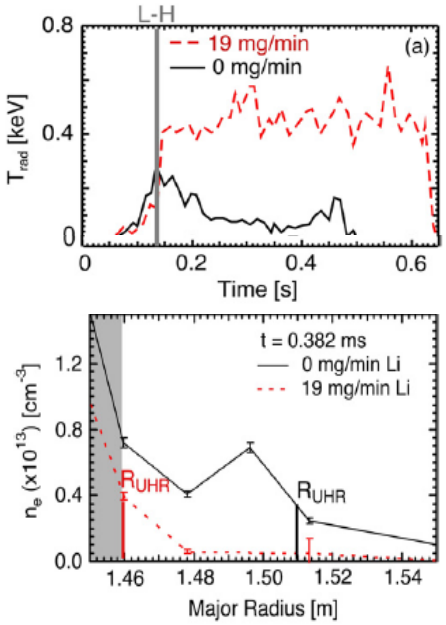

Fig. 112. (a) The EBW coupling efficiency in H-mode with and without lithium in the scrape-off-layer. (b) The Thomsons scattering n_e profiles with and without lithium in the scrape-off-layer for H-mode. Reprinted with permission S. J. Diem et al., *Phys. Rev. Lett.* **103**, 015002 (2009). Copyright (2009) American Physical Society.

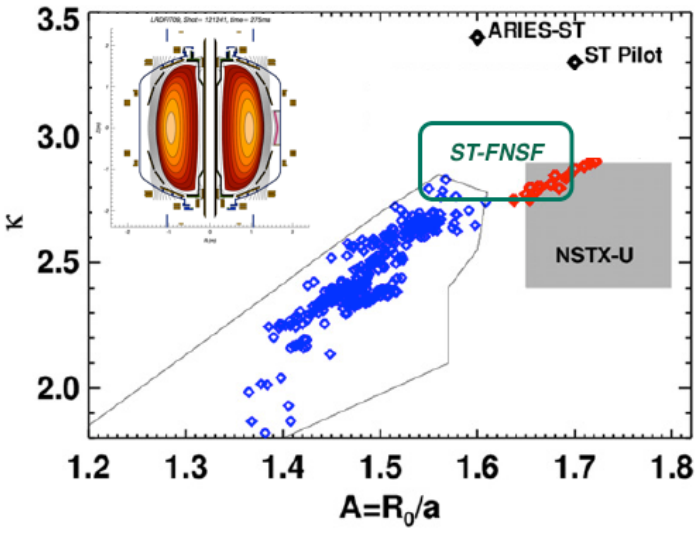

Fig. 113. Plot of elongation versus aspect ratio for NSTX discharges. The black line encloses the historical NSTX operating space for discharges with flat-top duration exceeding 0.5 s, and specific high-performance discharges are indicated in blue. The points collected in the high aspect-ratio experiment are indicated in red. The approximate future device operating space is as labeled. Inset shows $\kappa = 3$ NSTX equilibrium. Reprinted with permission from S.P. Gerhardt et al., *Nucl. Fusion* **51** 033004 (2011). Copyright (2011) Institute of Physics.

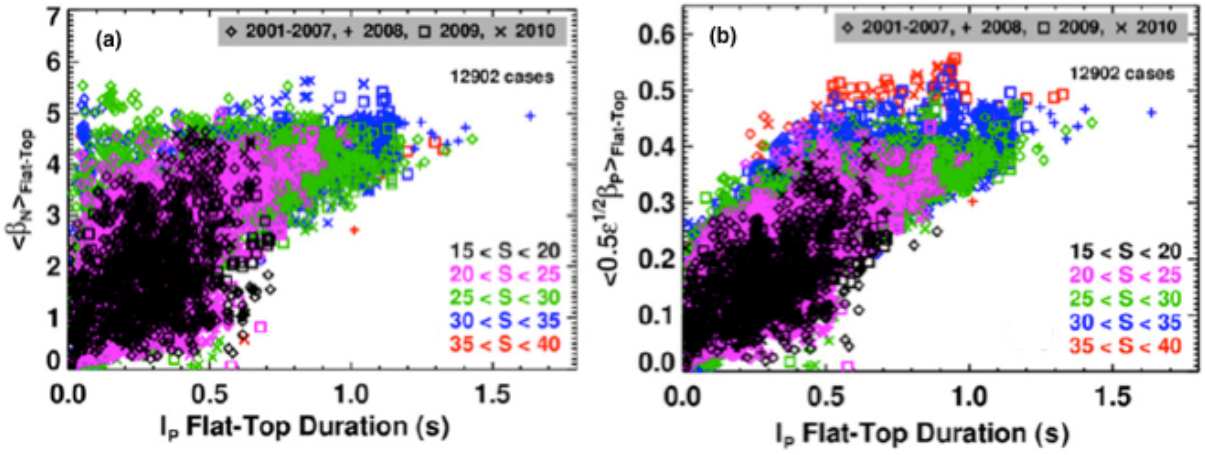

Fig. 114. Flat-top average of global performance parameters plotted against the I_p flat-top duration. The colors represent different values of the shape parameter. The symbols are indicative of the year when the discharge was taken, as indicated in the legend. The quantities shown are (*a*) β_N and (*b*) 0.5 $\sqrt{\varepsilon}\beta_P$. Reprinted with permission from S.P. Gerhardt et al., *Nucl. Fusion* **51** 073031 (2011). Copyright (2011) Institute of Physics.

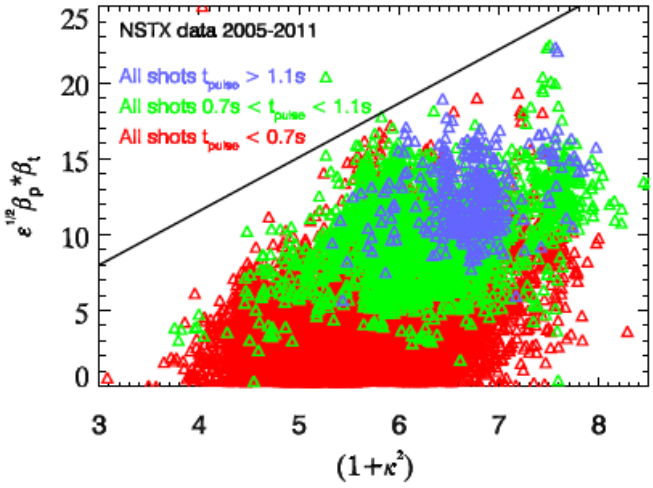

Fig. 115. The quantity $\varepsilon^{1/2}\beta_p\beta_t$ averaged over the plasma current flattop is plotted against $1+\kappa^2$, also averaged over the current flattop. The straight line in the figure is meant to guide the eye. Reprinted with permission from D. A. Gates.

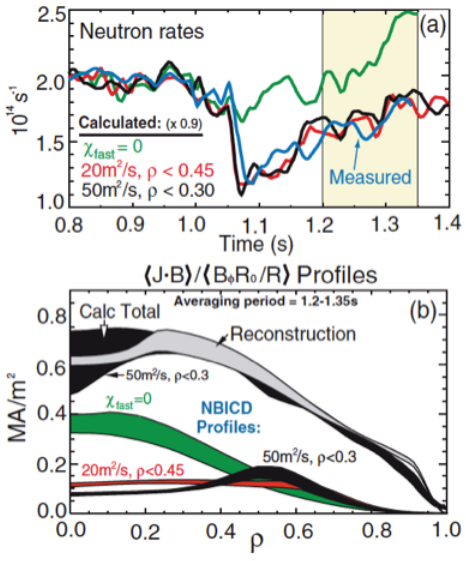

Fig. 117. (a) Measured (blue line) and calculated neutron rates (x 0.9) and (b) comparison of reconstructed (gray) and calculated (black) total parallel current density profile for t = 1.2–1.35 s for the best-fit fast-ion diffusivity model. NBICD profiles for the diffusivities of (a) are also shown. Reprinted with permission J. E. Menard et al., *Phys. Rev. Lett.* **97**, 095002 (2006). Copyright (2006) American Physical Society.

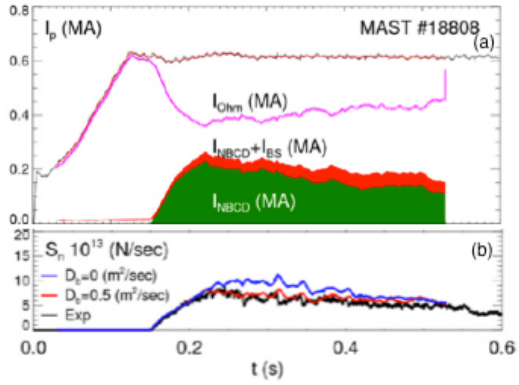

Fig. 116. (a) TRANSP simulated distribution of the total plasma current, I_p, between Ohmic, bootstrap and neutral beam driven components for $D_b = 0.5\text{m}^2\ \text{s}^{-1}$. (b) Experimentally observed neutron yield is compared with TRANSP simulations for $D_b = 0$ and $0.5\text{m}^2\ \text{s}^{-1}$. Reprinted with permission from M. Turnyanskiy et al., *Nucl. Fusion* **49,** 065002 (2009). Copyright (2009) Institute of Physics.

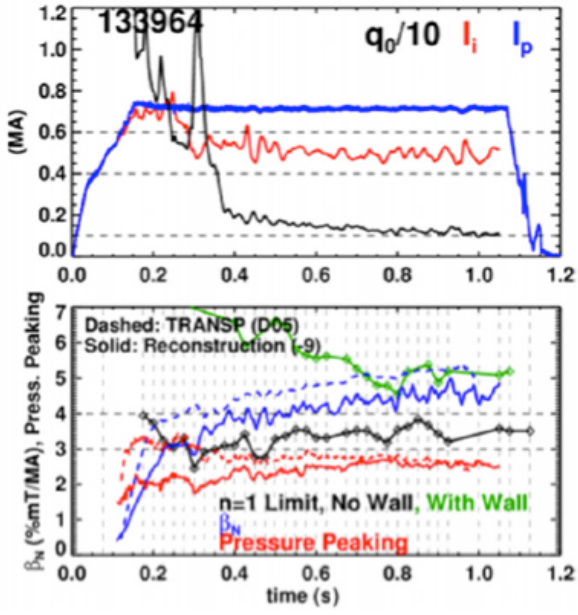

Fig. 118. A high-β_p (0.7MA and 0.48 T) scenario NSTX discharge with lower-l_i and higher pressure peaking. (a) The plasma current, internal inductance and central safety factor as labeled. (b) The normalized β, pressure peaking factor and no- and with-wall stability limits. Reprinted with permission from of S.P. Gerhardt, et al., *Nucl. Fusion* **51** 073031 (2011) . Copyright (2011) Institute of Physics

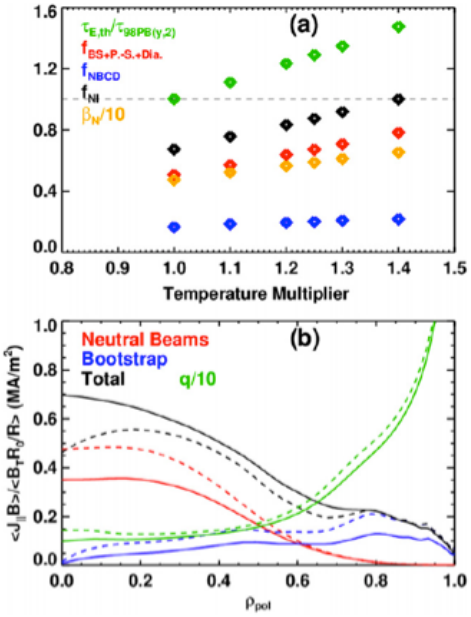

Fig. 119. (a) Dependence of the confinement time, pressure-driven current fraction, beam current drive fraction, total non-inductive fraction and β_N on the temperature multiplier in the TRANSP simulations, and (*b*) profiles for the base configuration (solid) and fully non-inductive configuration (dashed). Reprinted with permission from of S.P. Gerhardt, et al., *Nucl. Fusion* **51** 073031 (2011) . Copyright (2011) Institute of Physics.

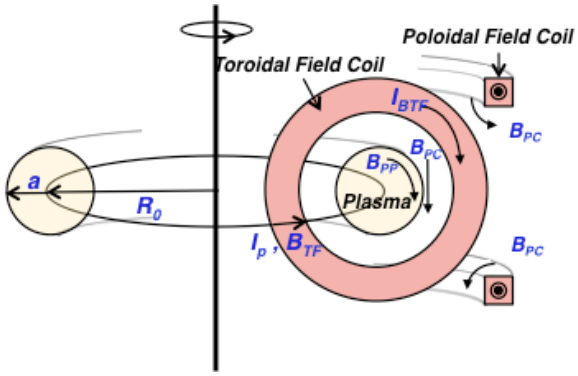

Figure 120. Basic characteristic of a simple circuler tokamak

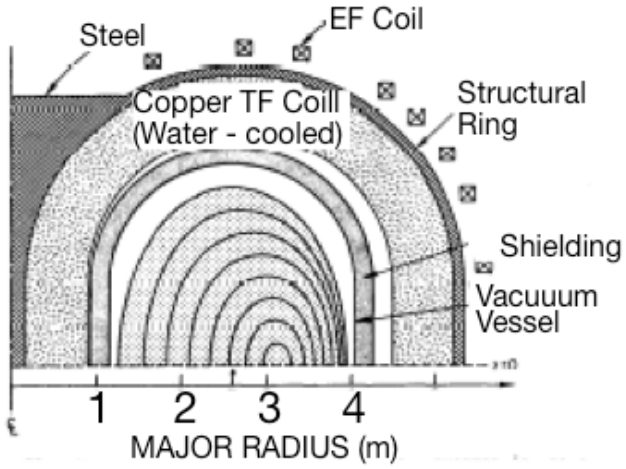

Fig. 121. Elevation view of illustration design for SMARTOR (Small-Aspect-Ratio Torus). EF coil positions are schematic only. B_{TF} = 11 T at R = 0.9m. Reprinted with permission from D.L. Jassby.